UNIVERSITAT POLITÈCNICA DE VALÈNCIA

INSTITUTO INTERUNIVERSITARIO DE INVESTIGACIÓN DE RECONOCIMIENTO MOLECULAR Y DESARROLLO TECNOLÓGICO

Development of enzyme-functionalized hybrid mesoporous nanodevices for advanced chemical communication

PhD. THESIS

Submitted by

Beatriz de Luis Fernández

PhD. Supervisors:

Prof. Ramón Martínez Máñez
Prof. Félix Sancenón Galarza
Dr. Antoni Llopis Lorente

Valencia, July 2021

RAMÓN MARTÍNEZ MÁÑEZ, PhD in Chemistry and Professor at the *Universitat Politècnica de València*, FÉLIX SANCENÓN GALARZA, PhD in Chemistry and Lecturer at the *Universitat Politècnica de València* and ANTONI LLOPIS LORENTE, PhD in Chemistry and Research Associate at the *Eindhoven University of Technology*

CERTIFY:

That the work *"**Development of enzyme-functionalized hybrid mesoporous nanodevices for advanced chemical communication**"* has been developed by Beatriz de Luis Fernández under their supervision in the Instituto Interuniversitario de Investigación de Reconocimiento Molecular y Desarrollo Tecnológico (IDM) of the *Universitat Politècnica de València*, as a Thesis Project in order to obtain the degree of PhD in Chemistry at the *Universitat Politècnica de València.*

Valencia, June 9th 2021.

Prof. Félix Sancenón Galarza Dr. Antoni Llopis Lorente

Prof. Ramón Martínez Máñez

A mis padres,
por apoyarme incondicionalmente en cada paso.

“Sigue nadando”.

Resumen

La presente tesis doctoral titulada “Desarrollo de nanodispositivos mesoporosos híbridos funcionalizados con enzimas para comunicación química avanzada” se centra en el diseño, síntesis y caracterización de varios nanodispositivos híbridos orgánico-inorgánicos, utilizando como soporte nanopartículas de sílice mesoporosa equipadas con enzimas y puertas moleculares, los cuales muestran capacidades comunicativas además de la evaluación de diferentes estrategias de comunicación.

El primer capítulo incluye un resumen de diferentes conceptos sobre los que se fundamentan los estudios realizados tales como nanotecnología, materiales de sílice mesoporosa, materiales con puertas moleculares que reaccionan a estímulos específicos, partículas Janus y biocomputación. Finalmente, se incluyen conceptos básicos acerca de la comunicación química, materiales y estrategias empleados hasta ahora y ejemplos representativos.

A continuación, en el segundo capítulo, se presentan los objetivos generales de esta tesis doctoral que son abordados en los siguientes capítulos experimentales.

El tercer capítulo muestra un sistema de biocomputación para liberación basado en nanopartículas Janus de oro-sílice mesoporosa capaces de comunicarse con el entorno procesando la información e imitando la función lógica booleana propia de un demultiplexer y que resulta en la liberación controlada de la carga. En particular, el nanodispositivo está formado por la enzima galactosa deshidrogenasa anclada en el oro mientras que la parte de sílice mesoporosa se carga con un profluoróforo (4-metilumbeliferil-β-*D*-galactopiranósido) y se funcionaliza con una nanoválvula supramolecular que responde a pH (β-ciclodextrina:benzimidazol). La enzima β-galactosidasa unida a la β-ciclodextrina completa el diseño. El nanodispositivo se comporta como un demultiplexer ya que es capaz de leer información molecular del ambiente (lactosa) y producir una respuesta (galactosa + glucosa). Solo en presencia de una especie directora (NAD^+), un segundo producto es generado (ácido galactónico) debido a la cascada concatenada de reacciones enzimáticas que llevan a la liberación y activación de la carga encapsulada.

Finalmente se muestra que dicho nanodispositivo puede llevar a cabo sus funciones en medios complejos como en células cancerígenas.

En el cuarto capítulo, se presenta un modelo circular de comunicación dentro de una red de tres nanopartículas diferentes basado en el intercambio jerárquicamente programado de mensajes químicos. La parte mesoporosa del nanodispositivo 1 (**S1**$_{\beta gal}$) es cargada con la especie fluorescente $[Ru(bpy)_3]Cl_2$ y tapada con cadenas de oligo(etilenglicol) que contienen puentes disulfuro y que funcionan como puertas moleculares, mientras que la enzima β-galactosidasa es unida a la parte del oro. En la nanopartícula 2 (**S2**$_{galox}$), la enzima galactosa oxidasa es inmovilizada en la cara del oro mientras que la sílice mesoporosa es cargada con 4-(bromometil)benzoato de metilo y los poros tapados con un derivado de arilboronato autoinmolante sensible a H_2O_2 que forma un complejo huésped-anfitrión con β-ciclodextrina. Finalmente, el nanodispositivo 3 (**S3**$_{est}$) es funcionalizado con la enzima esterasa en la parte del oro, cargada con la especie reductora hidroclururo de tris(2-carboxietil)fosfina (TCEP) en la parte mesoporosa y tapada con una nanoválvula supramolecular que responde a pH (β-ciclodextrina:benzimidazol). El proceso de comunicación se activa en presencia de lactosa (estímulo de entrada) la cual es hidrolizada por la β-galactosidasa de **S1**$_{\beta gal}$ para generar galactosa (mensajero 1) que es oxidada por la galactosa oxidasa de **S2**$_{galox}$ para producir H_2O_2. H_2O_2 abre la puerta molecular de **S2**$_{galox}$ liberando el derivado de benzoato (mensajero 2) que es detectado por la esterasa anclada a **S3**$_{est}$ y transformada en el correspondiente ácido benzoico. La bajada de pH local induce la apertura de la nanoválvula sensible a pH liberando el TCEP (mensajero 3). El TCEP cierra el círculo y rompe la puerta molecular de **S1**$_{\beta gal}$ que subsecuentemente libera la señal final de fluorescencia.

En el quinto capítulo, se muestra un modelo interactivo de comunicación química entre una nanopartícula Janus abiótica y un organismo vivo (*Saccharomyces cerevisiae*). En particular, el nanodispositivo está basado en nanopartículas funcionalizadas con glucosa oxidasa en la parte del oro, cargadas con el genotóxico fleomicina y tapadas con la puerta molecular sensible a pH (β-ciclodextrina:benzimidazol). El microorganismo usado en el estudio es una levadura modificada que expresa GFP bajo el control del promotor del gen RNR3; la

transcripción de dicho gen es inducida con la exposición a agentes que dañan el ADN. La ruta de comunicación interactiva empieza con la adición de sacarosa (estímulo de entrada) la cual es hidrolizada en glucosa por la invertasa localizada en el espacio periplásmico de las levaduras y que difunde al nanodispositivo donde es trasformada en el correspondiente ácido por la glucosa oxidasa de la parte del oro. La bajada local de pH da lugar a la apertura de la nanoválvula sensible a pH del nanovehículo y con ello a la liberación de fleomicina (mensaje de vuelta) que induce la expresión de GFP (señal de salida) en las levaduras.

En el sexto capítulo, proponemos una estrategia para establecer una comunicación lineal entre dos microorganismos diferentes que no interactúan entre ellos mediada por un nanodispositivo que actúa como traductor químico. El nanotraductor está basado en nanopartículas mesoporosas de sílice cargadas con el genotóxico fleomicina y tapadas con una puerta molecular sensible al pH (β-ciclodextrina:benzimidazol). Los microorganismos involucrados son bacterias *Escherichia coli* modificadas para expresar β-galactosidasa y levaduras *Saccharomyces cerevisiae* modificadas que expresan GFP ante la exposición a agentes de dañan el ADN ya que su transcripción está controlada por el promotor del gen RNR3. La ruta de comunicación lineal se dispara al añadir lactosa (estímulo de entrada) la cual es detectada e hidrolizada en glucosa y galactosa por las bacterias *E. coli* modificadas para expresar β-galactosidasa. La glucosa (mensajero 1) es entonces trasmitida y detectada por la glucosa oxidasa del nanodispositivo abiótico y oxidada a ácido glucónico induciendo la apertura de la nanoválvula del contenedor mesoporoso. La fleomicina confinada (mensajero 2) es liberada y difunde a las levaduras *S. cerevisiae* que decodifican la información y activan la transcripción de GFP generando una señal fluorescente.

Finalmente, las conclusiones generales de la presente tesis doctoral son expuestas en el capítulo siete. El estudio de las capacidades comunicativas de los nanodispositivos mesoporosos funcionalizados con enzimas permite la construcción de estrategias de cooperación entre diferentes entidades que permiten funcionalidades que van más allá que aquellas llevadas a cabo por agentes individuales. Esperamos que los resultados obtenidos inspiren aplicaciones

futuras en diferentes áreas tales como biomedicina, nanorobots, materiales que imiten la naturaleza y tecnologías de la información.

Resum

La present tesi doctoral titulada "Desenvolupament de nanodispositius mesoporosos híbrids funcionalitzats amb enzims per comunicació química avançada" es centra en el disseny, síntesi i caracterització de diversos nanodispositius híbrids orgànic-inorgànics, utilitzant com a suport nanopartícules de sílice mesoporosa equipades amb enzims i portes moleculars, i que mostren capacitats comunicatives a més de l'avaluació de diferents estratègies de comunicació.

El primer capítol inclou un resum de diferents conceptes sobre els quals es fonamenten els estudis realitzats com ara nanotecnologia, materials de sílice mesoporosa, materials amb portes moleculars que reaccionen a estímuls específics, partícules Janus i biocomputació. Finalment, s'inclouen conceptes bàsics sobre la comunicació química, materials i estratègies utilitzades fins ara i exemples representatius.

A continuació, en el segon capítol, es presenten els objectius generals d'aquesta tesi doctoral que són abordats en els següents capítols experimentals.

El tercer capítol mostra un sistema de biocomputació per alliberament basat en nanopartícules Janus d'or-sílice mesoporosa capaços de comunicar-se amb l'entorn processant la informació i imitant la funció lògica booleana pròpia d'un demultiplexer i que resulta en l'alliberament controlat de la càrrega. En particular, el nanodispositiu està format per l'enzim galactosa deshidrogenasa ancorada en l'or mentre que la part de sílice mesoporosa es carrega amb un profluoròfor (4-metilumbeliferil-β-D-galactopiranòsid) i es funcionalitza amb una nanovàlvula supramolecular que respon a pH (β-ciclodextrina:benzimidazol). L'enzim β-galactosidasa unit a la β-ciclodextrina completa el disseny. El nanodispositiu es comporta com un demultiplexer ja que és capaç de llegir informació molecular de l'ambient (lactosa) i produir una resposta (galactosa + glucosa). Només en presència d'una espècie directora (NAD^+), un segon producte és generat (àcid galactònic) a causa de la cascada concatenada de reaccions enzimàtiques que porten a l'alliberament i activació de la càrrega encapsulada.

Finalment es mostra que aquest nanodispositiu pot dur a terme les seves funcions en mitjans complexos com en cèl·lules canceroses.

En el quart capítol, es presenta un model circular de comunicació dins d'una xarxa de tres nanopartícules diferents basat en l'intercanvi jeràrquicament programat de missatges químics. La part mesoporosa del nanodispositiu 1 (**S1**$_{\beta gal}$) es carrega amb l'espècie fluorescent $[Ru(bpy)_3]Cl_2$ i es tapa amb cadenes d'oligo(etilenglicol) que contenen ponts disulfur i que funcionen com portes moleculars, mentre que l'enzim β-galactosidasa s'immobilitza a la part de l'or. A la nanopartícula 2 (**S2**$_{galox}$), l'enzim galactosa oxidasa s'immobilitza a la cara de l'or mentre que la sílice mesoporosa es carrega amb 4-(bromometil)benzoat de metil i els porus són tapats amb un derivat d'arilboronat autoimmolant sensible a H_2O_2 que forma un complex hoste-amfitrió amb β-ciclodextrina. Finalment, el nanodispositu 3 (**S3**$_{est}$) es funcionalitza amb l'enzim esterasa en la part de l'or, es carrega amb l'espècie reductora hidroclurur de tris (2-carboxietil) fosfina (TCEP) a la part mesoporosa i es tapa amb una nanoválvula supramolecular que respon a pH (β-ciclodextrina:benzimidazol). El procés de comunicació s'activa en presència de lactosa (espècie d'entrada), la qual és hidrolitzada per la β-galactosidasa de **S1**$_{\beta gal}$ per a generar galactosa (missatger 1) que és oxidat per la galactosa oxidasa de **S2**$_{galox}$ per produir H_2O_2. H_2O_2 obri la porta molecular de **S2**$_{galox}$ alliberant el derivat de benzoat (missatger 2) que és detectat per l'esterasa ancorada a **S3**$_{est}$ i transformat en el corresponent àcid benzoic. La baixada de pH local indueix l'obertura de la nanovàlvula sensible a pH alliberant el TCEP (missatger 3). El TCEP tanca el cercle i trenca la porta molecular de **S1**$_{\beta gal}$ que subseqüentment allibera el senyal final de fluorescència.

En el cinqué capítol, es mostra un model interactiu de comunicació química entre una nanopartícula Janus abiòtica i un organisme viu (*Saccharomyces cerevisiae*). En particular, el nanodispositiu està basat en nanopartícules funcionalitzades amb glucosa oxidasa en la part de l'or, carregades amb el genotòxic fleomicina i tapades amb la porta molecular sensible a pH (β-ciclodextrina:benzimidazol). El microorganisme utilitzat en l'estudi és un rent modificat que expressa GFP sota el control del promotor del gen RNR3; la transcripció d'aquest gen és induïda amb l'exposició a agents que danyen l'ADN. La

ruta de comunicació interactiva comença amb l'addició de sacarosa (estímul d'entrada) la qual és hidrolitzada en glucosa per la invertasa localitzada en l'espai periplasmàtic dels rents i que difon al nanodispositiu on és transformada en el corresponent àcid per la glucosa oxidasa de la part de l'or. La baixada local de pH dona lloc a l'obertura de la nanoválvula sensible a pH del nanovehicle i amb això l'alliberament de fleomicina (missatge de tornada) que indueix l'expressió de GFP (senyal de sortida) en el rent.

En el sisé capítol, proposem una estratègia per establir una comunicació lineal entre dos microorganismes diferents que no interactuen entre ells facilitada per un nanodispositiu que actua com a traductor químic. El nanotraductor està basat en nanopartícules mesoporoses de sílice carregades amb el genotòxic fleomicina i tapades amb una porta molecular sensible al pH (β-ciclodextrina:benzimidazol). Els microorganismes involucrats són bacteris *Escherichia coli* modificats per expressar β-galactosidasa i rents *Saccharomyces cerevisiae* modificats que expressen GFP davant l'exposició a agents que danyen l'ADN ja que la seua transcripció està controlada pel promotor del gen RNR3. La ruta de comunicació lineal es dispara a l'afegir lactosa (estímul d'entrada) la qual és detectada i hidrolitzada en glucosa i galactosa pels bacteris *E. coli* modificades per expressar β-galactosidasa. La glucosa (missatger 1) és aleshores transmesa i detectada per la glucosa oxidasa del nanodispositiu abiòtic i oxidada a àcid glucònic induint l'obertura de la nanovàlvula del contenidor mesoporós. La fleomicina confinada (missatger 2) és alliberada i difon a les cèl·lules de *S. cerevisiae* que descodifiquen la informació i activen la transcripció de GFP generant un senyal fluorescent.

Finalment, les conclusions generals de la present tesi doctoral són exposades en el capítol set. L'estudi de les capacitats comunicatives dels nanodispositius mesoporosos funcionalitzats amb enzims permet la construcció d'estratègies de cooperació entre diferents entitats que permeten funcionalitats que van més enllà que aquelles dutes a terme per agents individuals. Esperem que els resultats obtinguts inspiren aplicacions futures en diferents àrees com ara biomedicina, nanorobots, materials que imiten la naturalesa i tecnologies de la informació.

Abstract

This PhD Thesis entitled “Development of enzyme-functionalized hybrid mesoporous nanodevices for advanced chemical communication” is focused on the design, synthesis and characterization of several hybrid organic-inorganic nanodevices using mesoporous silica nanoparticles equipped with enzymes and molecular gates which display communication capabilities as well as the design and evaluation of different communication strategies.

The first chapter includes an overview of the different concepts which lay the foundations of the presented studies such as nanotechnology, mesoporous silica materials, stimuli-responsive gated materials, Janus particles and biocomputing. Basic concepts of chemical communication, materials and enabling technologies employed so far and representative examples in this field are also included.

Next, in the second chapter, the general objectives of this PhD Thesis that are addressed in the following experimental chapters are presented.

The third chapter shows a biocomputing delivery system based on Janus gold-mesoporous silica nanoparticles capable of chemically communicating with the environment and processing the information mimicking a demultiplexer Boolean logic function which results in a programmed cargo release. In particular, the nanodevice is functionalized with the enzyme galactose dehydrogenase on the gold face, loaded with a model pro-fluorophore (4-methylumbelliferyl-β-*D*-galactopyranoside) and capped with a pH-responsive supramolecular nanovalve (β-cyclodextrin:benzimidazole). The enzyme β-galactosidase attached to the β-cyclodextrin completes the design. The nanodevice behaves as a demultiplexer as it is capable of reading molecular information from the environment (lactose) and producing an output (galactose + glucose). Only in the presence of an addressing input (NAD^+), a second output (galactonic acid) is generated due to a concatenated cascade of enzymatic reactions that leads to the delivery of the entrapped cargo and activation. Finally, it is shown that such nanodevice is operative in complex media such as cancer cells.

In the fourth chapter, it is presented a circular model of communication within a network of three different nanoparticles based on the hierarchically programmed exchange of chemical messages. The mesoporous face of nanodevice 1 (**S1$_{\beta gal}$**) is loaded with the fluorescent dye $[Ru(bpy)_3]Cl_2$ and capped with disulfide-containing oligo(ethylene glycol) chains acting as gatekeepers, whereas the enzyme β-galactosidase is attached to the gold face. In nanoparticle 2 (**S2$_{galox}$**), the enzyme galactose oxidase is immobilized on the Au face, while the mesoporous silica is loaded with methyl 4-(bromomethyl)benzoate and the mesopores capped with a H_2O_2-sensitive self-immolative arylboronate derivative which forms a host-guest complex with β-cyclodextrin. Finally, the nanodevice 3 (**S3$_{est}$**) is functionalized with the enzyme esterase on the Au face, loaded with the reductive species tris(2-carboxyethyl)phosphine hydrochloride (TCEP) in the mesoporous face and capped with a pH-responsive supramolecular nanovalve (β-cyclodextrin:benzimidazole). The communication is triggered in the presence of lactose (input) which is hydrolyzed by β-galactosidase on **S1$_{\beta gal}$** to generate galactose (messenger 1) which is oxidized to produce H_2O_2 by galactose oxidase in **S2$_{galox}$**. H_2O_2 uncaps the gatekeeper of **S2$_{galox}$** releasing a benzoate derivative (messenger 2) that is sensed by the esterase anchored on **S3$_{est}$** and transformed into the corresponding benzoic acid. The local drop of pH induces the dethreading of the pH-sensitive nanovalve of **S3$_{est}$** and release of TCEP (messenger 3). TCEP closes the circle and cleaves the molecular gate of **S1$_{\beta gal}$** that subsequently releases the final fluorescent output signal.

In the fifth chapter, it is showed an interactive model of chemical communication between an abiotic Janus nanoparticle and a living organism (*Saccharomyces cerevisiae*). In particular, the nanodevice is based on Janus gold-mesoporous silica nanoparticles functionalized with glucose oxidase on the Au face, loaded with the genotoxin phleomycin and capped with a pH-responsive (β-cyclodextrin:benzimidazole) gatekeeper. The microorganism used in the studies is an engineered budding yeast that expresses GFP under the control of the RNR3 promoter; RNR3 gene transcription is induced upon exposure to DNA-damaging agents. The interactive communication pathway starts with the addition of sucrose (input) which is hydrolyzed into glucose by invertase located in periplasmic space

of yeasts and diffuses to the nanodevice where it is transformed into the corresponding acid by glucose oxidase on the Au face. The local drop in pH leads to uncapping of the pH-sensitive nanovalve in the nanocarrier and the release of phleomycin (feedback messenger) that induces GFP expression (output) in yeasts.

In the sixth chapter, we propose a strategy to establish linear communication between two different non-interacting microorganisms mediated by a nanodevice which acts as a chemical "nanotranslator". The "nanotranslator" is based on mesoporous silica nanoparticles loaded with the genotoxin phleomycin and capped with a pH-responsive (β-cyclodextrin:benzimidazole) gatekeeper. The microorganisms involved are engineered β-galactosidase-expressing *Escherichia coli* bacteria and a budding yeast strain (*Saccharomyces cerevisiae*) which expresses GFP upon exposure to DNA-damaging agents since its transcription is controlled by the RNR3 promoter. The linear communication pathway is triggered by adding lactose (input) which is sensed and hydrolysed by the engineered β-galactosidase-expressing *E. coli* into glucose and galactose. Glucose (messenger 1) is then transmitted and detected by glucose oxidase on the abiotic nanodevice and oxidized to gluconic acid inducing the uncapping of the pH-sensitive nanovalve on the mesoporous nanocarrier. The entrapped phleomycin (messenger 2) is released and diffuses to *S. cerevisiae* that decodes the information and activates GFP transcription reporting a fluorescent signal.

Finally, the general conclusions from this PhD Thesis are presented in chapter seven. The study of communication capabilities of enzyme-functionalized mesoporous nanodevices enables the construction of strategies of cooperation between different entities allowing sophisticated functionalities that go beyond those carried out by individual agents. We hope that the obtained results inspire future applications in different areas such as biomedicine, nanorobots, life-like materials and information technologies.

Publications

Results of this PhD Thesis and other contributions have resulted in the following scientific publications:

- **B. de Luis**, A. Llopis-Lorente, J. Martínez-Latorre, F. Sancenón, C. López, J. R. Murguía and R. Martínez-Máñez. "Nano-Programmed Cross-Kingdom Cell Communication". Submitted, **2021.**

- **B. de Luis**, A. Llopis-Lorente, F. Sancenón and R. Martínez-Máñez. "Engineering chemical communication between micro/nanosystems". *Chemical Society Reviews*, accepted, **2021**.

- **B. de Luis**, Á. Morellá-Aucejo, A. Llopis-Lorente, T. M. Godoy-Reyes, R. Villalonga, E. Aznar, F. Sancenón and R. Martínez-Máñez. "A chemical circular communication network at the nanoscale". *Chemical Science*, **2021**, *12*, 1551-1559.

- **B. de Luis**, A. García-Fernández, A. Llopis-Lorente, R. Villalonga, F. Sancenón and R. Martínez-Máñez. "A 1-to-2 demultiplexer hybrid nanocarrier for cargo delivery and activation". *Chemical Communications,* **2020**, *56*, 9974-9977.

- **B. de Luis**, A. Llopis-Lorente, P. Rincón, J. Gadea, F. Sancenón, E. Aznar, R. Villalonga, J. R. Murguía and R. Martínez-Máñez. "An Interactive Model of Communication between Abiotic Nanodevices and Microorganisms". *Angewandte Chemie International Edition*, **2019**, *58*, 14986-14990.

- S. Jimenez-Falcao, N. Joga, A. García-Fernández, A. Llopis Lorente, D. Torres, **B. de Luis**, Félix Sancenón, P. Martínez-Ruiz, R. Martínez-Máñez and R. Villalonga. "Janus nanocarrier powered by bi-enzymatic cascade system for smart delivery". *Journal of Materials Chemistry B,* **2019**, *7*, 4669-4676.

- S. Jimenez-Falcao, **B. de Luis**, A. García-Fernández, A. Llopis-Lorente, P. Díez, A. Sánchez, F. Sancenón, P. Martínez-Ruiz, R. Martínez-Máñez and R. Villalonga. "Glucose-responsive enzyme-controlled mesoporous nanomachine with a layer-by-layer supramolecular architecture". *ACS Applied Bio Materials,* **2019***, 2,* 3321-3328.

- A. Llopis-Lorente, **B. de Luis**, A. García-Férnandez, S. Jimenez-Falcao, M. Orzáez, F. Sancenón, R. Villalonga and R. Martínez-Máñez. "Hybrid Nanocarriers Act by Processing Logic Tasks: Toward the Design of Nanobots Capable of Reading Information from the Environment". *ACS Applied Materials & Interfaces,* **2018**, *10*, 26494-26500.

- L. Pascual, C. Cerqueira-Coutinho, A. García-Fernández, **B. de Luis**, E. Soares Bernardos, M. Souza Albernaz, S. Missailidis, R. Martínez-Máñez, R. Santos-Oliveira, M. Orzáez and F. Sancenón. "MUC1 aptamer-capped mesoporous silica nanoparticles for controlled drug delivery and radio-imaging applications". *Nanomedicine*, **2017**, *13*, 2495-2505.

- A. Llopis-Lorente, **B. de Luis**, A. García-Férnández, P. Díez, A. Sánchez, M. D. Marcos, R. Villalonga, R. Martínez-Máñez and F. Sancenón. "Au-Mesoporous Silica Nanoparticles Gated with Disulfide-Linked Oligo(Ethylene Glycol) Chains for Tunable Cargo Delivery Mediated by an Integrated Enzymatic Control Unit". *Journal of Materials Chemistry B,* **2017**, *5*, 6734-6739.

Abbreviations and Acronyms

ABTS	2,2′-Azino-bis(3-ethylbenzothiazoline-6-sulfonic acid)
ACN	Acetonitrile
ACs	Artificial cells
ADH	Alcohol dehydrogenase
ADP	Adenosine diphosphate
AGS	Amyloglucosidase
AHL	*N*-acyl-L-homoserine lactone
AI-2	Autoinducer-2
AMP	Adenosine monophosphate
ATP	Adenosine triphosphate
Au	Gold
AuNPs	Gold nanoparticles
APTES	3-aminopropyltriethoxysilane
BDNF	Brain-derived neurotrophic factor
BET	Brunauer-Emmet-Teller
BJH	Barret-Joyner-Halenda
BSA	Bovine serum albumin
CTABr	Cetyltrimethylamonium bromide
^{13}C MAS-NMR	Carbon-13 magic angle spinning nuclear magnetic resonance
CFU	Colony-forming unit
C4-CoA	Butyrylcoenzyme A
C4-HSL	*N*-butyryl-L-homoserine lactone
d	Doublet
DEMUX	Demultiplexer
DMEM	Dulbecco's Modified Eagle's Medium
DLS	Dynamic light scattering
DNA	Deoxyribonucleic acid
DOPC	1,2-dioleoyl-*sn*-glycero-3-phosphocholine
DTAB	Dodecyltrimethylammonium bromide

DTSSP	3,3'-dithiobis(sulfosuccinimidyl) propionate
EA	Elemental analysis
EDC	*N*-(3-dimethylaminopropyl)-*N*^{l}-ethylcarbodiimide
EDX	Energy dispersive X-ray spectroscopy
Enz	Enzyme
Est	Esterase
FBS	Fetal bovine serum
GalDH	Galactose dehydrogenase
Galox	Galactose oxidase
GDH	Glucose dehydrogenase
GFP	Green fluorescent protein
GOx	Glucose oxidase
GPb	Glycogen phosphorylase b
GUV	Giant unilamellar vesicles
G6PDH	Glucose-6-phosphate dehydrogenase
^{1}H NMR	Proton nuclear magnetic resonance
ICT	Information and communication technology
IFN	Interferon-ɣ
INV	Invertase
IPTG	Isopropyl-β-D-thiogalactoside
IUPAC	International Union of Pure and Applied Chemistry
HRP	Horseadish peroxidase
LBA	Luria-Bertani medium containing ampicillin
m	Multiplet
MCM	Mobile Composition of Matter
MPTMS	3-mercaptopropyltrimethoxysilane
MS	Mesoporous silica
MSNPs	Mesoporous silica nanoparticles
MUB	4-methylumbellilferone
MUG	4-methylumbelliferyl-β-D-galactopyranoside
NAD^{+}	Nicotinamide adenine dinucleotide

NADH	Nicotinamide adenine dinucleotide reduced
NHS	*N*-hydroxysuccinimide
NMR	Nuclear magnetic resonance
NPS	Nanoparticles
PBS	Phosphate buffer saline
PDDA	Poly(diallydimethylammonium)
PEG	Polyethylene glycol
PMG	Phosphoglucomutase
PMOs	Periodic mesoporous organosilicas
PNIPAAM	Poly(*N*-isopropylacrylamide)
PS	Polystyrene
PXRD	Powder x-ray diffraction
RA	9-*cis*-retinoic acid
RBC	Red blood cells
Ref	Reference
RFP	Red fluorescent protein
RNR3	Ribonucleotide reductase 3
ROS	Reactive oxygen species
$[Ru(bpy)_3]Cl_2$	Tris(2,2′-bipyridyl)dichlororuthenium(II)
$[Ru(bpy)_3]^{2+}$	Tris(2,2′-bipyridyl)ruthenium(II)
s	Singlet
SAH	*S*-adenosylhomocysteine
SARS-CoV-2	Severe acute respiratory syndrome coronavirus 2
SAM	*S*-adenosyl-methionine
SEM	Scanning electron microscopy
SI	Supporting Information
STEM	Scanning transmission electron microscopy
TBOS	Tetrabutyl orthosilicate
TCEP	Tris(2-carboxyethyl)phosphine hydrochloride
TEM	Transmission electron microscopy
TEOS	Tetraethyl orthosilicate

TGA	Thermogravimetric analysis
THF	Tetrahydrofuran
TMOS	Tetramethyl orthosilicate
TXTL	Cell-free transcription-translation
U	Enzymatic units
UV/vis	Ultraviolet-visible
X-Gal	5-bromo-4-chloro-3-indolyl-β-D-galacto-pyranoside
YPD	Yeast extract Peptone Dextrose
WST-1	Water Soluble Tetrazolium-1 (cell proliferation reagent)
3OC12HSL	*N*-3-(oxododecanoyl)-L-homoserine lactone
3OC6HSL	*N*-(3-oxohexanoyl)-L-homoserine lactone
4-NP	4-nitrophenol
β-*CD*	β-cyclodextrin
β-*gal*	β-galactosidase
β-*gal-CD*	β-galactosidase-functionalized β-cyclodextrin
λ_{abs}	Absorption wavelegth
λ_{em}	Emission wavelength
λ_{exc}	Excitation wavelength

Table of Contents

Chapter 1. General introduction

1.1 Nanotechnology

Nanotechnology is the discipline originated by the convergence of chemistry, material science, physics, engineering, and biology which deals with the synthesis and application of matter on the nanoscale. The word *nano* derives from the ancient Greek prefix *nanos* meaning "dwarf". The scientific world has adopted this term to describe the billionth (10^{-9}) part of some unit scale thus a nanometer (nm) is nine times smaller than a meter. A typical atom ranges from 0.1 to 0.5 nm, SARS-CoV-2 virus is 60-140 nm,[1] a bacterium is about 1 µm (1000 nm), a human cell is approximately 100 µm in diameter (10^5 nm) and, in a closer approach to our vision scale, a tennis ball is 10^8 nm (Figure 1).[2]

[1] N. Zhu, D. Zhang, W. Wang, X. Li, B. Yang, J. Song, X. Zhao, B. Huang, W. Shi, R. Lu, P. Niu, F. Zhan, X. Ma, D. Wang, W. Xu, G. Wu, G. F. Gao, W. Tan, *N. Engl. J. Med.*, **2020**, *382*, 727.
[2] B. S. Murty, P. Shankar, B. Raj, B. B. Rath, J. Murday, *Textbook of Nanoscience and Nanotechnology*, Springer, **2016**.

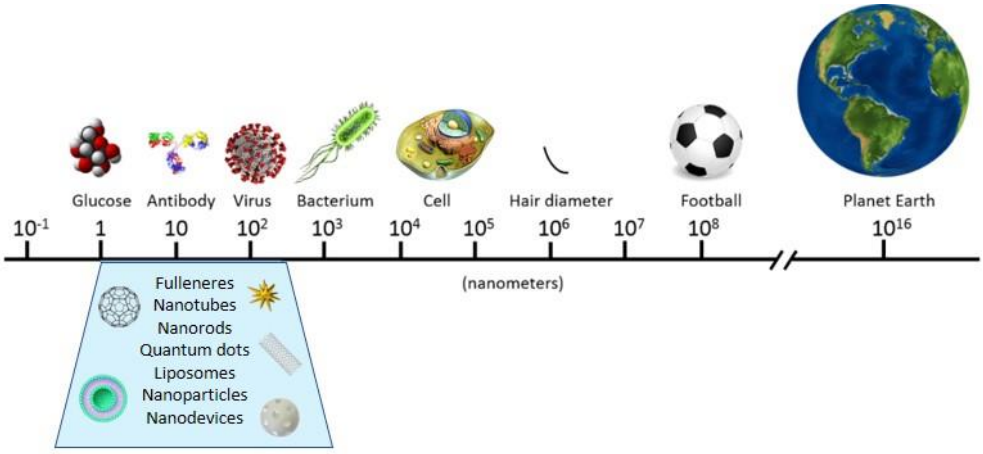

Figure 1. Scheme to compare the range of sizes of biomolecules, nanomaterials, living organisms and other items. *Adapted from A. Llopis-Lorente, Enzyme-functionalized hybrid mesoporous nanodevices for sensing, controlled release and molecular communication, PhD Dissertation, Universitat Politècnica de València,* ***2019****.*

The Nobel Laureate in Physics Richard Feynman was the one who opened up the nanotechnology field with his lecture "*There's plenty of room at the bottom*" at the annual meeting of the American Physical Society in 1959.[3] He encouraged the whole scientific community to inspire from Nature and focus on manipulating and studying things on the small scale. Although Feynman is considered the father of the nanotechnology, it was Norio Taniguchi the first who introduced the term "nanotechnology" at the International Conference on Precision Engineering in 1974.[4] He used the concept to refer to a production technology for precision manufacture with nanometer tolerances. In the 80s, Eric Drexler joined both scientific and technical points of view and advocated the interdisciplinary of the field in his book *Engines of Creation: The Coming Era of Nanotechnology*.[5] In

[3] R. P. Feynman, *Caltech Eng. Sci.* **1960**, *23*, 22.
[4] N. Taniguchi, *Proc. Intl. Conf. Prod. Eng. Tokyo, Part II, Japan Society of Precision Engineering*, **1974**.
[5] E. Drexler, *Engines of Creation: The Coming Era of Nanotechnology*, Anchor, **1987**.

particular, he pointed out the key role of chemistry in building nanomachines able to manipulate matter at the molecular level thus transforming our technology from the bottom-up and predicting a huge technologic revolution in the following years.

One of the peculiarities of the nanoscale is that materials display properties substantially different and often superior to those displayed by single atoms or bulk counterparts with the same composition.[6] This fact has attracted great attention to the understanding, development and discovery of nanomaterials which are those which have at least one of the dimensions in the nanometric range. They can be carbon-based, organic-based, inorganic-based or hybrid. Some examples of nanomaterials are carbon nanotubes, graphene, fullerenes, micelles, liposomes, nanocoatings, nanoparticles, metal organic frameworks or quantum dots. One of the most outstanding properties of nanomaterials is their high specific surface since, geometrically, the surface-to-volume ratio is inversely proportional to the size (Figure 2). This attribute is interesting for catalysis purposes, high-efficient functionalization and encapsulation in porous substrates.

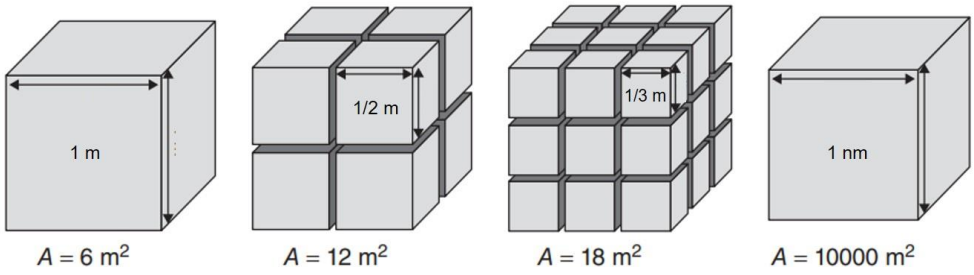

Figure 2. Exponential increases in specific surface area (surface area per unit of mass) for cubes ranging from meter to nanosize. *Adapted from ref. 6 Copyright © 2016 by John Wiley & Sons.*

Since the introduction of the concept, nanotechnology has been explored with enthusiasm from different scientific disciplines and has experienced a rapid

[6] N. Kumar, S. Kumbhat, *Essentials in Nanoscience and Nanotechnology*, John Wiley & Sons, Inc, **2016**.

progress gaining growing importance in society. It has entailed a significant impact in different areas such as biomedicine, materials design, electronics, information and communications technology, energy production and catalysis, among others. Nanomedicine can be defined as the application of nanotechnology for medical purposes (diagnosis, therapy, prevention and monitoring). One of the most studied approaches in this field is the development of drug delivery nanosystems able to release drugs at specific regions or cells, increasing the efficacy of treatments and avoiding adverse side effects.[7] Regarding information and communications technology and electronics, nanotechnology addresses the continuous demand to enhance information storage capacity while reducing weight, size and power consumption. One of the crucial advances achieved with miniaturization are nanoscale transistors which enable new information-processing strategies by exploiting quantum effects and molecular electronics.[5]

Nanotechnology is already considered as the industrial revolution of the 21st century and it is expected to open new futuristic frontiers as further scientific breakthroughs are achieved. Bearing this in mind, unforeseen applications will be found in the near future. Furthermore, the confluence of different research areas and the increasingly close collaboration between academics and industry facilitates a continuous innovation which is quickly incorporated to our daily life.

1.2 Mesoporous silica materials in advanced applications

Porous materials have been one of the most widely studied and developed substrates in nanotechnology due to their large surface area within a relatively small volume enabling appealing applications: catalysis, sensing, separation by

[7] C. Li, J. Wang, Y. Wang, H. Gao, G. Wei, Y. Huang, H. Yu, Y. Gan, Y. Wang, L. Mei, H. Chen, H. Hui, Z. Zhang, Y. Jin, *Acta Pharm. Sin. B*, **2019**, *9*, 1145.

adsorption, storage and drug delivery.[8] According to IUPAC, porous materials are classified regarding the pore size as microporous (< 2 nm), mesoporous (2-50 nm) and macroporous (> 50 nm).[9]

The interest in porous materials started in the 20th century when McBain discovered that some natural minerals retained molecules up to 5 Å in diameter according to their pore size.[10] Barrer and coworkers reported this selective adsorption also in zeolites,[11] which are crystalline microporous aluminosilicate materials that occur naturally but can be synthesized as well to module their size and shape and subsequently their separation properties. This opened a fruitful research field based on the development of industrial adsorbents for purification techniques and also drew attention to its potential use in heterogeneous catalysis.[12]

In this context, Mobil Oil Company researchers were working, as other petroleum corporations, in identifying new zeolites and exploring other kinds of materials with pores over 1 nm to be employed in hydrocarbon refining. It was in 1992 when they reported the synthesis of a family of porous silica solids known as M41S phases with pore diameters from approximately 2 to 10 nm.[13] This family comprises mainly three types of materials identified as Mobile Composition of Matter (MCM) which differ in their mesopores arrangement: MCM-41, MCM-48 and MCM-50 with a hexagonal, cubic and lamellar arrangement, respectively (Figure 3).

[8] a) M. E. Davis, *Nature* **2002**, *417*, 813; b) Z. Li, J. C. Barnes, A. Bosoy, J. F. Stoddart, J. I. Zink, *Chem. Soc. Rev.* **2012**, *41*, 2590.
[9] IUPAC, *Pure appl. Chem.* **1972**, *31*, 578.
[10] J. W. McBain, *J. Phys. Chem.* **1933**, *37*, 149.
[11] R. M. Barrer, D. W. Brook, *Trans. Faraday Soc.* **1953**, *49*, 1049.
[12] M.E. Davis, *Ind. Eng. Chem*. **1991**, *30*, 1675.
[13] C. T. Kresge, M. E. Leonowicz, W. J. Roth, J. C. Vartuli, J. S. Beck, *Nature* **1992**, *359*, 710.

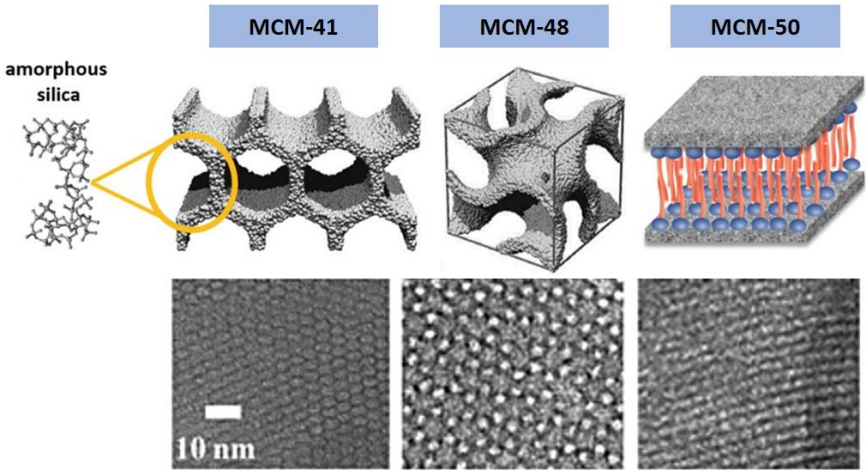

Figure 3. Representation of the M41S family of mesoporous silica materials with the corresponding TEM images of the pore network bellow. *Adapted from Chem. Soc. Rev.* ***2013****, 42, 3663, Copyright © 2013 by The Royal Society of Chemistry and from Handbook of Ecomaterials,* ***2017****, Copyright © 2017 by Springer International Publishing.*

Among M41S phases, MCM-41 structure stands up as it is characterized by very large specific surface areas (up to 1200 $m^2 \cdot g^{-1}$), well-defined ordered pore distribution (hexagonal), tuneable pore sizes (2-10 nm), large adsorption pore volume (0.7-1 $cm^3 \cdot g^{-1}$), amorphous pore walls, chemical inertness, biocompatibility, thermal stability, easy and inexpensive synthesis and easy surface functionalization.[14] Pore size range and volume make MCM-41 a convenient scaffold for the adsorption and hosting of multiple molecules which cannot diffuse into a smaller matrix.

1.2.1 Synthesis of mesoporous silica nanoparticles

The synthesis of mesoporous phases M41S couples inorganic and organic components by combining hydrothermal synthesis and a liquid templating

[14] J. G. Croissant, Y. Fatieiev, A. Almalik, N. M. Khashab, *Adv. Healthcare Mater.* **2018**, *7*, 1700831.

mechanism. It is based on the strategy reported by Stöber in 1968.[15] It requires a solvent, a silica precursor, an organic surfactant and a catalyst. In general, the procedure starts with the dissolution of the surfactant in a polar solvent which behaves as a structure-directing agent by forming ordered arrangements. After a stirring period in a basic pH at a certain temperature, the silica source is added and following a mechanism of hydrolysis (silanol groups formation, Si-OH), polymerization and condensation, a network of siloxane bonds (Si-O-Si) is created around the ordered surfactant used as a template. Different morphologies can be obtained by adjusting different parameters such as the pH value, the surfactant species (anionic, cationic or non-charged of different sizes), the silica source (tetraethyl orthosilicate (TEOS), tetramethyl orthosilicate (TMOS) or tetrabutyl orthosilicate (TBOS), for example), surfactant/silica precursos ratios as well as the addition of cosolvents or heteroatoms, variations in ionic strength, temperature, stirring speed and reaction time.[16] Finally, the material is isolated and dried and the pores become accessible by removing the surfactant template via calcination or solvent extraction processes (acidic reflux). Furthermore, the high temperature reached in calcination promotes additional condensation of the structure.

Regarding the particular material used during this PhD Thesis, 100 nm MCM-41 mesoporous silica nanoparticles (MSNPs) are obtained by dissolving the cationic salt *n*-cetyltrimethylammonium bromide (CTABr) in deionized water basified by adding NaOH while the temperature increases until reaching 80 °C. In this period surfactant forms micelles which subsequently rearrange forming ordered superstructures similar to channels of micelles in a hexagonal disposition. Then the silica precursor tetraethyl orthosilicate (TEOS) is added dropwise starting the condensation over the template turning the colourless solution into a turbid

[15] W. Stöber, A. Fink, E. J. Bohn, *J. Colloid Interf. Sci.* **1968**, *26*, 62.
[16] S.-H. Wu, C.-Y. Mou, H.-P. Lin, *Chem. Soc. Rev*. **2013**, *42*, 3862.

white suspension which is kept stirring for 2 hours. Finally, the solid is isolated by centrifugation, washed several times with water until neutral pH and dried at 70 °C overnight. To obtain the final mesoporous nanoparticles the solid is calcined at 550 °C in an oxidant atmosphere for 5 hours in order to remove the surfactant (Figure 4). As a result, the final MCM-41 mesoporous scaffold presents cylindrical unidirectional channels of pores with a diameter of approximately 2.5 nm.

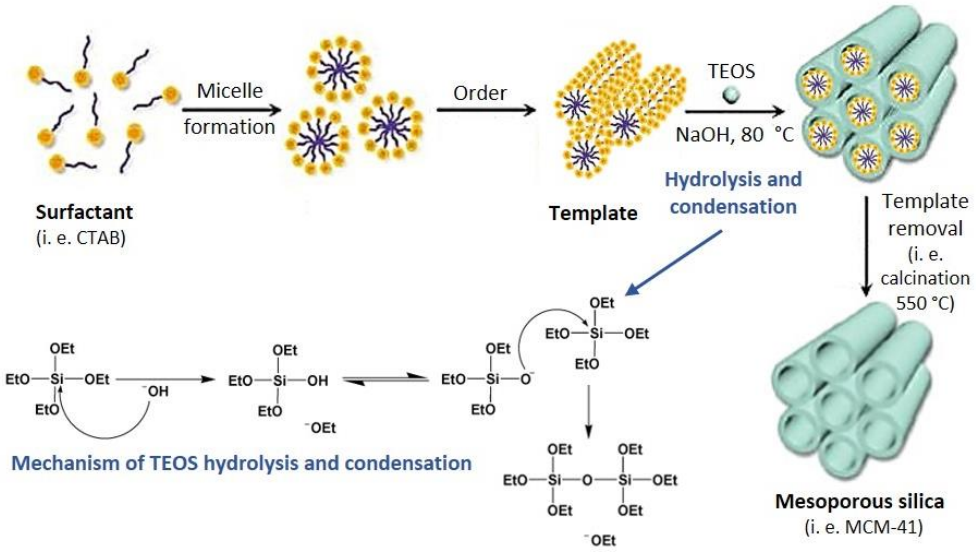

Figure 4. Schematic representation of the synthetic route to obtain MCM-41 mesoporous silica nanoparticles on the top and mechanism of TEOS hydrolysis and condensation in basic medium at the bottom. *Adapted from Adv. Mater.* ***2020****, 1907035. Copyright © 2020 by Wiley-VCH.*

1.2.2 Functionalization of mesoporous silica materials

The external surface of mesoporous silica materials presents a high density of silanol groups (Si-OH) which enable the incorporation of organic groups (functionalization) resulting in hybrid organic-inorganic materials. This symbiosis entails the decisive increment in potential applications which go beyond those achieved by the isolated components. There are three different strategies to

functionalize hybrid materials: (i) grafting, (ii) co-condensation and (iii) the preparation of Periodic Mesoporous Organosilicas (PMOs).[17]

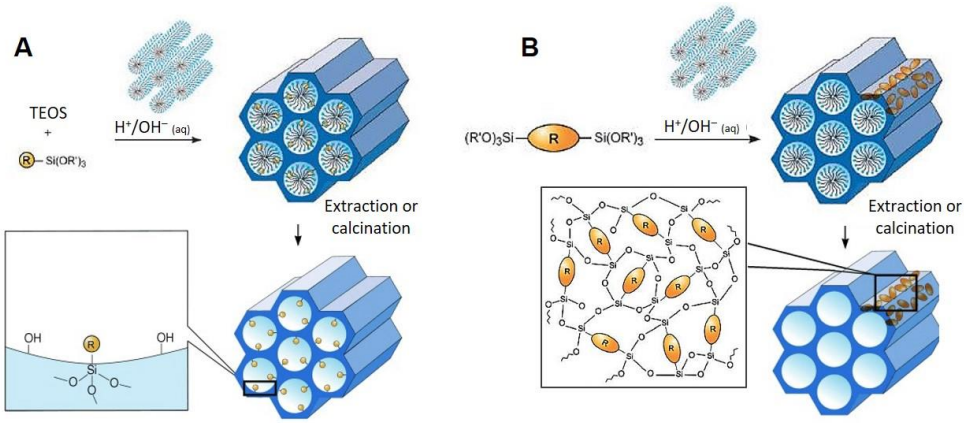

Figure 5. (A) Co-condensation procedure and **(B)** preparation of Periodic Mesoporous Organosilicas for functionalization of the silica surface of mesoporous materials with organic groups where R represents and organic functional group. *Reprinted with permission from ref. 17 Copyright © 2006 by Wiley-VCH.*

The co-condensation method and the preparation of Periodic Mesoporous Organosilicas involves functionalization during the synthesis (one-pot synthesis or direct synthesis). ***Co-condensation*** consists of the simultaneous addition of the silica source and organosilanes (X-R-Si(OR')$_3$, being X-R and R' organic groups) in the presence of the structure-directing agent leading to a structure with organic moieties covalently attached to the external surface and inside the pore walls (Figure 5A). For the preparation of ***Periodic Mesoporous Organosilicas***, bridged organosilica precursors ((R'O)$_3$-Si-R-Si-(OR')$_3$) are employed incorporating homogeneously organic groups in the silica matrix through covalent bonds (Figure 5B). However, both procedures present some drawbacks as some functional groups are difficult to incorporate preserving the order in the mesostructures.

[17] F. Hoffmann, M. Cornelius, J. Morell, M. Fröba, *Angew. Chem. Int. Ed.* **2006**, *45,* 3216.

The procedure employed in the functionalization of mesoporous silica materials in this Thesis is the ***grafting*** protocol, a postsynthetic strategy. It consists of the reaction of the above mentioned silanol groups (Si-OH) present in the silica surface with organosilanes (X-R-Si(OR')$_3$) after the preparation of the mesoporous material and surfactant removal (Figure 6). Some examples of the functional groups added after a nucleophilic substitution reaction (or simple condensation) between the silanols and commercially available trialkosyxilanes are amines, thiols, halides and isocyanates (X-= -NH_2, -SH, -I, -Cl, -NCO).

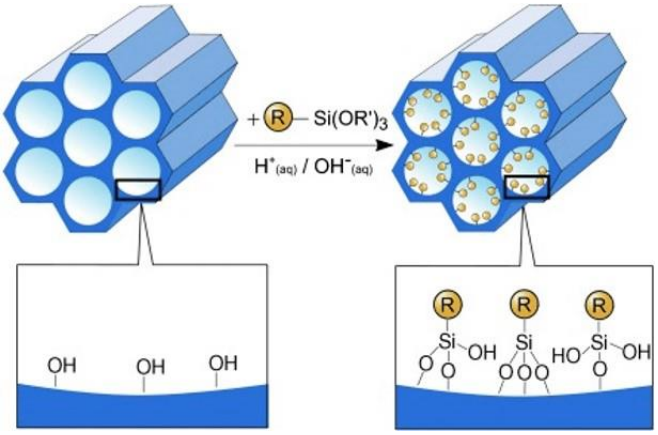

Figure 6. Grafting protocol for functionalization of mesoporous silica with organic groups where R represents an organic functional group. *Reprinted with permission from ref. 17 Copyright © 2006 by Wiley-VCH.*

This alternative is the most commonly used strategy as organic groups are preferentially located on the external surface of the inorganic matrix. Therefore, inner pores are free to further functionalization resulting in dual-functionalized solids. Moreover, another important advantage of this protocol is that the mesoporous structure is maintained and the synthesis of the hybrid solids can be scaled up obtaining large amounts in just one reaction.

1.2.3 Characterization of mesoporous silica materials

Along the preparation of hybrid mesoporous silica materials it is necessary to assess the preservation of the mesoporous structure as well as to analyse the physical properties and composition of the final solids. Several standard techniques are employed to characterize the nanomaterials developed in this Thesis.

Powder X-ray diffraction (PXRD) is a non-destructive technique which provides detailed information about the crystallographic structure. When an X-ray source is projected over a sample, the atoms of the material diffract the X-ray beams in different directions with different intensities and angles according to the atoms distribution. These beams are then collected by a detector to obtain the PXRD patterns (intensity of diffracted beams as a function of the angle of the incident light). These plots are based on the Bragg's law ($2d \cdot \sin\theta = n\lambda$) which establishes that given a distance *d* between atomic planes in an ordered structure (sample) only the X-ray beams at certain angles of incidence θ are reflected (constructive interferences, nλ) resulting in the plotted intensity peaks (Figure 7A). Therefore, there are characteristic PXRD patterns for each ordered material which are indexed and can be used to study the composition and atomic distribution of solids.

Referring to mesoporous silica materials, although the Si and O atoms do not follow a periodic arrangement in the silica matrix, PXRD technique is employed to determine the ordered pore distribution. The characteristic pattern of MCM-41 structure depicts four intensity peaks at low angles corresponding to (100), (110), (200) and (210) Bragg diffraction peaks (Figure 7B). All the diffractograms in this Thesis were obtained with a powder X-ray diffractometer Bruker AXS D8 using Cu-Kα radiation.

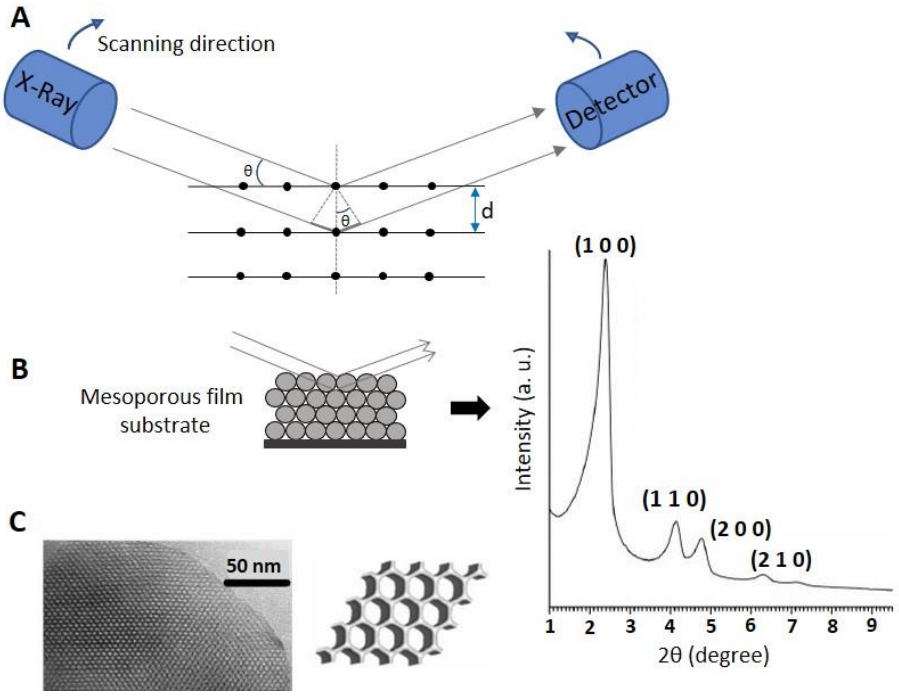

Figure 7. Scheme of X-Ray diffraction experiment. **(A)** Considering a spacing between diffracting planes *d* in an ordered solid, only some incident angles θ lead to a constructive interference (refraction peak) according to Bragg's law (2d sin θ = n λ). **(B)** Characteristic PXRD pattern of MCM-41 based mesoporous silica materials. **(C)** Transmission Electron Microscopy (TEM) image and scheme showing the corresponding hexagonal pore distribution. *Adapted from Chem. Soc. Rev.* ***2013****, 42, 3708. Copyright © 2013 by The Royal Society of Chemistry.*

Transmission Electron Microscopy (TEM) and **Scanning Electron Microscopy (SEM)** are magnification tools which allow the visualization of the morphology and the size of materials with high resolution. Although both techniques employ an electron beam, TEM offers valuable information about the internal structure of the sample as it detects transmitted electrons (which pass through the sample) whereas SEM detects the electrons reflected by the sample providing information about the surface. In addition, **Scanning Transmission Electron Microscopy** coupled with **Energy Dispersive X-ray Spectroscopy (STEM-**

EDX) is used for composition analysis by mapping the different elements in the sample. It employs a high-energy electron beam which displaces electrons from the inner shell of the atoms producing an electronic migration from the outer shell which emits characteristic X-ray wavelengths depending on the element. In this Thesis, TEM images were obtained using a microscopy JEOL JEM-1010 operating at 100 kV and EDX analysis were obtained using a microscopy JEOL JEM-2100F operating at 200 kV.

Nitrogen adsorption-desorption isotherms provide detailed information about pore volume, pore size and specific surface area in porous materials. These curves plot the stepwise multilayer adsorption of a material as the ratio between the quantities of adsorbate (N_2) adsorbed per gram of porous material (adsorbent) as a function of the relative pressure. In this context, empty pores are related in the curve with a high amount of N_2 adsorbed and filled pores with a low amount of N_2 adsorbed. Moreover, the absence of hysteresis loops is ascribed to the homogeneity of the pore arrangement. Isotherms are classified into six types according to the structure of the material being type IV and V typical of porous adsorbents.[18] These curves can be described by mathematical models. The Brunauer-Emmet-Teller (BET) method[19] is usually employed to determine specific surface area and the Barret-Joyner-Halenda (BJH) model[20] is employed to calculate the pore size and the specific pore volume. Nitrogen adsorption-desorption isotherms in this Thesis were obtained using a Micromeritics ASAP2010 Analyzer.

Dynamic light scattering (DLS) allows the determination of the hydrodynamic diameter and size distribution of the particles in colloidal suspension due to the correlation between the fluctuation in scattered light attending the

[18] K. S.W. Sing, D. H. Everett, R. A. W. Haul, L. Moscou, R. A. Pierotti, J. Rouquerol, T. Siemieniewska, *Pure Appl. Chem.* **1985**, *57*, 603.
[19] S. Brunauer, P. H. Emmett, T. Teller, *J. Am. Chem. Soc.* **1938**, *60*, 309.
[20] E. P. Barrett, L. G. Joyner, P. P. Halenda, *J. Am. Chem. Soc.* **1951**, *73*, 373.

Brownian motion of the particles upon laser irradiation. There is also a correlation between the fluctuation in the light scattered by particles and their electrophoretic mobility upon voltage applying which allows the determination of zeta potential values ascribed to the charges on the surface of the particles. Hydrodynamic diameter and zeta potential were obtained using a Malvern Zeta sizer Nano ZS operating with a laser of 633 nm.

As regards the organic functionalization in the prepared materials, it can be evaluated with different techniques such as elemental analysis (EA) and thermogravimetric measurements (TGA). In this thesis the employed method was **elemental analysis (EA)** which consists of the combustion of a weighed small amount of sample in a special furnace determining the percent by weight of some atoms: carbon, hydrogen, nitrogen and sulfur. This information can be related to the quantity of organic molecules anchored to the material during the functionalization steps. EA in this Thesis was performed using a LECO CHNS-932 and a CE Instruments CHNS1100 Elemental Analyzer.

1.3 Stimuli-responsive gated materials

The preparation of hybrid nanomaterials by functionalizing inorganic scaffolds with organic assemblies prompted the development of a wide range of advanced applications in different fields which could not be achieved by inorganic materials.[21] In this scenario, stimuli-responsive gated materials have attracted high interest as they are able to retain a cargo in the pore voids and release it upon the application of selected external stimuli. Gated materials are basically composed of two subunits: (i) an inorganic porous support in which a cargo is loaded and (ii)

[21] a) M. Faustini, L. Nicole, E. Ruiz-Hitzky, C. Sanchez, *Adv. Funct. Mater*. **2018**, *28*, 1704158; b) K. Ariga, D. T. Leong, T. Mori, *Adv. Funct. Mater.* **2017**, 1702905.

switchable or cleavagable (supra)molecular assemblies (known as molecular gates, gatekeepers or nanovalves) grafted onto the external surface acting as gatekeepers. Molecular gates can be finely designed to confine a payload and only in the presence of a determined stimulus they switch their conformation or size leading to a spatio-temporal controlled release (Figure 8).[22]

Since the first reported example in 2003 by Fujiwara and coworkers,[23] gated materials have been widely explored. For instance, different inorganic porous supports such silica nanoparticles,[24] silica-coated metal nanoparticles,[25] anodic alumina[26] and bioactive glasses[27] have been employed for a number of different applications. Among them, mesoporous silica nanoparticles (MSNPs) are probably the most commonly used due to the previously described suitable properties regarding their biocompatibility, high loading capacity, high specific surface and versatility enabled by an easy functionalization via well-known chemistry methodologies.[28] As regards the cargo, dyes, fluorophores or small molecules as drugs have been frequently utilized for sensing and biomedical applications.[29] Considering the gatekeepers, multiple molecular gates composed of

[22] S. Alberti, G. J. A. A. Soler-Illia, O. Azzaroni, *Chem. Commun*. **2015**, *51*, 6050.
[23] N. K. Mal, M. Fujiwara, Y. Tanaka, *Nature* **2003**, *421*, 350.
[24] a) T. D. Nguyen, K. C. -F. Leung, M. Liong, Y. Liu, J. Fraser Stoddart, J. I. Zink, *Adv. Funct. Mater.* **2007**, *17*, 2101; b) E. Climent, A. Bernardos, R. Martínez-Máñez, Á. Maquieira, M. D. Marcos, N. Pastor-Navarro, R. Puchades, F. Sancenón, J. Soto, P. Amorós, *J. Am. Chem. Soc.* **2009**, *131*, 14075; c) E. Poyatos-Racionero, É. Pérez-Esteve, M. D. Marcos, J. M. Barat, R. Martínez-Máñez, E. Aznar, A. Bernardos, *ChemistryOpen* **2019**, *8*, 1052.
[25] a) W.-P. Li, P.-Y. Liao, C.-H. Su, C.-S. Yeh, *J. Am. Chem. Soc.* **2014**, *136*, 10062; b) A. Hernández-Montoto, M. Gorbe, A. Llopis-Lorente, J. M. Terrés, R. Montes, R. Cao-Milán, B. Díaz de Greñu, M. Alfonso, M. Orzaez, M. D. Marcos, R. Martínez-Máñez, F. Sancenón, *Chem. Commun.* **2019**, *55*, 9039.
[26] a) L. Pla, S. Santiago-Felipe, M. Á. Tormo-Más, J. Pemán, F. Sancenón, E. Aznar, R. Martínez-Máñez, *Sensor Actuat. B Chem*. **2020**, 128281; b) L. Pla, E. Xifré-Pérez, A. Ribes, E. Aznar, M. D. Marcos, L. F. Marsal, R. Martínez-Máñez, F. Sancenón, *ChemPlusChem* **2017**, *82*, 337.
[27] L. Polo, N. Gómez-Cerezo, A. García-Fernández, E. Aznar, J.-L. Vivancos, D. Arcos, M. Vallet-Regí, R. Martínez-Máñez, *Chemistry.* **2018**, *24*, 18944.
[28] P. Yang, S. Gai, J. Lin, *Chem. Soc. Rev.* **2012**, *41*, 3679.
[29] E. Aznar, M. Oroval, Ll. Pascual, J. R. Murguía, R. Martínez-Máñez, F. Sancenón, *Chem. Rev.* **2016**, *116*, 561.

supramolecular entities, polymers, bulky organic molecules, peptides, DNA, enzymes, inorganic nanoparticles or combinations of them responding to stimuli such as pH,[30] redox potentials,[31] light,[32] temperature,[33] magnetic fields,[34] target molecules[35] or enzymes[36] have been implemented.

Specifically, in the works reported in this PhD Thesis, hybrid mesoporous silica nanodevices with molecular gates sensitive to pH and redox species have been employed.

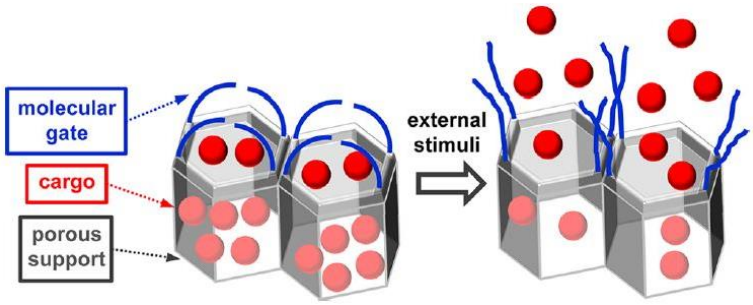

Figure 8. Scheme of the operation of a gated material. *Reprinted with permission from ref. 29 Copyright © 2016 by American Chemical Society.*

[30] a) S. Angelos, Y. -W. Yang, K. Patel, J. F. Stoddart, J. I. Zink, *Angew. Chem. Int. Ed*. **2008**, *47*, 2222; b) A. Bernardos, E. Aznar, C. Coll, R. Martínez-Máñez, J. M. Barat, M. D. Marcos, F. Sancenón, J. Soto, *J. Control. Release* **2008**, *131*, 181.

[31] a) R. Liu, X. Zhao, T. Wu, P. Feng, *J. Am. Chem. Soc.* **2008**, *130*, 14418; b) T. D. Nguyen, H. R. Tseng, P. C. Celestre, A. H. Flood, Y. Liu, J. F. Stoddart, J. I. Zink, *Proc. Natl. Acad. Sci. U. S. A.* **2005**, *102*, 10029.

[32] a) Q. Lin, Q. Huang, C. Li, C. Bao, Z. Liu, F. Li, L. Zhu, L. *J. Am. Chem. Soc.* **2010**, *132*, 10645; b) D. He, X. He, K. Wang, J. Cao, Y. Zhao, *Langmuir* **2012**, *28*, 4003.

[33] E. Yu, I. Galiana, R. Martínez-Máñez, P. Stroeve, M. D. Marcos, E. Aznar, F. Sancenón, J. R. Murguía, P. Amorós, *Colloids Surf. B* **2015**, *135*, 652.

[34] E. Bringas, O. Koysuren, D. V. Quach, M. Mahmoudi, E. Aznar, J. D. Roehling, M. D. Marcos, R. Martínez-Máñez, P. Stroeve, *Chem. Commun.* **2012**, *48*, 5647.

[35] a) Y. Zhao, B. G. Trewyn, I. I. Slowing, V. S.-Y. Lin, *J. Am. Chem. Soc.* **2009**, *131*, 8398; b) À. Ribes, E. Aznar, A. Bernardos, M. D. Marcos, P. Amorós, R. Martínez-Máñez, F. Sancenón, *Chem. Eur. J.* **2017**, *23*, 8581.

[36] a) A. Bernardos, E. Aznar, M. D. Marcos, R. Martínez-Máñez, F. Sancenón, J. Soto, J. M. Barat, P. Amorós, *Angew. Chem. Int. Ed.* **2009**, *48*, 5884; b) D. Yang, T. Wang, Z. Su, L. Xue, R. Mo, C. Zhang, *ACS Appl. Mater. Interfaces* **2016**, *8*, 22431.

pH-triggered gated materials have been widely applied in applications in nanomedicine owing to physiological pH differences. For instance, the extracellular pH is neutral whereas endosomal and lysosomal vesicles formed during endocytosis are slightly acid.[37] In addition, acidic microenvironments are often found in tumour and inflammatory tissues.[38] This fact avoids undesired release in extracellular media and healthy tissues. The operation of the pH-driven molecular gates is based on changes in polarity (attraction/repulsion interactions), conformation or rupture of the gate structures resulting in the opening or closing of the system. Several capping agents with these properties have been developed such as supramolecular ensembles or polymers with pH-hydrolysable linkages, multilayered polyelectrolytes, electrostatic biomolecules (i.e. DNA, proteins) and supramolecular inclusion complexes, among others.

Redox-driven gated materials have also been widely explored due to the important role of redox agents and redox reactions in biological scenarios. It is known that intracellular and extracellular space have a different concentration of reducing agents and cancer cells show a significant increase in redox activity compared to normal cells.[39] Such differences are exploited to control the delivery of nanocarriers equipped with redox-sensitive molecular gates. Some of these capping structures are based on the oxidation and reduction of certain moieties in supramolecular ensembles composed of macrocycles and organic chains leading to a change in conformation or displacement which unblocks the pore voids, being some of them reversible. Another strategy applied is the cleavage of disulfide bonds in the presence of reducing agents and the cleavage of bonds sensitive to reactive oxygen species (ROS) such as hydrogen peroxide H_2O_2, superoxide anion $\cdot O_2^-$ and

[37] M. Zhu, G. Nie, H. meng, T. Xia, A. Nel, Y. Zhao, *Acc. Chem. Res.* **2013**, *46*, 622.
[38] Y. Kato, S. Ozawa, C. Miyamoto, Y. Maehata, A. Suzuki, T. Maeda, Y. Baba, *Cancer Cell Int.*, **2013**, *13*, 89.
[39] A. Acharya, I. Das, D. Chandhok, T. Saha, *Oxid. Med. Cell Longev.* **2010**, *3*, 23.

hydroxyl radical ·OH. These linkages are incorporated in bulky (bio)molecules, polymers or supramolecular complexes grafted on the surface of the scaffold and their rupture results in the release of the entrapped cargo.[40]

As already indicated, the stimuli which triggers the release in gated materials may come from the physiological environment, but they may also come from enzymatic reactions being these enzymes integrated in the same nanodevice. These anchored enzymes act as "effectors" that are the agents that tune the delivery activity of the molecular gates. These "control units" handle the chemical information of the media (substrates) and transform it into new species that regulate the state of the capping agent (open or closed).[41] In this context, the proximity between effectors and gatekeepers enhances the fine tuning of the mass transport from the pores. In addition, the use of immobilized enzymes in nanocarriers increases selectivity in cargo delivery as these biomolecules specifically recognizes their substrates, ability which is very difficult to achieve with abiotic chemical counterparts.

A smart formula to incorporate enzymes to nanodevices is using them as caps as well as effectors. Enzymes can be directly grafted onto the surface of the inorganic scaffolds by organic linkers, retained via attractive interactions with grafted ensembles or convalently bonded to gatekeepers.[42] Metallic particles may also be attached to mesoporous supports to enable enzyme immobilization which, combined with previously mentioned methodologies, allows double enzymatic functionalization.[43] This kind of devices that have two (or more) surfaces with

[40] J. -J. Hu, Q. Lei, M. -Y. Peng, D. -W. Zheng, Y. -X. Chen, X. -Z. Zhang, *Biomaterials* **2017**, *128*, 136.
[41] R. Villalonga, P. Díez, A. Sánchez, E. Aznar, R. Martínez-Máñez, J. M. Pingarrón, *Chem. Eur. J.* **2013**, *19*, 7889.
[42] A. Llopis-Lorente, B. Lozano-Torres, A. Bernardos, R. Martínez-Máñez, F. Sancenón, *J. Mater. Chem. B* **2017**, *5*, 3069.
[43] S. Jiménez-Falcao, N. Joga, A. García-Fernández, A. Llopis Lorente, D. Torres, B. de Luis, F. Sancenón, P. Martínez-Ruiz, R. Martínez-Máñez, R. Villalonga*, J. Mater. Chem. B* **2019**, *7*, 4669.

different chemical and physical properties are called *Janus* devices and enable advanced controlled release applications which are exploited in this PhD Thesis.

1.4 Janus particles

Janus particles are anisotropic systems which have two (or more) surfaces, structures or compartments on different sides.[44] These particles are named after the Roman god *Janus* which is usually represented with two faces looking at opposite directions: the past and the future (Figure 9). *Janus* is the god of doors, beginnings and endings, and transitions. This symbology is explained by the fact that to finish something and start a new beginning it is necessary to pass through a door, starting in one side and ending in the other side. The name of the first month of the year, January, is believed to come from *Janus*.

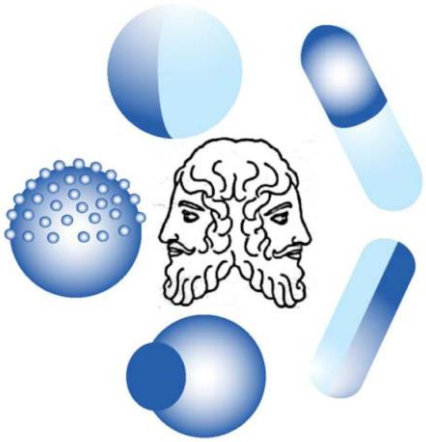

Figure 9. Representation of Roman god Janus and different designs of Janus particles. *Reprinted with permission from ref. 44 Copyright © 2016 by The Royal Society of Chemistry.*

[44] Y. Yi, L. Sanchez, Y. Gao, Y. Yu, *Analyst* **2016**, *141*, 3526.

The term Janus was first employed in scientific field by C. Casagrande and M. Veyssie in 1989 who prepared glass spherical particles with one hemispheric hydrophobic and the other hydrophilic, being amphiphilic solids.[45] However, it was Pierre-Gilles de Gennes, eminent physicist in soft matter, who introduced this concept during his Nobel Laureate speech in 1991 attracting the attention of the scientific community.[46] Since then, multiple polymeric, inorganic and hybrid Janus materials have been synthesized at the micro and the nanoscale. Taking into account that their performance strongly depends on their shape, size, composition and surface chemistry, synthetic methodologies must assess controlled and reproducible properties. The most commonly used strategies are the metal vapour deposition method, the emulsion method and block copolymers photopolymerization, cross-linking or self-assembly by microfluidics equipments.[47]

Being composed of two or more parts with different physical and chemical properties, Janus particles can be differently functionalized displaying different behaviours which may be individually activated under certain conditions or may be synergically coupled to carry out sequential advanced executions. This multifunctional nature let envisage numerous and diverse applications in areas such as sensing, catalysis, stabilizing agents, electronics, drug delivery and theranostics.[44]

The Janus particles employed in this PhD Thesis consist of a gold nanoparticle of *ca.* 20 nm covalently attached to a *ca.* 100 nm mesoporous silica nanoparticle, named Janus Au-mesoporous silica nanoparticles. Gold surface allows functionalization by sulfur chemistry whereas silica surface, as previously described, by means of organosilanes. Janus Au-mesoporous silica nanoparticles are prepared following an adaptation of the Pickering emulsion route which is an

[45] C. Casagrande, P. Fabre, E. Raphael, M. Veyssie, *Europhys. Lett.* **1989**, *9*, 251.
[46] P. G. de Gennes, *Science* **1992**, *256*, 495.
[47] H. Su, C.-A. Hurd Price, L. Jing, Q. Tian, J. Liu, K. Qian, *Materials Today Bio* **2019**, *4*, 100033.

emulsion of oil droplets in water which is stabilized by solid particles adsorbed onto the interface between the two liquid immiscible phases preventing the droplets from coalescing. This phenomenon was described by S. U. Pickering in 1907 and applied for the first time in Janus particle preparation in 2003 by Granick and colleagues.[48] They heated wax and water under magnetic stirring to create an emulsion of dispersed wax droplets in water and added silica microparticles as stabilizers. After cooling down, the wax solidified and the particles were retained at the interface forming colloidosomes. In them, one part of the silica particles was exposed to the aqueous phase while the other was embedded in the wax (see Figure 10). This situation enabled the desired duality as regards surface functionalization: the exposed side may be functionalized in the first place and then, after wax removal by dissolving it in organic solvents, the functionalization of the opposite side may be carried out. The appealing advantages of this emulsion route is that it allows to obtain larger amounts of particles as well as the easy-operation and low cost compared to other synthetic methodologies.

In particular, for Janus Au-mesoporous silica nanoparticles preparation, the exposed side of *ca.* 100 nm mesoporous silica nanoparticle is functionalized with a thiolated organosilane derivative (3-mercaptopropyltrimethoxysilane, MPTMS). The posterior addition of *ca.* 20 nm gold nanoparticles results in the consequent attachment by Au-S bonding. The removal of the wax yields the bare Janus particles as shown in Figure 10.

Janus Au-mesoporous silica nanoparticles were conceived and first prepared by Villalonga, Pingarrón and coworkers in 2013 to construct an H_2O_2 electrochemical biosensor.[49] In this system the enzyme horseradish peroxidase (HRP) was attached to silica face by 3-aminopropyltriethoxysilane (APTES) and

[48] L. Song, S. Jiang, S. Granick, *Langmuir* **2006**, *22*, 9495.
[49] A. Sánchez, P. Díez, P. Martínez-Ruíz, R. Villalonga, J. M. Pingarrón, *Electrochem. Commun.* **2013**, *30*, 51.

glutaraldehyde. The gold face was functionalized with two elements: (i) methoxypoly(ethylene glycol) by direct interaction between gold and sulfur and (ii) streptavidin via 3,3'-dithiobis(sulfosuccinimidyl propionate) (DTSSP). PEG derivative was employed to increase nanoparticle dispersion in water and streptavidin to immobilize the device to a biotin-functionalized gold electrode. This biotin-streptavidin anchoring strategy showed improved recognition efficiency (cathodic current increase) in the presence of the analyte compared to systems prepared employing the usual simple deposition-adsorption methodology.

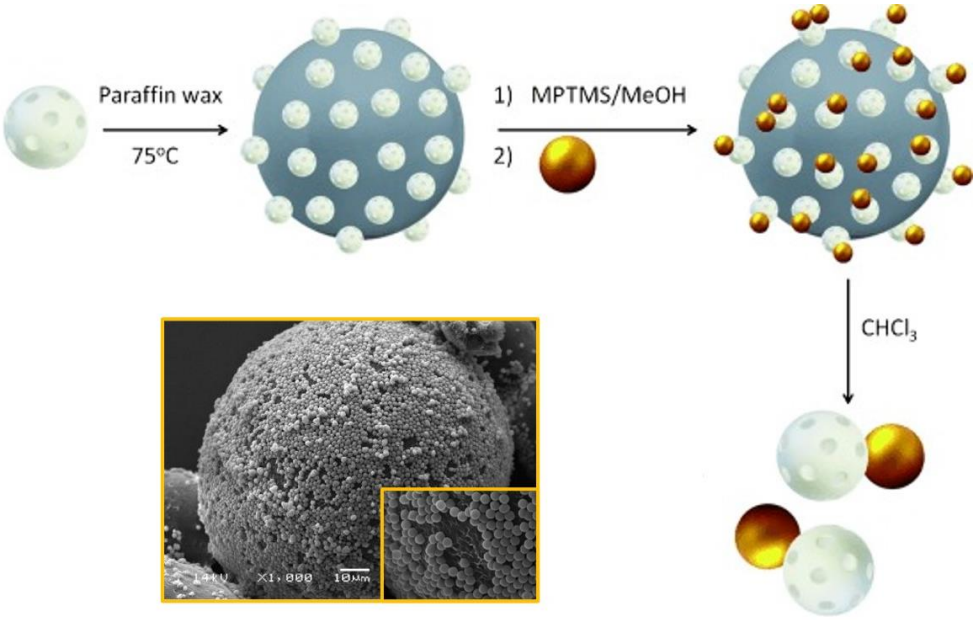

Figure 10. Schematic representation of the synthesis of Janus Au-mesoporous silica nanoparticles and SEM images of silica particles forming a monolayer on the surface of a wax colloidosome. *Adapted from ref. 41 Copyright © 2013 by Wiley-VCH and from ref. 48 Copyright © 2006 by American Chemical Society*.

Villalonga, Pingarrón, Martínez-Máñez and coworkers also reported in 2013 the first use of this Janus Au-mesoporous silica nanoparticles as nanodevices for controlled release.[41] They prepared a stimuli-responsive gating system for

controlled delivery of a cargo comprising a "control unit" and a gated nanocarrier (Figure 11). The control unit consisted of an enzyme (effector) anchored to the gold particle capable of handling the environmental chemical information (input) and transforming it into new species that control the state of the gatekeeper. In this context, chemical microenvironments are created around the nanoparticles enabling the effective intracommunication between the enzyme on the Au face and the silica support. In particular, they entrapped a dye in the mesoporous container, blocked the pores with a pH-responsive capping agent (3-(2-aminoethylamino)propyltrimethoxy silane) that is closed when protonated and used immobilized urease as the effector molecule. Starting from an aqueous solution at pH 5, when urea was present in the surroundings of the nanodevice, urease catalyzed its transformation into CO_2 and NH_3 leading to progressive alkaline pH values which deprotonated aminoethylamino moieties consequently provoking the gate opening and cargo released.

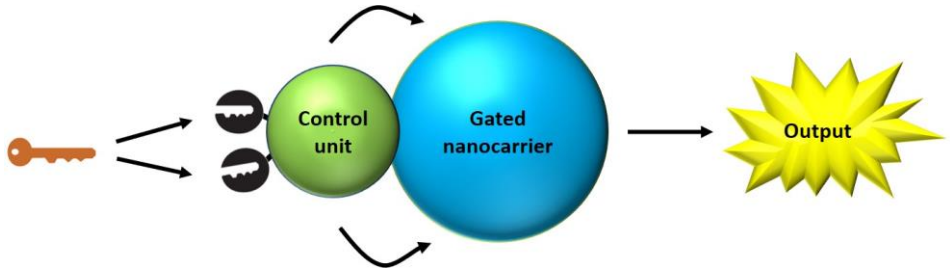

Figure 11. Representation of a Janus Au-MS nanodevice comprising a control unit that regulates the cargo delivery in the gated nanocarrier.

The incorporation of enzymes as control units to gated ensembles forming this type of Janus nanoarchitecture represents an appealing approach to design smart devices capable of finely tuning their cargo release. Furthermore, the inclusion of two or more enzymes (effectors) in the same device opens more complex behaviours. Not only it allows to widen the conditions under which the

device is activated but the immobilization of several enzymes performing concatenated transformations allows to tune even more the specific circumstances which trigger cargo delivery. Given the versatility of the enzymes and the tremendous variety offered by hybrid nanomaterials in terms of the nature of cargos, functionalization and targeting approaches by means of well-known chemistry methodologies,[29] it is easy to imagine multiple varied applications involving sophisticated executions. Up to know, enzyme-functionalized gated Janus Au-mesoporous silica nanoparticles have been employed in sensing[50] and biomedicine[51] performing advanced tasks such as targeted on-command delivery,[52] self-propulsion,[53] chemical communication[54] and logic biocomputing[55] (see Figures 12 and 13).

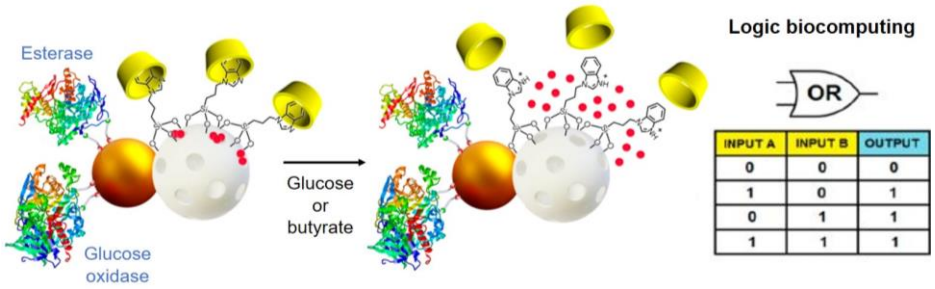

Figure 12. Nanocarrier displaying an OR logic gate behaviour translating the presence "1" or absence "0" of two possible inputs into a YES/NOT output which is delivery "1" or no delivery "0". *Adapted from ref. 55 Copyright © 2014 by American Chemical Society.*

[50] A. Llopis-Lorente, R. Villalonga, M. D. Marcos, R. Martínez-Máñez, F. Sancenón, *Chem. Eur. J.* **2019**, *25*, 3575.
[51] A. Llopis-Lorente, P. Díez, C. de la Torre, A. Sánchez, Félix Sancenón, E. Aznar, M. D. Marcos, P. Martínez-Ruíz, R. Martínez-Máñez, R. Villalonga, *Chem. Eur. J.* **2017**, *23*, 4276.
[52] A. Llopis-Lorente, B. de Luis, A. García-Fernández, P. Díez, A. Sánchez, M. D. Marcos, R. Villalonga, R. Martínez-Máñez, F. Sancenón, *J. Mater. Chem. B* **2017**, *5*, 6734.
[53] A. Llopis-Lorente, A. García-Fernández, E. Lucena-Sánchez, P. Díez, F. Sancenón, R. Villalonga, D. A. Wilson, R. Martínez-Máñez, *Chem. Commun*. **2019**, *55*, 13164.
[54] A. Llopis-Lorente, P. Díez, A. Sánchez, M. D. Marcos, F. Sancenón, P. Martínez-Ruiz, R. Villalonga, R. Martínez-Máñez, *Nat. Commun.* **2017**, *8*, 15511.
[55] P. Díez, A. Sánchez, M. Gamella, P. Martínez-Ruíz, E. Aznar, C. de la Torre, J. R. Murguía, R. Martínez-Máñez, R. Villalonga, J. M. Pingarrón, *J. Am. Chem. Soc.* **2014**, *136*, 9116.

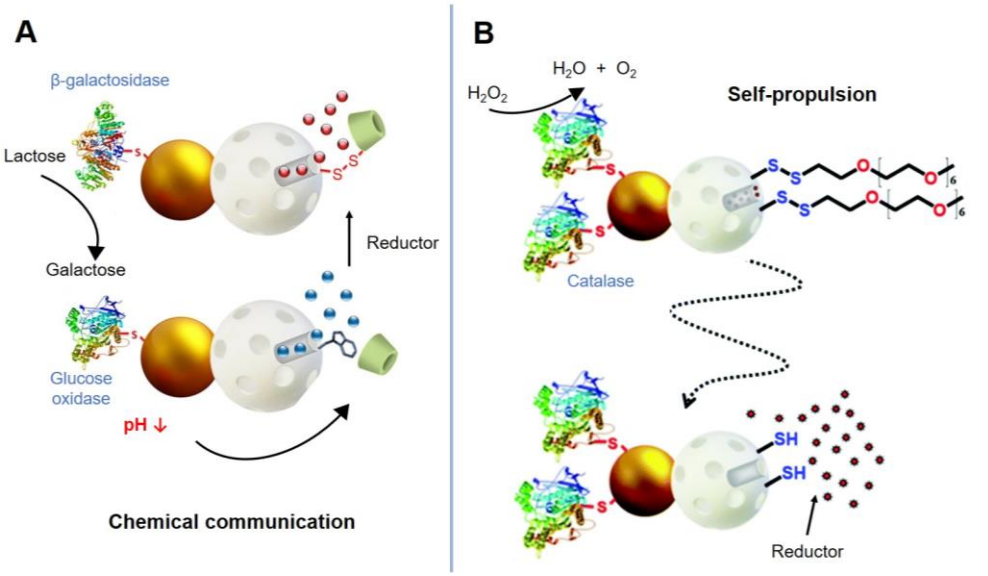

Figure 13. Schemes of sophisticated tasks carried out by enzyme-functionalized gated Janus Au-mesoporous silica nanoparticles. **(A)** Biunivocal chemical communication between two nanodevices. *Adapted from ref. 54 Copyright © 2017 by Nature Publishing Group.* **(B)** Nanomotor performing self-propulsion and on-command cargo delivery. *Adapted from ref. 53 Copyright © 2019 by The Royal Society of Chemistry.*

1.5 Biocomputing

Intelligence can be defined as the ability to sense the environment, analyze information and respond accordingly adapting to the surroundings.[56] The cooperative development of different scientific areas such as synthetic biology, chemistry, and material sciences in addition to the progress in the comprehension of cellular processes have enabled the construction of *smart* nanodevices capable of operating autonomously.[57] These so-called "nanobots", term coming from "robots in the nanoscale", are produced by assembling biological and/or abiotic

[56] R. B. Fletcher, J. Hattie, *Intelligence and Intelligence Testing*, Taylor and Francis, **2011**.
[57] X. Zhang, L. Chen, K. H. Lim, S. Gonuguntla, K. W. Lim, D. Pranantyo, W. P. Yong, W. J. T. Yam, Z. Low, W. J. Teo, H. P. Nien, Q. W. Loh, S. Soh, *Adv. Mater.* **2019**, *31*, 1804540.

nanocomponents. They are programmed to carry out a specific task when necessary, after processing the available physiological information. In this way, nanobots open a wide and attractive range of potential applications in the field of medicine.

Information analysis is usually performed using the language of Boolean algebra which is based on binary values. For instance, in electronics electrical parameters (current and voltage) are not binary by nature but defining a threshold voltage they can be converted into binary values (0 and 1). If the signal voltage is below the threshold, the signal represents a 0 whereas when the signal voltage is above the threshold, the signal represents a 1.[58] The term "logic gates" is used to describe operators that implement basic functions within the binary system; they process combinations of binary inputs (0 and 1) and produce a single binary output. A logic gate is schematically represented by a logic symbol and a truth table. Logic symbols are unique shapes that indicate the operator functionality and truth tables list every possible input combination and the corresponding output. Some Boolean logic gates are AND, NAND, OR, NOR, XOR, XNOR and INHIB gates. For instance, the AND gate is a basic operator which only has 1 as an output when all the inputs are 1 (Figure 14A). By combining basic logic gates in larger circuits more complex logical operations are achieved such as half adders, multiplexers, demultiplexers, encoders and decoders.[59] As an example, a 1-to-2 demultiplexer processes one input and select only one of the possible 2 outputs depending on the presence or absence of an additional input (addressing input). It can be implemented by connecting two AND logic gates operating in parallel and one NOT logic gate (Figure 14B).

[58] B J. LaMeres, *Introduction to Logic Circuits & Logic Design with Verilog*, Springer, **2019**.
[59] S. P. Dandamudi, *Fundamentals of Computer Organization and Design*, Springer, **2003**.

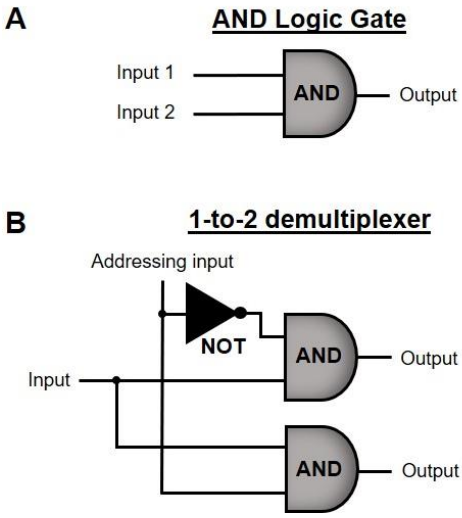

Input 1	Input 2	Output
0	0	0
0	1	0
1	0	0
1	1	1

Input	Add. input	Output 1	Output 2
0	0	0	0
0	1	0	0
1	0	1	0
1	1	0	1

Figure 14. (A) Representation of a 2-input AND logic gate symbol and its corresponding truth table. **(B)** Representation of a 1-to-2 demultiplexer logic symbol and its truth table.

Following this strategy, nanobots are able to analyze physiological information. Neither chemical nor biochemical reactions are naturally binary processes, but they can be interpreted as such by defining a molecular concentration threshold. Input 0 (NO) is commonly considered as the absence of the molecular species whereas input 1 (YES) is a certain concentration above the threshold that is significantly different from zero. In these terms, biocomputing is the science which uses biocompatible reactions as the hardware to implement computational logic operations by processing information and transducing them into binary (YES/NO) decisions.[60]

Since the pioneering work in 1993 by de Silva and coworkers[61] who reported the first parallelism between a photonic molecule sensitive to two different ions and an AND logic gate behaviour, several structures have been successfully applied in processing biochemical information mimicking electronic

[60] a) S. Mailloux, E. Katz, *Biocatalysis* **2014**, *1*, 13; b) Y. Benenson, *Nat. Rev.* **2012**, *13*, 455.
[61] P. A. de Silva, N. H. Q. Gunaratne, C. P. McCoy, *Nature* **1993**, *364*, 42.

counterparts. Some examples are proteins,[62] peptides,[63] enzymes,[64] DNA[65] and organic molecules[66] among others which show the specificity and compatibility required to operate in biological environments.

In particular, enzyme logic systems have attracted growing interest as they naturally respond to metabolites at physiological concentrations. In addition, enzymatic reactions can be concatenated to perform biocatalytic cascades mimicking complex logic networks.[67] For instance, Katz and coworkers designed a system of four coordinated enzymes in solution (alcohol dehydrogenase, amyloglucosidase, invertase and glucose dehydrogenase) which processed up to four different chemical inputs and operated as three chained logic gates in a circuitry (Figure 15).[68] The presence of each input (NADH, acetaldehyde, maltose and sucrose) was represented as 1 and the absence as 0 in binary notation. Depending on the combination of inputs, a different path of enzymatic reactions was followed resulting (1) or not (0) in a lowering in the pH value (output) which was recorded by an electrode functionalized with a pH-sensitive polymer. When the reduced form of nicotinamide adenine dinucleotide (NADH) and acetaldehyde were present in the solution, alcohol dehydrogenase produced NAD^+ and ethanol, operating as an AND logic gate. Glucose was produced either by invertase or amyloglucosidase in the presence of sucrose or maltose respectively, mimicking an OR logic gate. Finally, the generated NAD^+ and glucose were processed by glucose

[62] A. S. Deonarine, S. M. Clark, L. Konermann, *Futur. Gener. Comput. Syst.* **2003**, *19*, 87.
[63] G. Ashkenasy, Z. Dadon, S. Alesebi, N. Wagner, N. Ashkenasy, *Isr. J. Chem.* **2011**, *51*, 106.
[64] E. Katz, V. Privman, *Chem. Soc. Rev.* **2010**, *39*, 1835.
[65] L. Yue, S. Wang, S. Lilienthal, V. Wulf, F. Remacle, R. D. Levine, I. Willner, *J. Am. Chem. Soc.* **2018**, *140*, 8721.
[66] S. Erbas-Cakmak, S. Kolemen, A. C. Sedgwick, T. Gunnlaugsson, T. D. James, J. Yoon, E. U. Akkaya, *Chem. Soc. Rev.* **2018**, *47*, 2228.
[67] a) R. Baron, O. Lioubashevski, E. Katz, T. Niazov, I. Willner, *Angew. Chem. Int. Ed.* **2006**, *45*, 1572; b) E. Katz, *ChemPhysChem.* **2019**, *20*, 9; c) T. Niazov, R. Baron, E. Katz, O. Lioubashevski, I. Willner, *Proc. Natl. Acad. Sci. U. S. A.* **2006**, *103*, 17160; d) M. Privman, T. K. Tam, M. Pita, E. Katz, *J. Am. Chem. Soc.* **2009**, *131*, 1314.
[68] T. K. Tam, M. Pita, M. Ornatska, E. Katz, *Bioelectrochemistry* **2009**, *76*, 4.

dehydrogenase (as another AND logic gate) resulting in the formation of gluconic acid and provoking a drop in the pH solution. From the corresponding truth table (Figure 15C) it was observed that only three combinations of inputs led to the acidic output (NADH + acetaldehyde + maltose; NADH + acetaldehyde + sucrose and NADH + acetaldehyde + maltose + sucrose). In this manner, Katz and coworkers revealed the potential use of enzymes as building units of advanced biocomputing networks capable of performing sophisticated logic operations.

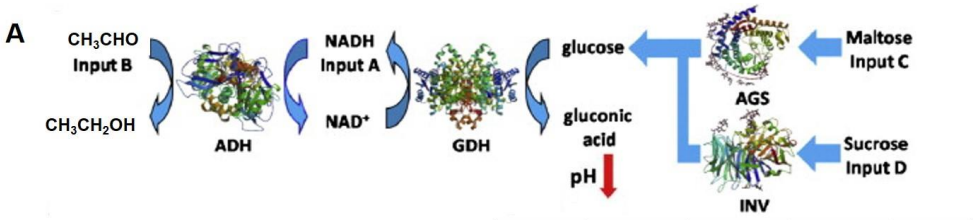

B

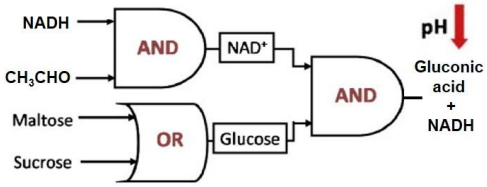

C

Input A (NADH)	Input B (CH_3CHO)	Input C (Maltose)	Input D (Sucrose)	Output
0	0	0	0	0
0	1	0	0	0
1	0	0	0	0
0	0	1	0	0
0	0	0	1	0
1	1	0	0	0
1	0	1	0	0
1	0	0	1	0
0	1	1	0	0
0	1	0	1	0
0	0	1	1	0
1	1	1	0	1
1	1	0	1	1
1	0	1	1	0
0	1	1	1	0
1	1	1	1	1

Figure 15. (A) Representation of a four-enzyme biocatalytic cascade (alcohol dehydrogenase (ADH), amyloglucosidase (AGS), invertase (INV) and glucose dehydrogenase (GDH)) triggered by suitable combinations of four possible inputs: NADH, acetaldehyde, maltose and sucrose. **(B)** Representation of the equivalent logic circuitry composed of three concatenated logic gates and **(C)** its truth table. *Adapted from ref. 68 Copyright © 2009 by Elsevier B.V.*

In addition to the analysis of the surrounding information, biocomputing machinery can be coupled to an actuator transducing the final biochemical output into different functionalities.[69] The interfacing of biocomputing systems with optical methods or electrodes results in novel digital biosensors.[60] Likewise, they can be implemented in stimuli-responsive materials for controlled-release applications leading to the next generation of decision-making devices.[70] Nanodevices with built-in logics are especially interesting for theranostics purposes since they might are capable of reading out concentration changes of specific biomarkers and autonomously respond via cargo delivery (drugs or imaging agents).

Janus Au-mesoporous silica capped nanoparticles represent an appropriate scaffold to couple biocomputing elements (enzymes) and delivery functionalities due to their double nature which allows enzyme anchoring (gold face) as well as cargo entrapment (mesoporous face). Pingarrón, Villalonga, Martínez-Máñez and coworkers reported for the first time in 2014 Janus-type nanoparticles which behaved as a logical OR operator.[55] Mesoporous container was loaded with a dye (tris(bipyridine)ruthenium(II) chloride, $[Ru(bpy)_3]Cl_2$) and capped with a pH-responsive β-cyclodextrin-benzimidazole inclusion complex nanovalve whereas glucose oxidase and esterase where immobilized on the Au surface. Using binary notation, presence of each stimulus and finally cargo delivery was represented as 1 while absence of them or no release as 0. Both, in the presence of glucose or ethyl butyrate, the enzymatic reactions performed by the nanodevice led to a reduction of the pH in the solution (gluconic acid or butyric acid production) resulting in the gate opening and cargo release (Figure 12). Besides, by anchoring another enzyme to the gold unit (urease) they achieved an INHIBIT logic behaviour. When urea was

[69] E. Katz, *ChemPhysChem* **2017**, *18*, 1688.
[70] A. A. Tregubov, P. I. Nikitin, M. P. Nikitin, *Chem. Rev.* **2018**, *118*, 10294.

present, urease catalyzed its hydrolysis into CO_2 and NH_3 increasing the solution pH value thus inhibiting gate opening. Finally, the nanodevice operation was successfully tested in HeLa cancer cells demonstrating its suitability for in-cell applications. In that case, the nanocontainer was loaded with a cytotoxic molecule (doxorubicin) provoking apoptotic cellular death as final output.

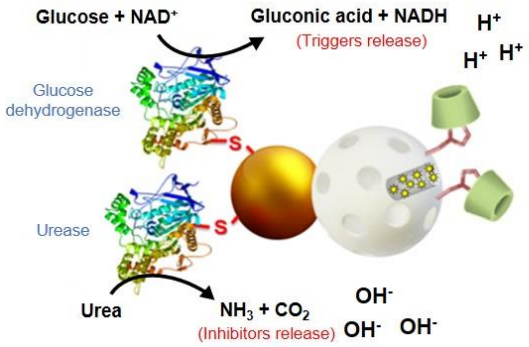

INHIBIT Operator

Input A (Glucose)	Input B (NAD^+)	Input C (Urea)	Output (Release)
0	0	0	0
0	1	0	0
1	0	0	0
0	0	1	0
1	0	1	0
0	1	1	0
1	1	0	1
1	1	1	0

Figure 16. Representation of a Janus Au-mesoporous silica capped nanoparticle functionalized with glucose dehydrogenase and urease on the gold surface which mimics an INHIBIT logic operator switching off an AND logic gate when 3 inputs are present (glucose, NAD^+ and urea) and the corresponding system truth table. *Adapted from ref. 71 Copyright © 2018 by American Chemical Society.*

Following the same methodology, Martínez-Máñez, Villalonga, and coworkers described in 2018 another enzyme-functionalized Janus Au-mesoporous silica capped nanoparticles acting as an AND or INHIBIT logic gate.[71] The mesoporous container was loaded and capped with the same dye ($[Ru(bpy)_3]Cl_2$) and a supramolecular pH-responsive nanovalve (β-cyclodextrin-benzimidazole inclusion complex) whereas the gold unit was functionalized with glucose dehydrogenase and urease. As mentioned before, it is the combination of these

[71] A. Llopis-Lorente, B. de Luis, A. García-Fernández, S. Jimenez-Falcao, M. Orzáez, F. Sancenón, R. Villalonga, R. Martínez-Máñez, *ACS Appl. Mater. Interfaces* **2018**, *10*, 26494.

enzymes (biocomputing machinery) which determinates the nanodevice logic behaviour. Only when both glucose and the enzymatic cofactor nicotinamide adenine dinucleotide (NAD^+) were present in the solution, cargo release was triggered due to the gluconic acid production by glucose dehydrogenase (AND operator). When urea was also present, the hydrolysis carried out by urease increased the pH subsequently switching off the AND gate and the release (INHIBIT operator, Figure 16). They also demonstrated the nanodevice logic performance in complex biological settings (HeLa cancer cells).

As described, enzyme-functionalized nanodevices may be employed for biomedical purposes analysing physiological information, identifying abnormal levels of specific chemical molecules indicative of health disorders and producing convenient responses such as signalling (diagnosis), homeostasis (self-regulation) or drug delivery. Enzymes provide the required biocomputing machinery for these purposes. Bearing in mind the broad range of available enzymes and their nearly limitless combinations as well as the numerous gatekeepers responsive to multiple chemical inputs,[29] hybrid nanocarriers display an appealing potential to become a universal platform capable of implementing different Boolean logic operators, processing environmental chemical information. This concept is explored in Chapter 3 of this PhD Thesis.

However, taking into account the complexity of the cellular media, it is reasonable to consider that just an individual nanodevice with built-in logics would not successfully process all the available information and achieve a desired final action but a network of coordinated nanodevices performing advanced logic operations would be necessary for such task. In the same manner that logic gates are connected in serial or parallel to construct circuits with sophisticated operations (hardware), nanodevices can be designed and programmed to be integrated in a larger community in which different members work together enabling

functionalities that go beyond those carried out by individual agents. For this, nanodevices must be able to communicate effectively on equal terms that logic gates are physically wired in conventional electronics. This transmission of information from one entity to another is possible by designing double sender-receiver stimuli-responsive systems which interact with one another via the interchange of messengers. This means that the chemical output of one member is used as input by other member of the community, and then the successive second output acts as an input for another entity and so on, as it happens between neurons which communicate with each other by means of neurotransmitters. The study, comprehension and optimization of chemical communication processes, which are the aims of Chapters 4, 5 and 6 in this PhD Thesis, are key factors for the concatenation of several nanodevices into complex biocircuits, thus laying the foundations of future nanobots neural networks.[72]

1.6 Chemical communication

Chemical communication, based on the exchange of molecules as messengers, allows different entities to share information, cooperate and orchestrate collective behaviors. Strategies of chemical communication have been explored using different approaches that include nanomaterials, synthetic biology and information-processing tools. Moreover, the study of chemical communication between micro/nanosystems is becoming a key emergent topic in micro/nanotechnology, biomimicry and related areas. Although studies in this direction are very recent, they can be divided in two main categories: (i)

[72] a) L. Qian, E. Winfree, J. Bruck, *Nature* **2011**, *475*, 368; b) S. Kim, N. Kim, J. Seo, J. -E. Park, E. H. Song, S. Y. Choi, J. E. Kim, S. Cha, H. H. Park, J. -M. Nam, *Sci. Adv.* **2020**, *6*, eabb3348.

communication between abiotic systems and (ii) communication between living and abiotic systems.

The last decades have seen a tremendous progress in the design of micro- and nanoparticles for diverse applications in areas such as medicine, sensing, biotechnology and environmental science. Such small functional devices, with dimensions ranging from one to a few hundred nanometers, are usually constructed using a bottom-up approach by assembling abiotic and biological components into tailor-made micro/nanoarchitectures for a number of purposes.[57] In addition, another contemporary trend is the construction of artificial life-like systems that capture structural and functional aspects of the cell.[73] This biomimicry approach involves the design of microcompartments and nano-organelles combining micro/nanotechnology and/or synthetic biology methods. Notwithstanding, regardless of the context, most of these micro- and nanosystems reported to date have been studied as single non-interactive entities; whereas, in comparison, engineering communication involving micro/nanoparticles is a barely studied emerging topic. Thus, while new micro/nanodevices are reported every year, communication between them may expand the capabilities of single particles by allowing them to share information and to cooperate.

In communication theory terms, communication can be defined as the process of establishing a connection between two points for information exchange.[74] It involves a flow of information from the sender, at the first point of the network, to the receiver on another point at the target site. Communication is usually triggered by a certain stimulus on the first point – the stimulus induces the sender to encode a message for the receiver. In addition, communication also requires a shared language that both sender and receiver can understand, as well

[73] B. C. Buddingh', J. C. M. Van Hest, *Acc. Chem. Res.* **2017**, *50*, 769.
[74] I. F. Akyildiz, F. Brunetti, C. Blázquez, *Comput. Networks* **2008**, *52*, 2260.

as a suitable medium for the transmission of information. Finally, effective communication results in a desired action or response as the output of the process.

Although information and communication technologies (ICTs) have been crucial for technological development at the macroscale, the realization of communication between micro/nanomachines is not trivial and requires a different approach as compared to macroscale systems. In fact, especially at the nanoscale, traditional communication technologies are difficult to apply. In this context, an interesting approach for establishing communication is to mimic how nature communicates. In this scenario, chemical or molecular communication, based on transmitting and receiving information by means of molecules (chemical messengers) is one of the communication forms used by living organisms. This chemical communication, also known as molecular communication, offers interesting advantages such as the small nanoscale size of the chemical messengers, minimal energy requirements and the possibility to actuate in physiological and biological environments. In fact, the exchange of information via molecular messengers is the main way of communication across the natural world – it is ubiquitously used by biological systems and embraces from cell-to-cell communication, including the regulation of physiological functions, to the coordination of collective behaviors within communities of unicellular or pluricellular organisms.

Looking at nature, an illustrative example in this context is the utility of neurotransmitter molecules in the central and peripheral nervous system – for instance, neurons release acetylcholine to propagate information to neighbors and ultimately activate cholinergic receptors on muscle cells. In addition, neurons can also release other neurotransmitters to exert excitatory (e.g., glutamic acid) or inhibitory (e.g., γ-aminobutyric acid) effects. Another example is the release of insulin hormone by pancreas cells to the blood stream, to activate receptors and

induce glucose uptake in distant cells. At collective level, bacteria, insects (e.g., ants) and fish, among others, employ molecular messengers (i.e., pheromones) to execute coordinated functions. In particular, bacteria communicate via quorum sensing – individual bacterial cells secrete signaling molecules (the so-called autoinducers or quorum molecules) and upon reaching a threshold cell/autoinducer concentration, certain collective bacterial behaviors (such as swarm motility, virulence or biofilm formation) are activated. Similarly, members of termite populations and fish shoals secrete alarm molecules in response to environmental threats that alert peers and induce a collective response such us population escape or the release of defensive toxins. Another particular communication pathway in nature is represented by the concept of stigmergy; in this indirect mechanism the trace left by the first actor in the environment stimulates the subsequent behavior of the second.[75]

Inspired by biological systems, engineering chemical communication between micro/nanosystems is receiving increasing attention from scientists of diverse communities such as nanotechnology, stimuli-responsive materials, artificial cell research, synthetic biology, and microbiology. An indication of the youth of this research area is the fact that the majority of works have been published in the last five years and their number is still quite limited. Although chemical networks have been described using DNA, enzymes, or molecules in solution, communication networks using micro/nanosystems will lead to the design of systems of another level of complexity. In living systems, cells concentrate a number of chemical reactions, yet it is only when cells talk to one another (i.e. communicate) when they are able to organize in complex living organisms and more advanced functions appear that would not be possible in a solution containing all (bio)chemical components. In this scenario, the advantages of

[75] G. Theraulaz, E. Bonabeau, *Artif. Life* **1999**, *5*, 97.

micro/nanoparticles that communicate each to another are immediately obvious: they constitute the basis of a dynamically interacting network eventually resulting in certain autonomy. Establishing the basis of communication between micro/nanoparticles will bring relevant developments in the design of communities of nanoparticles achieving new smart functions. The importance of the topic relies not only on its novelty and interdisciplinarity, but it is also expected to provide breakthroughs in many areas.

1.6.1 General concepts

- **Models of communication**

A model of communication can be defined, in communication theory terms, as a general representation of the flow of information between different points following a specific pathway. Therefore, chemical communication networks can be established and described following different models (Figure 17). Although modes of communication can be almost unlimited, we will describe only those that are simpler and have been typically used in the examples reported by now.

In the **linear** model (Figure 17A), information is channeled from the sender and transmitted through a certain medium to the receiver. Upon receiving the message, the receiver decodes it and produces the output of the network. In this way, information transmission in the linear model follows a simple unidirectional pathway between two points. In some studies, this type of communication is also referred as sender-receiver communication. Combination of several linear communication pathways allows to construct more complex networks.

In a **cascade** system (Figure 17B), several members are hierarchically connected via subsequent linear pathways. In the simplest 3-member cascade, the

first receiver shows a double nature also acting as a subsequent sender in a second step. In this way, the initial source of information is separated from the output site by intermediate interconnected processes. In principle, the potential number of involved members is limitless; however, the possible loss of information when increasing the number of chained entities should be considered in this model.

An **interactive** model of communication can be considered as two linear pathways piled on top of each other (Figure 17C). It involves two entities with a double sender-receiver nature, which exchange information in a bidirectional way. In such systems, a message is transmitted from the sender to the receiver. Straightaway, the roles are reversed, and the receiver transmits a response (feedback) to the original sender, which now acts as receiver and executes an output.

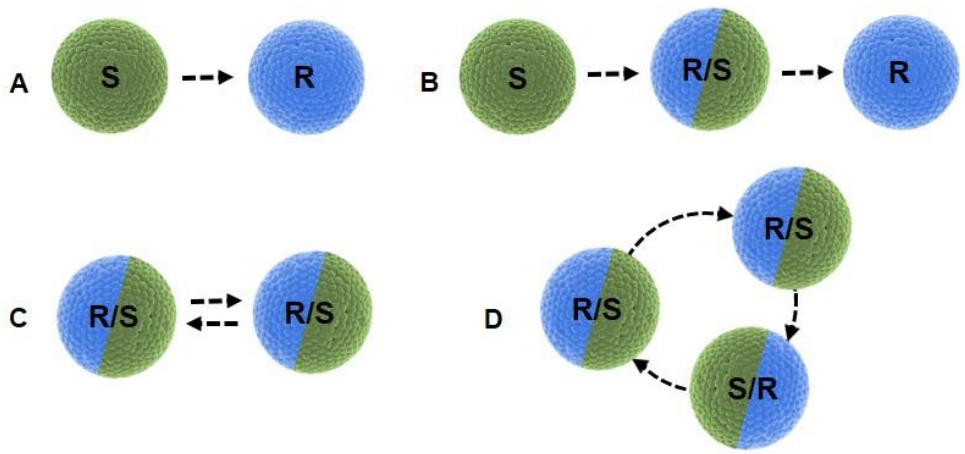

Figure 17. Schematics of different models of communication: **(A)** linear, **(B)** cascade, **(C)** interactive and **(D)** circular models of communication. S represents the sender of the information and R the receiver.

More complex variants of the main models can also be constructed. For instance, a **circular** network of communication is depicted in Figure 17D, in which

the flow of information is reminiscent to an interactive cascade – it enables initiation of the communication and output from the same entity after sequentially-programmed steps of information transmission with other members of the consortium. Another interesting possibility to be explored in combination with the communication models is the introduction of elements able to act as logic gates, which may enable to construct networks with multiple inputs/outputs. However, research in this sense is still very limited – efforts in the construction of complex pathways will be essential to stimulate further growth and support applications of communication at the micro/nanoscale.

- **Types of chemical signaling**

Chemical communication can occur across different length scales. Inspired in how nature communicates, there are four main types of chemical signaling in multicellular organisms based on the distance between signaling (sender) and responder (receiver) cells: autocrine (signal emission/reception by the same cell), juxtacrine (signaling across cell membranes in direct contact), paracrine (cells in very close vicinity) and endocrine (distant cells) (Figure 18).[76]

As it happens in natural cell-to-cell communication, distance is an important parameter when designing artificial systems. Based on this concept and related with the distance between point for information exchange, communication systems can be classified in two main sub-categories: (i) close proximity communication (juxtracrine/paracrine) or (ii) distant (endocrine) communication.

[76] J. T. Hancock, *Cell Signalling*, Oxford University Press, **2016**.

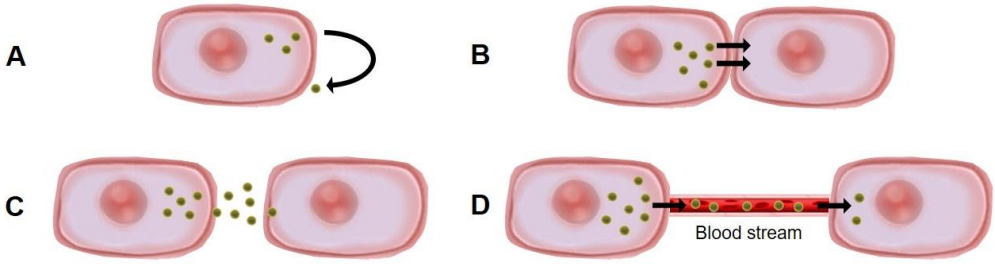

Figure 18. Types of chemical communication in cells: **(A)** autocrine, **(B)** juxtacrine, **(C)** paracrine and **(D)** endocrine.

- **Output of the communication network**

The final stage of the communication network is the transduction of the transmitted information using chemical messengers into a certain output (action/response). Typically, the output of the designed micro/nanosystems reported so far involves in most cases colorimetric, fluorescence or bioluminescent changes that can be generated by different ways such as: (i) an (enzymatic) reaction that generates a reporter, (ii) the delivery of encapsulated species to the solution, (iii) displacement from one site to another of labelled messengers (e.g., DNA strands) and (iv) expression of fluorescent/bioluminescent proteins in living organisms or synthetic cells. In addition, the modification of the motile behavior of active particles has also been reported.[77] Another interesting type of output is the induction of changes in living organisms such as growth inhibition, reduction of cell viability or genetic regulation. Finally, it should be noted that most of the reported studies are proof of concept systems and the development of communication

[77] C. Chen, X. Chang, H. Teymourian, D. E. Ramírez-Herrera, B. Esteban-Fernández de Ávila, X. Lu, J. Li, S. He, C. Fang, Y. Liang, F. Mou, J. Guan, J. Wang, *Angew. Chem. Int. Ed.* **2018**, *57*, 241.

systems that exhibit functional outputs is a key step to be explored more in detail towards realizing potential applications of communication concepts.

1.6.2 Enabling technologies for chemical communication

This section describes nanoparticles and microparticles used so far as senders or receivers of the information exchange in communication systems. Particles basically serve to isolate different parts of the whole system or reactions and send or receive chemical messengers to communicate different parts of the whole system. Micro- and nanoparticles involved in the studies detailed below comprise both organic and inorganic particles in which certain reactions take place or are simple containers able to deliver a certain chemical messenger when needed. Particles used so far and detailed below range from sizes of 15 nm to 2000 μm. This section also describes typically used information-processing tools that transform recognition of molecular messengers into propagation of the information.

- **Organic materials**

Following a bottom-up approach, several synthetic strategies for the creation of organic compartments at different length scales have been developed, which allow the assembly of molecular machinery for chemical communication, such as lipid vesicles (liposomes), proteinosomes, polymeric particles, and coacervates.[78]

Giant **liposomes** (size of 1-100 μm) containing encapsulated enzymes and/or other cargoes can be assembled by a technique known as droplet transfer.[79] In this method, the vesicles are formed by adding an aqueous solution (containing

[78] E. Rideau, R. Dimova, P. Schwille, F. R. Wurm, K. Landfester, *Chem. Soc. Rev.* **2018**, *47*, 8572.
[79] B. C. Buddingh', J. Elzinga, J. C. M. van Hest, *Nat. Commun.* **2020**, *11*, 1652.

the molecular cargo) into a lipid solution in paraffin, thus creating water-in-oil droplets that are later isolated by centrifugation. Alternatively, liposomes can be prepared by hydration of thin lipid films – this is particularly convenient when a size between 100 nm to 1 μm (namely, large lipid vesicles) is preferred.[80,81] In this second method, vesicle preparation starts with the formation of a lipid film (by evaporation of a chloroform-lipid solution) and subsequent hydration with the cargo solution, followed by extrusion (for size selection), and dialysis (to remove unencapsulated material). The liposome membrane is usually semi-permeable and only permits the diffusion of small non-charged molecules. When needed, membrane nanopores can be created by insertion of channel proteins such as α-hemolysin. This allows the feeding of external molecules through the pores and the release of reaction products, while keeping enzymes (and other large molecular ensembles) in the compartment. Similar, yet different to liposomes, **water-in-oil droplets** are lipid-stabilized aqueous microcompartments prepared by addition of an aqueous aliquot to a lipid-containing oil solution. Emulsification leads to the formation of lipid-stabilized aqueous droplets in an oil medium that can communicate when arranged in direct contact.

Proteinosomes are microcompartments (*ca.* 5-80 μm) formed by protein-polymer conjugates. A typical formulation for the assembly of proteinosomes, pioneered by the group of Mann, consists of cationized protein bovine serum albumin (BSA) covalently linked to poly(*N*-isopropylacrylamide) (PNIPAm).[82] The resulting amphiphilic protein-polymer conjugates are assembled (from an aqueous suspension) at the interface of water-oil Pickering emulsion, yielding microdroplets

[80] R. Lentini, S. P. Santero, F. Chizzolini, D. Cecchi, J. Fontana, M. Marchioretto, C. Del Bianco, J. L. Terrell, A. C. Spencer, L. Martini, M. Forlin, M. Assfalg, M. D. Serra, W. E. Bentley, S. S. Mansy, *Nat. Commun.* **2014**, *5*, 4012.
[81] R. Lentini, N. Y. Martín, M. Forlin, L. Belmonte, J. Fontana, M. Cornella, L. Martini, S. Tamburini, W. E. Bentley, O. Jousson, S. S. Mansy, *ACS Cent. Sci.* **2017**, *3*, 117.
[82] Y. Qiao, M. Li, R. Booth, S. Mann, *Nat. Chem.* **2017**, *9*, 110.

that are stabilized by membrane crosslinking and isolated by removal of the oil phase. Functional components useful for chemical communication such as enzymes, catalytic nanoparticles, or active species can be readily encapsulated in the compartment lumen by incorporation in the aqueous phase during their assembly. The typical proteinosome membrane has been demonstrated to allow the diffusion of small chemical messengers such as enzymatic substrates, reaction products and DNA strands.[83,84] Furthermore, other polymeric building blocks have also been employed for the preparation of proteinosomes, such as PNIPAm-*co*-methacrylic acid (PNIPAm-*co*-MAA), which allow to tune the permeability of the membrane as a function of the temperature.[85] In addition, in some examples the polymer is functionalized with terminal groups to regulate the interactions between different micro-compartments.[86]

As highly versatile building blocks of diverse nature, polymers can be used for the assembly of different types of **polymeric particles** with communication capabilities. For instance, Devaraj and co-workers developed polymer microcapsules from acrylate monomer with a size of 40 µm that were prepared using a microfluidic method involving formation of emulsion droplets and polymerization.[87] Such capsules have a rigid and mechanically stable surface with pores of diameters between 200 to 300 nm, which allow the permeation of macromolecules up to 2 MDa. On another hand, polymersomes are self-assembled vesicular compartments made from amphiphilic block copolymers that can be engineered with different sizes (from nm to several microns), shapes, and stimuli-

[83] A. Joesaar, S. Yang, B. Bögels, A. van der Linden, P. Pieters, B. V. V. S. P. Kumar, N. Dalchau, A. Phillips, S. Mann, T. F. A. de Greef, *Nat. Nanotechnol.* **2019**, *14*, 369.
[84] S. Yang, P. A. Pieters, A. Joesaar, B. W. A. Bögels, R. Brouwers, I. Myrgorodska, S. Mann, T. F. A. De Greef, *ACS Nano* **2020**, *14*, 15992.
[85] P. Gobbo, A. J. Patil, M. Li, R. Harniman, W. H. Briscoe, S. Mann, *Nat. Mater.* **2018**, *17*, 1145.
[86] P. Wen, X. Liu, L. Wang, M. Li, Y. Huang, X. Huang, S. Mann, *Small* **2017**, *13*, 1700467.
[87] H. Niederholtmeyer, C. Chaggan, N. K. Devaraj, *Nat. Commun.* **2018**, *9*, 5027.

responsiveness. Interestingly, nano- and giant polymeric capsules can be combined for the construction of hierarchical systems that mimic cellular structures.[78]

Coacervates are membrane-less crowded microdroplets of aggregated charged macromolecules such as synthetic polymers or nucleic acids held together by electrostatic and hydrophobic interactions. Formation of coacervates requires the combination of at least two main building blocks with opposite charges. Other components such as enzymes or nanoparticles can be entrapped in the microcompartment during the coacervation process or be sequestered from the solution with affinities depending on their hydrophobicity, charge and size. A common formulation for their preparation relies of the use of adenosine 5'-triphosphate (ATP) (as small anion) to induce coacervation by mixing with positively charged poly(diallydimethylammonium) (PDDA), yielding microdroplets of 1-50 μm.[82] In addition, the use of responsive positively charged polymers such as poly-lysine allows to assemble coacervates that can disassemble and release entrapped molecules in response to pH changes.[88] However, an important consideration is the intrinsic instability of these membrane-less compartments, especially in ionic media. To alleviate this problem, Williams and co-workers developed a coacervate platform based on oppositely charged amylose polymers (quaternized ammonium and carboxymethyl amylose, respectively) stabilized with a self-assembled terpolymeric membrane, comprising poly(ethylene glycol), poly(caprolactone-gradient-trimethylene carbonate) and poly(glutamic acid) (PEG-PCLgTMC-PGlu).[89]

- **Inorganic materials**

Inorganic materials can offer a fine control over their properties such as surface functionality, chemical stability and stimuli-responsive features. In general,

[88] Y. Qiao, M. Li, D. Qiu, S. Mann, *Angew. Chem. Int. Ed.* **2019**, *58*, 17758.
[89] A. F. Mason, B. C. Buddingh', D. S. Williams, J. C. M. Van Hest, *J. Am. Chem. Soc.* **2017**, *139*, 17309.

the assembly of inorganic-based materials is based on diverse nanoarchitectonics strategies that involve merging concepts of nanotechnology, supramolecular and molecular chemistry, and bio-related technologies.[57,21]

Among different types of **metallic nanoparticles**, gold nanoparticles offer several advantages such as their easy synthesis and functionalization, and interesting optical properties. In particular, spherical gold nanoparticles can be rapidly synthesized by reduction of a salt of Au(III) with sodium citrate (known as sodium citrate reduction method or also as Turkevich-Frens method), which gives monodisperse spherical particles with a tunable size between 15 to 40 nm. Non-spherical nanoparticles can also be prepared, such as nanorods and nanostars that absorb light in the near infrared region, as a strategy to develop light-responsive systems.[90] Taking advantage of the high affinity of thiol groups towards gold, their surface can be decorated with functional ligands by treatment with thiolated derivatives.[91] A major potential issue when working with gold nanoparticles is their stability since they might tend to aggregate in ionic media – this can be alleviated by functionalization with stabilizing agents, which are ligands that provide steric or charge stabilization.

One appealing concept for the design of communicating nanoparticles is the possibility to imbue them with cargo-release capabilities. Among different types of nanocarriers, **mesoporous silica nanoparticles** have been widely used for this purpose. Mesoporous silica offers interesting properties previously detailed in Section 1.2 such as low cost, biocompatibility, and a stable 3-D porous network with tunable pore size (i.e. 2-50 nm) which can be loaded with a variety of functional cargoes whereas their external surface can be functionalized with molecular,

[90] G. Von Maltzahn, J. H. Park, K. Y. Lin, N. Singh, C. Schwöppe, R. Mesters, W. E. Berdel, E. Ruoslahti, M. J. Sailor, S. N. Bhatia, *Nat. Mater.* **2011**, *10*, 545.
[91] P. Q. Ma, Q. Huang, H. D. Li, B. C. Yin, B. C. Ye, *J. Am. Chem. Soc.* **2020**, *142*, 3851.

supramolecular or biomolecular ensembles that prevent the release of the cargo until a certain stimulus is present.[29]

Colloidosomes are semipermeable microcapsules created by the assembly of micro- or nanoparticles at the interface of Pickering emulsions, stabilizing water in oil-droplets. After assembly at the droplet interface, the particles are cross-linked and the aqueous microdroplets are transferred to an aqueous phase. Biological components can be incorporated in the droplets dissolved in the water phase during the emulsification process. Interestingly, the nature of the particles determines the properties of the membrane, ranging from inert silica nanoparticles to catalytically active nanoparticles (e.g., containing iron, palladium or gold nanoclusters).[92]

- **Information-processing tools**

In order to participate in chemical communication networks, micro and nanosystems need to be equipped with molecular tools able to recognize molecular messengers and effectuate signal transduction by converting recognition into propagation of the information. Several options are usually employed for this purpose including the use of enzymes, cell-free transcription-translation machinery (TXTL), DNA displacement reactions, and responsive molecular ensembles.

Being the catalysts of life, enzymes are excellent candidates as decoding/encoding elements allowing the recognition of substrates and their transformation into new products as chemical messengers for information processing.[64] **Enzymatic reactions** are usually both highly specific and efficient, therefore being interesting to construct selective communication systems able to respond in a reasonably short time to a specific input and discriminate between

[92] S. Sun, M. Li, F. Dong, S. Wang, L. Tian, S. Mann, *Small* **2016**, *12*, 1920.

molecules of similar structure. Several enzymatic reactions have been concatenated in a single micro/nanosystem or at different sites of the communication network. This allows to construct communication pathways reminiscent to natural metabolic routes in a cascade-like cycle involving several enzymes.

Cell-free transcription-translation (TXTL) systems consist of cytoplasmic cell extracts which contain all the components needed (including nucleotides, ribosomes, enzymes, salts, etc.) to carry out *in vitro* protein expression.[93] These extracts are usually obtained as cell lysates (generally from *E. coli* bacteria) or purified and reconstituted (PURE-TXTL) and have become a popular tool in the synthetic biology field. Depending on the design of the network, DNA templates, inducers or repressor molecules may act as inputs of the genetic circuit – in turn, expression of the protein encoded in the system or enzymatic products derived from the protein acts as output of the TXTL extract. Expression of α-hemolysin has been the choice in several studies as this protein can induce the creation of pores in the vesicles containing the TXTL system, thus allowing the subsequent release of encapsulated cargoes as chemical messengers that would diffuse to the next micro/nanosystem of the network.

DNA displacement reactions have been traditionally studied in bulk solutions using a collection of different DNA strands.[94] Here, information processing relies on the specific hybridization of complementary sequences via Watson-Crick base pairings. Within this context, the term 'toehold' is used to identify the short nucleotide sequence in a DNA strand which pairing is key to initiate the displacement cascade. In particular, the displacement cascade is initiated by addition of an "invader strand" (input) that triggers concatenated strand migrations

[93] E. Dubuc, P. A. Pieters, A. J. van der Linden, J. C. van Hest, W. T. Huck, T. F. de Greef, *Curr. Opin. Biotechnol.* **2019**, *58*, 72.
[94] F. C. Simmel, B. Yurke, H. R. Singh, *Chem. Rev.* **2019**, *119*, 6326.

enabling the connection of multiple nucleic acid-based sites.[94] Displacements are relatively fast and therefore this allows communication in a relatively short time limited only by DNA diffusion between the components.

Molecular or supramolecular ensembles have also been used for information processing.[64] These have been mainly used as responsive supramolecular ensembles as capping agents in gated mesoporous silica nanoparticles able to switch their conformation or displace in the presence of a certain molecular stimulus allowing the delivery of chemical messengers connecting micro/nanosystem of the network. This is a versatile information-processing tool as there is a number of capping molecular and supramolecular ensembles able to respond to a great variety of bio(molecules).[29]

More complex information-processing functions can be programmed using **molecular biocomputing** based on Boolean logics.[29,95] The term "logic gate" is used, as previously explained in Section 1.5, to describe operators that implement basic functions based on processing combinations of binary inputs (0, meaning absence of input, and 1, presence) to produce (1) or not (0) an output. Common logic operators (AND, NAND, OR, NOR, XOR, XNOR and INHIBIT gates) may be implemented in micro/nanosystems to process the environmental information and their combination leads to larger circuits where more complex logical operations are achieved. Logic operations in communication communities between micro/nanoparticles are still scarce but have a great potential to design more complex communication networks.

[95] P. Remón, U. Pischel, *ChemPhysChem* **2017**, *18*, 1667.

1.6.3 Engineering communication between abiotic micro/nanosystems

Once described the different models of communication and chemical signaling as well as the most commonly used scaffolds and information-processing tools, a summary of representative examples on communication between abiotic micro/nanodevices is reported here. For easier comprehension, this section is divided attending to the proximity between the points of information exchange (close proximity or distant communication) and the communication strategy employed.

- **Close proximity communication**

The engineering of close proximity (juxtacrine/paracrine) communication strategies has been explored by designing abiotic systems able to undergo surface fusion (e.g., driven by electrostatic interactions) or exchange chemicals through surfaces in close proximity (e.g., by passive transport across membrane channels or via microenvironments). One of the first realizations of contact-based communication was developed by Huang and colleagues (Figure 19A).[86] It was based on the engineering of proteinosomes from a mixture of NH_2-BSA/PNIPAm and aldehyde-functionalized dextran (CHO-DEX). Two populations were prepared containing different fluorescent payloads (a blue and a red dye, respectively). The contact-induced fusion between both proteinosomes was based on the dynamic covalent equilibrium between superficial CHO- and -NH_2 yielding imine linkages between compartments. This resulted in the mixture of entrapped cargoes as the output of the system. The fusion process could be accelerated or inhibited with the addition or encapsulation of different species. For instance, the entrapment of glucose oxidase (GOx) and glucose in different populations of proteinosomes led to a faster interaction; as the enzyme-mediated gluconic acid production resulted in

the hydrolysis of imine moieties from the individual proteinosome chassis, thus leading to the generation of more complementary aldehyde and amine groups available for fusion with a partner particle. On the contrary, the addition of cinnamyl aldehyde reduced fusion events due to its competitive binding to free amine groups.

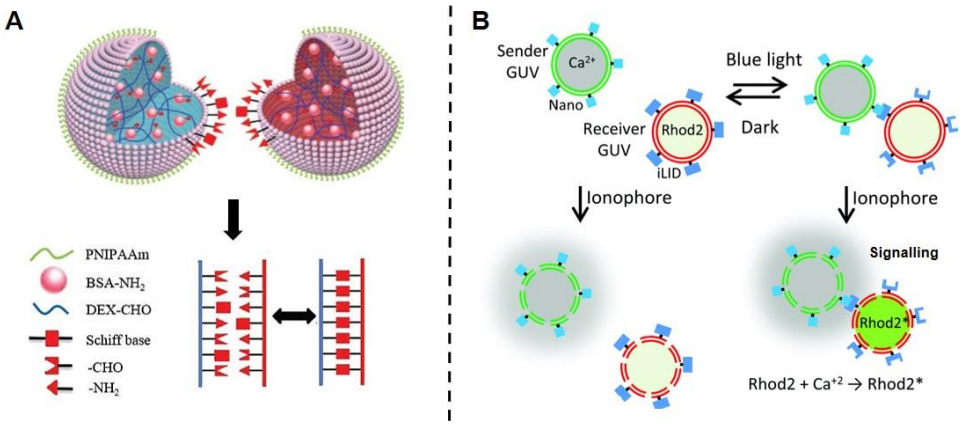

Figure 19. Representative examples of close proximity (juxtacrine/paracrine) communication between abiotic entities. **(A)** Contact-based fusion of proteinosomes driven by the formation of imine linkages at the interface between two compartments. *Reprinted with permission from ref. 86 Copyright © 2017 by John Wiley and Sons.* **(B)** Chemical signaling controlled by liposome adhesion mediated by proteins Nano and iLID, which bind to each other under blue light. Upon the addition of an ionophore, the chemical messenger in the first liposome (Ca^{2+}) passes through membranes and binds Rhod2 confined in the second liposome, which becomes fluorescent. *Reprinted with permission from ref. 96 Copyright © 2019 by Royal Society of Chemistry.*

Wegner and co-workers designed light-controlled adhesion and contact communication between two giant liposomes.[96] The external liposome surface was functionalized with complementary interacting proteins, which connected to each other under blue light and dissociate in the dark (Figure 19B). In particular,

[96] T. Chakraborty, S. M. Bartelt, J. Steinkühler, R. Dimova, S. V. Wegner, *Chem. Commun.* **2019**, *55*, 9448.

liposome 1 (sender) was loaded with Ca^{2+} and decorated with iLID protein, whereas liposome 2 (receiver) was loaded with Rhod2 (a Ca^{2+}-sensitive dye) and decorated with 'Nano' protein, the iLID binding partner. Then, sender-receiver adhesion was activated by irradiation with blue light and the communication was triggered upon addition of ionomycin (a Ca^{2+} transporter). Indeed, ionomycin was able to diffuse through the membrane and effectively transport Ca^{2+} from the sender to the receiver in close proximity. Subsequently, after light irradiation and ionomycin addition, the fluorescence of the receiver increased due to the Rhod2 response to Ca^{2+} which was transferred from the proximal sender liposome.

Mann and co-workers also explored a variation of such fusion-based communication strategy by designing a system with predatory-like behavior between proteinosomes (10-80 μm) and coacervates (1-15 μm).[82] The coacervate microdroplets were positively charged and made of PDDA/ATP monomers containing entrapped protease-K and the substrate Amplex Red. The BSA/PNIPAm proteinosomes were negatively charged and contained Pt nanoparticles with negative charge. After electrostatic binding of both compartments, the proteinosome chassis was dismantled into fragments and collapsed due to the (coacervate) protease-mediated lysis. Then, Pt nanoparticles (chemical messenger) were transferred and captured by the positive coacervates. As a result, this imbued the coacervates with peroxidase-like activity which generated a red fluorescent signal (output) due to the oxidation of Amplex Red to yield resorufin (Figure 20A).

Several examples of communication between attached inorganic nanoparticles have been developed by Martínez-Máñez and Villalonga *et al*.[55] In an illustrative example, the authors used Janus-type nanoparticles having opposing Au and mesoporous silica faces, functionalized with a pH-responsive inclusion complex between benzimidazole and β-cyclodextrin on the mesoporous silica surface and two effectors, GOx and esterase, immobilized on the Au face (previously depicted

in Figure 12). Moreover, the mesoporous face was additionally loaded with the fluorophore $[Ru(bpy)_3]Cl_2$. The nanodevice behaved as an enzymatic logical OR operator in which $[Ru(bpy)_3]Cl_2$ delivery is selectively fueled by the presence of glucose or ethyl butyrate (inputs). In particular, GOx catalyzed the oxidation of glucose, yielding *D*-glucono-1,5-lactone, which hydrolyzes in water to gluconic acid. Moreover, ethyl butyrate is catalytically hydrolyzed by esterase enzyme to ethanol and butyric acid. Both catalytic reactions resulted in the formation of an acid (i.e. gluconic acid or butyric acid) which induced a local reduction of the pH. Protons, from these generated acids in the Au face, caused the protonation of benzimidazole moieties on the mesoporous silica face which induced dethreading of the benzimidazole-β-cyclodextrin inclusion complex and cargo delivery.

In another example of communication between active particles in close proximity, Wang and co-workers reported communication between two types of catalytic spherical motors which resulted in enhanced motion as output (Figure 20B).[77] The sender motor was a polystyrene (PS)/Ni/Au/Ag Janus microsphere (*ca.* 5 μm). On the metal side, the inner Ni layer provided magnetic control while the external Ag layer decomposed H_2O_2 fuel to generate O_2 and propel the particle. The second motor (*ca.* 1 μm) was a SiO_2/Pt sphere and was propelled by Pt-induced H_2O_2 decomposition. Upon propulsion, the fuel induced Ag corrosion in the sender and subsequent partial release of Ag^+. This released Ag^+ acted as chemical messenger for the second (receiver) motor. When the two motors were in close proximity (less than one body length), the second motor could feel the Ag^+ messenger-rich microenvironment and significantly increased its speed. This was attributed to the deposition of Ag on the Pt surface, consequently enhancing the catalytic activity and motion of the second motor.

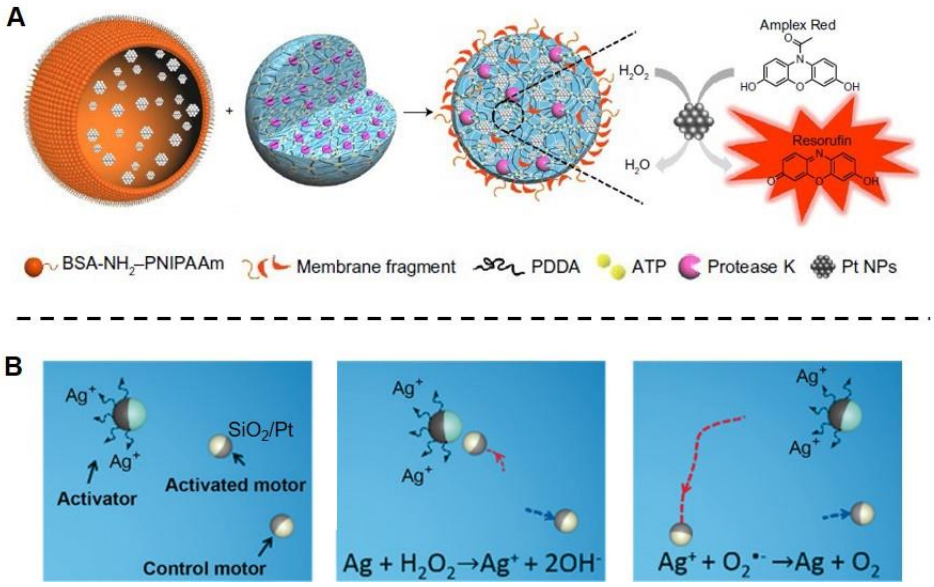

Figure 20. Representative examples of close proximity (juxtacrine/paracrine) communication between abiotic entities. **(A)** Predation behaviour of protease-K-containing coacervates (blue) which disintegrate proteinosomes (orange) that contain an aqueous dispersion of Pt nanoparticles (NPs) resulting in a killer protocell with peroxidase activity capable of oxidizing Amplex Red in solution to the fluorescent product resorufin. *Reprinted with permission from ref. 82 Copyright © 2017 by Springer Nature.* **(B)** Communication between a PS/Ni/Au/Ag motor (sender, propelled by Ag-induced H_2O_2 decomposition into O_2) and a SiO_2/Pt motor (receiver, propelled by Pt-induced H_2O_2 decomposition into O_2). Sender motor releases Ag^+ ions that are deposited on the Pt surface of the receiver motor. This results in the enhancement of receiver catalytic activity subsequently increasing its speed (activation) *Reprinted with permission from ref. 77 Copyright © 2018 by John Wiley and Sons.*

- **Distant communication**

In contrast to juxtacrine/paracrine (close proximity) communication described above, endocrine (distant) communication involves the diffusion of messengers through relatively large distances in the medium (i.e., the blood stream in the case of natural cells). Although, endocrine (distant) communication has gained popularity when designing chemical communication systems, potential information loss or slow response (e.g., by messenger dilution in the medium or

degradation) are important factors to be taken into account that can limit communication efficiency. Reported examples of communication between micro/nanodevices have been divided for clarity in different parts based on the use of enzymatic reactions, TXTL systems, DNA displacement reactions and gated nanocarriers.

Communication based on enzymatic reactions

Williams and van Hest and co-workers demonstrated linear chemical communication between two discrete populations of self-assembled terpolymeric membranized coacervates ranging from 1 to 10 μm (Figure 21A).[89] One population contained the enzyme GOx whereas the other contained HRP. The communication route consisted of an enzymatic cascade between the two populations which relied on the permeability of the copolymeric membranes to small molecules. Communication was triggered by addition of glucose (input) and Amplex Red (substrate). Glucose diffused through the membrane of the GOx-containing coacervate and was transformed into H_2O_2 and gluconic acid. H_2O_2 (the chemical messenger) diffused to the second population of coacervates where HRP transformed Amplex Red in the fluorescent resorufin as output of the communication system.

Van Hest and co-workers developed linear communication between two giant liposomes (*ca.* 20 μm) by allosteric amplification of a molecular signal.[79] In particular, sender vesicles were loaded with the enzyme apyrase; whereas receiver vesicles were equipped with phosphoglucomutase (PMG), glucose-6-phosphate dehydrogenase (G6PDH) and glycogen phosphorylase b (GPb) enzymes and glycogen. Upon addition of ATP (input), sender liposomes produced and released AMP (adenosine monophosphate, chemical messenger) which diffused towards receiver liposomes. Upon detection of AMP by the receiver, an allosteric activation

of GPb enzyme was induced, triggering an enzymatic cascade in the vesicle interior: i.e. conversion of glycogen to glucose-1-phosphate by AMP-activated GPb, conversion of glucose-1-phosphate to glucose-6-phosphate by PMG enzyme, and subsequent generation of NADH by G6PDH. NADH-fluorescence at 620 nm generated in the receiver liposomes was measured as the output signal of the communication network. Remarkably, the authors demonstrated that, thanks to the allosteric amplification mechanism, senders could communicate with receivers over long distances by localizing both communities at opposite sides on a channel device.

Mann, Li, Liu and co-workers designed a modular microreactor system based on the communication of different populations of DEAE-dextran/dsDNA (diethylaminoethyldextran chloride-double-stranded DNA) coacervates (*ca.* 5 μm) embedded in an agarose/alginate polysaccharide hydrogel under flow conditions (Figure 21B).[97] The first population (sender) contained positively charged TiO_2/Ag nanoparticles whereas the second population (receiver) was loaded with Amplex Red and G4-hemin DNAzyme which functioned as a peroxidase-mimic. First, each population was immobilized into separated hydrogel-based modules, and in a second step; sender and receiver-containing modules were connected in series by interfacial crosslinking. The modular microreactor system was studied under flow conditions. Under UV irradiation (input), photocatalytic reduction of dioxygen started in TiO_2/Ag-nanoparticles resulting in a H_2O_2 flux (chemical messenger) which diffused to the G4-hemin coacervates. This originated a migrating red fluorescence output as a result of the oxidation of Amplex Red to resorufin by coacervates on the receiver module. Interestingly, the authors showed that

[97] J. Liu, L. Tian, Y. Qiao, S. Zhou, A. J. Patil, K. Wang, M. Li, S. Mann, *Angew. Chem. Int. Ed.* **2020**, *59*, 6853.

spatiotemporal reaction control could be achieved depending on the droplet number density, intensity of UV irradiation, and chemical flux.

In a further advanced study, Mann and co-workers developed a consortium of three micronized protocells that communicated following a response-retaliation mechanism based on the combination of an enzymatic reaction, on-command cargo delivery and predation behavior (Figure 21C).[88] The first protocell (P) consisted of a BSA/PNIPAm proteinosome (*ca.* 25 μm) that encapsulated GOx. The second protocell (C_T) consisted of a coacervate (*ca.* 0.5 μm) made of pH-sensitive poly-lysine and ADP and containing proteinase K. The third protocell (C_K) consisted of a coacervate (*ca.* 2 μm) made of pH-resistant poly(diallyldimethylammonium chloride) and dextran sulfate. This third protocell (C_K) was adhered on the surface of the first one (P) by electrostatic interactions. The communication cycle was triggered by the presence of glucose (input), which was recognized by the first protocell (P) and transformed into gluconic acid (chemical messenger). Then, gluconic acid triggered the disassembly of the second protocell (C_T) by weakening the poly-lysine - ADP interaction, resulting in the release of proteinase K (second chemical messenger). Next, the third protocell (C_K) (with high partition constant for proteinase K) was capable of sequestering proteinase K from the environment. Finally, this third population of proteinase K-enriched coacervates (C_{K*}) degraded the proteinosomes (first population) by proteolytic action, resulting in the release of free proteinase K-enriched coacervates (C_{K*}).

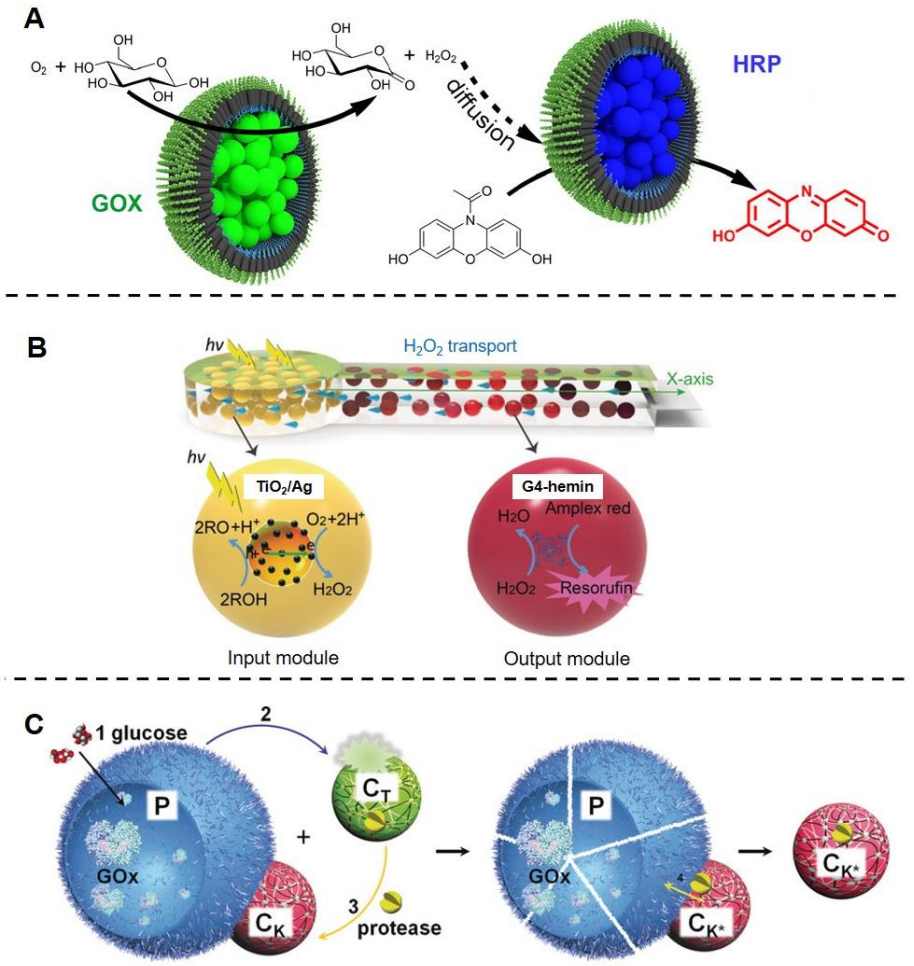

Figure 21. Representative examples of enzyme-mediated communication between distant abiotic entities. **(A)** Sender coacervate (containing GOx) generates H_2O_2 that diffuses to receiver coacervate (containing HRP), finally resulting in the formation of fluorescent resorufin from Amplex Red present in solution. *Reprinted with permission from ref. 89 Copyright © 2017 by American Chemical Society.* **(B)** Flow microreactor based on chemical communication: UV irradiation triggers H_2O_2 production by yellow coacervates, and H_2O_2 diffuses to red ones where the entrapped Amplex Red is oxidized to fluorescent resorufin. *Reprinted with permission from ref. 97 Copyright © 2015 by John Wiley and Sons.* **(C)** Response-retaliation behavior in synthetic protocell communities. GOx-containing proteinosomes (P) generate H^+ from glucose, inducing disassembly of pH-sensitive coacervates (C_T, second population). C_T releases protease which is captured by pH-insensitive coacervates (C_K, third population), resulting in the disassembly (predation) of the proteinosomes (first population). *Reprinted with permission from ref. 88 Copyright © 2019 by John Wiley and Sons.*

Communication based on TXTL systems

Devaraj and co-workers reported a communication system that consisted of a sender and a receiver cell mimic employing proteins as chemical messengers (Figure 22A).[87] The cell mimics consisted of porous acrylate microcapsules (*ca.* 40 μm in size) with an encapsulated clay-DNA hydrogel. Communication was activated by addition of TXTL reagents. These chemicals were able to diffuse through the microcapsule membrane and permeate in the inner clay-DNA hydrogel nuclei. Upon activation, the sender cell expressed T3 RNA polymerase (T3 RNAP, encoded in its clay-DNA hydrogel) and released it through the 200-300 nm membrane pores. The receiver contained a DNA-template for T3 RNAP-driven synthesis of green fluorescent protein (GFP). A specific plasmid was also incorporated in the hydrogel for binding the as-synthesized fusion protein and avoiding its leakage to the solution. Finally, as the output signal of the communication system, receiver cells became fluorescent due to protein expression.

In a collaborative work, Mann, Tang, Mansy and co-workers reported gene-directed communication between giant liposomes (acting as senders) and proteinosomes (acting as receivers) (Figure 22B).[98] Both platforms had a size of 5-10 μm. Sender vesicles encapsulated glucose, DNA encoding for α-hemolysin expression, and TXTL extract. In response to *N*-(3-oxohexanoyl)-L-homoserine lactone (3OC6HSL), acting as communication trigger, expression of α-hemolysin in the first community of particles induced the formation of membrane pores and subsequent release of the encapsulated glucose. The receiver particles were assembled from cross-linked GOx-PNIPAm nanoconjugates and also contained HRP enzyme. These receivers detected the diffused glucose and catalyzed the formation of D-glucono-δ-lactone and H_2O_2, which finally resulted in the HRP-mediated

[98] T. Y. D. Tang, D. Cecchi, G. Fracasso, D. Accardi, A. Coutable-Pennarun, S. S. Mansy, A. W. Perriman, J. L. R. Anderson, S. Mann, *ACS Synth. Biol.* **2018**, *7*, 339.

reaction between the peroxide and Amplex Red (present in the medium) generating fluorescent resorufin as the output signal.

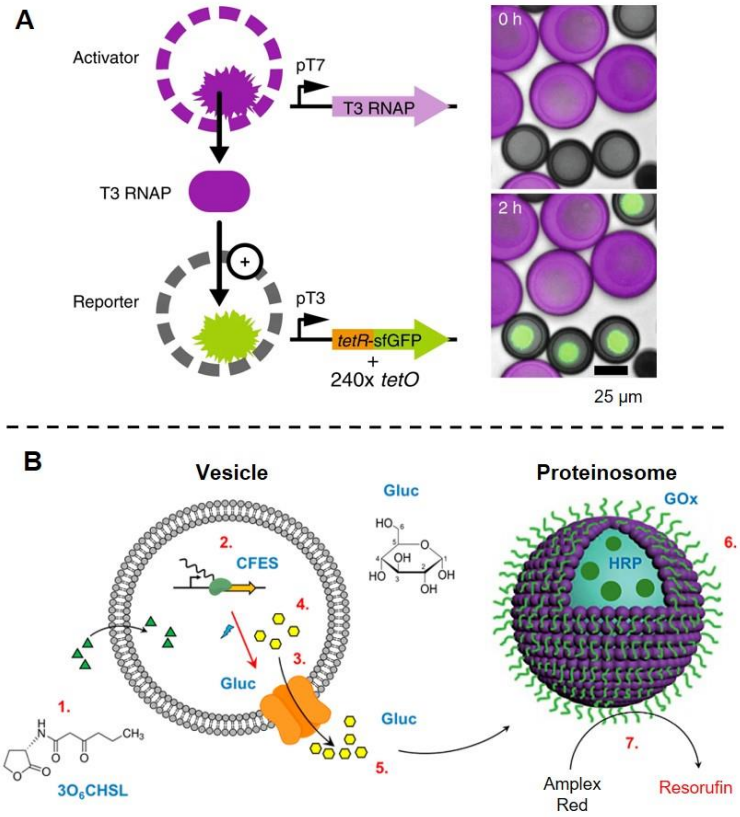

Figure 22. Representative examples of TXTL-mediated communication between distant abiotic entities. **(A)** Sender polymeric microcapsules (purple, rhodamine B-labelled) synthesize and release T3 RNA polymerase (T3 RNAP) as chemical messenger that activates the expression of GFP in the second population (green). *Reprinted with permission from ref. 87 Copyright © 2018 by Springer Nature.* **(B)** 3OC6HSL (input) induces α-hemolysin expression in liposomes creating pores which release the encapsulated glucose (chemical messenger). Glucose diffuses to HRP-containing GOx-proteinosomes, where a cascade reaction is subsequently triggered, resulting in the oxidation of Amplex Red (present in solution) into fluorescent resorufin. *Adapted with permission from ref. 98 Copyright © 2018 by American Chemical Society.*

Boyden and co-workers developed genetic communication circuits between two populations of liposomes based on the encapsulation of stimuli-responsive TXTL cascades.[99] The first population (sender) contained IPTG (isopropyl-β-D-thiogalactoside, non-permeable molecule) and a gene for α-hemolysin transcription in response to arabinose (membrane permeable). Upon addition of arabinose, this first population released IPTG due to the creation of pores by α-hemolysin production that was detected by a second liposome population (acting as receiver/reporter). This receiver population contained an IPTG-responsive gene that resulted in the production of luciferase, resulting in subsequent bioluminescence signaling. In addition, the authors showed the modularity of their platform by developing another system based on different messenger molecules. In this second example the sender liposomes responded to theophylline releasing doxycycline, which was detected by the receiver liposomes resulting in expression of luciferase.

Communication based on DNA displacement reactions

De Greef and Mann and co-workers developed DNA-based communication between proteinosomes following different pathways (cascade, bidirectional and AND/OR-logic, Figure 23).[83] For their preparation, firstly, a biotinylated DNA strand (gate strand) was covalently anchored to streptavidin-functionalized proteinosomes made of BSA/PNIPAm. Then, a second DNA strand was incorporated to the particles by partial hybridization with the first. For cascade communication, two proteinosome populations were spatially distributed in a microfluidic trapping array that allowed for confocal microscopy visualization. Both populations incorporated fluorophore-labelled DNA gate strands (Cy5 for population 1 and

[99] K. P. Adamala, D. A. Martin-Alarcon, K. R. Guthrie-Honea, E. S. Boyden, *Nat. Chem.* **2017**, *9*, 431.

Alexa546 for population 2) partially hybridized with quencher-labelled output strands. As communication trigger, an externally added input strand induced the displacement and release of the quencher-labelled output strand (messenger 1) from population 1. This messenger was detected by population 2 (receiver) via a toehold-mediated displacement of its quencher strand, resulting in activation of proteinosome 2 fluorescence (due to Alexa546). Signal amplification was implemented by using fuel strands which displaced the input strand therefore recycling the initial signal to react with another particle. Based on this principle, the authors extended the communication to a third population, that sensed quencher strand released from population 2 (messenger 2), resulting in the activation of a fluorescent signaling in population 3. For bidirectional communication between two populations, the output strand of population 2 was designed to deactivate fluorescence in population 1. In this example, upon addition of the input, population 1 released its quencher output strand (messenger 1) and became temporarily fluorescent (due to activation of its Cy5-labelled gate strand). The messenger 1 was sensed by population 2 which responded with an activation of its Cy3 fluorescence and released a displaced output strand (feedback messenger). Finally, this feedback messenger diffused to population 1 and acted as orthogonal inhibitor strand, resulting in deactivation of population 1 fluorescence. For logic communication, the authors designed communities of three different proteinosomes with AND/OR behavior. In the AND system, two different input strands were recognized by population 1 and 2, respectively, inducing the release of two output strands. The DNA architecture in population 3 responded selectively to the simultaneous combination of messenger output strands from 1 and 2. As result, population 3 became fluorescent due to Cy5-activation signaling. In the OR system, population 3 was designed to sense and respond to messengers from population 1 or 2, independently.

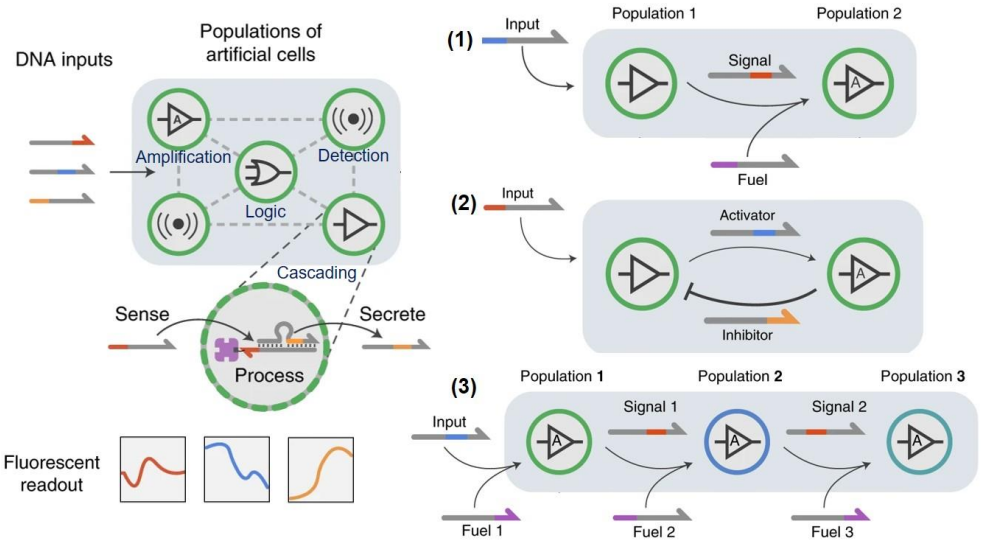

Figure 23. Representative example of DNA-mediated communication between distant abiotic entities. Strategy based on DNA-displacement and exchange between proteinosomes. A DNA strand (input) is sensed and processed inside the proteinosomes that subsequently secrete another DNA strand. An abundant fuel strand allows amplification of the initial input by promoting its displacement. All DNA stands are labelled to follow the whole operation by confocal microscopy. Different pathways have been developed such as **(1)** linear, **(2)** interactive and **(3)** cascade communication. *Adapted with permission from ref. 83 Copyright © 2019 by Springer Nature.*

In a recent report, Mann and de Greef's groups presented light-activated DNA-based communication between proteinosomes.[84] A single sender was surrounded by receiver proteinosomes in a microfluidic trapping array. Upon laser irradiation a messenger DNA strand (anchored via photolabile nitrobenzyl groups) was released from the sender and diffused to the receivers. Similarly as above, the messenger strand induced the displacement of a quencher and subsequent activation of receiver's fluorescent strand. Interestingly, this created an activation pattern as a function of time and the receiver's distance to the sender. In addition, the authors combined two different senders to activate receivers following an AND behavior and studied various factors affecting communication such as spatial density and permeability of the receivers (Figure 24).

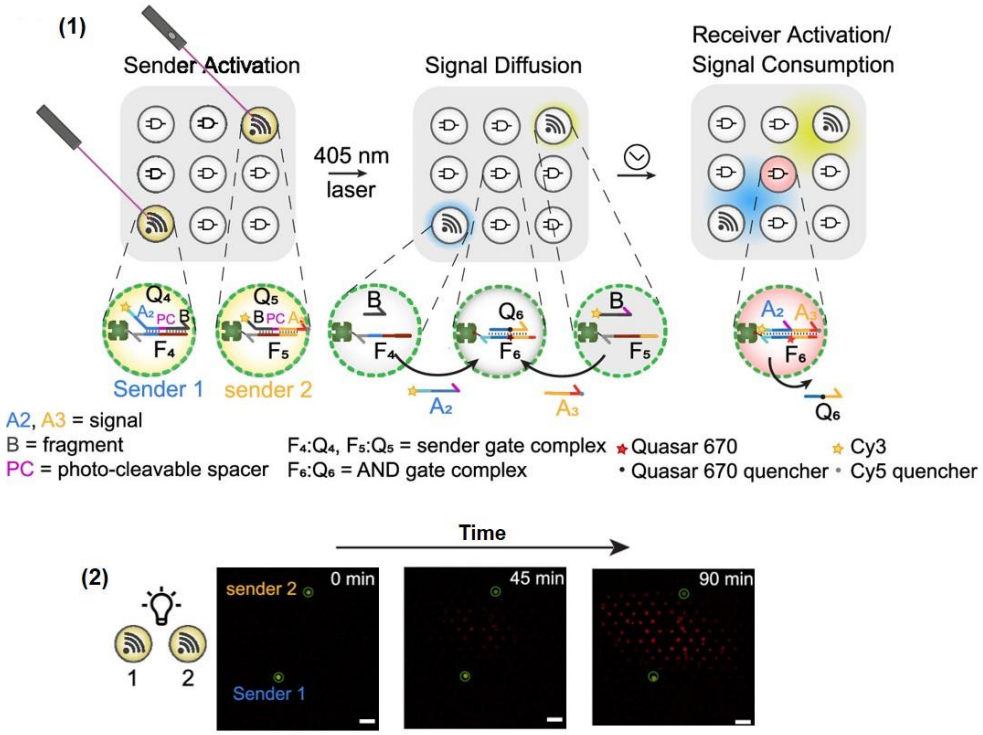

Figure 24. Representative example of DNA-mediated communication between distant abiotic entities. AND gate-like communication between proteinosomes. **(1)** Laser irradiation promotes photocleavage of gate complexes F_4:Q_4 and F_5:Q_5 in sender 1 and sender 2 releasing A2+B and A3+B fragments, respectively. Both fragments cooperatively hybridize to receiver's gate complex F_6:Q_6 yielding a fluorescent output. **(2)** Confocal images of the described strategy between two senders and several receivers at different times. Scale bars=150 µm. *Reprinted with permission from ref. 84 Copyright © 2020 by American Chemical Society.*

Yin and Ye and co-workers reported cascade communication between three types of gold nanoparticles (20 nm in size) functionalized with DNA.[91] DNA machinery of nanoparticle 1 and 3 (NP-1, NP-3) consisted of different sequences containing: (i) a thiol-modified strand, covalently attached to the NP-surface, (ii) a second strand (B1 and B3 strands, respectively) hybridized to the first and functionalized with a fluorophore quenched by the gold nanoparticle, (iii) a hairpin-locked single strand (covalently attached to the NP-surface, to control displacement

cascades). NP-2 contained a thiol-modified strand hybridized to a second strand (B2 strand), and a third strand partially hybridized to the second. Another two 'helper' strands were present in the medium (D1 and D2 strands). The communication cascade was triggered upon addition of an input DNA strand (I-strand). This was recognized by the DNA machinery on NP-1 and induced the formation and release of B1-D1 double stranded DNA hybrids, which diffused as a first chemical messenger for NP-2. Then, this first messenger was recognized by NP-2 and induced the reorganization of the DNA nanostructures on the gold surface. As a result, NP-2 released a second chemical messenger (B2-D2 hybrid strand) that was sent for NP-3. Recognition of this messenger by NP-3, triggered the formation and release of B3-I hybrids, producing an increase in fluorescent signal as the output of the communication network.

Communication based on gated nanocarriers

Martínez-Máñez and co-workers pioneered the utility of gated nanoparticles with stimuli-responsive cargo delivery capabilities to develop chemical communication systems. In their first contribution, the authors designed a cascade-like system of three gated nanoparticles (*ca.* 100 nm) which communicated with one another via the exchange of two chemical messengers (Figure 25).[100] The first nanoparticle was loaded with the reducing agent tris(2-carboxyethyl)phosphine (TCEP) and capped with a polysaccharide derivative (glucidex). The second nanoparticle contained the surfactant dodecyltrimethyl ammonium bromide (DTAB) and was capped with poly(ethylene glycol) (PEG) chains grafted to the silica surface via disulfide bonds. The third nanoparticle had an entrapped dye (safranin O) and its delivery was blocked by a lipid bilayer (1,2-

[100] C. Giménez, E. Climent, E. Aznar, R. Martínez-Máñez, F. Sancenón, M. D. Marcos, P. Amorós, K. Rurack, *Angew. Chem. Int. Ed.* **2014**, *53*, 12629.

dioleoyl-*sn*-glycero-3-phosphocholine, DOPC). The communication chain began with the addition of pancreatin (input), which induced enzymatic hydrolysis of the polysaccharide attached to the first nanoparticle resulting in the release of TCEP (first chemical messenger). This first messenger reduced the disulfide linkages on the second nanoparticle disassembling the molecular gate and delivering DTAB (second chemical messenger) – subsequently, the released DTAB was capable of disrupting the lipid bilayer of the third nanoparticle. Eventually, safranin O was delivered from the third nanoparticle generating a fluorescent signal in the solution as the final output of the system.

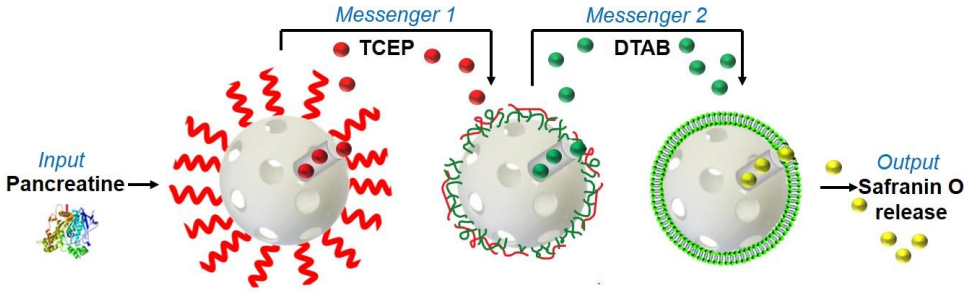

Figure 25. Representative example of communication between three gated nanocarriers. Cascade communication between gated mesoporous silica nanoparticles with different entrapped cargoes. The enzyme pancreatin (input) degrades the polysaccharide that caps nanoparticle 1 releasing the reductive species TCEP (messenger 1). TCEP diffuses to nanoparticle 2 and cleaves the disulfide-containing PEG chains inducing delivery of the second chemical messenger (DTAB). Eventually, DTAB disassembles the lipidic bilayer of the last nanoparticle and induces the release of a dye (safranin O, output).

Increasing the complexity of linear pathways, Martínez-Máñez and Villalonga and co-workers developed an interactive model of communication between nanoparticles based on enzymatic processes and the interchange of delivered chemical messengers.[54] The system employed two different Janus Au-mesoporous silica gated nanodevices (*ca.* 120 nm) in which the enzymes anchored to the Au face controlled the operation (cargo delivery) of the mesoporous gated

material (Figure 26). The first nanodevice was loaded with a dye ($[Ru(bpy)_3]Cl_2$) and capped with β-cyclodextrin (attached by means of disulfide bonds to the mesoporous unit) and functionalized with enzyme β-galactosidase (β-Gal) on the Au face. The second nanodevice contained a reducing agent (*N*-acetyl-L-cysteine) as entrapped cargo and was capped with a pH-responsive benzimidazole-β-cyclodextrin supramolecular nanovalve on the mesoporous face. Glucose oxidase (GOx) was anchored to the Au face. The biunivocal communication started with the hydrolysis of lactose (input) into galactose and glucose by β-galactosidase of the first nanoparticle. The produced glucose diffused to the second nanodevice where it was recognized and oxidized into gluconic acid by GOx on the Au face. This reaction induced a local drop in pH which caused the dethreading of the molecular gate of the second nanodevice and resulted in the delivery of entrapped *N*-acetyl-L-cysteine. This molecular messenger was transmitted as a feedback toward the first nanodevice, where it induced the rupture of the disulfide linkages on the molecular gate. Subsequently, the dye entrapped on the first nanodevice was finally released into the medium generating a colorimetric signal as the final output of the network.

In a more recent work, the same authors developed a more complex circular network of communication within a community of three nanodevices that communicate through a hierarchically programmed flow of chemical information. This system is described in Chapter 4.[101]

[101] B. de Luis, Á. Morellá-Aucejo, A. Llopis-Lorente, T. M. Godoy-Reyes, R. Villalonga, E. Aznar, F. Sancenón, R. Martínez-Máñez, *Chem. Sci.* **2021**, *12*, 1551.

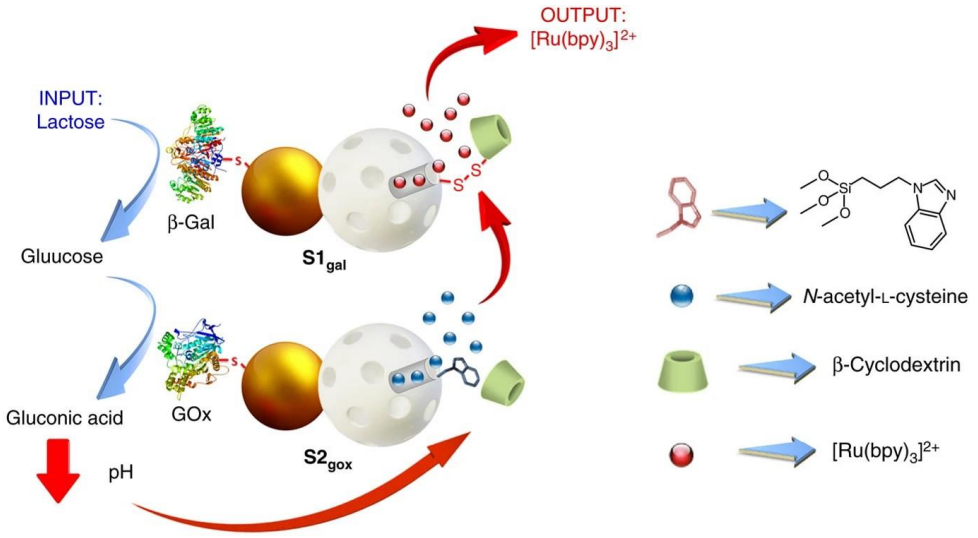

Figure 26. Representative example of communication between gated nanocarriers. Interactive model of communication between enzyme-functionalized Janus Au-mesoporous gated silica nanoparticles. Lactose (input) is transformed by β-galactosidase (β-Gal) on nanoparticle 1 (**S1$_{gal}$**, sender) into glucose, which is oxidized by GOx into gluconic acid on nanoparticle 2 (**S2$_{gox}$**, receiver). The local drop of pH results in the uncapping of the nanodevice 2 releasing the cargo (*N*-acetyl-L-cysteine), which diffuses back to **S1$_{gal}$** as a feedback messenger inducing the release of $[Ru(bpy)_3]Cl_2$. *Reprinted with permission from ref. 54 Copyright © 2017 by Springer Nature.*

1.6.4 Engineering communication between abiotic micro/nanodevices and living systems

Communication between abiotic nanoparticles and living systems opens the possibility of designing more complex particles able to read information from the environment (as input of the communication protocol) and interact with cells or tissues to achieve new and advanced functions which can not be achieved by the simple interaction of micro/nanoparticles or (bio)molecules with living systems, giving the particles principles of autonomy. As in the section above, a summary of

representative examples is provided. It is divided in close proximity and distant communication and also attending to the communication strategy employed.

- **Close proximity communication**

Simmel and co-workers developed communication between water-in-oil-droplets (50 µm) containing a TXTL system (population 1) and a *E. coli* bacterial cells (population 2) spatially arranged in a linear (1D geometry) chain (Figure 27A).[102] Droplets were produced using a microfluidic device by appropriate mixing of a surfactant-containing oil phase with a cargo-containing aqueous solution and arranged using a microfluidic capillary. By adding *S*-adenosyl methionine (SAM, trigger), the engineered transcription/translation constructs on one droplet expressed *N*-(3-oxo-hexanoyl)-L-homoserine lactone (AHL) that diffused to neighbor droplet compartments containing bacterium cells. Upon sensing of this molecule, droplet-encapsulated bacteria activated the synthesis of green fluorescent protein (GFP) as the output signal of the communication system. Additionally, the authors also built the reverse communication pathway (from bacteria-containing droplets to cell-free receiver droplets), by encapsulating AHL-producing bacteria (sender droplet) and an AHL-responsive GFP-expressing TXTL system (receiver droplet).

Mann and co-workers designed linear communication between giant liposomes and a red blood cells in direct contact (Figure 27B).[103] Control over the spatial positioning and arrangement in close proximity of giant liposomes and natural cells was achieved using ultrasounds in a custom-made acoustic trapping device. Upon addition of glucose and diffusion through membrane pores, the GOx-

[102] M. Schwarz-Schilling, L. Aufinger, A. Mückl, F. C. Simmel, *Integr. Biol.* **2016**, *8*, 564.
[103] X. Wang, L. Tian, Y. Ren, Z. Zhao, H. Du, Z. Zhang, B. W. Drinkwater, S. Mann, X. Han, *Small* **2020**, *16*, 1906394.

loaded liposome (sender) catalyzed the formation and release of H_2O_2 (chemical messenger). The red blood cell (receiver) sensed the presence of this messenger and induced the transformation of Amplex Red (present in the medium) into fluorescent resorufin (thanks to the intrinsic peroxidase activity of red-blood cells) as the output signal of the communication.

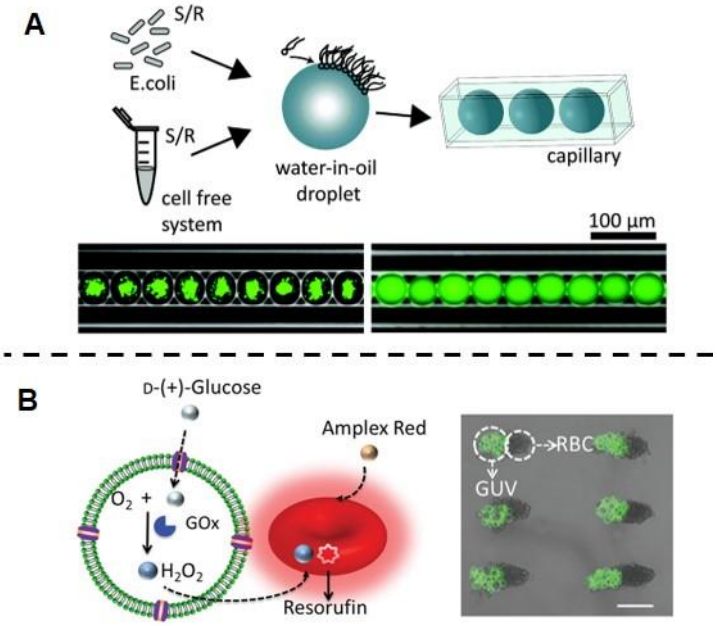

Figure 27. Representative examples of communication between abiotic entities and living systems in close proximity. **(A)** Construction of communication systems by encapsulation of *E. coli* and cell-free TXTL machinery in water-in-oil droplets and arrangement in a squared glass capillary. By flowing or encapsulating transcriptional inducers (communication trigger), senders produced and transmitted messengers to neighbors, that expressed GFP as the output of the system. *Reprinted with permission from ref. 102 Copyright © 2016 by Royal Society of Chemistry.* **(B)** Communication between GOx-containing giant liposomes (GUV) and red blood cells (RBC, with peroxidase activity). Uptake of glucose generates H_2O_2 inside liposomes which is transmitted to cells capable of oxidizing Amplex Red to fluorescent resorufin. Colonies of liposomes and RBCs are spatially organized into extended arrays (right and below) to study fluorescent output spatial and temporal diffusion. Scale bars=50 µm. *Reprinted with permission from ref. 103 Copyright © 2020 by John Wiley and Sons.*

In another similar study, Mann, Han and colleges co-trapped GOx-loaded giant liposomes (sender) with HepG2 cancer cells (receiver) (Figure 28).[104] H_2O_2 transmission induced cancer cell death as demonstrated by cell staining with propidium iodide. Finally, the authors proved the versatility of the employed methodology by establishing communication between liposomes containing IPTG and IPTG-responsive *E. coli* cells engineered with a plasmid encoding for GFP expression. Addition of melittin (input) induced the creation of pores in the lipid membrane (due to melittin-intercalation) which led to the subsequent transfer of IPTG (messenger) from the liposome to the bacteria. A remarkable increase in cell fluorescence (due to IPTG-responsive GFP expression) was observed as the output signal.

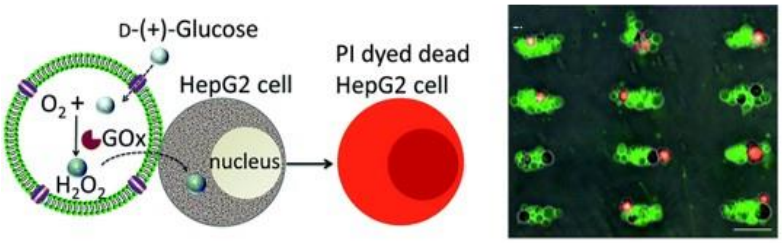

Figure 28. Representative examples of communication between abiotic entities and living systems in close proximity. Liposomes induce death of HepG2 cancer cells in co-trapped clusters via GOx-mediated H_2O_2 generation. On the right, microscopy images of liposomes (green) and HepG2 cells (red) after staining with PI (propidium iodide) to determine cell death. Scale bar=50 μm. *Reprinted with permission from ref. 104 Copyright © 2019 by Royal Society of Chemistry.*

[104] X. Wang, L. Tian, H. Du, M. Li, W. Mu, B. W. Drinkwater, X. Han, S. Mann, *Chem. Sci.* **2019**, *10*, 9446.

- **Distant communication**

As above, reported examples of distant communication between micro/nanodevices and living systems have been divided in different parts based on the use of enzymatic reactions, TXTL systems, DNA displacement reactions and gated nanocarriers.

Communication based on enzymatic reactions

Payne and co-workers developed one-way communication between protein-functionalized gelatin-alginate beads (sender) and engineered *E. coli* cells (receiver), triggered by *S*-adenosylhomocysteine (SAH).[105] In particular, Pfs-LuxS fusion protein was grafted onto gelatin-alginate spherical beads (2 mm diameter). Pfs and LuxS are two biosynthetic enzymes capable of catalyzing the formation of autoinducer 2 (AI-2, quorum molecule) in a cascade reaction. In the presence of SAH (input), the bead catalyzed the production of AI-2 (messenger) that diffused to bacteria (receiver) (Figure 29A). The bacteria sensed the presence of this chemical messenger and activated the expression of red fluorescent protein (RFP) as the output optical signal. In addition, the authors also showed the use of gelatin-alginate beads to entrap AI-2-producing *E. coli*, thus creating hybrid senders. These senders were capable of emitting AI-2 and inducing a free receiver bacterium to express RFP and become fluorescent. Finally, the authors fabricated beads capable of housing internal communication between Pfs-LuxS fusion protein (for SAH input detection and AI-2 production) and AI-2-responsive bacteria (that expressed fluorescent protein as the output).

[105] Y. Liu, H.-C. Wu, M. Chhuan, J. L. Terrell, C.-Y. Tsao, W. E. Bentley, G. F. Payne, *ACS Biomater. Sci. Eng.* **2015**, *1*, 320.

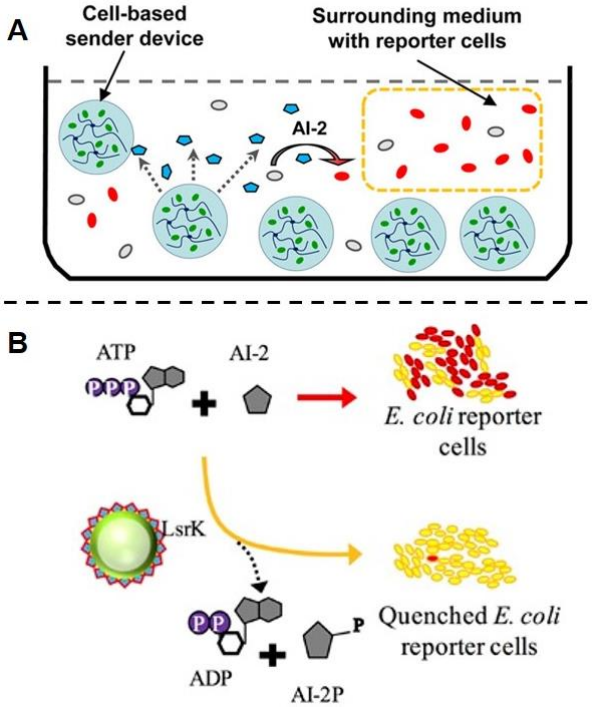

Figure 29. Representative examples of enzyme-based distant communication between abiotic entities and living organisms. **(A)** Communication between gelatin-alginate beads containing AI-2-producing bacteria (green) and reporter engineered cells (grey) in the surrounding environment. The enzymatic generation of AI-2 (blue pentagons) in the beads (senders) is detected by reporter cells that trigger expression of RFP. *Reprinted with permission from ref. 105 Copyright © 2015 by American Chemical Society.* **(B)** Communication between alginate-chitosan capsules functionalized with AI-2 processing kinase enzymes (LsrK) and AI-2-responsive *E. coli* reporter cells (red fluorescence expression). When ATP is present in solution, LsrK transforms AI-2 into a species which is not internalized by bacteria so protein expression is quenched. *Reprinted with permission from ref. 106 Copyright © 2018 by John Wiley and Sons.*

Bentley and co-workers showed the possibility to modulate bacterial quorum sensing pathways using enzyme-based artificial ensembles. The authors developed spherical polymeric capsules capable of quenching bacterial

communication via alteration of the bacterial AI-2 pathway.[106] Capsules (2 mm diameter) were prepared from alginate and chitosan and functionalized with AI-2 processing kinase enzyme (LsrK). In the absence of the capsules, *E. coli* reporter cells communicated by means of AI-2 as quorum signaling molecule which activated the expression of red fluorescent protein (Figure 29B). However, in the presence of the capsule, the quorum messenger was depleted due its phosphorylation with ATP by the capsule-kinase activity. ATP was either added to the medium or contained within the capsule. Therefore, the capsules functioned as communication quenchers and subsequently blocked AI-2 driven protein expression and fluorescent signal emission.

Communication based on TXTL systems

Mansy and co-workers presented an artificial cell activated by a chemical input (theophylline) that released a chemical messenger (IPTG) that activated a response in *E. coli* (Figure 30).[80] The artificial cell consisted of a liposome (1 μm) containing IPTG, DNA, and transcription-translation machinery. The DNA template activated translation in response to theophylline, resulting in the synthesis of the pore forming protein α-hemolysin inside the vesicle. As a consequence, IPTG (chemical messenger) was released from the vesicle and received by *E. coli*. As the output signal of the communication system, engineered *E. coli* became fluorescent due to GFP expression in response to IPTG. This linear communication was also confirmed by measuring gene expression from the *lac* operon of natural *E. coli* (induced by the presence of IPTG).

[106] M. K. Rhoads, P. Hauk, J. Terrell, C. Y. Tsao, H. Oh, S. R. Raghavan, S. S. Mansy, G. F. Payne, W. E. Bentley, *Biotechnol. Bioeng.* **2018**, *115*, 278.

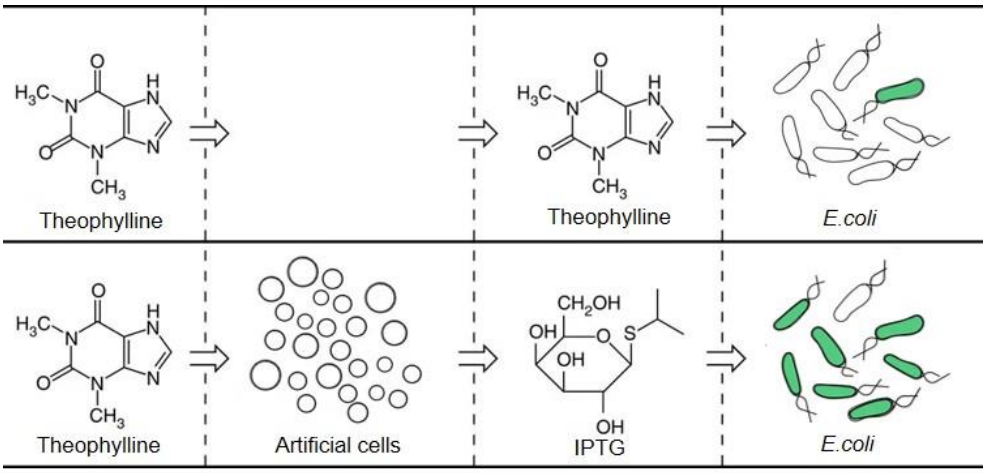

Figure 30. Representative example of TXTL-based distant communication between abiotic entities and living organisms. Upon theophylline processing, liposomes release IPTG which is sensed by engineered *E. coli* triggering the expression of GFP. *Adapted with permission from ref. 80 Copyright © 2014 by Springer Nature.*

Stano and co-workers developed a linear pathway to communicate TXTL-loaded giant liposomes (sender) with *Pseudomonas aeruginosa* bacteria (receiver) (Figure 31).[107] The communication route started in the TXTL-loaded giant liposomes with the constitutive production of the RhlI enzyme (without input addition, from encapsulated components). This enzyme catalyzed the formation of the signaling molecule C4-HSL (*N*-butyryl-L-homoserine lactone, acting as chemical messenger) from two encapsulated precursors (*S*-adenosyl-methionine and butyrylcoenzyme A, SAM and C4-CoA). C4-HSL traversed the lipid membrane, diffused through the medium and reached *P. aeruginosa* cells. The receiving cells contained a C4-HSL-responsive genetic circuit that produced bioluminescence as the output of the system.

[107] G. Rampioni, F. D'Angelo, M. Messina, A. Zennaro, Y. Kuruma, D. Tofani, L. Leoni, P. Stano, *Chem. Commun.* **2018**, *54*, 2090.

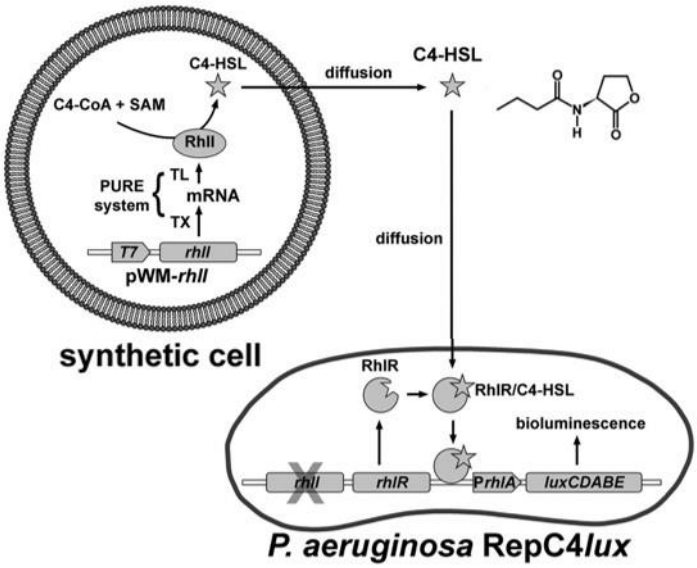

Figure 31. Representative example of TXTL-based distant communication between abiotic entities and living organisms. From encapsulated precursors (C4-CoA and SAM), giant vesicles synthesize C4-HSL (messenger) which freely diffuses to *P. aeruginosa* cells inducing bioluminescence (Lux protein). *Adapted with permission from ref. 107 Copyright © 2018 by Royal Society of Chemistry.*

Mansy and co-workers developed TXTL-loaded liposomes capable of communicating with bacteria by both sensing and synthesizing quorum molecules (Figure 32),[81] thus designing different communication pathways. In a cascade-like network, 3OC6HSL (first chemical messenger) secreted by *V. fischeri* bacteria (sender cell), induced TXTL-loaded liposomes to synthesize *N*-3-(oxododecanoyl)-homoserine lactone (3OC12HSL). In turn, 3OC12HSL acted as second chemical messenger diffusing from the liposomes to *E. coli* (receiver cell). This receiver cell expressed GFP as the output signal of the communication cascade. In a different cascade, TXTL-loaded liposomes expressed the enzyme AiiA in response to 3OC6HSL emitted by *V. fischeri* (sender cell). Then, these AiiA-expressing liposomes degraded (thanks to the AiiA activity) 3OC12HSL quorum molecules of *P. aerouginosa* and prevented biofilm formation. In a final system, TXTL-loaded

liposomes were designed to stablish interactive communication with *V. fischeri*. In response to small amounts of 3OC6HSL from *V. fischeri,* TXTL-loaded liposomes activated a genetic construct that produced more 3OC6HSL. The resulting higher levels of 3OC6HSL induced *V. fischeri* to activate GFP expression producing in a higher luminescence as the output of the system.

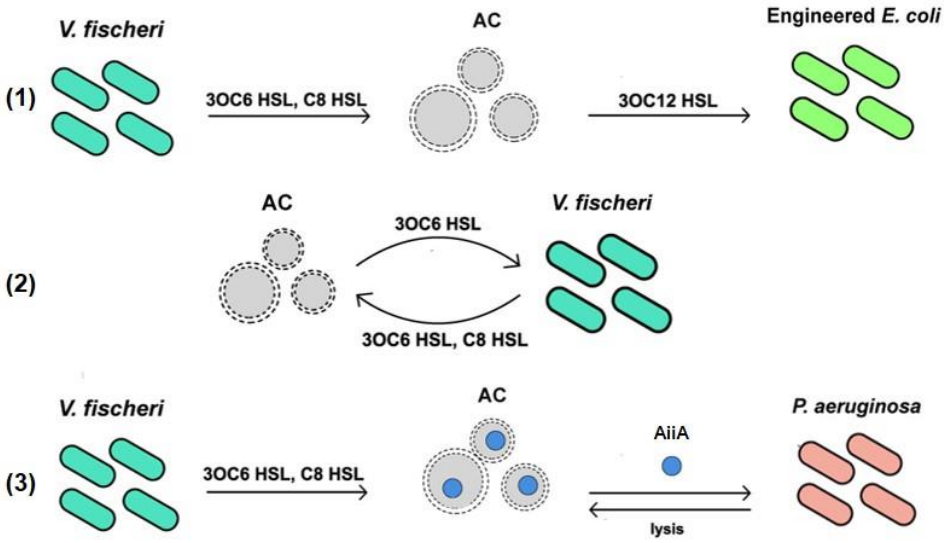

Figure 32. Representative example of TXTL-based distant communication between abiotic entities and living organisms. Artificial cells (AC) **(1)** mediate communication between *V. fischeri* and engineered *E. coli* bacteria, and **(2)** are capable of two-way communication with *V. fischeri* by sensing and synthesizing quorum molecules. **(3)** *V. fischeri* emits quorum molecules that induces AC to express AiiA enzyme. Subsequently, this AiiA activity disrupts biofilm formation of *P. aeruginosa*. *Adapted with permission from ref. 81 Copyright © 2017 by American Chemical Society.*

Tan and collaborators also designed communication networks between TXTL-loaded giant liposomes and engineered bacteria.[108] The authors evaluated firstly a linear communication scheme. The sender entity consisted of a liposome

[108] Y. Ding, L. E. Contreras-Llano, E. Morris, M. Mao, C. Tan, *ACS Appl. Mater. Interfaces* **2018**, *10*, 30137.

that expressed EsaI (acyl-homoserine-lactone synthase) and subsequently released AHL (chemical messenger) to the external medium. The receiver bacteria, with engineered DNA, contained the promoter EsaR and a GFP-encoding plasmid, thus when AHL penetrated in the receiver bacteria, EsaR repressor bound AHL subsequently triggering GFP expression as the reporter protein. In addition, the authors showed that another communication system could be designed by engineering sender (EsaI-expressing) bacteria and receiver (GFP-expressing) liposomes. In a final system, the authors also explored a feedback communication – in this case, the second entity carried a plasmid which expressed an antimicrobial peptide. Following the same genetic regulation pathway than the linear scheme, the expression of the antimicrobial peptide in the receiver was triggered by AHL secreted by the sender. Upon accumulation to a certain level, the antimicrobial peptide was released from the receiving entity and diffused to the first entity (bacteria or liposomes) inducing its lysis as the output of the network.

Mansy and co-workers achieved the activation of neural differentiation via the construction of TXTL-loaded micron-sized liposomes that communicated with eukaryotic cells (engineered human embryonic kidney cells and murine neural stem cells).[109] Liposomes contained three different DNA templates that coded for brain-derived neurotrophic factor, i.e. BDNF, responsible of neuronal differentiation and synapse formation/stabilization, LuxR (a 3OC6HSL-responsive transcriptional repressor) and perfringolysin O (PFO, a pore-forming protein). As the expression of PFO was regulated by LuxR, only in the presence of 3OC6HSL (input) the subsequent formation of pores allowed BDNF delivery (chemical messenger). Such artificial cells were able to communicate with GFP-expressing BDNF-responsive engineered human embryonic kidney cells (HEK293T cell line) by direct co-incubation, and with

[109] D. Toparlak, J. Zasso, S. Bridi, M. D. Serra, P. MacChi, L. Conti, M. L. Baudet, S. S. Mansy, *Sci. Adv.* **2020**, *6*, 4920.

murine neural stem cells by incubation employing Transwell plates. As reporters (outputs) of the communication pathways, GFP signal was measured in HEK239T cells and neural differentiation was evaluated by immunostaining cell counting in murine neural stem cells (Figure 33).

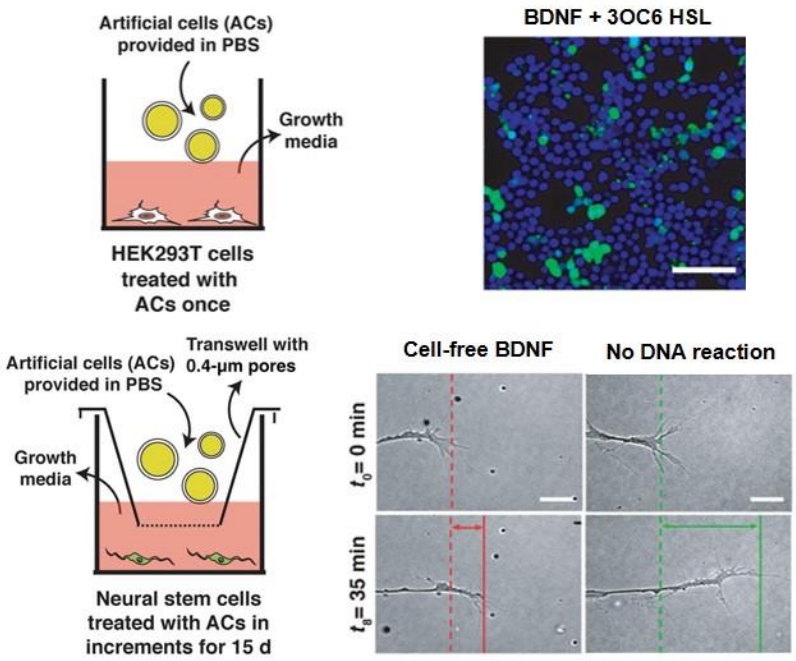

Figure 33. Representative example of TXTL-based distant communication between abiotic entities and living organisms. At the top, cocultivation of 3OC6HSL-responsive artificial cells (ACs) and engineered BDNF-sensitive HEK293T cells (top). Below, transwell coculture of the same kind of ACs and mouse neural stem cells. Upon 3OC6HSL addition, ACs produce brain-derived neurotrophic factor (BDNF) which triggers GFP expression in HEK293T cells (top, right) and differentiation of neural stem cells (below, right). Scale bars are 50 µm and 10 µm, respectively. *Adapted with permission from ref. 109 Copyright © 2020 by American Association for the Advancement of Science.*

Communication based on gated nanocarriers

The on-command delivery of an entrapped cargo from a synthetic nanodevice to induce an output signal in an organism by means of chemical

communication was demonstrated by Martínez-Máñez and co-workers. They constructed an interactive model of communication involving stimuli-responsive gated nanocarriers and yeast cells as model microorganism which is detailed in Chapter 5. Furthermore, they also developed a strategy to communicate different species (bacteria and cell yeasts) by means of a stimuli-responsive nanodevice which acts as a chemical translator between both organisms. This study is detailed in Chapter 6.

1.6.5 Communication through stigmergy

In contrast to collective behaviors mediated by communication between micro/nanoparticles and micro/nanoparticles with cells via the interchange of chemical messengers, many swarm systems found in nature communicate by modifying the environment. This concept is called stigmergy. Just to mention some examples in nature, ants deposit and sense chemical signals to form trails to sources of food and termites are able to build complex structures by modifying and locally sensing their physical environment. The concept of stigmergy, first proposed by the French entomologist Pierre-Paul Grasse, has been used to analyze self-organizing activities in a wide range of domains, including social insects, robotics, web communities and human society.[75] Yet, it is still poorly understood, as such its full power remains underappreciated and examples using micro/nanoparticles remains almost unexplored. In this communication protocol the trace left by an action in a medium stimulates subsequent actions. Stigmergy enables complex, coordinated activity without any need for planning, simultaneous presence, or even mutual awareness between the involved systems. The resulting self-organization is driven by a combination of positive and negative feedbacks, and it has usually the advantage of amplifying beneficial developments while suppressing errors. In this

communication protocol, one can imagine different communities of nanoparticles one of which performs an action and the trace of this action on the medium stimulates the performance of a second community of nanoparticles.

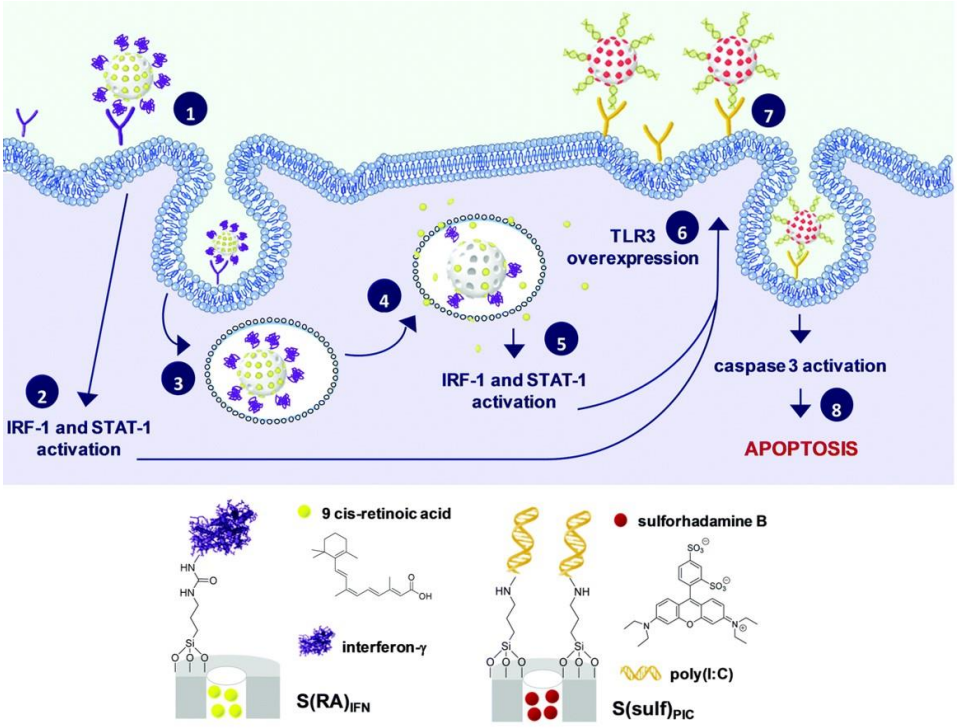

Figure 27. Representative example of a stigmergy communication strategy. Nanodevice 1 releases 9-*cis*-retionic acid and interferon-γ in cells and enhances the overexpression of membrane TLR3 receptors. As a consequence, a second nanodevice carrying polyinosinic-polycytidylic acid (poly(I:C)) is later endocyted more effectively and induces cell apoptosis. *Reprinted with permission from ref. 110 Copyright © 2020 by The Royal Society of Chemistry.*

For instance, Martínez-Máñez and coworkers recently described a nanoparticle-cell-nanoparticle communication route by stigmergy.[110] They employed two populations of mesoporous silica nanoparticles (*ca.* 100 nm) to kill

[110] A. Ultimo, C. De La Torre, C. Giménez, E. Aznar, C. Coll, M. D. Marcos, J. R. Murguía, R. Martínez-Máñez, F. Sancenón, *Chem. Commun.* **2020**, *56*, 7273.

SK-BR-3 breast cancer cells (Figure 27). Population 1 was loaded with 9-*cis*-retinoic acid (RA) and capped with interferon-ɣ (IFN). Population 2 was loaded with a fluorophore (sulforhodamine B) and capped with polyinosinic-polycytidylic acid (poly(I:C)). In a first step, the first community of nanoparticles interacted with the IFN receptors on the cell membrane. Upon the cell uptake, the gating ensembles were degraded by lysosomal activity releasing 9-*cis*-retinoic acid. Both RA and IFN induced the expression of the TLR3 receptor in the cells. This mechanism favored the performance of the second community of nanoparticles as the capping poly(I:C) strongly interacted with TLR3 facilitating the internalization of the nanoparticles. Poly(I:C) acted not only as targeting ligand but also had a cytotoxic effect since it activated apoptotic signaling pathways. The final release of the entrapped fluorophore enabled the assessment of the cooperative strategy by confocal microscopy. Cell viability studies also confirmed the successful induction of cancer cell elimination by stigmergy.

Towards a more advanced application, Bhatia and co-workers combined nanoparticles and the concept of stigmergy for synergistic cancer theranostic applications.[90] The authors used PEG-coated gold nanorods that showed tumor-targeting behavior (first entity). Moreover, they also designed magnetofluorescent iron oxide nanoworms and doxorubicin-loaded liposomes, which were functionalized with coagulation-targeting peptides (i.e., a fibrin-binding peptide and a glutamine-containing peptide to target transglutaminase FXIII) (second entity). Studies with these nanoparticles were carried out *in vivo* in a MDA-MB-435 tumor mice model. In a first step, PEG-nanorods were accumulated in tumors thanks to enhanced penetration through angiogenic blood vessels. NIR irradiation of the accumulated PEG-nanorods led to a local heating that disrupted tumor vessels and activated a coagulation cascade. This coagulation cascade subsequently induced the overexpression of the proteins transglutaminase FXIII and polymerized

fibrin. These proteins were targeted by the second wave of coagulation-targeting peptide-functionalized nanoparticles which resulted in accumulation of these nanoparticles around the tumor area. Iron oxide and nanorods acted as imaging agents, whereas doxorubicin-loaded liposomes acted as drug delivery vehicles with anti-tumor properties (Figure 28). In both examples, the trace on the medium of the action of a first community of nanoparticles stimulates the performance of a second community of nanoparticles by stigmergy.

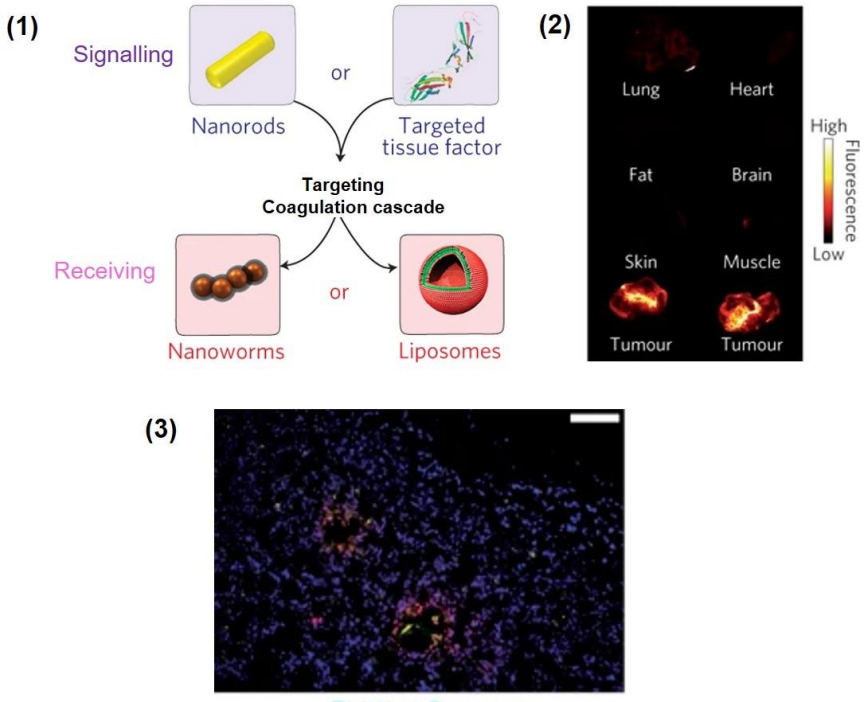

Figure 28. Representative example of a stigmergy communication strategy. **(1)** Theracnostics stigmergy strategy which employs signaling components (tumor-targeted plasmonic gold nanorods or tumor-targeted truncated tissue factor proteins) to activate a coagulation cascade that is targeted by receiving nanocomponents (iron oxide nanoworms or drug-loaded liposomes). **(2)** Nanoworms fluorescence imaging of mice organs after 24 h of injection revealing tumor targeting. **(3)** Histopathological analysis of tumor sections after 96 h of injection, demonstrating presence of doxorubicin from liposomes (red=doxorubicin, blue=nuclear stain). Scale bar=100 µm. *Adapted with permission from ref. 90 Copyright © 2011 by Springer Nature.*

1.6.6 Outlook

The idea of implementing communication capabilities in abiotic devices to construct strategies of cooperation between different entities inside networks allows sophisticated functionalities that go beyond those carried out by individual agents. The engineering of communication between micro/nanosystems has started to pick up steam in the last few years and scientists from different areas have been attracted to this endeavor. However, despite the progress, the field is still in its infancy and several challenges to be addressed in future research can be highlighted. In fact, to date, most of the research have been directed towards fundamental and proof-of-concept studies although some applications in different fields can be inferred from some illustrative works.

The development of more complex communication networks should be explored with the aim to integrate coordinated multicomponent communities of micro/nanodevices with advanced capabilities. A challenge is to understand which individual micro/nanoparticle communication processes could give rise to collective behaviors. Moreover, there are many open points about transmission and reception that need answering, such as: (i) which molecules should be used to encode information, (ii) how these molecules will be recognized, (iii) how to convert recognition into propagation of information, (iv) how to report information and (v) how to obtain cooperative behavior by using communication at the micro/nanoscale. Addressing these questions is no trivial matter, and a more complete and advanced experimental realization of these systems is still to come.

Finally, future studies should evolve towards the study of communication systems in realistic settings (e.g., *in vivo*) and the demonstration of actual applications. For instance, particles that communicate could be used to amplify molecular signals for sensing applications, to program chemical synthesis or for smart drug delivery. In this sense, the concept of stigmergy is highly appealing as it

allows the development of complex systems in which there is not mutual awareness between involved micro/nanoparticles, yet they are able to communicate through actions on the medium by a first swarm of micro/nanodevices that stimulates the performance of a second community of micro/nanoparticles. In addition, evolution of communication paradigms will require the collaboration of researchers from different fields embracing from basic micro/nanodevice design, knowledge of how to encode/decode information and construct chemical networks at the micro/nanoscale, to realistic evaluation and (bio)-related applications. Overall, the engineering of chemical communication between micro/nanosystems will lay the foundations of future applications in different areas such as biomedicine, nanorobots, life-like materials and information technologies among others.

In this context, this PhD Thesis has explored the communication capabilities of enzyme-functionalized hybrid mesoporous nanodevices starting from the logic processing of environmental chemical information, the transmission of such information within a community of nanodevices as well as the inclusion of living organisms and even different species in the communication pathway.

Chapter 2. Objectives

Given the relevance of implementing communication capabilities in smart nanodevices and materials, this PhD Thesis has aimed to contribute to the field of nanotechnology upon the design and development of chemical communication strategies involving enzyme-functionalized hybrid nanodevices.

In particular, we have focused on the design, preparation and characterization of nanodevices based on loaded mesoporous silica nanoparticles equipped with enzymatic effectors and molecular gates as well as the evaluation and optimization of their communicative aptitudes in different scenarios.

The specific objectives that have been addressed are:

- To prepare a delivery nanocarrier that chemically communicates with the environment mimicking a Boolean logic function (1-to-2 demultiplexer) and evaluate its performance in cancer cells.

- To design a system of circular communication between thee different nanodevices based on the exchange of chemical messengers mediated by enzymes and molecular gates.

- To develop an interactive model of chemical communication between an abiotic nanodevice and a living organism.

- To demonstrate that it is possible to induce cross-kingdom communication involving two different cells and tailor-made nanodevices acting as “nanotranslators”.

Chapter 3. A 1-to-2 Demultiplexer Hybrid Nanocarrier for Cargo Delivery and Activation

A 1-to-2 Demultiplexer Hybrid Nanocarrier for Cargo Delivery and Activation

Beatriz de Luis,[a,b] Alba García-Fernández,[a,b,c] Antoni Llopis-Lorente,[a,b] Reynaldo Villalonga,[e] Félix Sancenón,[a,b] and Ramón Martínez-Máñez*[a,b,c,d]

[a] Instituto Interuniversitario de Investigación de Reconocimiento Molecular y Desarrollo Tecnológico (IDM), Universitat Politècnica de València, Universitat de València, Camino de Vera s/n, 46022 Valencia, Spain. E-mail: rmaez@qim.upv.es

[b] CIBER de Bioingeniería, Biomateriales y Nanomedicina (CIBER-BBN), Spain.

[c] Unidad Mixta UPV-CIPF de Investigación en Mecanismos de Enfermedades y Nanomedicina, Universitat Politècnica de València, Centro de Investigación Príncipe Felipe, Valencia, Spain.

[d] Unidad Mixta de Investigación en Nanomedicina y Sensores, Universitat Politècnica de València, Instituto de Investigación Sanitaria La Fe, Valencia, Spain

[e] Nanosensors & Nanomachines Group, Department of Analytical Chemistry, Faculty of Chemistry, Complutense University of Madrid, Madrid, Spain.

Published online: July 24, 2020

(Reprinted with permission from *Chem. Commun.* **2020***, 56,* 9974*.*

3.1 Abstract

A biocomputing strategy implemented in hybrid nanocarriers for controlled cargo delivery is described. The nanodevice consists of enzyme-functionalized Janus Au-mesoporous silica nanoparticles, which behave as an electronic demultiplexer (DEMUX). The nanocarrier is capable of reading molecular information from the environment (lactose) and selecting one of two possible outputs (galactose production or 4-methylumbellilferone release and activation) depending on the presence of an addressing input (NAD^+).

3.2 Introduction

Research in the field of nanorobotics is a current topic in science since it offers promising tools in a great number of different áreas including diagnostics and therapeutic strategies.[1] Futuristic nanobots are expected to have specific functionalities such as (i) being able to read information from the environment, (ii) having autonomous movement and (iii) being able to communicate with other nanobots for instance through the interchange of chemical messengers.[2] In this scenario, an attractive characteristic of nanoparticles is to design them so that they are able to sense the environment and act accordingly. Although simple controlled release nanoparticles already perform this action, since they deliver a cargo on-command in the presence of certain stimuli, it is desirable in this field to design more advanced nanosystems capable of performing complex biocomputing operations.

Biocomputing science, which involves studies on biocompatible reactions utilized for information processing and signal transduction into YES/NO decisions, has been gaining increasing attention.[3] This behavior mimics the binary (0,1) format

of Boolean logic operations in electronics. To date, different discrete and sequential logic gates based on enzymatic reactions, fluorescence or absorption switches and DNA cross-linking, cleavage or strand displacements among others have been developed.[4-7] These are capable of logically processing multiple input signals into a final YES/NO output. However, few such systems have been implemented in nanodevices for controlled-release applications. Moreover, considering the environmental complexity at the cellular level, it is reasonable to consider that biocomputing networks of nanodevices with built-in logics should be required to successfully process all the available information and achieve a desired final action.

With the aim of broadening the scope and exploring the implementation of biocomputing operations in stimuli-responsive delivery applications, herein, we report the design and preparation of a nanodevice that imitates a 1-to-2 demultiplexer reading the molecular information from the environment and selecting a response. Demultiplexers (DEMUX) are digital electronic components used to switch signals between different channels in a circuitry.[8-11] 1-to-2 demultiplexers process 1 input and select only one of the possible 2 outputs depending on the presence or absence of an additional input (addressing input). They can be implemented by connecting two AND logic gates operating in parallel and one NOT logic gate (Scheme 1). Previous work by Willner and co-workers showcased the realization of a DNA-based demultiplexer for the assembly of DNAzyme nanostructures.[11]

Here, we have implemented this behaviour by programmed concatenation of enzyme-based reactions integrated in a drug delivery nanocarrier conferring the ability to analyze potential physiological scenarios and actuate (cargo release) only when needed. Besides, by taking advantage of the efficiency and versatility of enzymes, the whole mechanism is complemented with the extra functionality of in situ cargo activation once delivered.[12] In this way, we expand the utility of

mesoporous carriers by introducing different biocomputing elements that can be integrated into a complex nanodevice, as a versatile strategy for the design of nanosystems with logic programmable behaviour. Typical nanocarriers release their cargo in the presence of a single stimulus, whereas nanocarriers with biocomputing demultiplexer capabilities could be useful for the design of more selective delivery systems targeting certain cells or tissues where two stimuli are simultaneously present. For instance, cancer cells have been demonstrated to exhibit elevated levels of both saccharide uptake and NAD^+/NADH.[13,14]

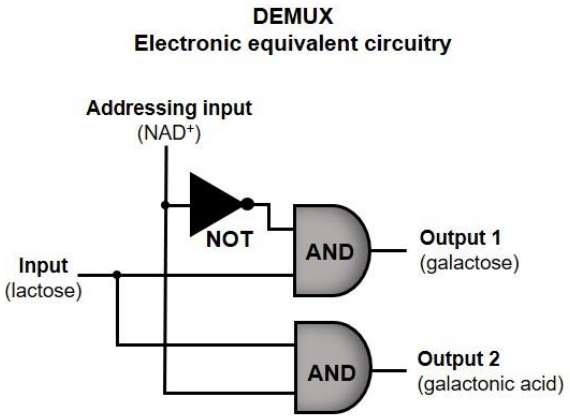

Input (lactose)	Addressing input (NAD^+)	Output 1 (galactose)	Output 2 (galactonic acid)
0	0	0	0
0	1	0	0
1	0	1	0
1	1	0	1

Scheme 1. In descending order: representation of a 1-to-2 demultiplexer following electronic symbology and the equivalent switching device, and the representation of the equivalent combinatorial logic circuitry and the corresponding Truth Table that describes the behaviour of the system.

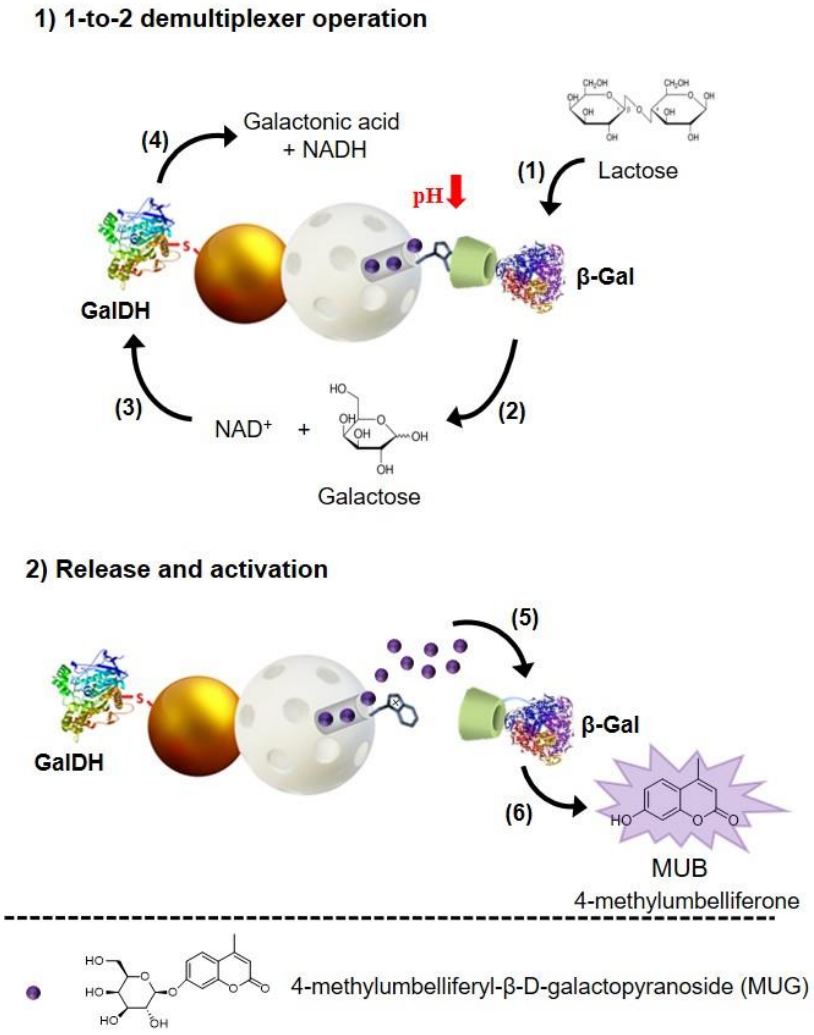

Scheme 2. Illustration of the nanodevice concatenated three-step enzymatic cascade when the input (lactose) and the addressing input (NAD^+) are present leading to MUG release and subsequent activation into strong fluorescent MUB.

The nanocarrier (**S1$_{enz}$**) is based on Janus Au-mesoporous silica nanoparticles, which are functionalized with the enzyme galactose dehydrogenase (GalDH) on the gold face. The mesoporous unit is loaded with a model pro-fluorophore (4-methylumbelliferyl-β-D-galactopyranoside, MUG) and capped with a pH-responsive supramolecular nanovalve consisting of an inclusion complex

between a benzimidazole derivative and β-cyclodextrin (see Scheme S1 in Supporting Information, SI). The enzyme β-galactosidase (β-Gal) attached to the β-cyclodextrin completes the design.

The operation of the final **S1$_{enz}$** nanodevice is depicted in Scheme 2. **S1$_{enz}$** is able to sense the presence of lactose (1), which is transformed into glucose and galactose by the enzyme β-Gal (2). The generated galactose (3) is ''output 1''. Moreover, when the enzymatic co-factor NAD^+ is also present in the environment, the galactose is oxidized to galactono-ɣ-lactone by the GalDH enzyme on the Au face. This lactone is spontaneously converted into galactonic acid (4), which is ''output 2''. When only ''output 1'' is generated, no cargo delivery is observed; however, if ''output 2'' is obtained (galactonic acid), a local decrease of the pH causes protonation of the benzimidazole groups (pK_a = 5.55)[15] and dethreading of the inclusion complex, triggering the delivery of the entrapped MUG (5) from the mesoporous face. In addition, an additional cargo activation is accomplished by the hydrolysis of the glycosidic bond of the released MUG by the β-Gal enzyme inducing the appearance of a highly fluorescent emission (6) due to the formation of 4-methylumbellilferone (MUB). This activation step might be crucial in situations where the payload needs to be derivatized to overcome solubility and stability troubles during the device assembly but reactivated when delivered at the target site.[16]

The Janus Au-mesoporous silica nanoarchitecture allowed the anchorage of two different enzymes to the same nanodevice (one on the Au face, and the other on the silica face) via different chemistries. In our system, the importance of the selected strategy relies on two main factors: (i) there is more space for β-Gal immobilization (which is less active than GalDH) on the benzimidazole-mesoporous surface; and (ii) GalDH, which is commercialized in much lower quantities (as compared to β-Gal), can be directly immobilized on the Au face without the need for previous derivatization. Based on enzymatic assays (see the SI), the amounts of

β-Gal and GalDH on **S1$_{enz}$** were determined to be 51 and 13 mg per g nanoparticle, respectively (i.e., 7:3 β-Gal:GalDH ratio), with lower β-Gal activity (0.007 U·mg^{-1}) as compared to GalDH (1.05 U·mg^{-1}).

3.3 Results and discussion

After the synthesis and characterization of the nanodevice **S1$_{enz}$** using standard techniques (see the SI), the 1-to-2 demultiplexer behaviour was examined. For this purpose, **S1$_{enz}$** (1 mg·mL^{-1}) was suspended in an aqueous solution at pH 7.5 (20 mM sodium sulphate) in the absence and presence of selected stimuli (lactose, galactose, NAD^+, galactose + NAD^+, and lactose + NAD^+) and the emission of the generated MUB at 445 nm (λ_{ex} = 365 nm) was measured. In the absence of stimuli (the black curve in Figure 1), a low MUB emission was found (less than 10% of the maximum observed), which is ascribed to some remaining not fully capped pores. Negligible MUB fluorescence was also observed when **S1$_{enz}$** was suspended in the presence of only galactose (the orange curve), only lactose (the green curve) and only NAD^+ (the pink curve), all of them at 1 mM concentration. As a clear contrast, a marked MUG release/activation from **S1$_{enz}$** was observed in the presence of the addressing inputs NAD^+ and lactose (both at 1 mM) (Figure 1), which is ascribed to the triggering of the whole programmed enzymatic pathway, as shown in Scheme 2. Moreover, we also observed that when galactose (instead of lactose) and NAD^+ (1 mM) were used as inputs, MUG release and activation were achieved faster (*ca.* 90% after 60 min) (the red curve in Figure 1). This faster response is in agreement with the omission of the first step of the enzymatic cascade. In this case, dethreading of the supramolecular complex and pore opening occur via direct transformation of galactose into galactonic acid by GalDH without depending on the previous activity of β-Gal. In additional control experiments, the **S1$_{enz}$** response was tested in the presence of other saccharides (glucose, fructose

and sucrose at 1 mM) and the addressing input concentration (NAD^+) was set to 1 mM. In all cases, negligible cargo delivery after 4 h was observed (Figure S11, SI), pointing out the high specificity of the delivery system.

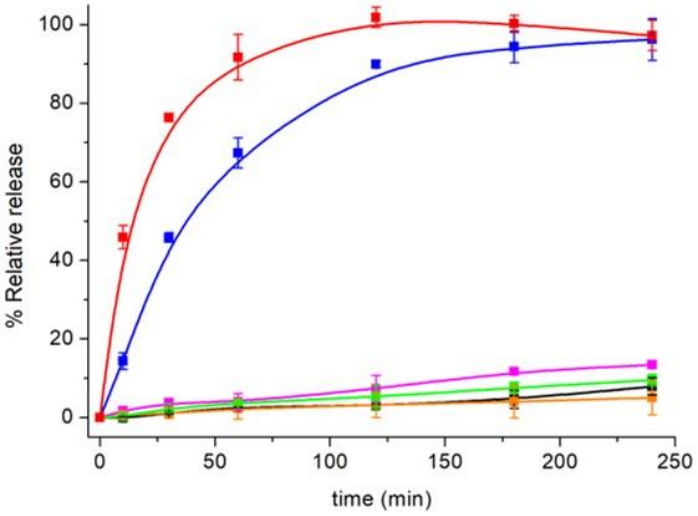

Figure 1. Normalized controlled release kinetic profiles obtained for solid **S1$_{enz}$** in the absence of stimulus (blank, black curve); in the presence of NAD^+ 1 mM (pink), in the presence of galactose 1 mM (orange); in the presence of lactose 1 mM (green) and in the presence of both lactose and NAD^+ 1 mM (blue) and galactose and NAD^+ 1 mM (red).

The crucial role played by both immobilized enzymes in the delivery/activation mechanism was tested using two new nanodevices lacking the enzyme GalDH (**S1$_{\beta Gal}$**) or the enzyme β-Gal (**S1$_{GalDH}$**). The MUG delivery/activation process was studied with **S1$_{\beta Gal}$** and **S1$_{GalDH}$** in the presence of both lactose + NAD^+ at 1 mM concentration after 4 h. It was found that only when both enzymes are immobilized on the nanodevice (**S1$_{enz}$**) can the fluorophore MUB form, whereas in the case of **S1$_{\beta Gal}$** and **S1$_{GalDH}$** nanoparticles, negligible MUG release/activation was observed since the cascade enzymatic reaction could not be completed (Figure 2). Additionally, in order to demonstrate the β-galactosidase-mediated activation of MUG into MUB, we studied the response of the nanodevice lacking β-galactosidase

(**S1**$_{GalDH}$) by protonation of the benzimidazole subunits by dropping the pH of the aqueous solution to 4.5. Under these conditions, negligible MUB fluorescence was observed (Figure S12, SI) since the supramolecular complex between benzimidazole and β-cyclodextrin was dethreaded but the released MUG was not activated into the highly emissive MUB derivative due to the lack of β-galactosidase. However, when the β-Gal enzyme was added to the suspension, a marked MUB emission was observed. Thus, MUG activation is ascribed to the presence of the β-Gal enzyme and not to the changes in the environmental chemical external conditions such as pH variations.

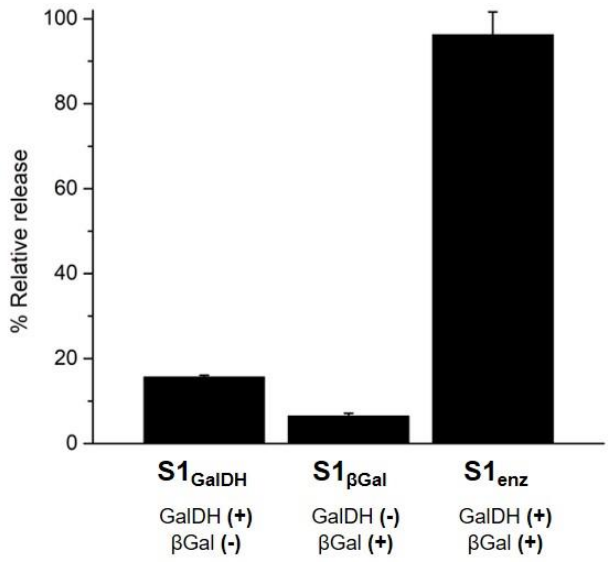

Figure 2. Normalized cargo release of different solids with (+) or without (-) immobilized enzymes in presence of lactose and NAD^+ 1 mM after 4 h of addition.

Finally, we demonstrated the possible use of this 1-to-2 demultiplexer at the cellular level. First, we assessed the biocompatibility of **S1**$_{enz}$ by cell viability assays, which revealed that the nanodevice was well-tolerated by HeLa cells at concentrations up to 200 mg·mL^{-1} after 24 h of exposure (Figure S13, SI). In a further

experiment, **S1$_{enz}$** (75 mg·mL^{-1}) was internalized into the HeLa cells and then the cells were incubated in the absence or presence of lactose. After 24 hours, MUB associated fluorescence was assessed by confocal microscopy (Figure 3).

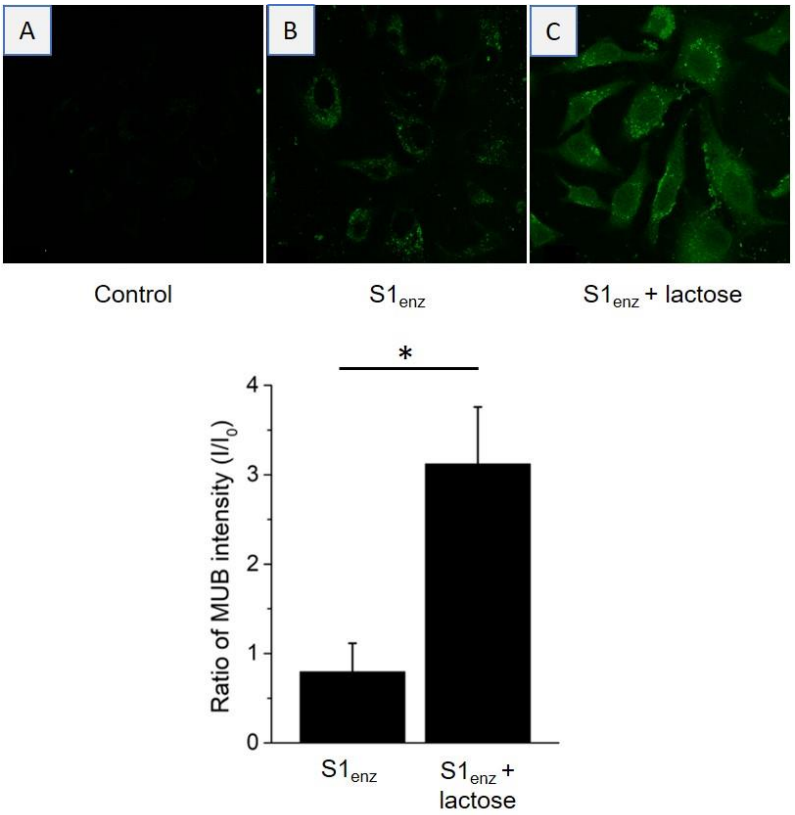

Figure 3. Top: controlled cargo release studies of **S1$_{enz}$** in HeLa cells. **(A)** HeLa cells without any treatment, **(B)** HeLa cells treated with 75 µg·mL^{-1} of **S1$_{enz}$** and **(C)** HeLa cells treated with 75 µg·mL^{-1} of **S1$_{enz}$** in the presence of lactose 1 mM. Below: ratio of mean fluorescence intensity (I/I_0) of MUB signal in HeLa cells for both treatments (**S1$_{enz}$** and **S1$_{enz}$**+lactose) (* $p < 0.05$).

Control untreated HeLa cells (Figure 3A) showed negligible emission upon excitation at 405 nm, while HeLa cells incubated with **S1$_{enz}$** (Figure 3B) showed a residual background signal attributed to cargo delivery from some remaining uncapped pores. In contrast, a marked emission was observed when HeLa cells

were treated with the nanodevice and lactose (Figure 3C, see the SI for details). Under these conditions, **S1$_{enz}$** was able to transform lactose into galactose and glucose. The galactose formed in the presence of NAD^+ (which is a biomolecule naturally available in cells)[13] started the enzymatic cascade reactions, which released MUG and ultimately activated this molecule into a highly emissive MUB fluorophore, as shown in Scheme 2. Moreover, the fluorescence intensity of the confocal images of each treatment was quantified (Figure 3, below) and a 3-fold enhancement was observed for the HeLa cells treated with **S1$_{enz}$** + lactose when compared to the cells incubated with the nanodevice alone, **S1$_{enz}$**.

3.4 Conclusions

In conclusion, we report herein the design, synthesis, characterization and operation of a new nanodevice (**S1$_{enz}$**) capable of reading information from the environment and processing this information, imitating a 1-to-2 demultiplexer. Cargo delivery and activation are only observed in the presence of both lactose and NAD^+, in a process mediated by GalDH and β-Gal. The 1-to-2 demultiplexer nanodevice is operative in aqueous solution and also when internalized in cells. Although we are aware that the illustrated system is a proof of concept, it describes a paradigm beyond the simple on-command release and activation of a cargo by leveraging organism intrinsic biomolecules. We present the use of enzyme-functionalized hybrid mesoporous nanodevices as a valuable and versatile strategy to tailor different biocomputing elements that may be implemented in individual smart nanobots acting according to environmental information.[17] We also envisage the interconnection of these nanodevices by means of chemical communication,[18] creating complex networks that operate as advanced electronic circuitries performing sophisticated actions. In the drug delivery field, this strategy may open up unexploited prospects in smart therapies and personalized treatments.[19]

Acknowledgements. The authors wish to thank the Spanish Government (projects RTI2018-100910-B-C41 (MCUI/AEI/FEDER, UE), CTQ2017-87954-P), the Generalitat Valenciana (PROMETEO 2018/024), the Comunidad de Madrid (IND2017/BMD-7642) and CIBER-BBN (NANOCOMMUNITY project) for support.

3.5 References

1. F. Soto and R. Chrostowski, *Front. Bioeng. Biotechnol.* **2018**, *6*, 170.
2. X. Zhang, L. Chen, K. H. Lim, S. Gonuguntla, K. W. Lim, D. Pranantyo, W. P. Yong, W. J. T. Yam, Z. Low, W. J. Teo, H. P. Nien, Q. W. Loh and S. Soh, *Adv. Mater.* **2019**, *31*, 1804540.
3. S. Mailloux and E. Katz, *Biocatalysis* **2014**, *1*, 13.
4. E. Katz, *ChemPhysChem* **2019**, *20*, 9.
5. S. Erbas-Cakmak, S. Kolemen, A. C. Sedgwick, T. Gunnlaugsson, T. D. James, J. Yoon and E. U. Akkaya, *Chem. Soc. Rev.* **2018**, *47*, 2228.
6. H. Su, J. Xu, Q. Wang, F. Wang and X. Zhou, *Nat. Commun.* **2019**, *10*, 5390.
7. R. Orbach, B. Willner and I. Willner, *Chem. Commun.* **2015**, *51*, 4144.
8. M. A. Arugula, V. Bocharova, J. Halamek, M. Pita and E. Katz*, J. Phys. Chem. B* **2010**, *114*, 5222.
9. J. Andreasson, S. D. Straight, S. Bandyopadhyay, R. H. Mitchell, T. A. Moore, A. L. Moore and D. Gust, *J. Phys. Chem. C* **2007**, *111*, 14274.
10. I. S. Turan, G. Gunaydin, S. Ayan and E. U. Akkaya, *Nat. Comm.* **2018**, *9*, 805.
11. R. Orbach, F. Remacle, R. D. Levine and I. Willner, *Chem. Sci.* **2014**, *5*, 1074.
12. C. Luo, J. Sun, B. Sun and Z. He, *Trends Pharmacol. Sci.* **2014**, *35*, 556.
13. J. V. Moreira, M. Hamraz, M. Abolhassani, E. Bigan, S. Pérès, L. Pauvelé, M. L. Nogueira, J. -M. Steyaert and L. Schwartz, *Metabolites* **2016**, *6*, 33.
14. K. Adekola, S. T. Rosen and M. Shanmugam, *Curr. Opin. Oncol.* **2012**, *24*, 650.
15. G. Jerez, G. Kaufman, M. Prystai, S. Schenkeveld and K. K. Donkor, *J. Sep. Sci.* **2009**, *32*, 1087.
16. Z. Guon, *Acta Pharm. Sin. B* **2017**, *7*, 119.
17. A. Llopis-Lorente, B. de Luis, A. García-Fernández, M. Orzáez, F. Sancenón, R. Villalonga and R. Martínez-Máñez, *ACS Appl. Mater. Interfaces* **2018**, *10*, 26494.
18. A. Llopis-Lorente, P. Díez, A. Sánchez, M. D. Marcos, F. Sancenón, P. Martínez-Ruiz, R. Villalonga and R. Martínez-Máñez, *Nat. Commun.* **2017**, *8*, 15511.
19. A. A. Tregubov, P. I. Nikitin and M. P. Nikitin, *Chem. Rev.* **2018**, *118*, 10294.

3.6 Supporting Information

Chemicals

Tetraethyl orthosilicate (TEOS), *n*-cetyltrimethylammonium bromide (CTABr), sodium hydroxide (NaOH), gold(III) chloride trihydrate ($HAuCl_4 \cdot 3H_2O$), sodium citrate tribasic dihydrate, (3-mercaptopropyl) trimethoxysilane, paraffin wax, 3-mercaptopropionic acid, 4-methylumbelliferyl β-D-galactopyranoside, (3-iodopropyl) trimethoxysilane, benzimidazole, triethylamine, β-cyclodextrin, β-galactosidase from *Aspergillus oryzae*, β-galactose dehydrogenase S of *Pseudomonas fluorescens* from *E. coli*, *N*-(3-dimethylaminopropyl)-*N*'-ethylcarbodiimide hydrochloride (EDC), *N*-hydroxysuccinimide (NHS), D-(+)-lactose monohydrate, β-nicotinamide adenine dinucleotide hydrate (NAD^+), D-(+)-galactose, glucose oxidase from *Aspergillus niger*, 2,2'-azino-bis(3-ethylbenzothiazoline-6-sulfonic acid) diammonium salt (ABTS) and peroxidase from horseradish (HRP) from Sigma-Aldrich and used without further purification.

Sodium sulfate anhydrous, sodium dihydrogen phosphate monohydrate, disodium hydrogen phosphate heptahydrate, ethanol, chloroform, toluene and anhydrous acetonitrile were provided by Scharlau.

For cell culture, Dulbecco's Phosphate Buffered Saline (PBS), Dulbecco's Modified Eagle's Medium (DMEM) - high glucose, Fetal Bovine Serum (FBS) and Hoechst 33342 were purchased from Sigma-Aldrich. Cell proliferation reagent WST-1 was obtained from Roche Applied Science. HeLa human cervix adenocarcinoma cells were purchased from the German Resource Centre for Biological Materials (DSMZ).

General Methods

Powder X-ray diffraction (PXRD), transmission electron microscopy (TEM), N_2 adsorption-desorption isotherms, UV-visible and fluorescence spectrophotometry, dynamic light scattering (DLS) and elemental analysis techniques were employed for materials characterization. PXRD measurements were performed on a Seifert 3000TT diffractometer using CuKα radiation at low angles ($1.3 < 2\theta < 8.3$, with steps of 0.04 degrees and 3 seconds for step) and high angles ($35 < 2\theta < 80$ with steps of 0.04 degrees and 1 second for step). TEM images were acquired using a JEOL TEM-1010 Electron microscope working at 100 kV. Additionally, TEM coupled with energy dispersive X-ray spectroscopy (TEM-EDX) was used for element mapping using a JEOL TEM-2100F microscope. DLS studies were performed using a ZetaSizer Nano ZS (Malvern). N_2 adsorption-desorption isotherms were recorded on a Micromeritics TriStar II Plus automated analyzer. Samples were previously degassed at 90 °C in vacuum overnight and measurements were performed at 77 K. UV-visible spectra were recorded with a JASCO V-650 Spectrophotometer. Fluorescence measurements were carried out in a JASCO FP-8500 Spectrophotometer. Elemental analysis was performed using a LECO CHNS-932 Elemental Analyzer. Cell viability measurements were taken with a Wallac 1420 workstation. Confocal microscopy imaging was performed with a Leica TCS SP8 AOBS (Leica Microsystems Heidelberg GmbH) inverted laser scanning confocal microscope.

Synthesis of mesoporous silica nanoparticles (MSNPs)

1.00 g (2.74 mmol) of *n*-cetyltrimethylammonium bromide (CTABr) was dissolved in 480 mL of deionized water. Then, the pH was basified by adding 3.5 mL of a 2 $mol \cdot L^{-1}$ NaOH solution and the temperature was increased to 80 °C. Next, tetraethyl orthosilicate (TEOS) (5 mL, 22.4 mmol) was added dropwise into the

solution. Magnetic stirring was kept for 2 h to give a white suspension. Finally, the solid was isolated by centrifugation, washed several times with water until neutral pH and dried at 70 °C overnight (as-synthesized MSNPs). To obtain the final MCM-41 type mesoporous nanoparticles (**MSNPs**), the as-synthesized solid was calcined at 550 °C in an oxidant atmosphere for 5 h in order to remove the surfactant.

Synthesis of gold nanoparticles

Gold nanoparticles were synthesized following the Turkevich-Frens method.[1] 100 mL of a 0.3 mM $HAuCl_4 \cdot 3H_2O$ solution were brought to 135 °C under stirring and refluxing. Then, 1.5 mL of a 1 % sodium citrate solution was added to yield gold nanoparticles of *ca.* 20 nm. The initially pale-yellow colour turned to purple-black and finally red wine in 10 min. After this, the colloidal suspension was cooled to room temperature under stirring. This protocol was repeated 4 times until obtaining 400 mL of the colloidal gold nanoparticles suspension.

Synthesis of Janus Au-mesoporous silica nanoparticles (S0)

180 mg of mesoporous silica nanoparticles (**MSNPs**) were dispersed in 9 mL of an aqueous solution (6.7 % ethanol) followed by addition of *n*-cetyltrimethylammonium bromide (CTABr, 1 μM). The mixture was heated at 75 °C, and then 1 g of paraffin wax was added. Once the paraffin was melted, the mixture was vigorously stirred for 15 min using a homogenizer (Ultra-Turrax T-8, IKA). Then, the mixture was further stirred for 1 h at 75 °C using a magnetic stirrer. The resulting Pickering emulsion was then cooled to room temperature, diluted with 10 mL of methanol and reacted with 200 μL of (3-mercaptopropyl) trimethoxysilane for 3 h. The solid was collected by centrifugation and washed with methanol. For gold attachment, the partially mercapto-functionalized nanoparticles were dispersed in 68 mL of methanol and added over the 400 mL of the colloidal gold nanoparticles

suspension previously synthesized. The mixture was stirred overnight at room temperature. Then, the solid was isolated by filtration and exhaustively washed with chloroform and hexane. The solid was dried and ground. This process finally yielded the Janus Au-mesoporous silica nanoparticles (**S0**).

Synthesis of S1

For the preparation of **S1**, 60 mg of **S0** were suspended in anhydrous acetonitrile (4 mL) and reacted with 60 µL of (3-iodopropyl) trimethoxysilane for 5.5 h. The solid was isolated by centrifugation, washed with acetonitrile and dried at 70 °C overnight. To functionalize the surface with benzimidazole moieties, 0.25 g of benzimidazole and 990 µL of triethylamine were mixed with 20 mL of toluene and heated for 20 min at 80 °C in order to prepare a saturated solution of benzimidazole. 10 mL of this suspension were added over 60 mg of the previously prepared nanoparticles. The mixture was stirred at 80 °C for three days. Afterward, the benzimidazole-functionalized solid was isolated by centrifugation and washed with toluene. To functionalize the gold face, the resulting solid was suspended in 5 mL of acetonitrile and reacted with 50 µL of 3-mercaptopropionic acid for 1 h. This solid (**S0-benz**) was centrifuged, washed with toluene and with water and dried at 70 °C overnight. Next, the loading process was carried out by suspending the solid in 15 mL of a concentrated solution of 4-methylumbelliferyl-β-D-galactopyranoside hydrochloride in 50 mM phosphate buffer at pH 7.5 (20 mg, 3.9 mM). The mixture was stirred overnight (**S0-MUG**). Then, the loaded support was capped by the addition of 367.5 µL of a 64 $mg \cdot mL^{-1}$ solution of β-cyclodextrin-modified β-galactosidase derivative (β-gal-CD, synthesized as previously reported)[2] to the aqueous loading suspension and stirred overnight. Finally, the solid was centrifuged, washed thoroughly with 50 mM phosphate buffer at pH 7.5 and dried under vacuum. This process yielded solid **S1**.

Synthesis of $S1_{enz}$

8 mg of **S1** were suspended in 3 mL of 50 mM sodium phosphate buffer at pH 7.5. Then, 2.5 mg of *N*-(3-dimethylaminopropyl)-*N*'-ethylcarbodiimide hydrochloride (EDC), 2.5 mg of *N*-hydroxysuccinimide (NHS) and 120 µL of the enzyme galactose dehydrogenase were added and the suspension was stirred overnight at 10 °C. The solid was isolated by centrifugation and washed several times with cold 50 mM sodium phosphate buffer (pH 7.5). The resulting **$S1_{enz}$** was kept wet in refrigerator until use.

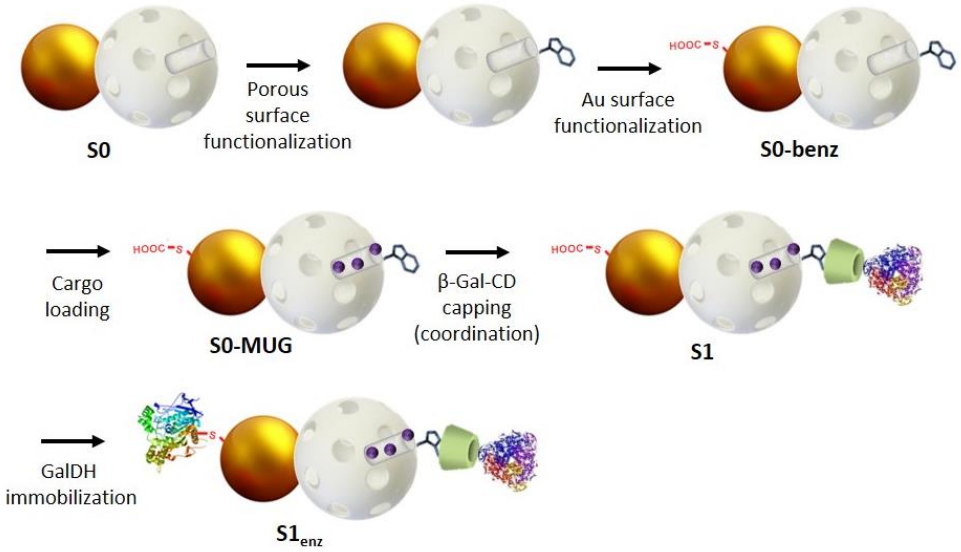

Scheme S1. Illustration of nanodevice assembly.

The assembly of the nanodevice starts with the porous surface functionalization (with benzimidazole moieties) and the Au surface functionalization (with 3-mercaptopropionic acid). Then the loading step consists of suspending the previously obtained functionalizated mesoporous scaffold in a concentrated solution of the cargo in phosphate buffer at pH 7.5. Then this mixture is stirred overnight. Afterwards, the loaded support is capped by adding a solution

of β-gal-CD and stirring overnight. The attached benzimidazole and dissolved β-CD forms an inclusion complex (complex formation constant of 104±8 M^{-1})[3] based on Van der Waals forces and hydrophobic interactions[4] which acts as a cap entrapping the payload (Scheme S1). Then the solid is isolated by centrifuging and it is intensively washed by several cycles of resuspension and centrifugation in phosphate buffer at pH 7.5 to remove the excess of the cargo present in the solution and also adsorbed into the pore voids which may have not been capped. Despite the excess of the capping ensemble employed and the subsequent washing steps, achieving total capping efficiency is not possible and some residual cargo delivery was observed (Figure 1, main text). As regards the nanodevice operation, upon recognition of the saccharide input, the local pH drops below the pK_a benzimidazole value (pK_a=5.55)[5] due to the generation of galactonic acid by galactose dehydrogenase, causing the protonation of benzimidazole groups. As a result, noncovalent interactions decrease leading to the dissociation of the host-guest complex and provoking the release of the cargo from the pores.

Materials Characterization

Solids were characterized by standard techniques.

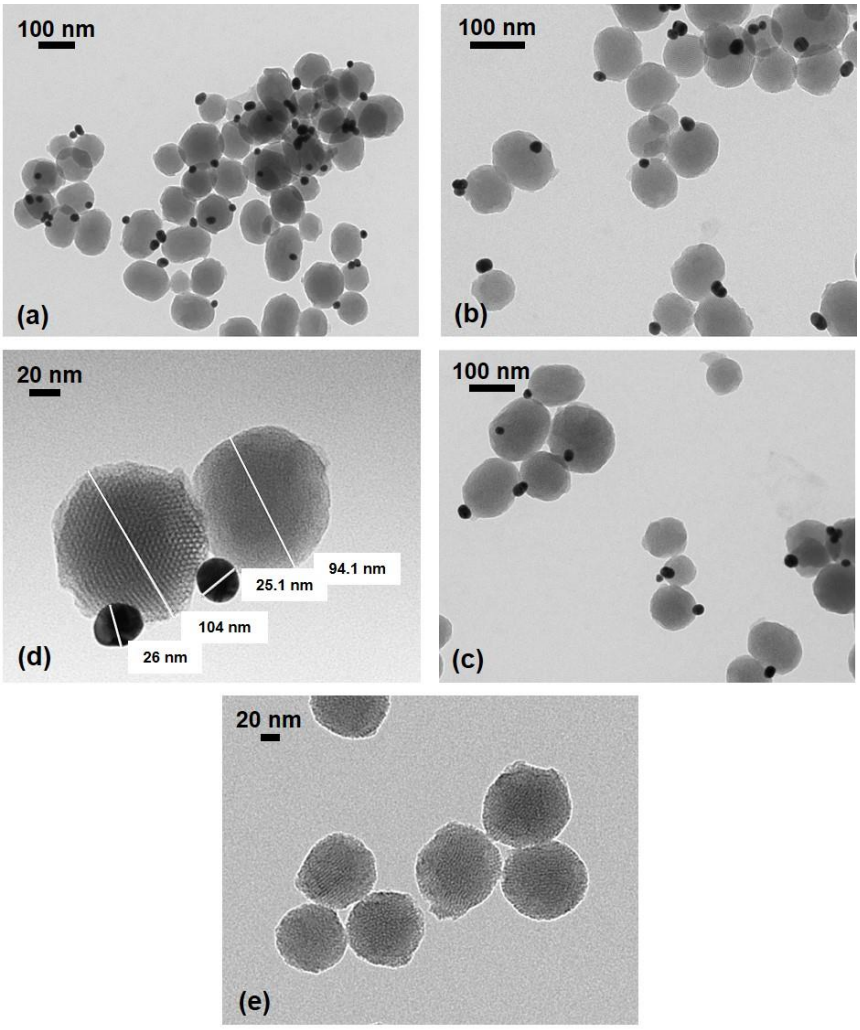

Figure S1. TEM images of (a-d) Janus Au-mesoporous silica nanoparticles **S0** and (e) **calcined MSNPs**.

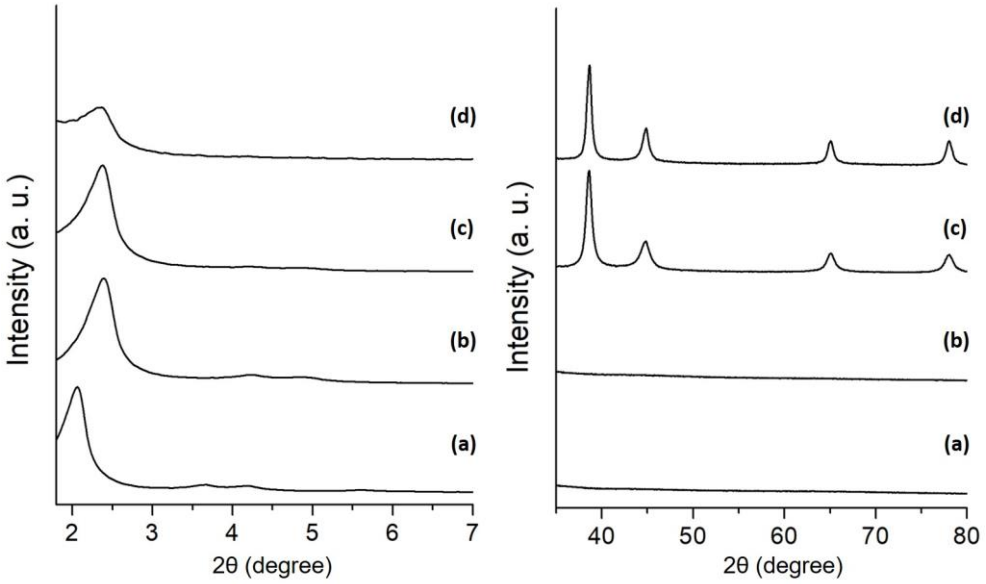

Figure S2. Powder X-ray diffraction patterns of (a) **as-made MSNPs**, (b) **calcined MSNPs**, (c) Janus Au-mesoporous silica nanoparticles **S0** and (d) solid **S1** at low (left) and high (right) angles.

Figure S2 shows the powder X-ray diffraction patterns at low ($1.5 < 2\theta < 7$) and at high angles ($35 < 2\theta < 80$) of **as-made MSNPs**, **calcined MSNPs**, **S0** and **S1**. At low angles, the **as-made MSNPs** (a) shows characteristic low-angle reflections. For the **calcined MSNPs** (b), we observed a slight displacement of the peaks related to the condensation of silanol groups during the calcination process. These low-angle typical peaks are preserved in the Janus Au-mesoporous silica nanoparticles **S0** (c). The presence of the (100) peak in the PXRD patterns in the solid **S1** indicated that the different chemical modifications, functionalization and cargo loading had not damaged the mesoporous structure. Moreover, the high-angle diffraction pattern of the Janus colloids **S0** and **S1** showed the cubic gold characteristic (111), (200), (220) and (331) diffraction peaks, confirming the presence of gold nanocrystals and the Janus Au-MS architecture.[6] Powder X-ray diffraction pattern of $\mathbf{S1_{enz}}$ was not obtained due to the low quantity collected in the synthesis but the

not-harsh enzyme immobilization procedure is not expected to affect the mesoporous structure.

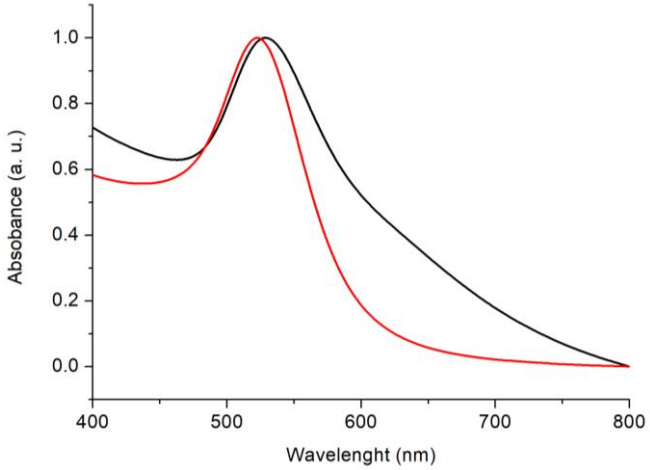

Figure S3. Normalized UV-Visible spectra of the gold nanoparticles (red) and Janus Au-mesoporous silica nanoparticles **S0** (black).

UV/vis measurements in aqueous solution were performed on the as-synthesized gold nanoparticles and on Janus Au-mesoporous silica nanoparticles **S0** (by suspending 1 mg of solid in 1 mL of distilled water). The starting gold colloid shows a single absorption band at 523 nm, characteristic of the surface plasmon resonance of spherically shaped nanospheres with an approximately 20 nm diameter (Figure S3). In the **S0** spectrum, there is a redshift of the absorbance maximum (530 nm) and a broadening of the band (Figure S3). These two facts can be ascribed to the increase in the refractive index around the gold nanospheres due to the MSNPs attachment and to light refraction produced by silica.[7]

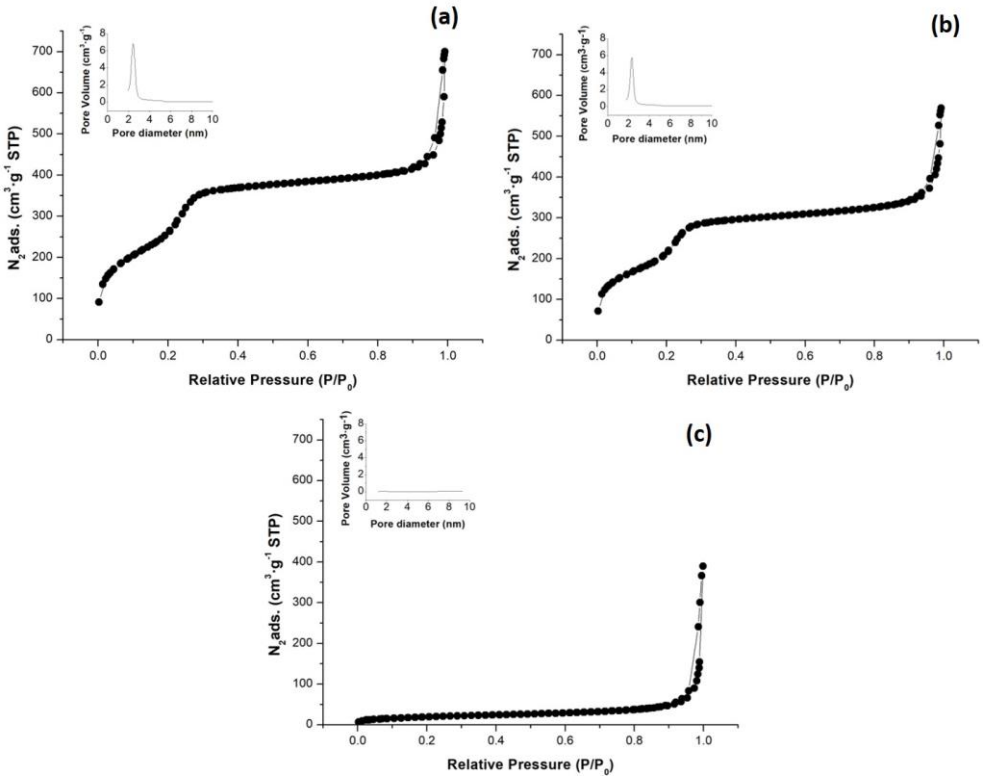

Figure S4. The N_2 adsorption-desorption isotherms for (a) the **calcined MSNPs**, (b) Janus Au-mesoporous silica nanoparticles **S0** and (c) functionalized and loaded solid **S1**.

The N_2 adsorption-desorption isotherms of the **calcined MSNPs** and Janus Au-MS nanoparticles **S0** show an adsorption step at intermediate P/P_0 value 0.3, which is characteristic for mesoporous solids with empty pores (Figure S4). This step is related to the nitrogen condensation inside the mesopores by capillarity. The absence of a hysteresis loop in this interval and the narrow BJH pore distribution suggest the existence of uniform cylindrical mesopores. Application of the BET model results in a value for the total specific surface of 960 $m^2 \cdot g^{-1}$ for **calcined MSNPs** and 799 $m^2 \cdot g^{-1}$ for Janus Au-mesoporous silica nanoparticles **S0**. Total specific surface area for **S1** significantly decreased to 74 $m^2 \cdot g^{-1}$ due to the cargo

loading inside the mesopores. In order to calculate pore size and total pore volume, BJH model was applied on the adsorption band of the isotherm for $P/P_0 < 0.6$ (associated to adsorption inside the pores). N_2 adsorption-desorption isotherms for the functionalized and loaded solid **S1** show a significant decrease in N_2 volume adsorbed and are flat when compared (at the same scale) to those from **MSNPs** and **S0** (Figure S4). This indicates that there is a significant pore blocking accordingly the loading and capping processes. BET specific values, pore volumes and pore sizes calculated from N_2 adsorption-desorption isotherms for **MSNPs**, Janus Au-MS nanoparticles **S0** and **S1** are listed in Table S1.

Table S1. BET specific surface area, pore volumes and pore sizes calculated from N_2 adsorption-desorption isotherms for selected materials.

Solid	S_{BET} [$m^2 \cdot g^{-1}$]	Pore Volume [$cm^3 \cdot g^{-1}$]	Pore size [nm]
Calcined MSNPs	960 ± 13	0.70	2.44
S0	799 ± 23	0.56	2.33
S1	74 ± 1	0.05	- -

The zeta potential and hydrodynamic size were also measured by dynamic light scattering (DLS) (Table S2 and Figure S5, respectively). For carrying out the experiments, the corresponding materials were suspended in distilled water at pH 7 at a concentration of 0.01 $mg \cdot mL^{-1}$.

Table S2. Zeta potential values determined by DLS for the different materials.

Sample	Zeta Potential (mV)
MSNPs	-34.4 ± 0.6
S0	-33.6 ± 0.8
S0-benz	-29.6 ± 0.5
S1	-42.4 ± 1.4
S1$_{enz}$	-39.7 ± 1.5

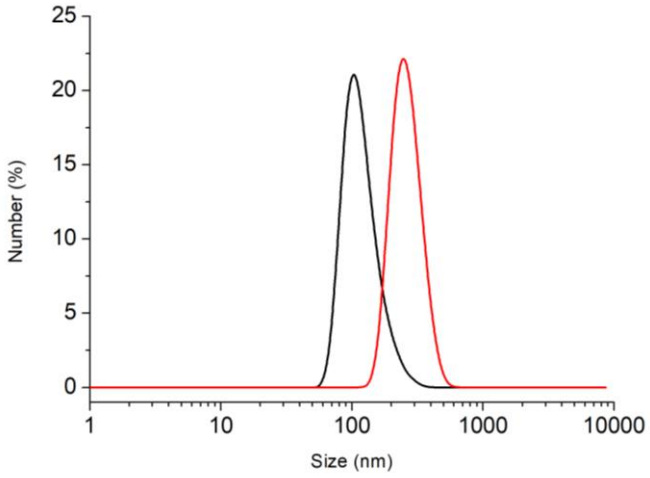

Figure S5. Hydrodynamic diameter distribution (nm) determined by DLS for Janus Au-mesoporous silica nanoparticles **S0** (120 ± 12, black) and final solid **S1$_{enz}$** (265 ± 14, red).

From elemental analysis data (Table S3), composition of solids was calculated. Considering the data obtained from the analysis of **S0-MUG** (loaded and functionalized solid), the amount of $(CH_2)_3$-benzimidazole was determined as 18.8

mg·g^{-1} of solid and the cargo 4-methylumbelliferyl-β-D-galactopyranoside was estimated to be 171.1 mg·g^{-1}.

Table S3. Elemental analysis data.

Solid	% C	% H	% N
S0	1.84	2.62	0.10
S0-MUG	12.96	2.36	0.33

TEM-EDX mapping of the final nanodevice **S1$_{enz}$** shows the presence of nitrogen atoms in the whole scaffold, which is attributed to the immobilized enzyme (galactose dehydrogenase) in the gold face as well as the benzimidazole moiety of the molecular gate and the enzyme containing β-cyclodextrin derivative (β-galactosidase) in the mesoporous silica face (see Figure S6).

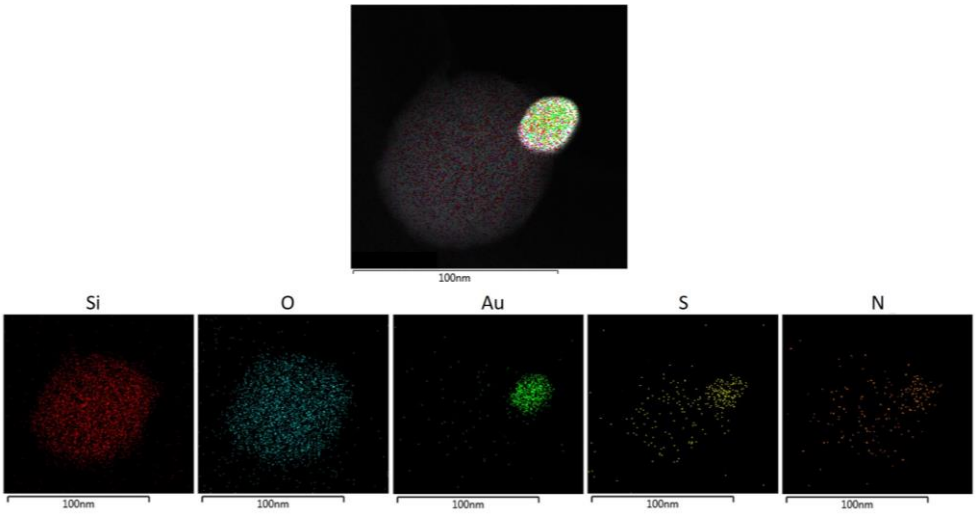

Figure S6. TEM-EDX element mapping of the gold region in the nanodevice **S1$_{enz}$**. Top: mapped area with layered atom composition. Bottom: mapping of different atoms.

In order to confirm the presence of the capping ensemble (β-cyclodextrin), ^{13}C MAS NMR of different solids were carried out. As can be seen in Figure S7, the benzimidazole-functionalized solid (**S0-benz**, red line) shows no aliphatic signals. Moreover, we prepared also the **S0-benz** solid additionally capped with β-cyclodextrin. In this case the ^{13}C MAS NMR spectrum shows a main aliphatic signal at 75 ppm which corresponds to the C-atoms linked to the O-atoms of β-cyclodextrin (blue line) as reported in the literature.[8]

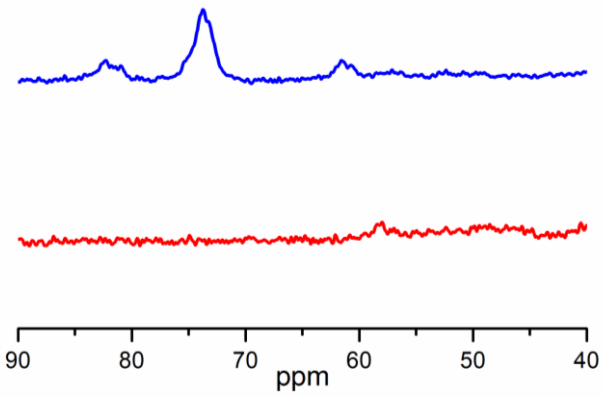

Figure S7. ^{13}C MAS NMR spectra for benzimidazole-functionalized solid (**S0-benz**, red line) and **S0-benz** capped with β-cyclodextrin (blue line).

Functionalization was also assessed by TEM imaging after staining the final nanodevice **S1$_{enz}$** with 1% uranyl acetate. The dark layer around the nanoparticles demonstrates a high coverage with organic matter (Figure S8).

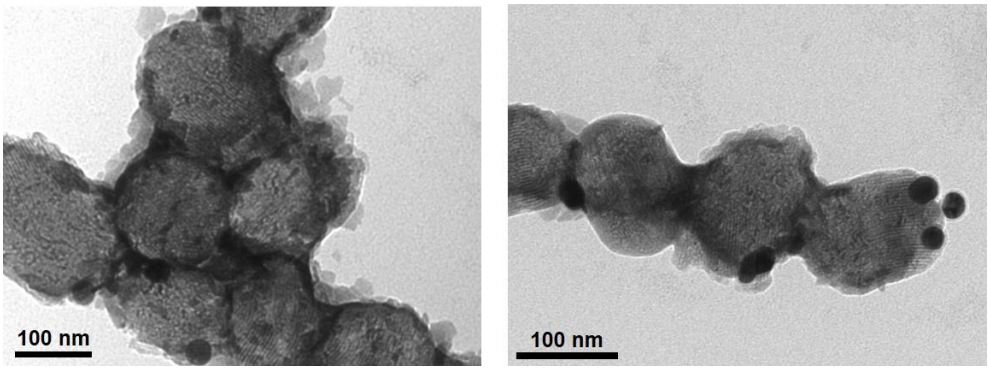

Figure S8. TEM images of **S1$_{enz}$** after staining with 1% uranyl acetate.

Enzyme activity assays

The immobilization of β-galactosidase was confirmed by running the corresponding enzyme activity assay and was calculated by applying the following formula:

$$\frac{Enzyme\ Units}{g} = \frac{(\Delta - \Delta_{blank}) \cdot V_T \cdot F_D}{\varepsilon_{chromop.} \cdot l \cdot V_S \cdot C_S}$$

Where, Δ is the slope of the graph (min^{-1}); Δ_{blank} is the slope of the graph for the blank (min^{-1}); V_T is the total volume in the cuvette; F_D is the dilution factor; $\varepsilon_{chromop.}$ is the molar extinction of the corresponding chromophore at a defined wavelength ($M^{-1}{\cdot}cm^{-1}$); l is the optical path in the cuvette (1 cm); V_S is the volume of the sample added (mL) and C_S is the concentration of sample added ($g{\cdot}mL^{-1}$).

The method we used in order to test β-galactosidase activity is based on the cleavage of lactose by β-galactosidase into galactose and glucose. Then, the glucose is oxidised by glucose oxidase leading to gluconic acid and hydrogen peroxide. Hydrogen peroxide reacts with ABTS (2,2'-azino-bis(3-ethylbenzothiazoline-6-sulfonic acid) diammonium salt) in the presence of

peroxidase (HRP) to form a blue-green product ($ABTS^{\cdot+}$) that can be followed UV-visible spectrophotometry (λ_{abs} = 418 nm).

Reactions for assaying β-galactosidase activity are:

$$D\text{-}lactose + H_2O \xrightarrow{\beta\text{-Galactosidase}} D\text{-}glucose + D\text{-}galactose$$

$$D\text{-}glucose + O_2 + H_2O \xrightarrow{\text{Glucose oxidase}} D\text{-}gluconic\ acid + H_2O_2$$

$$H_2O_2 + ABTS \xrightarrow{\text{HRP}} ABTS^{\cdot+} + H_2O$$

In order to check β-galactosidase activity, 250 µL of lactose (5 mg·mL^{-1}), 250 µL of ABTS solution (1 mg·mL^{-1}), 50 µL of glucose oxidase solution (1 mg·mL^{-1}) and 50 µL of HRP solution (2 mg·mL^{-1}) were placed in a quartz cuvette. All solutions had been prepared in 50 mM sodium phosphate buffer at pH 7.5. Then, 10 µL of either buffer (for blank), commercial enzyme solution in buffer (5 mg·mL^{-1}) or **S1$_{enz}$** suspension (5 mg·mL^{-1}) were added. The mixture was shaken and absorbance at 418 nm was monitored as a function of time. Whereas no change was observed in the absence of nanoparticles or commercial enzyme, a strong blue-green colour appeared in the presence of those. The increase in absorbance ($ABTS^{\cdot+}$ formation) as a function of time in the presence of **S1$_{enz}$** and the commercial enzyme solution is depicted in Figure S9. After applying the previously indicated formula (ε_{ABTS} at 418 nm = 36,000 M^{-1}·cm^{-1}), the activity of β-galactosidase on **S1$_{enz}$** and the activity of commercial β-galactosidase was determined. From this data, the quantity of enzyme per g of solid was inferred.

Table S4. Summary of the β-galactosidase activity assays.

β-gal on S1$_{enz}$	0.007 U per mg of solid
Commercial β-gal	0.131 U per mg of commercial enzyme
51 mg of β-galactosidase per g of **S1$_{enz}$**	

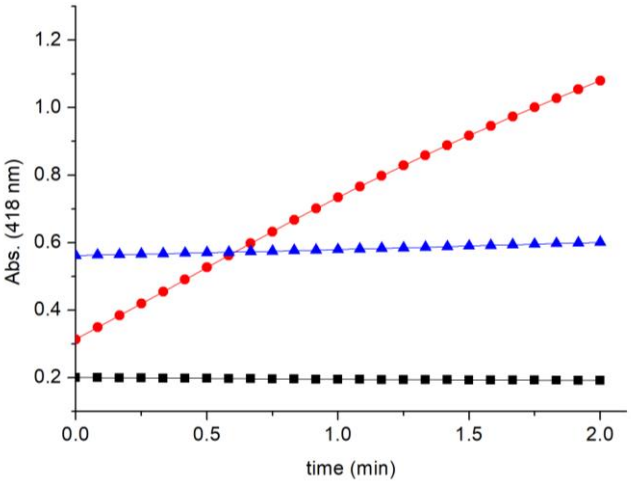

Figure S9. Monitoring of absorbance at 418 nm ($ABTS^{\cdot+}$ formation) due to β-galactosidase activity on nanoparticles **S1$_{enz}$** (blue), enzyme solution (red) and blank (black).

The immobilization of galactose dehydrogenase was also confirmed by testing its activity. This assay is based on the production of the fluorescent species NADH (reduced β-nicotinamide adenine dinucleotide) by galactose dehydrogenase which can be followed using fluorescence spectrophotometry (λ_{exc} = 340 nm; λ_{em} = 460 nm).

Reaction for assaying galactose dehydrogenase activity is:

$$D\text{-}galactose + NAD^{+} \xrightarrow{\text{Galactose dehydrogenase}} D\text{-}galactono\text{-}\gamma\text{-}lactone + NADH + H^{+}$$

In order to check galactose dehydrogenase activity, 250 µL of galactose 1 M (180 mg·mL^{-1}), 25 µL of NAD^{+} 20 mM solution (13.25 mg·mL^{-1}) and 475 µL of 50 mM sodium phosphate buffer at pH 7.5 were placed in a black walled cuvette. All solutions had been prepared in 50 mM sodium phosphate buffer at pH 7.5. Then, 5 µL of either buffer (for blank), commercial enzyme or **S1$_{enz}$** suspension (5 mg·mL^{-1}) were added. The mixture was incubated shaking for 2 min, centrifuged and

fluorescence at 460 nm was measured. A negligible fluorescent signal was observed in the absence of nanoparticles or commercial enzyme (Figure S10). However, emission bands, with a maximum located at 460 nm, for commercial enzyme and **S1$_{enz}$** suspension were observed (Figure S10). Considering the specifications of the commercial enzyme (80 U per mg of protein; bottle of 200 U·mL^{-1}), the activity of the nanoparticles was determined by proportionality.

Table S5. Summary of the galactose oxidase activity assays

GalDH on S1$_{enz}$	1.052 U per mg of solid
Commercial GalDH	80 U per mg of commercial enzyme
13 mg of galactose dehydrogenase per g of **S1$_{enz}$**	

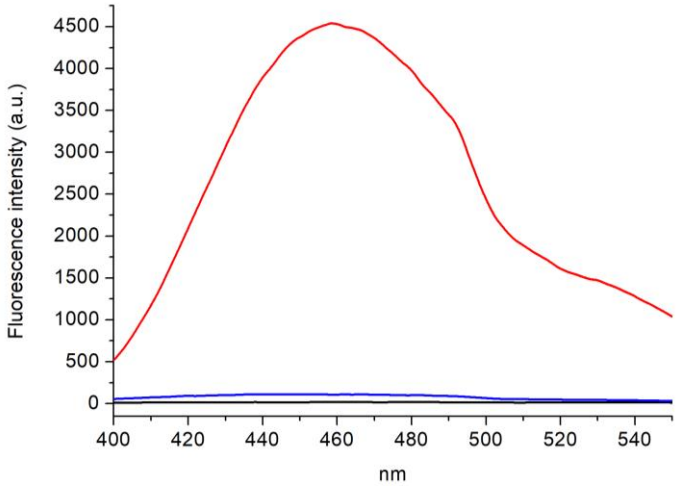

Figure S10. Fluorescent signals of NADH due to galactose dehydrogenase activity on nanoparticles **S1$_{enz}$** (blue), commercial enzyme (red) and blank (black).

From the data obtained (51 mg of β-galactosidase and 13 mg of galactose dehydrogenase per g of **S1$_{enz}$**) and considering the molecular weight of both

enzymes (β-Gal from *Aspergillus oryzae* = 110 kDa and GalDH from *Pseudomonas fluorescens* = 66 kDa)[9,10] and the equality Da=g·mol^{-1}, we can establish that the molecular ratio of both enzymes in **S1$_{enz}$** is approximately 7:3 (βGal:GalDH).

Release studies

Controlled release kinetic profile

For release experiments from **S1$_{enz}$**, the corresponding refrigerated solution of nanoparticles was washed with an aqueous solution (pH 7.5, 20 mM Na_2SO_4), divided into two fractions and brought to a final concentration of 1 mg·mL^{-1}. Both fractions were incubated shaking for 1 h. Then, the inputs (lactose + NAD$^+$) were added to a fraction (sample) while the same volume of aqueous solution was added to the other fraction (blank). The addition of the inputs was considered as the beginning of the release experiment (time = 0 min). Samples were shaken over time and aliquots were taken at scheduled times, centrifuged (2 min, 12000 rpm) to remove the nanoparticles and the fluorescence was measured (4-methylumbelliferone λ_{exc} = 365 nm, λ_{em} = 445 nm). Error bars in Figure 1 (main text) correspond to the s.d. from three independent experiments.

Specificity experiments

For specificity experiments of **S1$_{enz}$**, the corresponding refrigerated solution of nanoparticles was washed with an aqueous solution (pH 7.5, 20 mM Na_2SO_4), divided into six fractions and brought to a final concentration of 1 mg·mL^{-1}. All fractions were incubated for 1 h. Then, inputs (monosaccharides and disaccharides + NAD$^+$) were added considering this moment as the beginning of the experiment (time = 0 min). Samples were shaken over time and aliquots were taken after 4 h, centrifuged to remove the nanoparticles (2 min, 12000 rpm) and measured (4-

methylumbelliferone λ_{exc} = 365 nm, λ_{em} = 445 nm). Error bars in Figure S11 correspond to the s.d. from three independent experiments.

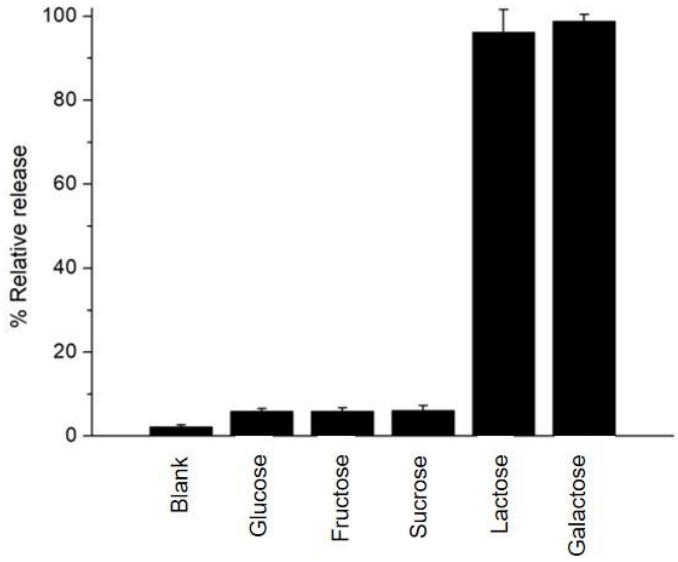

Figure S11. Normalized cargo release from **S1$_{enz}$** in the presence of NAD^+ 1 mM and different saccharides at 1 mM after 4 h.

Mechanism studies

In order to confirm the proposed mechanism, two different experiments were carried out:

Enzyme-dependence studies

For mechanism studies, the corresponding refrigerated solution of nanoparticles **S1$_{\beta Gal}$** (only β-galactosidase immobilized), **S1$_{GalDH}$** (only galactosidase dehydrogenase immobilized) and **S1$_{enz}$** were washed with an aqueous solution (pH 7.5, 20 mM Na_2SO_4) and brought to a final concentration of 1 mg·mL^{-1}. Double amount of **S1$_{enz}$** was washed and divided into two fractions to a final concentration of 1 mg·mL^{-1}. All fractions were incubated separately for 1 h. Then, inputs (lactose

+ NAD^+) were added to samples **S1$_{enz}$**, **S1$_{\beta Gal}$** and **S1$_{GalDH}$** while the same volume of aqueous solution was added to the other fraction of **S1$_{enz}$** as a negative control. The addition of the inputs was considered as the beginning of the experiment (time = 0 min). Samples were shaken for 4 h. Finally, samples were centrifuged (2 min, 12000 rpm) to remove the nanoparticles and the fluorescence was measured (4-methylumbelliferone λ_{exc} = 365 nm, λ_{em} = 445 nm). Error bars in Figure 2 (main text) correspond to the s.d. from three independent experiments.

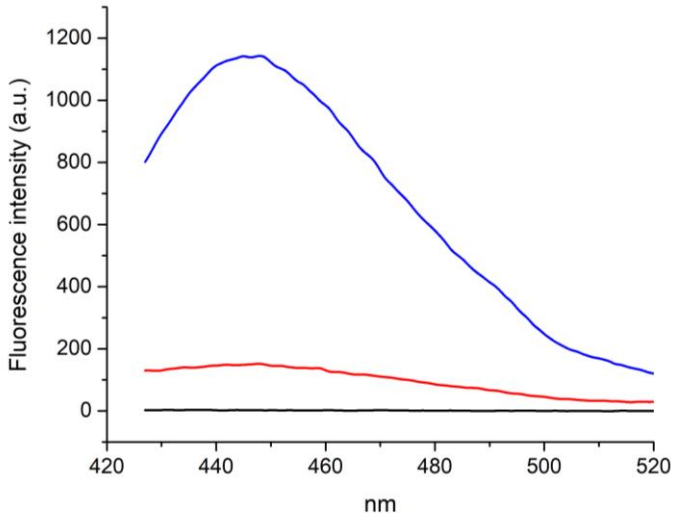

Figure S12. Fluorescent measurements of phosphate buffer 5 mM at pH 4.5 (black), supernatant of **S1$_{GalDH}$** (without β-galactosidase) incubated in phosphate buffer 5 mM at pH 4.5 (red), and supernatant of **S1$_{GalDH}$** (without β-galactosidase) incubated in phosphate buffer 5 mM at pH 4.5 and β-galactosidase (blue).

MUG β-galactosidase-mediated activation

The refrigerated solution of nanoparticles **S1$_{GalDH}$** (without β-galactosidase enzyme) was washed with phosphate buffer 5 mM at pH 4.5 and divided into two fractions to a final concentration of 1 mg·mL^{-1}. Samples were shaken for 4 h. Then, samples were centrifuged (2 min, 12000 rpm) to remove the nanoparticles and the fluorescence was measured (4-methylumbelliferone λ_{exc} = 365 nm, λ_{em} = 445 nm). After that, 10 µL of β-galactosidase (1 mg·mL^{-1}) were added to one fraction whereas

10 µL of phosphate buffer were added to the other. Samples were shaken for 1 h, centrifuged and the fluorescence was measured (Figure S12).

Cell experiments

Cell culture conditions

HeLa human cervix adenocarcinoma cells were purchased from the German Resource Centre for Biological Materials (DSMZ) and were growing in DMEM supplemented with 10% FBS. Cells were incubated at 37 °C in an atmosphere of 5% carbon dioxide and 95% air and underwent passage twice a week.

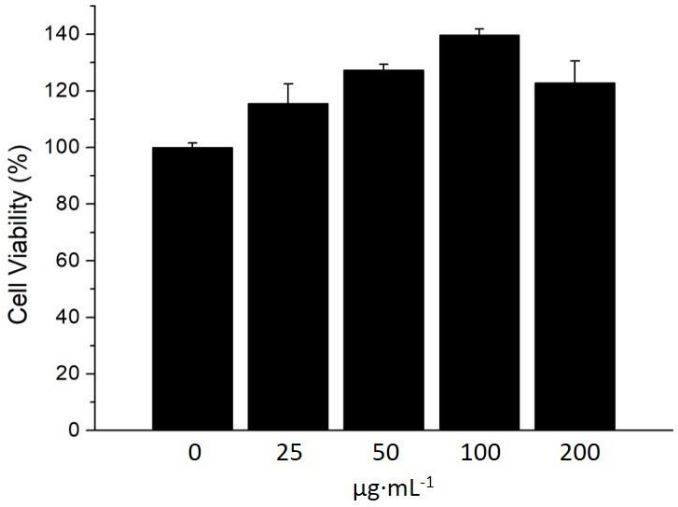

Figure S13. Cell viability studies of HeLa cells treated with different concentrations of **S1$_{enz}$**. Three independent experiments containing triplicates were carried out. Error bars correspond to the s.d.

Cell viability studies

The biocompatibility of **S1$_{enz}$** solid was tested *in vitro* in the Hela cells. For this purpose, Hela cells were seeded in a 96-well plate at 3500 cells/well and treated with different **S1$_{enz}$** concentrations (0, 25, 50, 100 and 200 µg·mL^{-1} in PBS). Cells were incubated for 24 h and the viability was determined by the WST-1 cell

proliferation assay. Finally, the cell viability was measured at λ_{abs} = 595 nm in the Wallac Workstation (Figure S13).

Controlled release of solid S1$_{enz}$ in HeLa cell line

Internalization and cargo delivery studies using **S1$_{enz}$** were performed in HeLa cells. For this purpose, Hela cells were seeded over glass coverslips at 300000 cells·mL^{-1} in 6-well plate and incubated at 37 °C for 24 h. Then, **S1$_{enz}$** was added to HeLa cells at 75 μg·mL^{-1} and cells were incubated for 1 h. Then cells were washed several times with PBS, new media was added and the nanoparticles were incubated in the absence or presence of lactose for 12 h. After 12 h, cells were washed several times with PBS and, finally, slides were visualized using a confocal microscope Leica TCS SP8 AOBS to follow the MUG release and activation into MUB using an excitation laser at λ_{exc} = 405 nm. Autofluorescence was discarded as no statistically significant differences were found between control and **S1$_{enz}$** treated cells. Three independent experiments were done, which gave similar results. Data in Figure 3 (main text) are expressed as mean ± s.e. Statistically significant differences were found between **S1$_{enz}$** and **S1$_{enz}$**+lactose treatments when paired one-way Anova tests were applied (* $p < 0.05$).

As endocytosis is generally the main mechanism of cellular uptake, nanodevices are firstly incorporated into early endosomes, promoting to late endosomes and finally joining lysosomes.[11] Therefore in the first place, fluorescence signals were accumulated in these endocytic compartments or vesicles surrounding perinuclear regions. Once the cargo was released and activated, we observed a remarkable diffused fluorescence pattern throughout the cytosol corresponding, in this case, to cells treated with nanoparticles plus lactose in which more efficient on-command delivery and activation is expected.

Supplementary references

1. a) J. A. Turkevich, P. C. Stevenson and J. Hillier, *Discuss. Faraday Soc.* 1951, **11**, 55; b) G. Frens, *Nat. Phys. Sci.* **1973**, *241*, 20.
2. a) E. Aznar, R. Villalonga, C. Giménez, F. Sancenón, M. D. Marcos, R. Martínez-Máñez, P. Díez, J. M. Pingarrón and P. Amorós, *Chem. Commun*. **2013**, *49*, 6391; b) M. Holzinger, L. Bouffier, R. Villalonga and S. Cosnier, *Biosens. Bioelectron.* **2009**, *24*, 1128; c) K. Hamasaki, H. Ikeda, A. Nakamura, A. Ueno, F. Toda, I. Suzuki and T. Osa, *J. Am. Chem. Soc.* **1993**, *115*, 5035.
3. F. O. Yousef, M. B. Zughul and A. A. Badwan, *J. Incl. Phenom. Macrocycl. Chem.* **2007**, *57*, 519.
4. L. Liu, W. -G. Li and G. -X. Guo, *J. Incl. Phenom. Macro.* **1999**, *34*, 291.
5. G. Jerez, G. Kaufman, M. Prystai, S. Schenkeveld and K. K. Donkor, *J. Sep. Sci.* **2009**, *32*, 1087.
6. R. Villalonga, P. Díez, A. Sánchez, E. Aznar, R. Martínez-Máñez and J. M. Pingarrón, *Chem. Eur. J.* **2013**, *19*, 7889.
7. K. L. Kelly, E. Coronado, L. L. Zhao and G. C. Schatz, *J. Phys. Chem. B* **2003**, *107*, 668.
8. H. Sfihi, A. P. Legrand, J. Doussot and A. Guy, *Colloids Surf. A Physicochem. Eng. Asp.* **1996**, *115*, 115.
9. M. M. Maksimainen, A. Lampio, M. Mertanen, O. Turunen and J. Rouvinen, *Int. J. Biol. Macromol*. **2013**, *60*, 109.
10. C. F. Mazitsos, D. J. Rigden, P. G. Tsoungas and Y. D. Clonis, *Eur. J. Biochem*. **2002**, *269*, 5391.
11. T. -G. Iversen, T. Skotland and K. Sandvig, *Nano Today* **2011**, *6*, 176.

Chapter 4. A Chemical Circular Communication Network at the Nanoscale

A Chemical Circular Communication Network at the Nanoscale

Beatriz de Luis,[a,b] Ángela Morellá-Aucejo,[a,b] Antoni Llopis-Lorente,[a,b] Tania M. Godoy-Reyes,[a,b] Reynaldo Villalonga,[e] Elena Aznar,[a,b] Félix Sancenón,[a,b] and Ramón Martínez-Máñez*[a,b,c,d]

[a] Instituto Interuniversitario de Investigación de Reconocimiento Molecular y Desarrollo Tecnológico (IDM), Universitat Politècnica de València, Universitat de València, Camino de Vera s/n, 46022 Valencia, Spain. E-mail: rmaez@qim.upv.es

[b] CIBER de Bioingeniería, Biomateriales y Nanomedicina (CIBER-BBN), Spain.

[c] Unidad Mixta UPV-CIPF de Investigación en Mecanismos de Enfermedades y Nanomedicina, Universitat Politècnica de València, Centro de Investigación Príncipe Felipe, Valencia, Spain.

[d] Unidad Mixta de Investigación en Nanomedicina y Sensores, Universitat Politècnica de València, Instituto de Investigación Sanitaria La Fe, Valencia, Spain

[e] Nanosensors & Nanomachines Group, Department of Analytical Chemistry, Faculty of Chemistry, Complutense University of Madrid, Madrid, Spain.

Published online: December 9, 2020

(Reprinted with permission from *Chem. Sci.* **2021**, *12*, 1551-1559.

4.1 Abstract

In nature, coordinated communication between different entities enables a group to accomplish sophisticated functionalities that go beyond those carried out by individual agents. The possibility of programming and developing coordinated communication networks at the nanoscale—based on the exchange of chemical messengers—may open new approaches in biomedical and communication areas. Here, a stimulus-responsive circular model of communication between three nanodevices based on enzyme-functionalized Janus Au–mesoporous silica capped nanoparticles is presented. The output in the community of nanoparticles is only observed after a hierarchically programmed flow of chemical information between the members.

4.2 Introduction

Chemical communication is based on the exchange of molecular messengers between different entities. In nature, living cells and organisms rely on chemical communication processes for sustaining vital biological functions.[1-4] For instance, organelles exchange messengers that allow cellular metabolism; neurons communicate by exchanging neurotransmitters; and physiological functions are regulated by hormone molecules segregated by distant cells. At a larger scale, insects, bacteria and pluricellular organisms communicate with peers by means of pheromones. Communication networks enable a group to share information and act together towards the achievement of a common goal.[5,6] Considering this aim, coordinated communication displays an essential role as it is necessary to organize the collective behaviour in a defined order to assure efficiency and productivity.[7,8] In fact, nature life is based on communication processes developed in coordinated

communities at the molecular scale involving the use of chemical messengers. As examples of coordinated groups, termite populations and fish shoals have chemically coordinated alarm systems in which a member detects an environment disturbance and secretes alarm molecules. Other members sense this message and expel chemical secretions, subsequently spreading alarm through the community and resulting in the articulation of a collective response (e.g., release of toxic/repellent chemicals or colony recruitment).[9-11]

Transferring communication capabilities to human-made nanoscale systems has attracted significant attention in recent years due to potential applications in areas such as biomedicine or ICT (Information and Communication Technologies).[12-16] Compared to traditional telecommunication technologies, chemical communication offers interesting features such as the reduced size of molecular transceivers and receivers, minimal power consumption and the ability to operate in biological and physiological environments. Several micro- and nanocarriers capable of interacting with living systems by means of sending or receiving chemical messengers have been developed.[17-23] Linear communication between particles or feedback between two particles has also been reported.[24,25] However, the field is still in its infancy and more complex communication communities should be demonstrated with the future aim to integrate coordinated multicomponent communities of nanodevices with advanced capabilities.[26-29] Strategies of cooperation and coordination between different nanoparticles may enable sophisticated functionalities that go beyond those carried out by individual agents. However, regardless of the aforementioned advancements made in the last years, the definition of technologies to support practical and useful applications of communication at nanoscale, while essential to motivate further growth of this field in the research community, is still very limited and still scarcely explored.

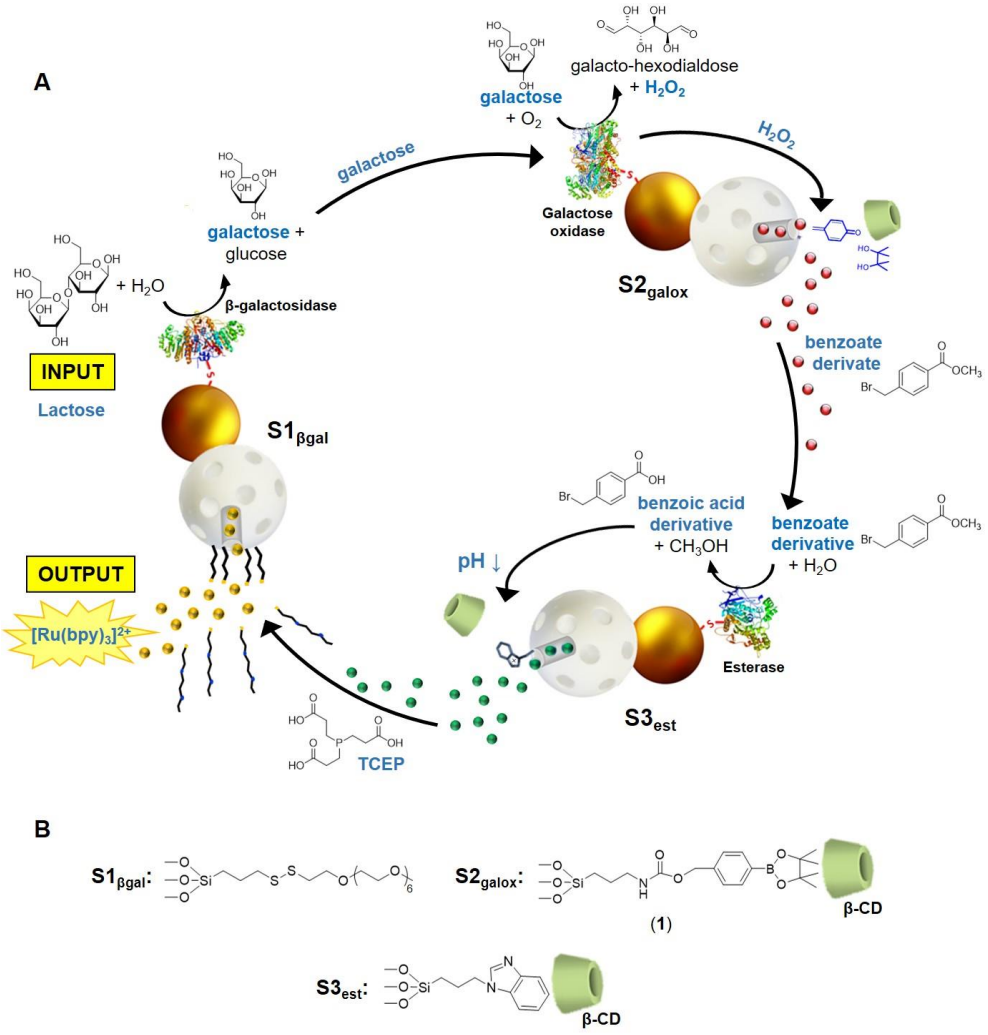

Figure 1. (A) Representation of the circular model of communication between three enzyme-functionalized Janus Au-mesoporous silica capped nanoparticles based on the programmed exchange of chemical messengers. **(B)** Representation of the molecular gatekeepers of each nanodevice. From left to right and top to bottom: disulfide-linked PEG chain, self-immolative arylboronate derivative (**1**)-β-cyclodextrin inclusion complex and benzimidazole-β-cyclodextrin inclusion complex.

In this scenario, we report herein a circular model of a multicomponent communication network of nanoparticles based on the exchange of chemical messages. Today it is well recognized the ubiquity of cyclic organization in biology

as it provides invaluable resources for controlling and orchestrating biological operations, giving rise to complex temporal dynamics in nature.[30] For instance, dynamical feedback is observed in biological reaction networks where metabolic processes regulate their activity or resupply the initial substrate in a cyclic manner. Our communication system consists of three enzyme-functionalized Janus Au-mesoporous silica nanoparticles (Au-MSNPs) which display a double receiver-sender behaviour,[31,32] as depicted in Figure 1A. The mesoporous face of nanodevice 1 (**S1**$_{\beta gal}$) is loaded with the fluorescent dye $[Ru(bpy)_3]Cl_2$ and capped with disulfide-containing oligo(ethylene glycol) chains (PEG) acting as gatekeepers, whereas the enzyme β-galactosidase (βgal) is attached to the gold face. In nanoparticle 2 (**S2**$_{galox}$), the enzyme galactose oxidase (galox) is immobilized on the Au face, while the mesoporous silica is loaded with methyl 4-(bromomethyl)benzoate and the mesopores capped with a H_2O_2-sensitive self-immolative arylboronate derivative (**1**) which forms a host-guest complex with β-cyclodextrin (Figure 1B).[33] Finally, the nanodevice 3 (**S3**$_{est}$) is functionalized with the enzyme esterase on the Au face, loaded with the reductive species tris(2-carboxyethyl)phosphine hydrochloride (TCEP) in the mesoporous face and capped with a pH responsive supramolecular nanovalve consisting of an inclusion complex between a benzimidazole moiety and β-cyclodextrin.[34]

As illustrated in Figure 1A, this circular communication is triggered in the presence of lactose (input). Lactose is transformed into galactose by the enzyme β-galactosidase attached to the gold face of **S1**$_{\beta gal}$. Galactose acts as a chemical messenger that is transmitted and sensed by galactose oxidase enzyme on **S2**$_{galox}$ resulting in the formation of galacto-hexodialdose and H_2O_2. Hydrogen peroxide triggers the self-immolative cleavage[33] of the gatekeeper on **S2**$_{galox}$ allowing the delivery of a benzoate derivative (methyl 4-(bromomethyl)benzoate) as a second chemical messenger that is detected by the enzyme esterase on **S3**$_{est}$ and

transformed into the corresponding benzoic acid derivative. Formation of benzoic acid induces a local drop of the pH causing the protonation of benzimidazole moieties,[35] dethreading of the nanovalve and the delivery of the reductive agent (TCEP) from $\mathbf{S3_{est}}$. TCEP acts as a third chemical messenger that closes the loop by communicating $\mathbf{S3_{est}}$ with $\mathbf{S1_{\beta gal}}$, as it produces the reductive cleavage of the disulfide bonds of the oligo(ethylene glycol) chains anchored to the mesoporous face of $\mathbf{S1_{\beta gal}}$. Eventually, the subsequent release of the dye $[Ru(bpy)_3]Cl_2$ from $\mathbf{S1_{\beta gal}}$ is produced as the output collective response of the communication network.

4.3 Results and discussion

Preparation and characterization of the nanodevices

Janus Au-MSNPs were prepared using gold nanoparticles (of *ca.* 20 nm obtained by reduction of $HAuCl_4 \cdot 3H_2O$ with sodium citrate) and MSNPs (of *ca.* 100 nm MCM-41-type nanoparticles obtained by an alkaline hydrolysis reaction), as adapted from a previous study.[31] MSNPs were partially imbedded at the interface of a Pickering emulsion, formed by paraffin wax (oily phase) and water-ethanol (aqueous phase). The un-masked MSNPs surface was decorated with reactive thiol groups, by reaction with (3-mercaptopropyl) trimethoxysilane, on which citrate-capped Au nanoparticles were subsequently attached. After removing the paraffin with chloroform, the starting Janus Au-MSNPs (**S0**) were obtained. **S1** was prepared loading **S0** with the $[Ru(bpy)_3]Cl_2 \cdot 6H_2O$ dye and protecting the Au face with 3-mercaptopropionic acid. The resulting solid was reacted with (3-mercaptopropyl) trimethoxysilane, with 2,2'-dipyridyl disulfide and then with O-(2-mercaptoethyl)-O'-methyl-hexa(ethylene glycol) to give the final capped Janus nanoparticles **S1**. $\mathbf{S1_{\beta gal}}$ was obtained from **S1** by anchoring β-galactosidase on the carboxylate-modified Au face by means of well-known crosslinking EDC/NHS chemistry resulting

in the coupling between the free amino groups of lysine residues from the enzyme and the activated Au carboxyl groups.[36] **S2** was prepared loading **S0** with methyl 4-(bromomethyl)benzoate and adding 3-mercaptopropionic acid to functionalize the gold face. The mesoporous face was reacted with the self-immolative molecule (**1**) (Figure 1B) and the system was capped by the formation of an inclusion complex between (**1**) and β-cyclodextrin (formation constant = 31.1 ± 0.7 M^{-1}).[37] For the preparation of $\mathbf{S2_{galox}}$, galactose oxidase was anchored on the Au face of **S2** following a similar procedure as previously described for $\mathbf{S1_{\beta gal}}$. **S3** was prepared by reacting the mesoporous face of **S0** with (3-iodopropyl)trimethoxysilane and then with benzimidazole. The resulting solid was treated with 3-mercaptopropionic acid, loaded with tris(2-carboxyethyl)phosphine and capped with β-cyclodextrin as it threads onto benzimidazole forming an inclusion complex (formation constant = 104 ± 8 M^{-1}).[34] $\mathbf{S3_{est}}$ was obtained anchoring the esterase enzyme on the Au face of **S3** following the above described EDC/NHS chemistry methodology. As control solids, $\mathbf{S2_{blank}}$ and $\mathbf{S3_{blank}}$ were prepared following the same procedure described for $\mathbf{S2_{galox}}$ and $\mathbf{S3_{est}}$ respectively but in this case the mesoporous container was not loaded.

The nanoparticles were characterized using standard techniques (Figures 2 and 3, for more details see Supporting Information, SI). Powder X-ray diffraction patterns at low ($1.5 < 2\theta < 7$) and at high angles ($35 < 2\theta < 80$) of different prepared nanoparticles showed in all cases low-angle reflections of mesoporous silica and high-angle cubic gold characteristic diffraction peaks (see also Figure S3 in SI). UV/vis of the synthesized Au nanoparticles showed a single surface plasmon absorption band at 524 nm, characteristic of spherically shaped nanospheres with approximately 20 nm diameter that was redshifted to 533 nm in **S0** (Figure S4). The presence of the mesoporous structure as well as Au nanoparticles was confirmed by transmission electron microscopy (TEM) (Figure 2B, additional images in Figure

S2), obtaining similar Au-MSNPs ratios as previously reported.[38] N_2 adsorption-desorption isotherms of the **calcined MSNPs** and Janus Au-MS nanoparticles **S0** showed an adsorption step at intermediate P/P_0 value 0.3 (Figure S5), which is characteristic for mesoporous solids with empty pores. Application of the BET model resulted in a value for the total specific surface of 1079 $m^2 \cdot g^{-1}$ for **calcined MSNPs** and 802 $m^2 \cdot g^{-1}$ for **S0**. Pore sizes and total pore volumes were calculated with the BJH model (Table S1). The hydrodynamic size and zeta potential of different solids were measured by dynamic light scattering (DLS) (Figure 2C and Table S2). **S0** showed a hydrodynamic diameter of 115 ± 4 nm that increased to 133 ± 18 nm, 143 ± 15 nm and 148 ± 18 nm for $\mathbf{S1}_{\beta gal}$, $\mathbf{S2}_{galox}$ and $\mathbf{S3}_{est}$ respectively, whereas Z potential of **S0** was -28.4 ± 0.5 and -31.3 ± 0.9, -26.3 ± 0.4 and -30.4 ± 0.7 for $\mathbf{S1}_{\beta gal}$, $\mathbf{S2}_{galox}$ and $\mathbf{S3}_{est}$. From elemental analysis and delivery studies the amounts of different components on the nanoparticles were calculated (Table S3). The presence of β-galactosidase, galactose oxidase and esterase enzymes on $\mathbf{S1}_{\beta gal}$, $\mathbf{S2}_{galox}$ and $\mathbf{S3}_{est}$ was confirmed by enzyme activity assays (Figure S6-S8, see SI for details) revealing activities of 0.001 U, 0.124 U and 0.165 U per mg of solid, respectively. TEM-EDX mapping of the final nanodevices $\mathbf{S1}_{\beta gal}$, $\mathbf{S2}_{galox}$ and $\mathbf{S3}_{est}$ confirmed the presence of the expected atoms in the solids. Images showed that gold surfaces were rich in sulfur atoms, strongly suggesting the preferential localization of the enzymes in the Au face (Figure 3, S9-S11) as they were immobilized by means of 3-mercaptopropionic acid. Moreover, the remarkable presence of sulfur atoms in the whole scaffold $\mathbf{S1}_{\beta gal}$ is attributed to the disulfide bonds of the gatekeeper PEG in the mesoporous face. In turn, the slight signal of sulfur atoms in $\mathbf{S2}_{galox}$ and $\mathbf{S3}_{est}$ is attributed to the (3-mercaptopropyl)trimethoxysilane employed to attach the gold nanoparticles to the silica container during the scaffold synthesis. Boron atoms and nitrogen atoms in $\mathbf{S2}_{galox}$ are ascribed to the boronic esters and carbamate groups of the gatekeepers

in **S2**$_{galox}$, whereas the abundance of nitrogen atoms in **S3**$_{est}$ is due to the presence of benzimidazole moieties.

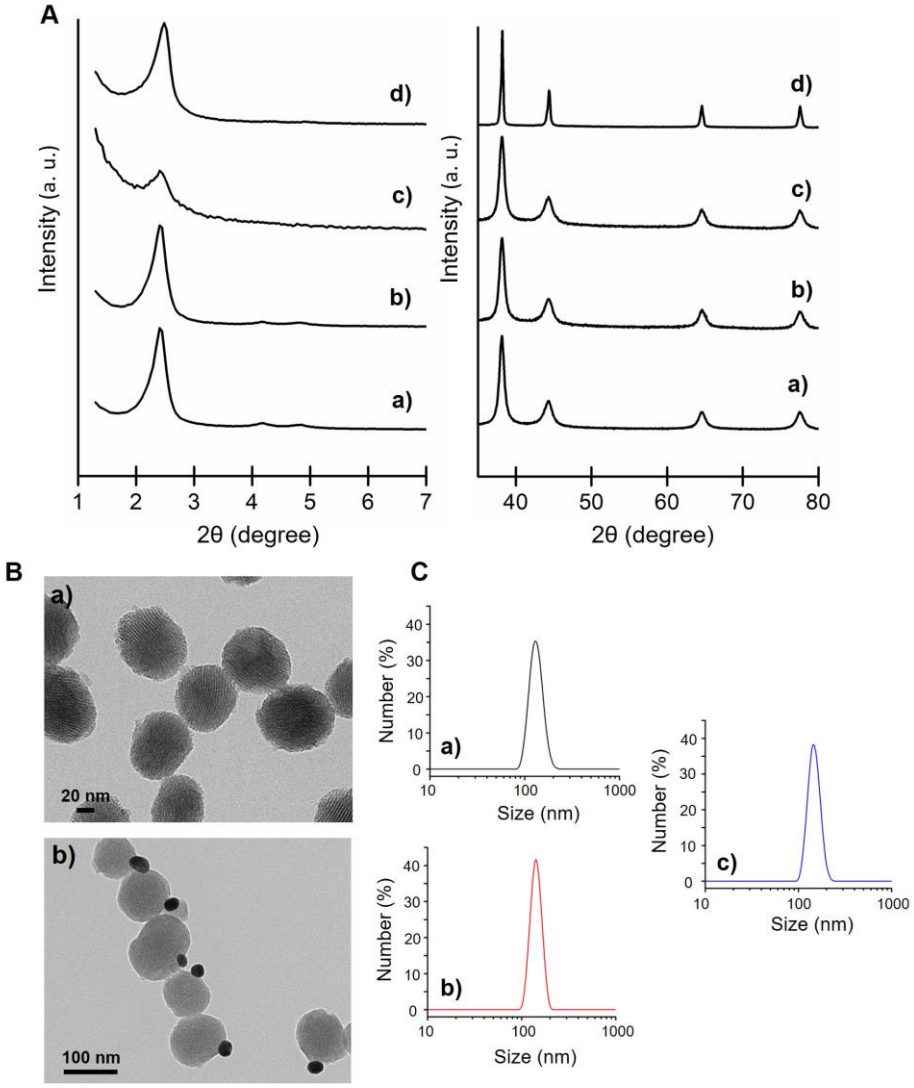

Figure 2. (A) Powder X-ray diffraction patterns of the solids (a) Janus Au-MS nanoparticles **S0**, (b) solid **S1**, (c) solid **S2** and (d) solid **S3** at low (left) and high (right) angles. **(B)** Representative TEM images of (a) **calcined MSNPs** and (b) Janus Au-MS nanoparticles **S0**. **(C)** Hydrodynamic diameter distribution (nm) determined by DLS for the final enzyme-functionalized nanodevices: (a) **S1**$_{\beta gal}$ (133 ± 18 nm), (b) **S2**$_{galox}$ (143 ± 15 nm) and (c) **S3**$_{est}$ (148 ± 18 nm).

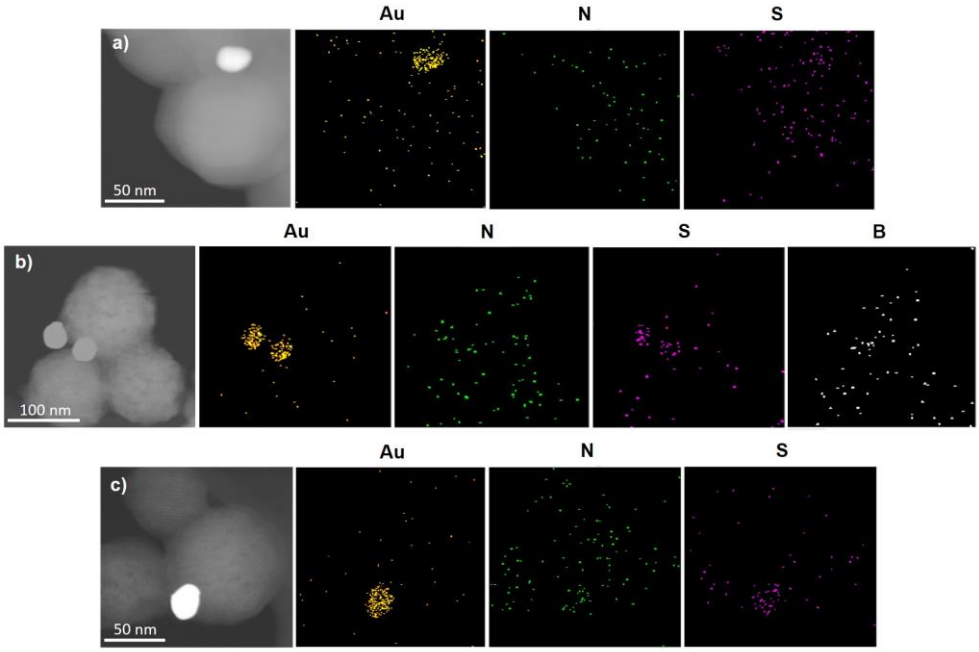

Figure 3. TEM-EDX element mapping of the nanodevice (a) **S1**$_{\beta gal}$, (b) **S2**$_{galox}$ and (c) **S3**$_{est}$.

Release studies

Individual studies. In a first step, we tested the ability of **S1**$_{\beta gal}$, **S2**$_{galox}$ and **S3**$_{est}$ nanodevices to recognize the corresponding input and subsequently deliver their payload. For this, we prepared $[Ru(bpy)_3]Cl_2$ (dye) loaded nanoparticles (**S1**$_{\beta gal}$, **S2**$_{galox}$-dye and **S3**$_{est}$-dye) and monitored dye release in shaken aqueous solutions at pH 7.5 (20 mM sodium sulfate) in the absence and in the presence of the corresponding input (TCEP for **S1**$_{\beta gal}$, galactose for **S2**$_{galox}$-dye and methyl 4-(bromomethyl) benzoate for **S3**$_{est}$-dye). Aliquots were taken at scheduled times, centrifuged to remove nanoparticles, and the fluorescent emission band of $[Ru(bpy)_3]Cl_2$ was measured at 595 nm (λ_{exc} = 453 nm). Individual delivery studies revealed payload release in the presence of the corresponding stimulus while imperceptible or very low dye delivery was observed in its absence (Figure 4).

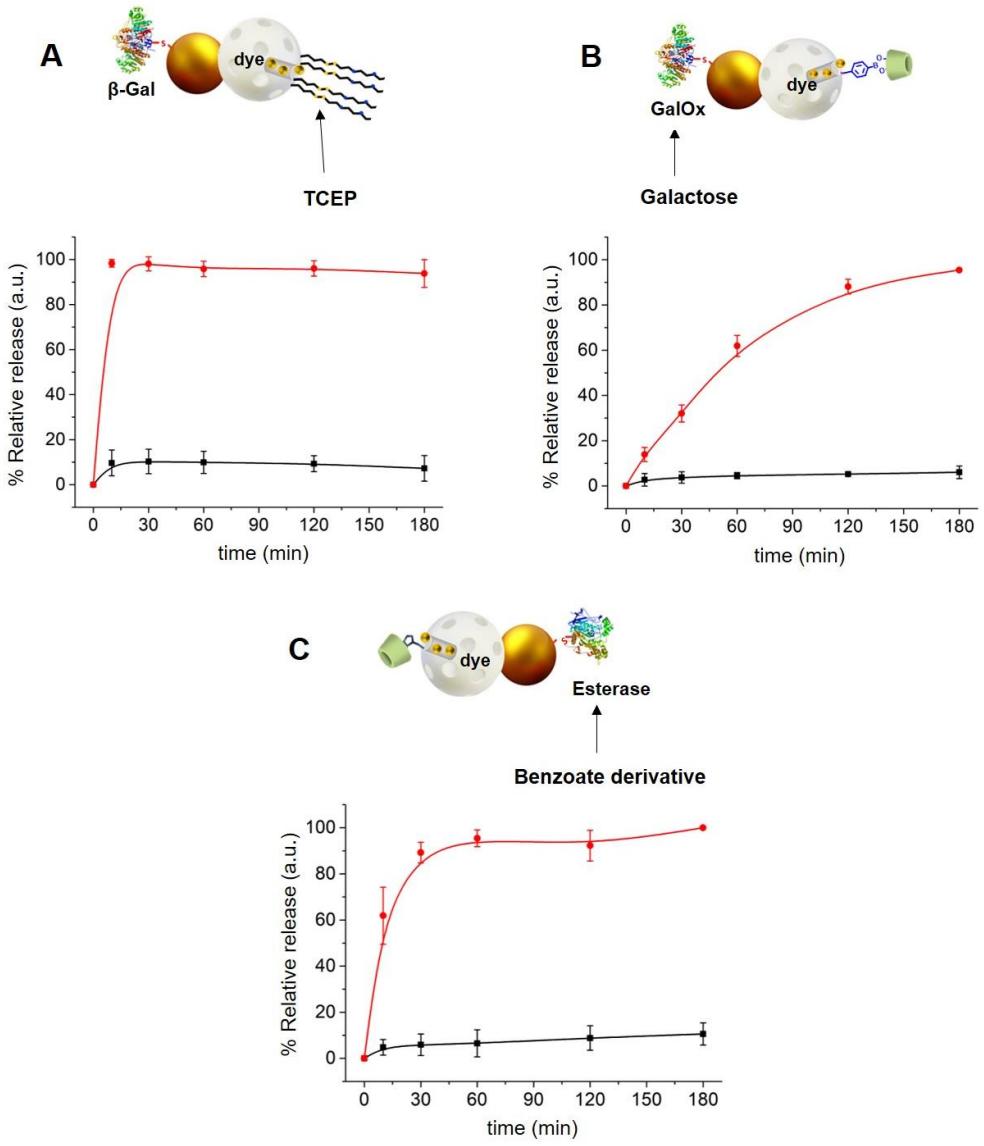

Figure 4. Schemes of the individual experiments and normalized cargo release kinetics from **(A) S1$_{\beta gal}$**, **(B) S2$_{galox}$**-dye and **(C) S3$_{est}$**-dye in the absence (black curves) and in the presence (red curves) of the corresponding input (TCEP at 1 mM, galactose at 50 mM and methyl 4-(bromomethyl) benzoate at 1 mM final concentration, respectively). Error bars correspond to the s.d. from three independent experiments.

Moreover, several release control experiments were carried out for each nanodevice employing their own chemical trigger as input (positive controls) and

the chemical trigger of the other nanocarriers (negative controls) revealing no potential interferences between them (Figures S12-S14 in SI). It was also proved that the presence of the corresponding enzyme in **S2**$_{galox}$-dye and **S3**$_{est}$-dye was necessary to achieve the nanodevice gate opening and the subsequent cargo release (Figures S13 and S14 in SI).

Linear communication between pairs of nanoparticles. Afterwards, in a further step to evaluate the feasibility of the communication network, we tested the linear communication between each pair of nanodevices [1-2 (**S1**$_{\beta gal}$/**S2**$_{galox}$-dye), 2-3 (**S2**$_{galox}$/**S3**$_{est}$-dye), 3-1 (**S3**$_{est}$/**S1**$_{\beta gal}$)]. For doing so, each pair was placed in solution and shaken in the absence and in the presence of the communication activating molecule (i.e. lactose for 1-2, galactose for 2-3, and methyl 4-(bromomethyl)benzoate for 3-1). The corresponding nanoparticle concentration conditions were adjusted considering the activity of immobilized enzymes and the solubility of methyl 4-(bromomethyl)benzoate. As shown in Figure 5, in the three cases a remarkable output (dye delivery) was observed in the presence of the corresponding chemical trigger while a low signal (dye delivery below 20%) was found in its absence. Besides, we confirmed the inability of lactose input to disrupt the disulfide bonds of the molecular gate on nanoparticle 1 (**S1**$_{\beta gal}$) (Figure S12) demonstrating that communication between pair 1-2 relied exclusively on the generation of messenger 1 (galactose) by β-galactosidase. All these experiments verified the establishment of linear communication pathways and successful exchange of chemical messages between pairs of nanodevices.

Circular communication. Finally, we tested the realization of the whole circular pattern of communication (Figure 1A). For these experiments, the three nanodevices (**S1**$_{\beta gal}$, **S2**$_{galox}$ and **S3**$_{est}$) were brought together in an aqueous solution

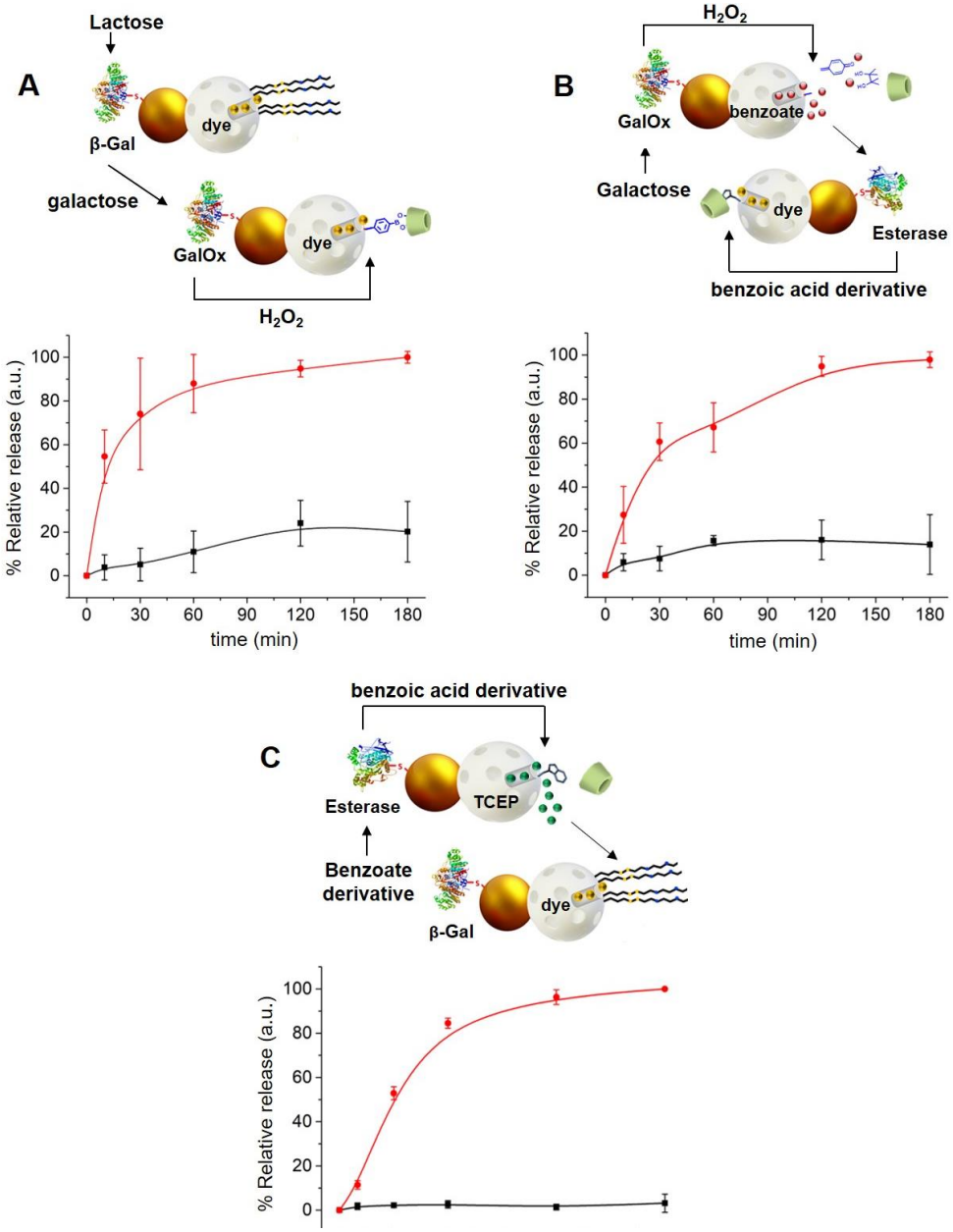

Figure 5. Schemes of the experiments and normalized cargo release kinetics from each pair of nanoparticles **(A)** 1-2 (**S1**$_{\beta gal}$/**S2**$_{galox}$-dye), **(B)** 2-3 (**S2**$_{galox}$/**S3**$_{est}$-dye) and **(C)** 3-1 (**S3**$_{est}$/**S1**$_{\beta gal}$) in the absence (black curves) and in the presence (red curves) of the corresponding input (lactose at 50 mM, galactose at 50 mM and methyl 4-(bromomethyl)benzoate at 1 mM final concentration, respectively). Error bars correspond to the s.d. from three independent experiments.

(20 mM sodium sulfate, pH 7.5) in the same reaction vessel and divided in two fractions fractions. After one hour of incubation, either water (for blank) or lactose 50 mM were added. Aliquots were taken at scheduled times, centrifuged to remove nanoparticles, and the emission at 595 nm of $[Ru(bpy)_3]Cl_2$ was measured. As depicted in Figure 6, there was a continuous steady delivery of the cargo from **S1**$_{\beta gal}$ in the presence of lactose. In contrast, delivery of less than 20% of the maximum delivery observed was found for the community of nanoparticles in the absence of the communication triggering molecule. From 10 hours ahead, the blank fraction (no input) stabilized whereas in the lactose fraction delivery continued sharply increasing until reaching saturation around 16 h.

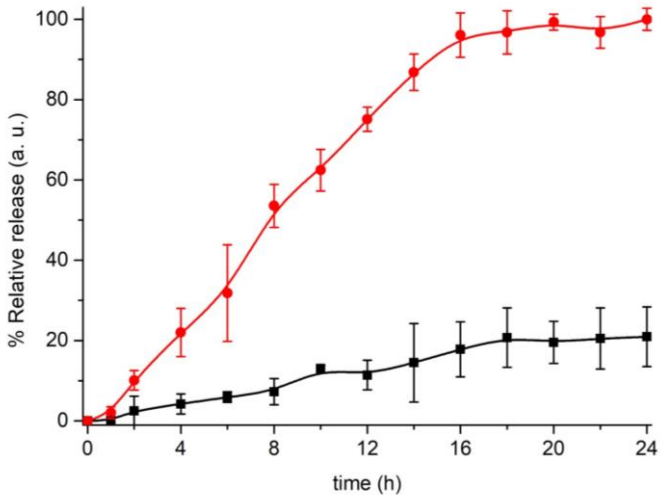

Figure 6. Validation of the circular chemical communication network between the nanodevices 1, 2 and 3. $[Ru(bpy)_3]Cl_2$ release from **S1**$_{\beta gal}$ in aqueous solution at pH 7.5 in the absence (black curve) and presence (red curve) of lactose (50 mM) in the complete community of nanoparticles (**S1**$_{\beta gal}$ /**S2**$_{galox}$/**S3**$_{est}$). Error bars correspond to the s.d. from three independent experiments.

In our design, triggers that open the gating mechanism are orthogonal as the chemical messenger generated in the Au face only opens the gated mesoporous silica nanoparticle to which the Au unit is attached. In such a community of

nanoparticles, release of the dye from **S1**$_{\beta gal}$ after the addition of a stimulus (i.e. lactose) only becomes effective after the circular communication of the nanoparticles in the sequence **S1**$_{\beta gal}$-**S2**$_{galox}$-**S3**$_{est}$-**S1**$_{\beta gal}$.

When building cooperative networks of nanoparticles, it is crucial to understand each component's function and rule out potential side interactions and/or incompatibilities between the communities of nanodevices, resulting for instance in "unintended cross-talk" between nanodevices. In order to discard such effects, we performed additional delivery studies in the same conditions previously described using different combinations with "uncomplete" nanoparticles (i.e., lacking either immobilized enzyme or cargo). As shown in Figure 7, all combinations tested —**S1**/**S2**$_{galox}$/**S3**$_{est}$ (lacking the enzyme on nanoparticle 1, bar B), **S1**$_{\beta gal}$/**S2**/**S3**$_{est}$ (lacking the enzyme on nanoparticle 2, bar C), **S1**$_{\beta gal}$/**S2**$_{galox}$/**S3** (lacking the enzyme on nanoparticle 3, bar D), **S1**$_{\beta gal}$/**S2**$_{blank}$/**S3**$_{est}$ (lacking the cargo in nanoparticle 2, bar E), and **S1**$_{\beta gal}$/**S2**$_{galox}$/**S3**$_{blank}$ (lacking the cargo in nanoparticle 3, bar F)— showed much lower delivery in the presence of lactose compared to the complete community of nanoparticles (**S1**$_{\beta gal}$/**S2**$_{galox}$/**S3**$_{est}$, bar K). When one nanoparticle was not complete, the communication channel was disrupted and information was lost. In addition, we also studied the effect of having the enzymes in the solution instead of anchored to the nanoparticles. In a typical experiment the communities of nanoparticles **S1**/**S2**/**S3** (all lacking the enzyme) were brought in aqueous solution and enzymes at equivalent catalytic concentrations than in **S1**$_{\beta gal}$/**S2**$_{galox}$/**S3**$_{est}$ were added to the mixture. As observed in Figure 7 (bar G), the output signal (i.e. $[Ru(bpy)_3]Cl_2$ release) of the combination **S1**/**S2**/**S3**/free enzymes was significantly lower compared to the response of the complete community which is ascribed to the dilution of the (free) enzyme-generated species in the solution. Moreover, the combinations **S1**$_{\beta gal}$/**S2**/**S3**$_{est}$/free galactose oxidase (bar I) and **S1**$_{\beta gal}$/**S2**$_{galox}$/**S3**/free esterase (bar J) at equivalent catalytic concentrations also

showed a low delivery. These data demonstrate the importance of having the enzymes anchored to nanoparticles, which allows the generation of chemical microenvironments around the nanoparticles enabling the effective intracommunication between the enzyme on the Au face and silica gatekeepers as previously reported.[25,31] Furthermore, the mixture **S1**/**S2**$_{galox}$/**S3**$_{est}$/free β-galactosidase (bar H) displayed a result comparable to the complete network; as β-galactosidase products act over a different nanoparticle (nanoparticle 2) the enzyme may or may not be attached to the nanoparticle 1 without disrupting the communication loop.

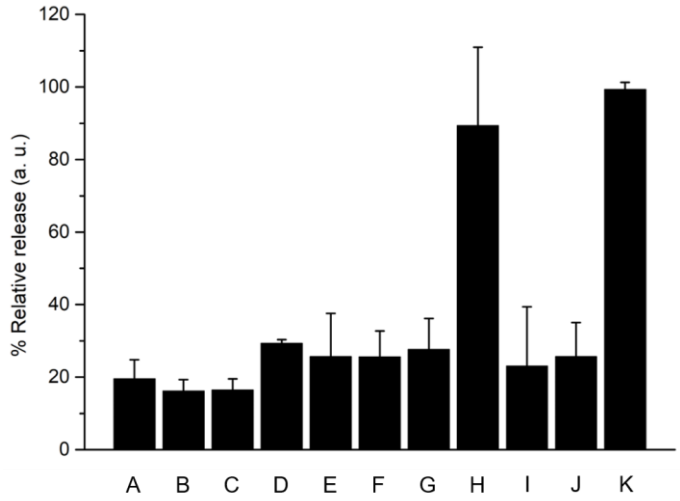

Figure 7. Output signal from different partially-equipped communities of nanoparticles. $[Ru(bpy)_3]Cl_2$ release in aqueous solution at pH 7.5 in the presence of lactose (50 mM) containing the mixtures **S1**/**S2**$_{galox}$/**S3**$_{est}$ (enzyme missing on nanoparticle 1, bar B), **S1**$_{βgal}$/**S2**/**S3**$_{est}$ (enzyme missing on nanoparticle 2, bar C), **S1**$_{βgal}$/**S2**$_{galox}$/**S3** (enzyme missing on nanoparticle 3, bar D), **S1**$_{βgal}$/**S2**$_{blank}$/**S3**$_{est}$ (cargo missing in nanoparticle 2, bar E), **S1**$_{βgal}$/**S2**$_{galox}$/**S3**$_{blank}$ (cargo missing in nanoparticle 3, bar F), **S1**/**S2**/**S3**/free enzymes in bulk solution (bar G), **S1**/**S2**$_{galox}$/**S3**$_{est}$/free β-galactosidase in bulk solution (bar H), **S1**$_{βgal}$/**S2**/**S3**$_{est}$/free galactose oxidase in bulk solution (bar I) and **S1**$_{βgal}$/**S2**$_{galox}$/**S3**/free esterase in bulk solution (bar J). Delivery from the full-equipped (**S1**$_{βgal}$/**S2**$_{galox}$/**S3**$_{est}$) system in the absence (bar A) and the presence (bar K) of lactose (50 mM) is also displayed for comparative purposes. Communication was successfully achieved only when all components were present (bar K). Error bars correspond to the s.d. from three independent experiments.

The behaviour of this circular model of communication between three nanodevices can be expressed in a Boolean logic table of 6 elements:[39,40] i.e. the triggering species (lactose), enzyme β-galactosidase, enzyme galactose oxidase, cargo of nanoparticle 2 (methyl 4-(bromomethyl)benzoate), enzyme esterase and cargo of nanoparticle 3 (TCEP). Among the 64 possible entries, only the combination of fully-equipped nanodevices **S1**$_{\beta gal}$/**S2**$_{galox}$/**S3**$_{est}$ leads to a circular communication and efficient [Ru(bpy)$_3$]Cl$_2$ release (Tables S4 and S5 in SI).

Efficiency studies. Communication efficiency, process efficiency and information loss are relevant aspects that should be considered when designing logic (chemical) communication systems. Three main processes/logical connections can be defined in our circular communication system: (i) connection 1-2 (**S1**$_{\beta gal}$-**S2**$_{galox}$), (ii) connection 2-3 (**S2**$_{galox}$-**S3**$_{est}$) and (iii) connection 3-1 (**S3**$_{est}$-**S1**$_{\beta gal}$). Thus, the circular communication involves information transmission from one site to another in a hierarchical way following the order 1-2-3-1. In such a circuit, maximum communication efficiency would produce the maximum dye release from site 1. Accordingly, we evaluated the efficiency of the circular information transmission by comparing the output of the 1-2-3-1 process to the maximum possible output from site 1, and also determined the communication efficiency of sections of the circuit, i.e. pathway 2-3-1 and pathway 3-1 by external activation on site 2 and site 3, respectively (see Figure 8A). For doing so, we ran delivery studies in parallel; (i) the dye-loaded nanoparticle **S1**$_{\beta gal}$ with TCEP as input set the maximum output (cargo delivery) as 100% efficiency; (ii) measuring cargo delivery from **S1**$_{\beta gal}$ in the **S3**$_{est}$-**S1**$_{\beta gal}$ pair with methyl 4-(bromomethyl) benzoate as input allowed to calculate the 3-1 efficiency, (ii) whereas measuring cargo delivery from **S1**$_{\beta gal}$ in the **S2**$_{galox}$-**S3**$_{est}$-**S1**$_{\beta gal}$ system with galactose or lactose as inputs allowed calculation of the communication efficiency of the 2-3-1 and 1-2-3-1 processes,

respectively. Cargo delivery from **S1**$_{\beta gal}$ without input was set as the background release. From these communication efficiency data the efficiency for each 1-2, 2-3 and 3-1 communication step (process efficiency) was also calculated (Figure 8B) (see SI for further information). For clarification, the different processes have been schematically represented in Figure 8C. All the experiments were carried out with the same methodology, nanoparticle concentrations and input concentration (50 mM) than that followed in the experiment of Figure 6 (details in SI).

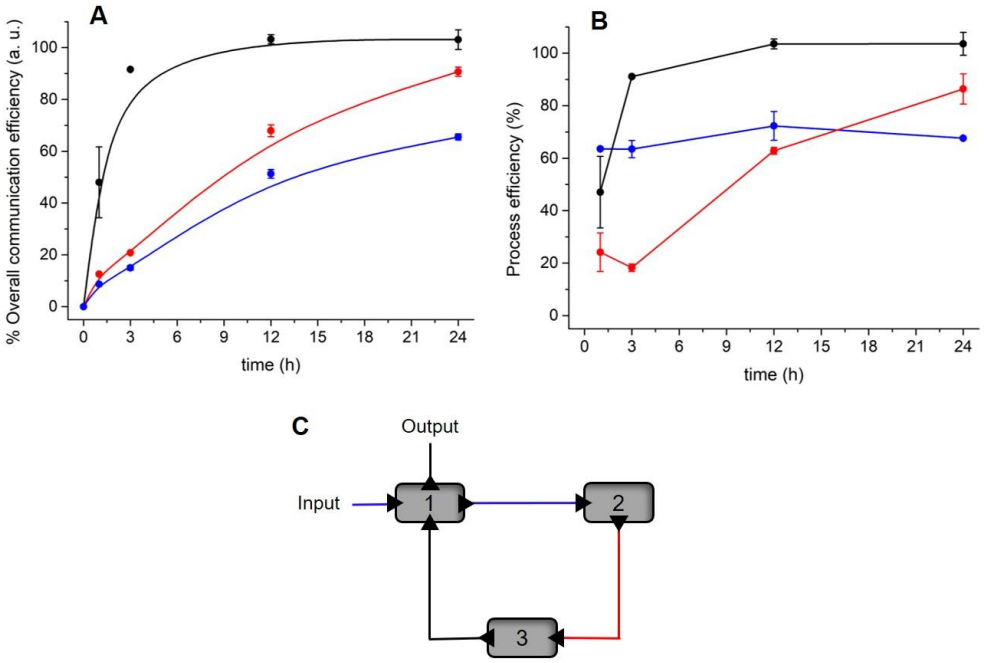

Figure 8. (A) Overall communication (information transmission) efficiency for: circular sequence 1-2-3-1 (**S1**$_{\beta gal}$-**S2**$_{galox}$-**S3**$_{est}$-**S1**$_{\beta gal}$, blue curve), sequence 2-3-1 (**S2**$_{galox}$- **S3**$_{est}$-**S1**$_{\beta gal}$, red curve) and sequence 3-1 (**S3**$_{est}$-**S1**$_{\beta gal}$, black curve). **(B)** Process efficiency for the different connections of the circular communication system: 1-2 (**S1**$_{\beta gal}$-**S2**$_{galox}$, blue curve), 2-3 (**S2**$_{galox}$-**S3**$_{est}$, red curve), and 3-1 (**S3**$_{est}$-**S1**$_{\beta gal}$, black curve). Error bars in (A) and (B) correspond to the s.d. from two independent experiments. **(C)** General schematics of the communication system. Each coloured path corresponds to curves in (B).

The results show that, as expected, the communication efficiency decreases by adding members (communications sites) and processes (connections) to the communication pathway resulting in certain chemical information loss (Figure 8A and S15). For instance, as depicted in Figure 8A, dye delivery from 1 (i.e. **S1**$_{\beta gal}$) in 3-1 reached maximum efficiency at 12 h whereas information transmission and delivery from 1 in the 2-3-1 section and the 1-2-3-1 circuit remain lower. In addition, at all times, communication efficiencies follow the tendency 3-1 > 2-3-1 > 1-2-3-1. In terms of information degradation after 24 h, no loss is observed for the shortest pathway (3-1) whereas it increases with the number of communication sites (members of the network), with 10% loss and 35% loss for 2-3-1 and 1-2-3-1 respectively (Figure S15). Information degradation within complex networks has been also observed by others both in solution and within immobilized communities.[41,42] Moreover, process efficiency (Figure 8B) shows that process 1-2 quickly reaches values of *ca.* 60-70% and remains approximately constant with time. It can also be observed that the main rate limiting process in our system is the connection 2-3.

Altogether, the results described in this section illustrate how the analysis of process/communication efficiencies can help understand the complex behaviour of communication systems, identify critical steps, and facilitate the design of optimized networks. In addition, chemical communication networks could be affected by spatial effects such as the relative distance between nanodevices/communication sites. Molecular messengers could be diluted in the medium before reaching its target,[41] directional information flow over distances in molecular communication circuits would require a fine control over the location of interacting nanodevices and messenger diffusion kinetics should be considered. In this study, we have conducted the experiments under stirring of solutions containing nanodevices; thus, diminishing the effect of particle location.

Notwithstanding, other works about chemical communication within communities of immobilized abiotic elements using microfluidic technologies have observed the importance of controlling geometrical patterning, chemical input concentrations and flow rate. Although so-far scarce, further studies in this direction will be important for advancing towards the design of chemical communication networks of nanodevices with spatiotemporal control over the information transmission.[42,43]

4.4 Conclusions

In summary, we present herein a circular model of communication between nanodevices based on enzyme-functionalized Janus Au-mesoporous silica capped nanoparticles. In the community of nanoparticles, the release of a cargo from a first nanoparticle (output) after the addition of a stimulus (i.e. lactose) is only observed after the circular communication of the nanoparticles in the sequence $\mathbf{S1}_{\beta gal}$-$\mathbf{S2}_{galox}$-$\mathbf{S3}_{est}$-$\mathbf{S1}_{\beta gal}$ as a result of the exchange of chemical messengers between the components of the group. The relatively slow communication (maximum delivery after 16 h) is ascribed to the number of chemical processes that have to occur to communicate, including enzymatic activation of different molecules, cargo diffusion from the pores to the solution and chemical messenger diffusion from one nanoparticle to another. Moreover, a calculation of the communication efficiency, process efficiency and information loss for the different steps of the communication path allowed us to better understand the communication network and determine the rate limiting processes. Several are the options to enhance communication; one of them is the use of nanoparticles equipped with nanomotors and several studies in this direction are being carried by us currently.[44,45] Overall, our network involves three enzymatic processes and the exchange of three chemical messengers (galactose, an ester derivative and the

reducing agent TCEP). Only the complete community of nanoparticles is capable of producing the desired output phenomenon (dye release), while incomplete communities do not succeed in transmitting the information. In spite of being similar to a cascade-like system, its potential scope is beyond a typical metabolomic pathway because it is not only limited to the chained enzyme substrates and products. For instance, the possibility of encapsulating a cargo enables communication between enzymes that otherwise could not naturally interact. Moreover, nanoparticles can be directed, concentrated in certain places, etc., allowing designing more advance communication systems, when compared with cascade-like system using chained enzymes in diluted solutions. Circular communication could be of relevance for designing networks enabling initiation of the communication and output from the same nanodevice after sequentially-programmed steps of information transmission with other nanodevices, thus potentially allowing feedback – this is an aspect that would not be possible with a linear pathway since signal detection and final response would occur on different sites. Although the presented design is a proof of concept which leads to a dye release as final output instead of the usual dynamical feedback observed in biological reaction cycles, it illustrates the potential of using abiotic nanodevices to design multistep signalling pathways. Our results demonstrate how artificial nanodevices can be connected by means of molecular communication, yielding systems that show a collective synergic behaviour. Although modelling of the present system was beyond of our scope, advances in the modelling of molecular communications could help in the design and understanding of chemical networks at the micro/nanoscale. A search of different modes of communication within groups of nanoparticles (such as the circular mode of communication reported here) is a key step to further develop more realistic nano-communities to perform specific and complex tasks at the nanoscale. Moreover, the possibility of combining

different nanoparticles and communicating them with living organisms[46-49] would allow to develop swarms of nanodevices able to interact with their neighbours and local environment leading to advanced systems with new cooperative functionalities. This would cause a deep impact in the way we understand the interaction between artificial nanodevices and nanodevices with living systems. We believe that the idea of developing multicomponent nanoscale cooperative communities capable of communicating and performing coordinated may open new directions in the near future in areas such as biomedicine and ICT.[50-55]

Acknowledgements. The authors wish to thank the Spanish Government (projects RTI2018-100910-B-C41 (MCUI/AEI/FEDER, UE), CTQ2017-87954-P), the Generalitat Valenciana (PROMETEO 2018/024), the Comunidad de Madrid (IND2017/BMD-7642) and CIBER-BBN (NANOCOMMUNITY project) for support.

4.5 References

1. D. Malak and O. B. Akan, *Nano. Commun. Netw*. **2012**, *3*, 19.
2. N. Deisig, F. Dupuy, S. Anton and M. Renou, *Insects* **2014**, *5*, 399.
3. M. E. Taga and B. L. Bassler, *Proc. Natl. Acad. Sci. U.S.A.* **2003**, *100*, 14549.
4. J. T. Hancock in *Cell Signalling*, 4th ed., Oxford University Press, Oxford, UK, **2016**.
5. D. J. Levi in *Group Dynamics for Teams*, 5th ed., SAGE Publications, Thousand Oaks, CA, USA, **2016**.
6. T. E. Harris and J. C. Sherblom in *Small Group and Team Communication,* 5th ed., Pearson, London, UK, **2010**.
7. J. H. Miller and S. Moser, *Complexity* **2004**, *9*, 31.
8. R. E. Rice, E. J. Zackrison and D. R. Seibold in *The International Encyclopedia of Organizational Communication*, 1st ed., John Wiley & Sons, NJ, USA, **2017**.
9. P. F. Cristaldo, V. Jandák, K. Kutalová, V. B. Rodrigues, M. Brothánek, O. Jirícek, O. DeSouza and J. Sobotník, *Biol. Open* **2015**, *4*, 1649.
10. J. S. M. Chia, E. S. Wall, C. L. Wee, T. A. J. Rowland, R. -K. Cheng, K. Cheow, K. Guillemin and S. Jesuthasan, *Nat. Commun.* **2019**, *10*, 3831.
11. T. Eisner, I. Kriston and D. J. Aneshansley, *Behav. Ecol. Sociobiol.* **1976**, *1*, 83.
12. I. F. Akyildiz, F. Brunetti and C. Blázquez, *Comput. Netw.* **2008**, *52*, 2260.
13. J. L. Marzo, J. M. Jornet and M. Pierobon, *Curr. Drug Targets* **2019**, *20*, 800.

14. I. F. Akyildiz, M. Pierobon, S. Balasubramaniam and Y. Koucheryavy, *IEEE Commun. Mag*. **2015**, *53*, 32.
15. M. E. Roth, O. Green, S. Gnaim and D. Shabat, *Chem. Rev*. **2016**, *116*, 1309.
16. X. Sun, D. Shabat, S. T. Phillips and E. V. Anslyn, *J. Phys. Org. Chem.* **2018**, *31*, e3827.
17. S. Campuzano, B. Esteban-Fernandez de Ávila, P. Yáñez-Sedeño, J. M. Pingarrón and J. Wang, *Chem. Sci.* **2017**, *8*, 6750.
18. E. Aznar, M. Oroval, L. Pascual, J. R. Murguía, R. Martínez-Máñez and F. Sancenón, *Chem. Rev.* **2016**, *116*, 561.
19. C. -A. Cheng, T. Deng, F. -C. Lin, Y. Cai and J. I. Zink, *Theranostics* **2019**, *9*, 3341.
20. A. Llopis-Lorente, B. Lozano-Torres, A. Bernardos, R. Martínez-Máñez and F. Sancenón, *J. Mater. Chem. B* **2017**, *5*, 3069.
21. M. Karimi, A. Ghasemi, P. Sahandi Zangabad, R. Rahighi, S. Masoud Moosavi Basri, H. Mirshekari, M. Amiri, Z. Shafaei Pishabad, A. Aslani, M. Bozorgomid, D. Ghosh, A. Beyzavi, A. Vaseghi, A. R. Aref, L. Haghani, S. Bahramia and M. R. Hamblin, *Chem. Soc. Rev.* **2016**, *45*, 1457.
22. A. Llopis-Lorente, P. Díez, A. Sánchez, M. D. Marcos, F. Sancenón, P. Martínez-Ruiz, R. Villalonga and R. Martínez-Máñez, *Nano Today* **2018**, *18*, 8.
23. H. Wang and M. Pumera, *Chem. Soc. Rev*. **2020**, *49*, 3211.
24. C. Giménez, E. Climent, E. Aznar, R. Martínez-Máñez, F. Sancenón, M. D. Marcos, P. Amorós and K. Rurack, *Angew. Chem. Int. Ed.* **2014**, *53*, 12629; *Angew. Chem.* **2014**, *126*, 12838.
25. A. Llopis-Lorente, P. Díez, A. Sánchez, M. D. Marcos, F. Sancenón, P. Martínez-Ruiz, R. Villalonga and R. Martínez-Máñez, *Nat. Commun*. **2017**, *8*, 15511.
26. C. Chen, X. Chang, H. Teymourian, D. E. Ramírez-Herrera, B. Esteban-Fernández de Ávila, X. Lu, J. Li, S. He, C. Fang, Y. Liang, F. Mou, J. Guan and J. Wang, *Angew. Chem. Int. Ed.* **2018**, *57*, 241; *Angew. Chem.* **2018**, *130*, 247.
27. Y. Qiao, M. Li, D. Qiu and S. Mann, *Angew. Chem. Int. Ed.* **2019**, *58*, 17758; *Angew. Chem.* **2019**, *131*, 17922.
28. T. Farrugia, A. W. Perriman, K. P. Sharma and S. Mann, *Chem. Comm.* **2017**, *53*, 2094.
29. W. Wang, W. Duan, S. Ahmed, A. Sen and T. Mallouk, *Acc. Chem. Res.* **2015**, *48*, 1938.
30. W. Bechtel and A. Abrahamsen in *Philosophy of Complex Systems*, 1st ed., Elsevier, Amsterdam, Netherlands, **2011**, Part 2, Ch. 1.
31. R. Villalonga, P. Díez, A. Sánchez, E. Aznar, R. Martínez-Máñez and J. M. Pingarrón, *Chem. Eur. J*. **2013**, *19*, 7889.
32. A. Llopis-Lorente, B. de Luis, A. García-Fernández, P. Díez, A. Sánchez, M. D. Marcos, R. Villalonga, R. Martínez-Máñez and F. Sancenón, *J. Mater. Chem. B* **2017**, *5*, 6734.
33. T. M. Godoy-Reyes, A. Llopis-Lorente, A. García-Fernández, P. Gaviña, A. M. Costero, R. Villalonga, F. Sancenón and R. Martínez-Máñez, *Org. Chem. Front.* **2019**, *6*, 1058.
34. F. O. Yousef, M. B. Zughul and A. A. Badwan, *J. Incl. Phenom. Macrocycl. Chem.* **2007**, *57*, 519.
35. G. Jerez, G. Kaufman, M. Prystai, S. Schenkeveld and K. K. Donkor, *J. Sep. Sci.* **2009**, *32*, 1087.
36. S. S. Wong and L. -J. C. Wong, *Enzyme Microb. Technol.* **1992**, *14*, 866.
37. A. Kasprzak, K. M. Borys, S. Molchanov and A. Adamczyk-Wozniak, *Carbohydr. Polym.* **2018**, *198*, 294.

38. A. Llopis-Lorente, B. de Luis, A. García-Fernández, S. Jiménez-Falcao, M Orzáez, F. Sancenón, R. Villalonga and R. Martínez-Máñez, *ACS Appl. Mater. Interfaces* **2018**, *10*, 26494.
39. S. Erbas-Cakmak, S. Kolemen, A. C. Sedgwick, T. Gunnlaugsson, T. D. James, J. Yoon and E. U. Akkaya, *Chem. Soc. Rev*. **2018**, *47*, 2228.
40. E. Katz, ed. in *Biomolecular Information Processing: From Logic Systems to Smart Sensors and Actuators*, 1st ed., John Wiley & Sons, NJ, USA, **2012**.
41. G. Gines, A. S. Zadorin, J. -C. Galas, T. Fujii, A. Estevez-Torres and Y. Rondelez, *Nat. Nanotechnol*. **2017**, *12*, 351.
42. L. Tian, M. Li, J. Liu, A. J. Patil, B. W. Drinkwater and S. Mann, *ACS Cent. Sci.* **2018**, *4*, 1551.
43. J. Liu, L. Tian, Y. Qiao, S. Zhou, A. J. Patil, K. Wang, Mei Li and Stephen Mann, *Angew. Chem. Int. Ed.* **2020**, *59*, 6853.
44. A. Llopis-Lorente, A. García-Fernández, E. Lucena-Sánchez, P. Díez, F. Sancenón, R. Villalonga, D. A. Wilson and R. Martínez-Máñez, *Chem. Commun.* **2019**, *55*, 13164.
45. A. Llopis-Lorente, A. García-Fernández, N. Murillo-Cremaes, A. C. Hortelão, T. Patiño, R. Villalonga, F. Sancenón, R. Martínez-Mañez and S. Sánchez, *ACS Nano* **2019**, *13*, 12171.
46. R. Lentini, N. Y. Martin, M. Forlin, L. Belmonte, J. Fontana, M. Cornella, L. Martini, S. Tamburini, W. E. Bentley, O. Jousson and S. S. Mansy, *ACS Cent. Sci.* **2017**, *3*, 117.
47. B. de Luis, A. Llopis-Lorente, P. Rincón, J. Gadea, F. Sancenón, E. Aznar, R. Villalonga, J. R. Murguía and R. Martínez-Máñez, *Angew. Chem. Int. Ed*. **2019**, *58*, 14986; *Angew. Chem.* **2019***, 131,* 15128.
48. C. G. Hebert, A. Gupta, R. Fernandes, C. Y. Tsao, J. J. Valdes and W. E. Bentley, *ACS Nano* **2010**, *4*, 6923.
49. M. Schwarz-Schilling, L. Aufinger, A. Mückl and F. C. Simmel, *Integr. Biol.* **2016**, *8*, 564.
50. S. Hauert and S. N. Bhatia, *Trends Biotechnol.* **2014**, *32*, 448.
51. N. Agoulmine, K. Kim, S. Kim, T. Rim, J.-S. Lee and M. Meyyappan, *IEEE Wirel. Commun.* **2012**, *19*, 42.
52. N. Farsad, *Mob. Comput. Commun. Rev*. **2018**, *22*, 5.
53. T. Nakano, M. J. Moore, F. Wei, A. V. Vasilakos and J. Shuai *IEEE Trans. Nanobioscience* **2012**, *11*, 135.
54. A. García-Fernández, E. Aznar, R. Martínez-Máñez and F. Sancenón, *Small* **2020**, *16*, 1902242.
55. O. B. Akan, H. Ramezani, T. Khan, N. A. Abbasi and M. Kuscu, *Proc. IEEE* **2017**, *105*, 306.

4.6 Supporting Information

Chemicals

Tetraethyl orthosilicate (TEOS), *n*-cetyltrimethylammonium bromide (CTABr), sodium hydroxide (NaOH), gold(III) chloride trihydrate ($HAuCl_4 \cdot 3H_2O$), sodium citrate tribasic dihydrate, (3-mercaptopropyl) trimethoxysilane, paraffin wax, 3-mercaptopropionic acid, tris(2,2′-bipyridyl)dichlororuthenium(II) hexahydrate ($[Ru(bpy)_3]Cl_2 \cdot 6H_2O$), 2,2'-dipyridyl disulfide, O-(2-mercaptoethyl)-O'-methyl-hexa(ethylene glycol), β-galactosidase from *Aspergillus oryzae*, methyl 4-(bromomethyl)benzoate, 3-(triethoxysilyl)propyl isocyanate, 4-(hydroxymethyl) phenyl boronic acid pinacol ester, galactose oxidase from *Dactylium dendroides*, sodium, tris(2-carboxyethyl)phosphine hydrochloride, (3-iodopropyl) trimethoxysilane, benzimidazole, triethylamine, β-cyclodextrin, esterase from porcine liver, *N*-(3-dimethylaminopropyl)-*N'*-ethylcarbodiimide hydrochloride (EDC), *N*-hydroxysuccinimide (NHS), D-(+)-galactose, D-(+)-lactose monohydrate, glucose oxidase from *Aspergillus niger*, 2,2′-azino-bis(3-ethylbenzothiazoline-6-sulfonic acid) diammonium salt (ABTS), peroxidase from horseradish (HRP) and 4-nitrophenyl butyrate were purchased from Sigma-Aldrich and used without further purification.

Sodium sulfate anhydrous, sodium dihydrogen phosphate monohydrate, disodium hydrogen phosphate heptahydrate, ethanol, chloroform, toluene, acetonitrile and anhydrous tetrahydrofuran were provided by Scharlau.

General Methods

Powder X-ray diffraction (PXRD), transmission electron microscopy (TEM), N_2 adsorption-desorption isotherms, UV-visible and fluorescence spectrophotometry, dynamic light scattering (DLS) and elemental analysis techniques were employed for materials characterization. PXRD measurements were performed on a Seifert 3000TT diffractometer using CuKα radiation at low angles ($1.3 < 2\theta < 8.3$, with steps of 0.04 degrees and 3 seconds for step) and high angles ($35 < 2\theta < 80$ with steps of 0.04 degrees and 1 second for step). TEM images were acquired using a JEOL TEM-1010 Electron microscope working at 100 kV. Additionally, TEM coupled with energy dispersive X-ray spectroscopy (TEM-EDX) was used for element mapping using a JEOL TEM-2100F microscope. ^{1}H spectra were recorded at 400 MHz on a Bruker 400 Avance III Spectrometer. DLS studies were performed using a ZetaSizer Nano ZS (Malvern). N_2 adsorption-desorption isotherms were recorded on a Micromeritics TriStar II Plus automated analyzer. Samples were previously degassed at 90 °C in vacuum overnight and measurements were performed at 77 °K. UV-visible spectra were recorded with a JASCO V-650 spectrophotometer. Fluorescence measurements were carried out in a JASCO FP-8500 spectrophotometer. Elemental analysis was performed using a LECO CHNS-932 Elemental Analyzer

Synthesis of the self-immolative arylboronate (1)

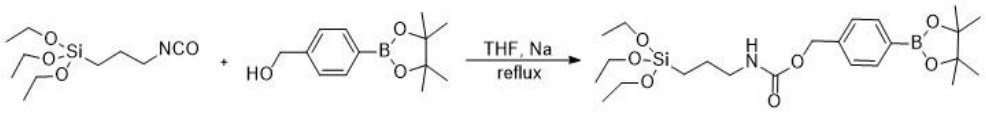

Figure S1. Synthesis of self-immolative arylboronate derivative (**1**).

4-(Hydroxymethyl) phenyl boronic acid pinacol ester (235 mg, 1.01 mmol) was dissolved in anhydrous THF (8 mL) and a small piece of Na (*ca*. 1 mg) was added.

After stirring 10 min under argon at room temperature, (3-isocyanatopropyl) triethoxysilane (249 µL, 1.01 mmol) was added dropwise and the mixture was stirred under reflux for 24 h. Then, the solvent was evaporated and sodium salts were removed with a CH_2Cl_2/H_2O extraction. This procedure led to the self-immolative molecule (**1**) with a 75% yield as a dark yellow oil.

^{1}H NMR (300 MHz, $CDCl_3$) δ 7.78 (d, 2H), 7.33 (d, 2H), 5.10 (s, 2H), 3.79 (m, 6H), 3.18 (m, 2H), 1.62 (m, 2H), 1.34 (s, 12H), 1.21 (m, 9H), 0.62 (m, 2H), in accordance to previous literature.[1]

Synthesis of mesoporous silica nanoparticles (MSNPs)

1.00 g (2.74 mmol) of *n*-cetyltrimethylammonium bromide (CTABr) was dissolved in 480 mL of deionized water. Then, the pH was basified by adding 3.5 mL of a 2 mol·L^{-1} NaOH solution and the temperature was increased to 80 °C. Next, tetraethyl orthosilicate (TEOS) (5 mL, 22.4 mmol) was added dropwise into the solution. Magnetic stirring was kept for 2 hours to give a white suspension. Finally, the solid was isolated by centrifugation, washed several times with water until neutral pH and dried at 70 °C overnight (as-synthesized **MSNPs**). To obtain the final mesoporous nanoparticles (**MSNPs**), the as-synthesized solid was calcined at 550 °C in an oxidant atmosphere for 5 hours in order to remove the surfactant.

Synthesis of gold nanoparticles

Gold nanoparticles were synthesized following the Turkevich-Frens method.[2,3] 100 mL of a 0.3 mM $HAuCl_4 \cdot 3H_2O$ solution were brought to 135 °C under stirring and refluxing. Then, 1.5 mL of a 1 % sodium citrate solution was added to yield gold nanoparticles of *ca.* 20 nm. The initially pale-yellow colour turned to purple-black and finally red wine in 10 minutes. After this, the colloidal suspension

was cooled to room temperature under stirring. This protocol was repeated 4 times until obtaining 400 mL of the colloidal gold nanoparticles suspension.

Synthesis of Janus Au-MS nanoparticles (S0)

180 mg of MCM-41 type mesoporous silica nanoparticles (**MSNPs**) were dispersed in 9 mL of an aqueous solution (6.7 % ethanol) followed by addition of *n*-cetyltrimethylammonium bromide (CTABr, 1 µM). The mixture was heated at 75 °C, and then 1 g of paraffin wax was added. Once the paraffin was melted, the mixture was vigorously stirred for 15 minutes using a homogenizer (Ultra-Turrax T-8, IKA). Then, the mixture was further stirred for 1 hour at 75 °C using a magnetic stirrer. The resulting Pickering emulsion was then cooled to room temperature, diluted with 10 mL of methanol and reacted with 200 µL of (3-mercaptopropyl) trimethoxysilane for 3 hours. The solid was collected by centrifugation and washed with methanol. For gold attachment, the partially mercapto-functionalized nanoparticles were dispersed in 68 mL of methanol and added over the 400 mL of the colloidal gold nanoparticles suspension previously synthesized. The mixture was stirred overnight at room temperature. Then, the solid was isolated by filtration and exhaustively washed with chloroform and hexane. The solid was dried and ground. This process finally yielded the Janus Au-mesoporous silica nanoparticles (Janus Au-MS nanoparticles, **S0**).

Synthesis of S1

For the preparation of **S1**, 50 mg of **S0** and 25 mg of $[Ru(bpy)_3]Cl_2 \cdot 6H_2O$ dye were suspended in acetonitrile (3 mL, 13 mM) and stirred overnight in order to achieve the loading of the pores. Then, the solid was isolated by centrifugation, washed with acetonitrile and dried under vacuum. Afterwards, in order to protect the gold face, this loaded solid was resuspended in ethanol (5 mL) and let to react

with 70 µL of 3-mercaptopropionic acid stirring for 1 hour at room temperature. The solid was isolated by centrifugation, washed twice with ethanol and allowed to air dry. Next, the resulting solid was resuspended in anhydrous acetonitrile (1.7 mL) and (3-mercaptopropyl)trimethoxysilane (93 µL, 0.5 mmol) was added. The suspension was stirred for 5.5 hours at room temperature and then, 2,2'-dipyridyl disulfide (110 mg, 0.5 mmol) was added to the reaction mixture. After stirring overnight at room temperature, the resulting solid was centrifuged, washed twice with acetonitrile and dried under vacuum. Finally, a mixture of this prepared solid and O-(2-mercaptoethyl)-O'-methyl-hexa(ethylene glycol) (50 µL, 0.15 mmol) was suspended in acetonitrile (3.33 mL) and was stirred overnight. The final capped Janus nanoparticles **S1** were isolated by centrifugation, washed with abundant acetonitrile and dried under vacuum.

Synthesis of $\mathbf{S1_{\beta gal}}$

8 mg of **S1** were suspended in 2 mL of 50 mM sodium phosphate buffer at pH 7.5. Then, 2.5 mg of *N*-(3-dimethylaminopropyl)-*N'*-ethylcarbodiimide hydrochloride (EDC), 2.5 mg of *N*-hydroxysuccinimide (NHS) and 10 mg of the enzyme β-galactosidase were added and the suspension was stirred overnight at 10 °C. The solid was isolated by centrifugation and washed several times with cold 50 mM sodium phosphate buffer (pH 7.5). The resulting $\mathbf{S1_{\beta gal}}$ was kept wet in refrigerator until use.

Synthesis of S2

In order to prepare the solid **S2**, 25 mg of **S0** were suspended in 1.8 mL of acetonitrile and treated with 25 µL of 3-mercaptopropionic acid to functionalize the gold face. The solution was stirred for 1 hour and then nanoparticles were isolated and washed twice by centrifugation with fresh acetonitrile. Once dried under

vacuum, these nanoparticles (25 mg) were loaded by stirring, for 24 h under argon atmosphere, 5 mL of an anhydrous acetonitrile solution containing 24 mg of methyl 4-(bromomethyl)benzoate (21 mM). Then, the self-immolative molecule (**1**) (70 mg, 0.14 mmol) was dissolved in 700 µL of anhydrous acetonitrile and added dropwise to the nanoparticle's suspension. The mixture was let to react for 5.5 h stirring at room temperature. Afterwards, the solid was isolated by centrifugation, washed twice with acetonitrile, twice with PBS buffer 5X (pH 7.5) and dried under vacuum overnight. The resulting nanoparticles and 90 mg of β-cyclodextrin were mixed in 5 mL of PBS buffer 5X (pH 7.5) and stirred overnight. Finally, the nanoparticles were isolated by centrifugation, washed 3 times with PBS buffer 5X (pH 7.5) and dried under vacuum. This process finally yielded the solid **S2**.

Synthesis of $S2_{galox}$

5 mg of **S2** were suspended in 1.4 mL of 50 mM sodium phosphate buffer at pH 7.5. Then, 1 mg of EDC, 1 mg of NHS and 100 µL of the commercial enzyme solution galactose oxidase were added and the suspension was stirred overnight at 10 °C. The solid was isolated by centrifugation and washed several times with cold 50 mM sodium phosphate buffer (pH 7.5). The resulting $\mathbf{S2_{galox}}$ was kept wet in refrigerator until use.

Synthesis of $S2_{blank}$

Solid $\mathbf{S2_{blank}}$ was prepared following the same procedure described for $\mathbf{S2_{galox}}$ but the mesoporous container was not loaded.

Synthesis of S3

For the preparation of **S3**, 60 mg of **S0** were suspended in anhydrous acetonitrile (4 mL) and reacted with 60 µL of (3-iodopropyl) trimethoxysilane for

5.5 hours. The solid was isolated by centrifugation, washed with acetonitrile and dried at 70 °C overnight. To functionalize the surface with benzimidazole moieties, 0.25 g of benzimidazole and 990 µL of triethylamine were mixed with 20 mL of toluene and heated for 20 min at 80 °C in order to prepare a saturated solution of benzimidazole. 10 mL of this suspension were added over 60 mg of the previously prepared nanoparticles. The mixture was stirred at 80 °C for three days. Afterward, the benzimidazole-functionalized solid was isolated by centrifugation and washed with toluene. To protect the gold face, the resulting solid was suspended in 5 mL of acetonitrile and reacted with 50 µL of 3-mercaptopropionic acid for 1 hour. This solid was centrifuged, washed with toluene and with water and let to dry at 70 °C overnight. Next, the loading process was carried out by suspending the solid in 8 mL of a concentrated solution in 50 mM phosphate buffer at pH 7.5 of tris(2-carboxyethyl)phosphine hydrochloride (25 mg, 12.5 mM). The solid was centrifuged, washed twice with 50 mM phosphate buffer at pH 7.5, once with ethanol and dried under vacuum. Finally, the solid was suspended with 20 mg of β-cyclodextrin in 12.5 mL of 50 mM sodium phosphate buffer at pH 7.5 and stirred overnight. The suspension was centrifuged, washed thoroughly with 50 mM phosphate buffer at pH 7.5 and dried under vacuum. This process finally yielded the solid **S3**.

Synthesis of $S3_{est}$

8 mg of **S3** were suspended in 4 mL of 50 mM sodium phosphate buffer at pH 7.5. Then, 2.5 mg of EDC, 2.5 mg of NHS and 2 mg of the enzyme esterase were added and the suspension was stirred overnight at 10 °C. The solid was isolated by centrifugation and washed several times with cold 50 mM sodium phosphate buffer (pH 7.5). The resulting $\mathbf{S3_{est}}$ was kept wet in refrigerator until use.

Synthesis of $S3_{blank}$

Solid $\mathbf{S3_{blank}}$ was prepared following the same procedure described for $\mathbf{S3_{est}}$ but the mesoporous container was not loaded.

Materials Characterization

Solids were characterized by standard techniques.

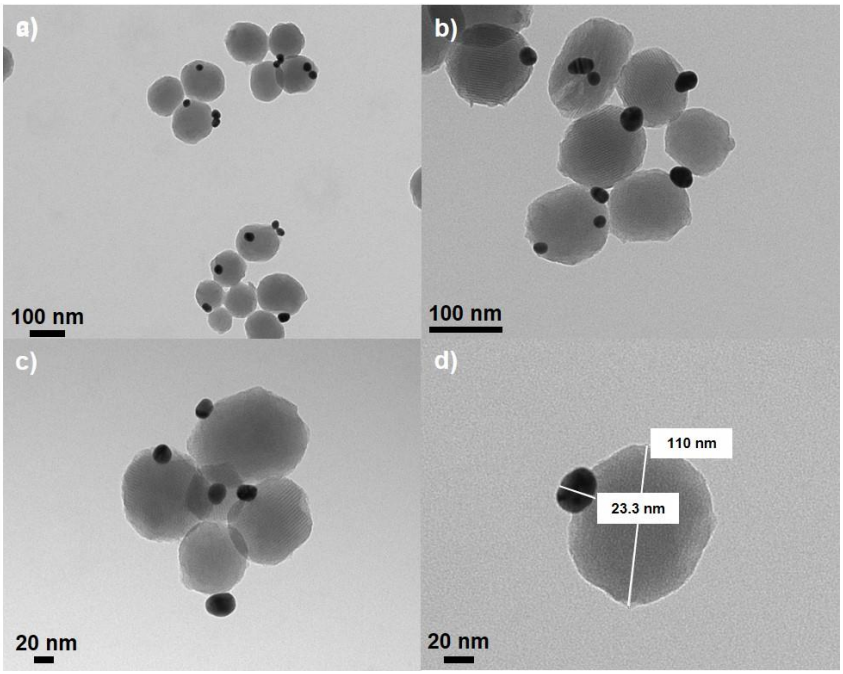

Figure S2. Additional TEM images of the Janus Au-MS nanoparticles **S0** (a-d).

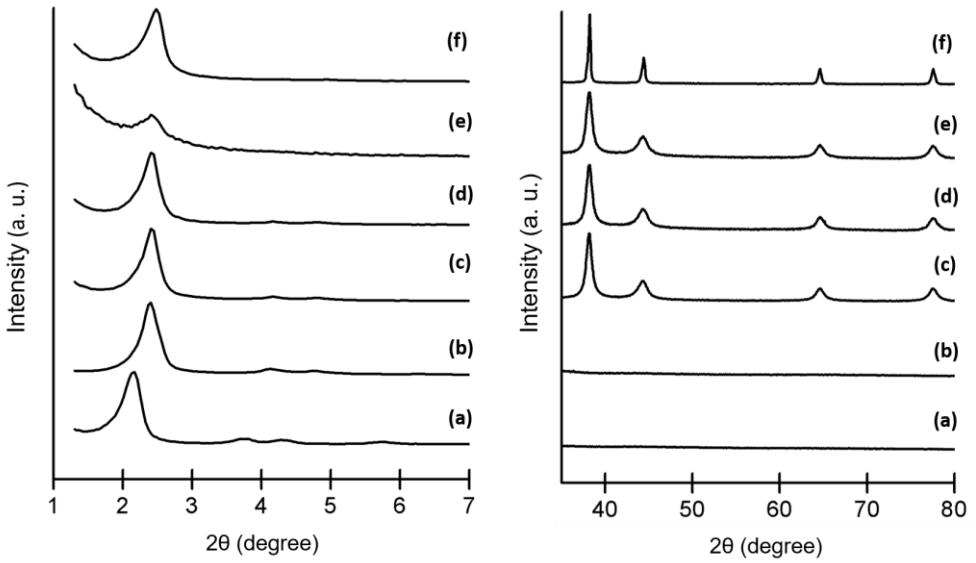

Figure S3. Powder X-ray diffraction patterns of the solids (a) **as-made MSNPs**, (b) **calcined MSNPs**, (c) Janus Au-MS nanoparticles **S0**, (d) solid **S1**, (e) solid **S2** and (f) solid **S3** at low (left) and high (right) angles.

Figure S3 shows powder X-ray diffraction patterns at low ($1.5 < 2\theta < 7$) and at high angles ($35 < 2\theta < 80$) of different prepared nanoparticles. At low angles, the **as-made MSNPs** shows characteristic low-angle reflections of mesoporous silica. In **calcined MSNPs** a slight displacement of the peaks related to the condensation of silanol groups during the calcination process was observed. These low-angle typical peaks are preserved in the Janus Au-MS nanoparticles **S0**. The presence of the (100) peak in the PXRD patterns in the solid **S1**, **S2** and **S3** indicated that the different chemical modifications, functionalization and cargo loading had not damaged the mesoporous structure. Moreover, the high-angle diffraction pattern of the Janus colloids **S0**, **S1**, **S2** and **S3** showed the cubic gold characteristic (111), (200), (220) and (331) diffraction peaks, confirming the presence of gold nanocrystals in the Janus Au-mesoporous silica architecture.[4] Powder X-ray diffraction pattern of nanoparticles containing enzymes were not obtained due to the low quantity

collected in the synthesis but the mild enzyme immobilization procedure is not expected to affect the Janus Au-mesoporous silica architecture.

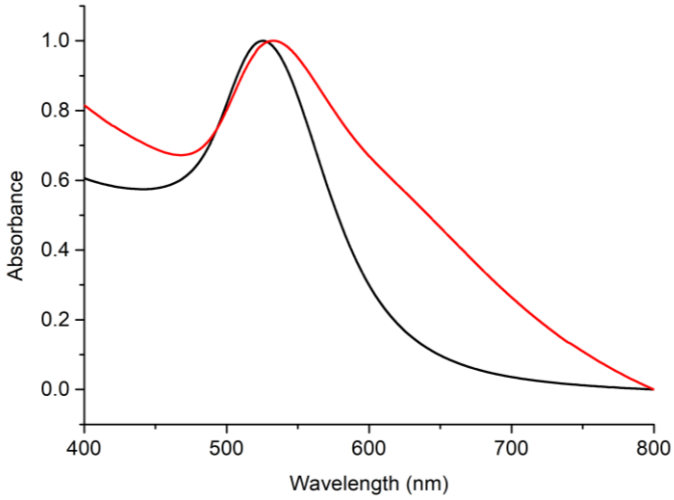

Figure S4. Normalized UV-Visible spectra of the gold nanoparticles (black) and Janus Au-MS nanoparticles **S0** (red).

UV/vis measurements in aqueous solution were performed on the as-synthesized gold nanoparticles and on Janus Au-MS nanoparticles **S0** (by suspending 1 mg of solid in 1 mL of distilled water). The starting gold colloid showed a single absorption band at 524 nm, characteristic of the surface plasmon resonance of spherically shaped nanospheres with approximately 20 nm diameter. In the **S0** spectrum, there is a redshift of the absorbance maximum (533 nm) and a broadening of the band when compared with the as-synthesized gold nanoparticles. These two facts can be ascribed to the increase in the refractive index around the gold nanospheres due to the mesoporous silica attachment and to light refraction produced by silica.[5]

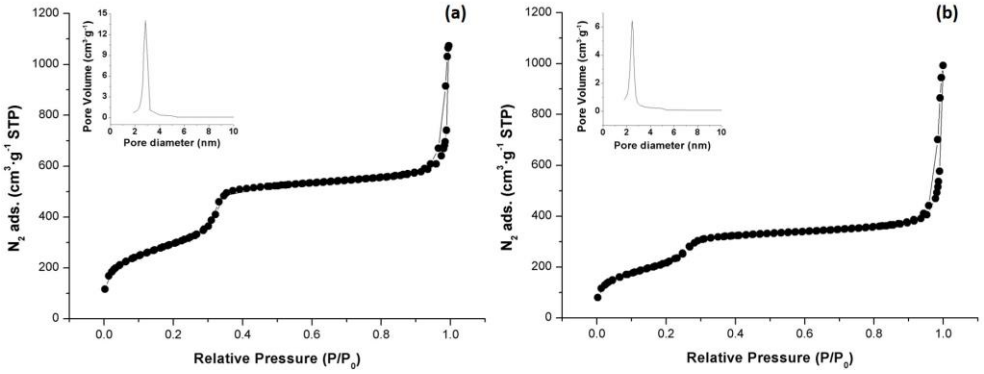

Figure S5. The N_2 adsorption-desorption isotherms for (a) the **calcined MSNPs** and (b) Janus Au-MS nanoparticles **S0**.

The N_2 adsorption-desorption isotherms of the **calcined MSNPs** and Janus Au-MS nanoparticles **S0** show an adsorption step at intermediate P/P_0 value 0.3, which is characteristic for mesoporous solids with empty pores. This step is related to the nitrogen condensation inside the mesopores by capillarity. The absence of a hysteresis loop in this interval and the narrow BJH pore distribution suggest the existence of uniform cylindrical mesopores. Application of the BET model resulted in a value for the total specific surface of 1079 $m^2 \cdot g^{-1}$ for **calcined MSNPs** and 802 $m^2 \cdot g^{-1}$ for Janus Au-MS nanoparticles **S0**. In order to calculate pore size and total pore volume, BJH model was applied on the adsorption band of the isotherm for $P/P_0 < 0.6$ (associated to adsorption inside the pores). BET specific values, pore volumes and pore sizes calculated from N_2 adsorption-desorption isotherms for **MSNPs** and Janus Au-MS nanoparticles **S0** are listed in Table S1.

Table S1. BET specific surface values, pore volumes and pore sizes calculated from N_2 adsorption-desorption isotherms for selected materials.

Solid	S_{BET} [$m^2 \cdot g^{-1}$]	Pore Volume [$cm^3 \cdot g^{-1}$]	Pore size [nm]
Calcined MSNPs	1079 ± 1	0.92	2.72
S0	802 ± 6	0.60	2.43

The zeta potential and hydrodynamic size of different solids were measured by dynamic light scattering (DLS) studies (Table S2 and Figure 2C in main text, respectively). For carrying out the experiments, the corresponding materials were suspended in distilled water at pH 7 at a concentration of 0.01 $mg \cdot mL^{-1}$.

Table S2. Zeta potential values determined by DLS for the different materials.

Sample	Zeta Potential (mV)
MSNPs	-29.7 ± 1
S0	-28.4 ± 0.5
S1	-35.2 ± 0.8
S2	-18.2 ± 1.2
S3	-36.7 ± 0.9
$S1_{\beta gal}$	-31.3 ± 0.9
$S2_{galox}$	-26.3 ± 0.4
$S3_{est}$	-30.4 ± 0.7

From elemental analysis data (Table S3), composition of solids was calculated. Considering the data obtained from the analysis of **S1**, the amount of oligo(ethylene glycol) grafted onto the mesoporous silica face was determined as 69.6 mg·g^{-1} of solid. The amount of $[Ru(bpy)_3]Cl_2$ loaded was estimated to be 70.9 mg·g^{-1} from delivery studies. From the analysis of **S2**, the amount of self-immolative molecular gate was determined to be 261.4 mg·g^{-1} of solid. The cargo was estimated by measuring the absorbance of methyl 4-(bromomethyl)benzoate remaining in solution (λ_{abs} = 243 nm in ACN; λ_{abs} = 244 nm in PBS buffer pH 7.5) during the steps for the synthesis of **S2**. The calibration curves indicate an amount of 83.3 mg of methyl 4-(bromomethyl)benzoate per g of **S2**. From the analysis of **S3**, the amount of $(CH_2)_3$-benzimidazole was determined as 12.5 mg·g^{-1} of solid and the cargo tris(2-carboxyethyl)phosphine was estimated to be 9.7 mg·g^{-1}.

Table S3. Elemental analysis data.

Solid	% C	% H	% N	% S
S0	1.84	2.02	0.13	0.38
S1	6.68	2.22	0.93	1.25
S2	8.69	2.46	1.15	0.31
S3	2.28	1.57	0.22	0.27

The immobilization of the enzymes was confirmed by running the corresponding enzyme activity assay and was calculated by applying the following formula:

$$\frac{Enzyme\ Units}{g} = \frac{(\Delta - \Delta_{blank}) \cdot V_T \cdot F_D}{\varepsilon_{chromop.} \cdot l \cdot V_S \cdot C_S}$$

Where, Δ is the slope of the graph (min^{-1}); Δ_{blank} is the slope of the graph for the blank (min^{-1}); V_T is the total volume in the cuvette; F_D is the dilution factor;

$\varepsilon_{chromop.}$ is the molar extinction of the corresponding chromophore at a defined wavelength ($M^{-1}\cdot cm^{-1}$); l is the optical path in the cuvette (1 cm); V_S is the volume of the sample added (mL); C_S is the concentration of sample added ($g\cdot mL^{-1}$).

The method we used to test β-galactosidase activity is based on the cleavage of lactose by β-galactosidase into galactose and glucose. Then, the glucose is oxidized by glucose oxidase leading to gluconic acid and hydrogen peroxide. Hydrogen peroxide reacts with ABTS (2,2'-azino-bis(3-ethylbenzothiazoline-6-sulfonic acid) diammonium salt) in the presence of peroxidase (HRP) to form a blue-green product ($ABTS^{\cdot+}$) that can be followed UV-visible spectrophotometry (λ_{abs} = 418 nm).

Reactions for assaying β-galactosidase activity:

$$D\text{-}lactose + H_2O \xrightarrow{\beta\text{-Galactosidase}} D\text{-}glucose + D\text{-}galactose$$

$$D\text{-}glucose + O_2 + H_2O \xrightarrow{\text{Glucose oxidase}} D\text{-}gluconic\ acid + H_2O_2$$

$$H_2O_2 + ABTS \xrightarrow{\text{HRP}} ABTS^{\cdot+} + H_2O$$

In a typical experiment to check β-galactosidase activity, 250 µL of lactose ($5\ mg\cdot mL^{-1}$), 250 µL of ABTS solution ($1\ mg\cdot mL^{-1}$), 50 µL of glucose oxidase solution ($1\ mg\cdot mL^{-1}$) and 50 µL of HRP solution ($2\ mg\cdot mL^{-1}$) were placed in a quartz cuvette. All solutions were prepared in 50 mM sodium phosphate buffer at pH 7.5. Then, 100 µL of either buffer (for blank), commercial enzyme solution in buffer ($5\ mg\cdot mL^{-1}$) or **S1**$_{\beta gal}$ suspension ($5\ mg\cdot mL^{-1}$) were added. The mixture was shaken and the absorbance at 418 nm was monitored as a function of time. Whereas no change was observed in the absence of nanoparticles or commercial enzyme, a strong blue-green colour appeared in the presence of those. The increase in absorbance ($ABTS^{\cdot+}$ formation) as a function of time in the presence of **S1**$_{\beta gal}$ and the commercial enzyme solution is depicted in Figure S6.

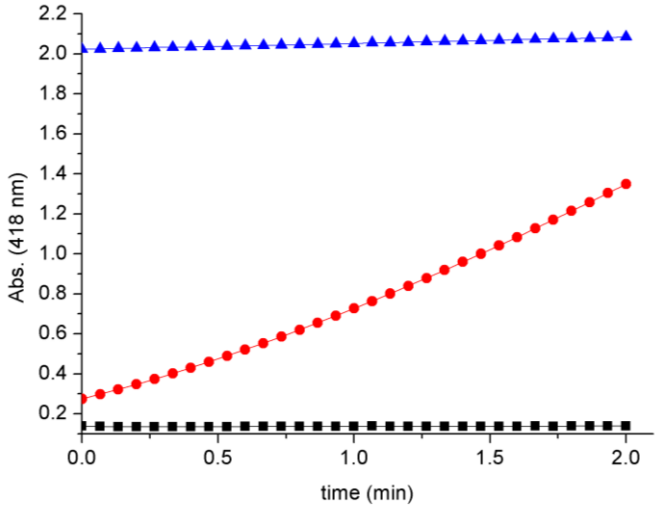

Figure S6. Monitoring of absorbance at 418 nm ($ABTS^{\cdot+}$ formation) due to β-galactosidase activity on nanoparticles **S1$_{βgal}$** (blue), commercial enzyme solution (red) and blank (black).

By applying the previously indicated formula (ε_{ABTS} at 418 nm = 36,000 $M^{-1} \cdot cm^{-1}$), the activity of β-galactosidase on **S1$_{βgal}$** was determined to be 0.001 U per mg of solid (0.006 $U \cdot mL^{-1}$ of solid suspension) whereas the activity of commercial β-galactosidase was determined to be 0.02 U per mg of commercial enzyme (0.11 $U \cdot mL^{-1}$ of enzyme solution). From this data, the corresponding amount of β-galactosidase on **S1$_{βgal}$** was estimated to be 56.10 mg of enzyme per g of solid.

The method used to test galactose oxidase activity is based on the oxidation of galactose by galactose oxidase leading to D-galacto-hexodialdose and hydrogen peroxide. Hydrogen peroxide reacts with ABTS (2,2'-azino-bis(3-ethylbenzothiazoline-6-sulfonic acid) diammonium salt) in the presence of peroxidase (HRP) to form a blue-green product ($ABTS^{\cdot+}$) that can be followed UV-visible spectrophotometry (λ_{abs} = 418 nm).

Reactions for assaying galactose oxidase activity:

$$D\text{-}galactose + O_2 + H_2O \xrightarrow{\text{Galactose oxidase}} D\text{-}galacturonic\ acid + D\text{-}galacto\text{-}hexadialdose + H_2O_2$$

$$H_2O_2 + ABTS \xrightarrow{\text{HRP}} ABTS^{\cdot+} + H_2O$$

In a typical experiment, 100 µL of galactose 20 mM (3.6 mg·mL^{-1}), 480 µL of ABTS solution (5 mg·mL^{-1}) and 10 µL of HRP solution (1 mg·mL^{-1}) were placed in a quartz cuvette. All solutions were prepared in 50 mM sodium phosphate buffer at pH 7.5. Then, 10 µL of either buffer (for blank), commercial enzyme (0.1 mg·mL^{-1}) or **S2$_{galox}$** (5 mg·mL^{-1}) were added. The mixture was shaken and absorbance at 418 nm was monitored as a function of time. Whereas no change was observed in the absence of nanoparticles or commercial enzyme, a strong blue-green colour appeared in the presence of those. The increase in absorbance ($ABTS^{\cdot+}$ formation) as a function of time in the presence of **S2$_{galox}$** and the commercial enzyme solution is depicted in Figure S7.

By applying the previously indicated formula (ε_{ABTS} at 418 nm = 36,000 M^{-1} · cm^{-1}), the activity of galactose oxidase on **S2$_{galox}$** was determined to be 0.124 U per mg of solid (0.620 U·mL^{-1} of solid suspension) whereas the activity of commercial galactose oxidase was determined to be 13.73 U per mg of commercial enzyme (1.33 U·mL^{-1} of enzyme solution). From this data, the corresponding amount of galactose oxidase on **S2$_{galox}$** was estimated to be 9.03 mg of enzyme per g of solid.

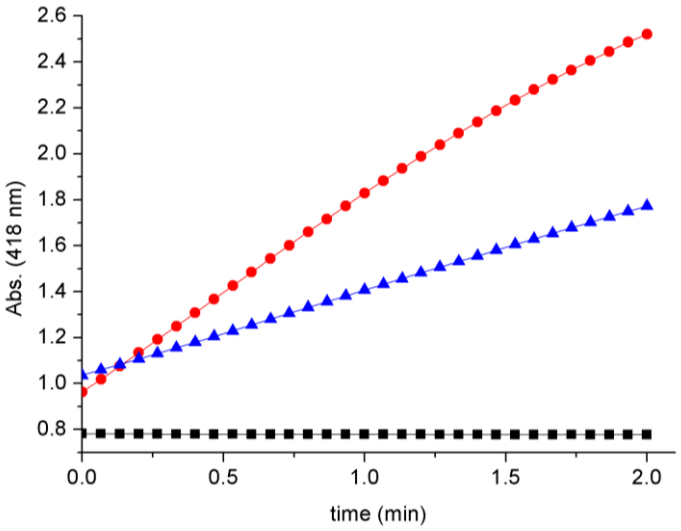

Figure S7. Monitoring of absorbance at 418 nm ($ABTS^{\cdot+}$ formation) due to galactose oxidase activity on nanoparticles **S2**$_{galox}$ (blue), commercial enzyme (red) and blank (black).

The method used to test esterase activity is based on the hydrolysis of 4-nitrophenyl butyrate by esterase into 4-nitrophenol (4-NP) and butyric acid. The yellow colour of 4-nitrophenol can be followed UV-visible spectrophotometry (λ_{abs} = 405 nm).

Reactions for assaying esterase activity:

$$4\text{-}nitrophenyl\ butyrate + H_2O \xrightarrow{\text{Esterase}} 4\text{-}nitrophenol + butyric\ acid$$

To check esterase activity, 100 µL of 4-nitrophenyl butyrate 10 mM (2.1 mg·mL^{-1} in 50 mM sodium phosphate buffer at pH 7.5) and 890 µL of 50 mM sodium phosphate buffer at pH 7.5 were placed in a quartz cuvette. Then, 10 µL of either, buffer (for blank), commercial enzyme solution (0.1 mg·mL^{-1}) or **S3**$_{est}$ suspension (5 mg·mL^{-1}) were added. The mixture was shaken and absorbance at 405 nm was monitored as a function of time. Whereas no change was observed in the absence of nanoparticles or commercial enzyme, a strong yellow colour appeared in the

presence of those. The increase in absorbance (4-nitrophenol formation) as a function of time in the presence of **S3**$_{est}$ and the commercial enzyme solution is depicted in Figure S8.

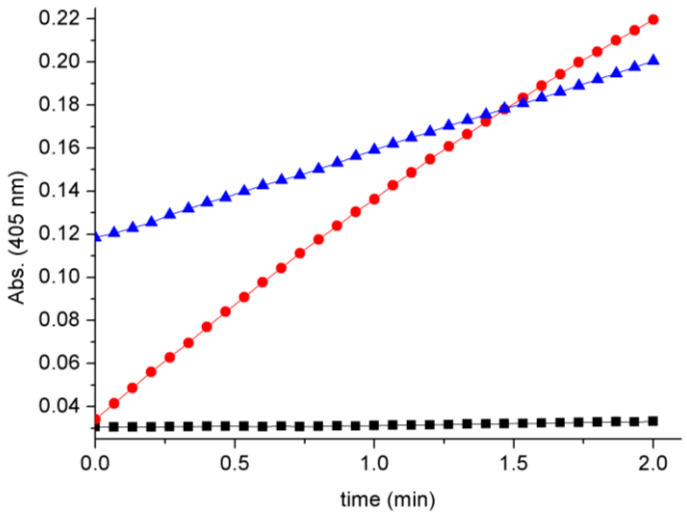

Figure S8. Monitoring of absorbance at 405 nm (4-nitrophenol formation) due to esterase activity on nanoparticles **S3**$_{est}$ (blue), commercial enzyme (red) and blank (black).

By applying the previously indicated formula ($\varepsilon_{4\text{-NP}}$ at 405 nm = 5,000 $M^{-1} \cdot cm^{-1}$), the activity of esterase on **S3**$_{est}$ was determined to be 0.165 U per mg of solid (0.824 $U \cdot mL^{-1}$ of solid suspension) whereas the activity of commercial esterase was determined to be 18.62 U per mg of commercial enzyme (1.86 $U \cdot mL^{-1}$ of enzyme solution). From this data, the corresponding amount of esterase on **S3**$_{est}$ was estimated to be 8.85 mg of enzyme per g of solid.

TEM-EDX mapping of the final nanodevices **S1**$_{\beta gal}$, **S2**$_{galox}$ and **S3**$_{est}$ confirmed the presence of the expected atoms in the solids. Images showed that gold surfaces were rich in sulfur atoms, strongly suggesting the preferential localization of the enzymes in the gold face (Figure S9, S10 and S11) as they are immobilized by means of 3-mercaptopropionic acid. Moreover, the presence of sulfur atoms in the whole

scaffold **S1** $_{\beta gal}$ is attributed to the disulfide bonds of the PEG moieties of the gatekeeper in the silica face while the slight signal of sulfur atoms in **S2**$_{galox}$ and **S3**$_{est}$ is attributed to the (3-mercaptopropyl) trimethoxysilane employed to attach the gold nanoparticles to the silica container during the scaffold synthesis. Boron atoms and nitrogen atoms signals in **S2**$_{galox}$ are due to the boronic esters and carbamate groups of the gatekeepers in **S2**$_{galox}$, whereas the abundance of nitrogen atoms in **S3**$_{est}$ is attributed to the presence of benzimidazole moieties.

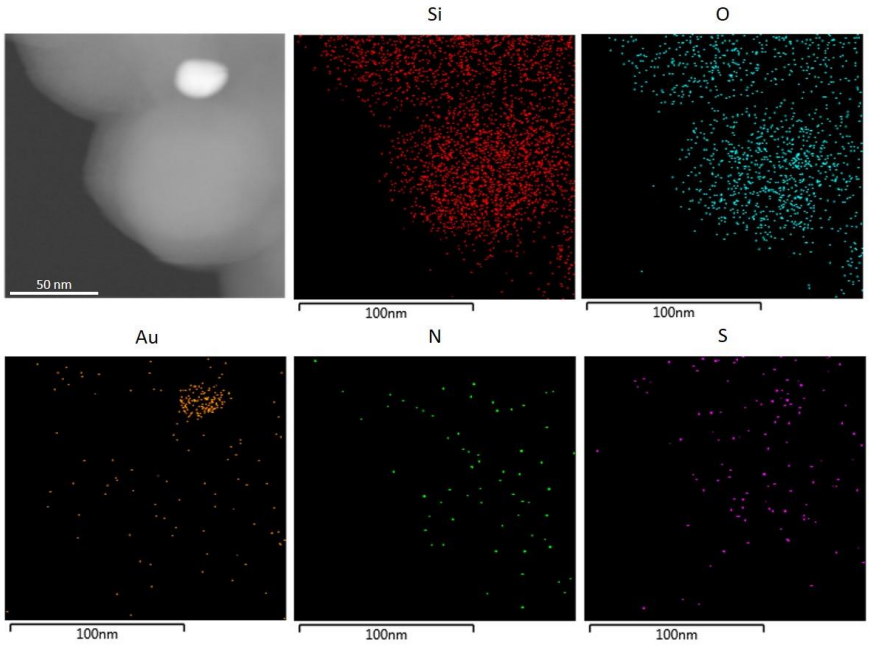

Figure S9. TEM-EDX element mapping of the nanodevice **S1**$_{\beta gal}$.

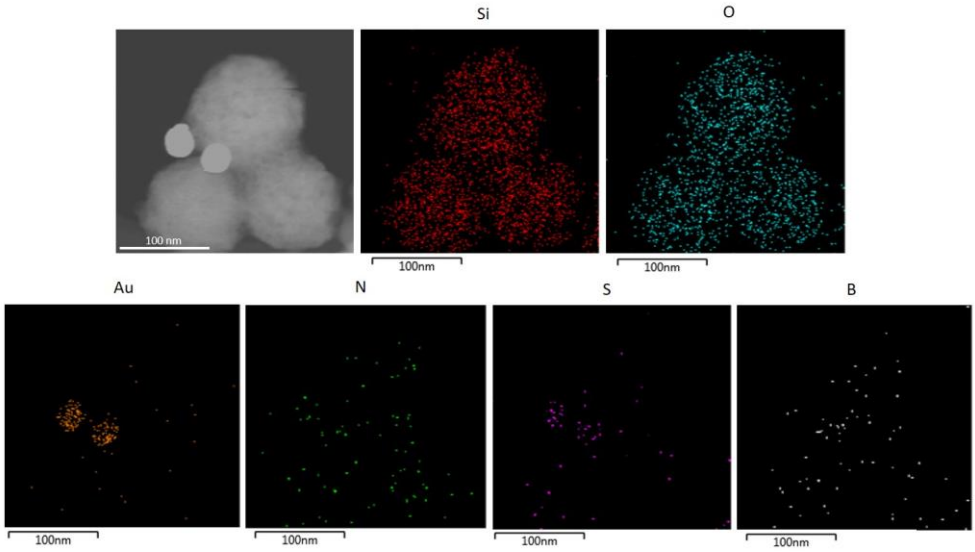

Figure S10. TEM-EDX element mapping of the nanodevice **S2$_{galox}$**.

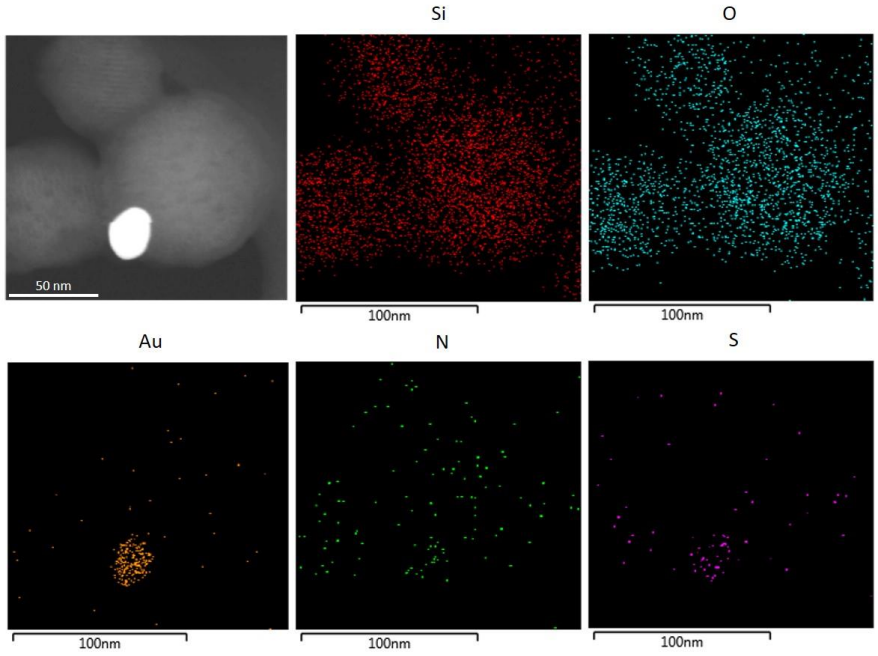

Figure S11. TEM-EDX element mapping of the nanodevice **S3$_{est}$**.

Release studies

Individual release studies

The corresponding refrigerated solution was washed first with an aqueous solution (pH 7.5, 20 mM Na_2SO_4), divided into two fractions and brought to certain final concentration. Both fractions were incubated shaking for 1 hour. Then, the input was added to one fraction (sample) while the same volume of aqueous solution was added to the other (blank). The addition of the input was considered as the beginning of the release experiment (time = 0 minutes). Samples were shaken over time and aliquots were taken at scheduled times, centrifuged (2 minutes, 12000 rpm) to remove the nanoparticles and the fluorescence was measured ($[Ru(bpy)_3]Cl_2$ λ_{exc} = 453 nm, λ_{em} = 595 nm). Final nanoparticle concentrations were 1 mg·mL^{-1} for **S1$_{\beta gal}$**; 2 mg·mL^{-1} for **S2$_{galox}$**-dye and 1 mg·mL^{-1} for **S3$_{est}$**-dye. Final input concentrations in each pair were TCEP 1 mM, galactose 50 mM and methyl 4-(bromomethyl)benzoate 1 mM + 2% of EtOH (to allow ester solubilization), respectively.

Additional individual studies

In order to confirm that each nanodevice delivery was only triggered by its corresponding stimulus, several positive (expected release) and negative controls (non-expected release) were carried out. For **S1$_{\beta gal}$**, galactose 50 mM, methyl 4-(bromomethyl)benzoate 1 mM + 2% of EtOH (negative controls) and tris(2-carboxyethyl)phosphine hydrochloride (TCEP) 1 mM (positive control) were tested as inputs. In addition, it was also proved that high concentrations of lactose did not trigger cargo delivery by employing 5, 10 and 50 mM of lactose (negative controls). For **S2$_{galox}$**-dye, methyl 4-(bromomethyl)benzoate 1 mM + 2% of EtOH, TCEP 1 mM (negative control), galactose 50 mM and H_2O_2 50 mM (positive control) were tested as inputs. Galactose 50 mM was also tested with the nanodevice **S2**-dye lacking the

enzyme. For **S3**$_{est}$-dye, TCEP 1 mM, galactose 50 mM (negative control), methyl 4-(bromomethyl)benzoate 1 mM + 2% of EtOH and HCl 1 mM (positive control) were tested as inputs. Methyl 4-(bromomethyl)benzoate 1 mM + 2% of EtOH was also tested with the nanodevice **S3**-dye lacking the enzyme.

In order to carry out these experiments, the corresponding refrigerated solution was washed with an aqueous solution (pH 7.5, 20 mM Na_2SO_4), divided into as many fractions as stimuli studied and brought to the final concentration (1 mg·mL^{-1} for **S1**$_{\beta gal}$, 2 mg·mL^{-1} for **S2**$_{galox}$-dye and 1 mg·mL^{-1} for **S3**$_{est}$-dye). All fractions were incubated shaking for 1 hour. Then, the inputs were added to the samples while the same volume of aqueous solution was added to the other fraction (blank). The addition of the inputs was considered as the beginning of the release experiment (time = 0 minutes). Samples were shaken over time and aliquots were taken at scheduled times, centrifuged (2 minutes, 12000 rpm) to remove the nanoparticles and the fluorescence was measured ($[Ru(bpy)_3]Cl_2$ λ_{exc} = 453 nm, λ_{em} = 595 nm). The results are shown in Figures S12, S13 and S14.

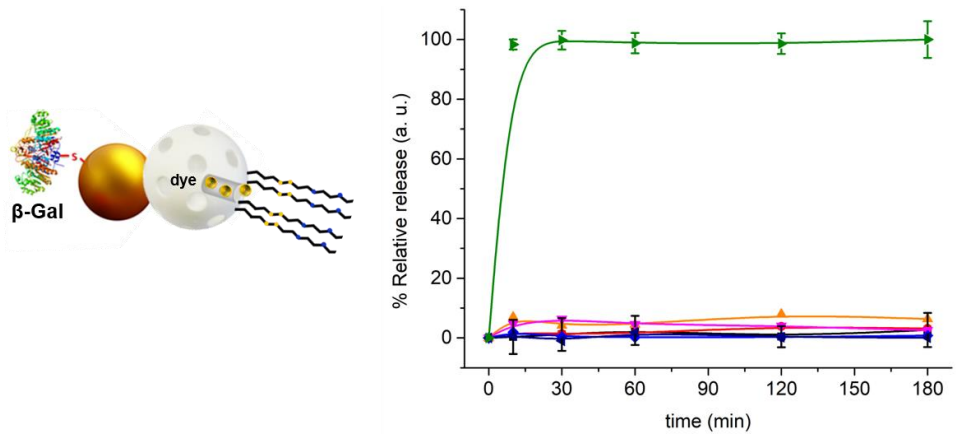

Figure S12. Normalized cargo release graphic from **S1**$_{\beta gal}$ in the absence of input (black curve) and in the presence of galactose 50 mM (red), methyl 4-(bromomethyl)benzoate 1 mM + 2% of EtOH (orange); lactose 5 (grey), 10 (light blue) and 50 mM (dark blue) compared to the release in the presence of TCEP 1 mM (green). Error bars correspond to the s.d. from three independent experiments.

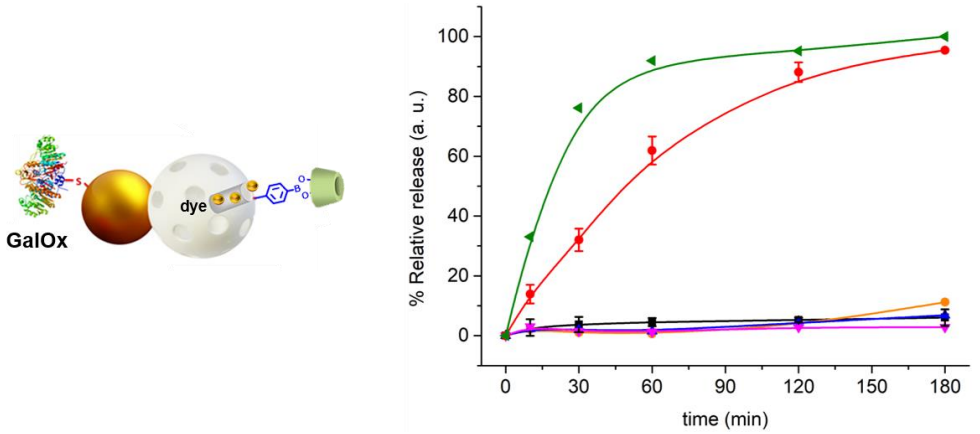

Figure S13. Normalized cargo release graphic from **S2$_{galox}$-dye** in the absence of input (black curve) and in the presence of methyl 4-(bromomethyl)benzoate 1 mM + 2% of EtOH (orange) , TCEP 1 mM (blue), galactose 50 mM (red) and H_2O_2 50 mM (green). Normalized cargo release from **S2**-dye (lacking the galox enzyme) in the presence of galactose 50 mM (grey) is also plotted. Error bars correspond to the s.d. from three independent experiments.

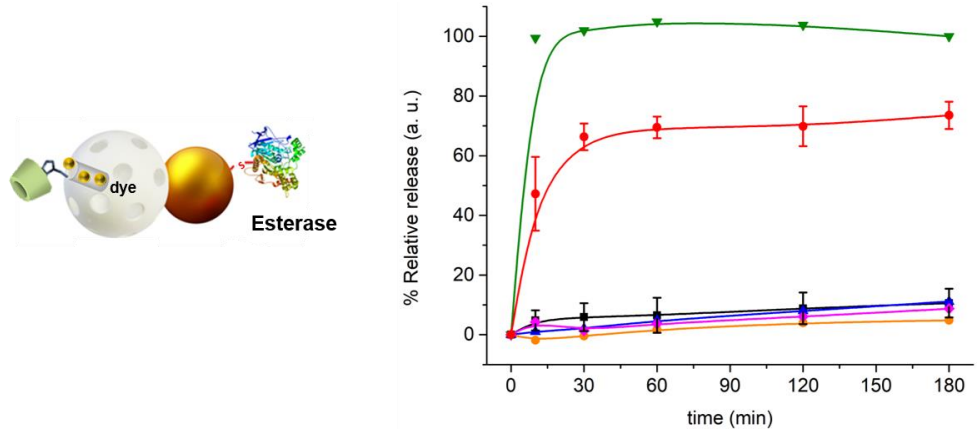

Figure S14. Normalized cargo release graphic from **S3$_{est}$**-dye in the absence of input (black curve) and in the presence of TCEP 1 mM (blue), galactose 50 mM (orange), methyl 4-(bromomethyl)benzoate 1 mM + 2% of EtOH (red) and HCl 1 mM (green). Normalized cargo release from **S3**-dye (enzyme missing) in the presence of methyl 4-(bromomethyl)benzoate 1 mM + 2% of EtOH (grey) is also plotted. Error bars correspond to the s.d. from three independent experiments.

Linear communication between pairs of nanoparticles

Each pair of the corresponding refrigerated solutions of nanoparticles were washed separately with an aqueous solution (pH 7.5, 20 mM Na_2SO_4) and incubated together shaking for 1 hour. Then, the mixture of both solids was divided into two fractions. Both fractions were incubated for another hour. Then, the input was added to one fraction (sample) while the same volume of aqueous solution was added to the other fraction (blank). The addition of the input was considered as the beginning of the release experiment (time = 0 minutes). Samples were shaken over time and aliquots were taken at scheduled times, centrifuged (2 minutes, 12000 rpm) to remove the nanoparticles and the fluorescence was measured ($[Ru(bpy)_3]Cl_2$ λ_{exc} = 453 nm, λ_{em} = 595 nm). Final nanoparticle concentrations were 3/1 mg·mL^{-1} for **S1$_{\beta gal}$**/**S2$_{galox}$**-dye pair; 2.5/0.5 mg·mL^{-1} for **S2$_{galox}$**/**S3$_{est}$**-dye pair; and 1/1 mg·mL^{-1} for **S3$_{est}$**/**S1$_{\beta gal}$** pair. Final input concentrations were 50 mM of lactose, 50 mM of galactose and 2% of EtOH+1 mM of methyl 4-(bromomethyl)benzoate for each pair, respectively.

Circular communication experiments

S1$_{\beta gal}$, **S2$_{galox}$** and **S3$_{est}$** were washed separately with an aqueous solution (pH 7.5, 20 mM Na_2SO_4) and separately incubated shaking for 1 hour. Then, the three solutions were mixed and equally divided into two fractions, each of them with a concentration of 3 mg·mL^{-1} of **S1$_{\beta gal}$**, 2.25 mg·mL^{-1} of **S2$_{galox}$** and 0.75 mg·mL^{-1} of **S3$_{est}$**. Both fractions were incubated for another hour with 2% of EtOH. Then, the input (lactose, final concentration 50 mM) was added to one fraction (sample) while the same volume of aqueous solution was added to the other fraction (blank). The addition of the input was considered as the beginning of the release experiment (time = 0 minutes). Samples were shaken over time and aliquots were taken at scheduled times, centrifuged (2 minutes, 12000 rpm) to remove the

nanoparticles and the fluorescence was measured ($[Ru(bpy)_3]Cl_2$ λ_{exc} = 453 nm, λ_{em} = 595 nm).

Control experiments

The same procedure as described above for the "*Circular communication experiments*" was followed with suspensions of:

S1/**S2**$_{galox}$/**S3**$_{est}$
S1$_{\beta Gal}$/**S2**/**S3**$_{est}$
S1$_{\beta Gal}$/**S2**$_{galox}$/**S3**
S1$_{\beta Gal}$/**S2**$_{blank}$/**S3**$_{est}$
S1$_{\beta Gal}$/**S2**$_{galox}$/**S3**$_{blank}$
S1/**S2**/**S3**/free enzymes
S1/**S2**$_{galox}$/**S3**$_{est}$/free β-galactosidase
S1$_{\beta Gal}$/**S2**/**S3**$_{est}$/free galactose oxidase
S1$_{\beta Gal}$/**S2**$_{galox}$ /**S3**/free esterase

For the release experiments in the community **S1**/**S2**/**S3**/free enzymes, **S1**/**S2**$_{galox}$/**S3**$_{est}$/free β-galactosidase, **S1**$_{\beta Gal}$/**S2**/**S3**$_{est}$/free galactose oxidase and **S1**$_{\beta Gal}$/**S2**$_{galox}$ /**S3**/free esterase, **S1**, **S2** and **S3** (3 mg·mL^{-1}, 2.25 mg·mL^{-1} and 0.75 mg·mL^{-1}, respectively) were placed in a recipient with β-galactosidase (0.006 U·mL^{-1}), galactose oxidase (0.62 U·mL^{-1}) and/or esterase (0.82 U·mL^{-1}). The results are plotted in Figure 7 (main text).

Efficiency experiments

The same experimental procedure as described above for the "*Circular communication experiments*" was followed. The same concentrations of nanoparticles and inputs (3 mg·mL^{-1} of **S1**$_{\beta gal}$, 2.25 mg·mL^{-1} of **S2**$_{galox}$, 0.75 mg·mL^{-1} of **S3**$_{est}$ and 50 mM of input) were also employed in suspensions of:

1) **S1**$_{\beta Gal}$ with no input + 2% of EtOH - [blank]
2) **S1**$_{\beta Gal}$ + TCEP 50 mM + 2% of EtOH - [set as 100% efficiency]
3) **S3**$_{est}$/**S1**$_{\beta Gal}$ + methyl 4-(bromomethyl)benzoate 50 mM + 2% of EtOH - [sequence **3-1**]
4) **S2**$_{galox}$/**S3**$_{est}$/**S1**$_{\beta Gal}$ + galactose 50 mM + 2% of EtOH - [sequence **2-3-1**]
5) **S1**$_{\beta Gal}$/**S2**$_{galox}$/**S3**$_{est}$ + lactose 50 mM + 2% of EtOH - [sequence **1-2-3-1**]

The communication efficiency of each sequence (Figure 8A in main text) was calculated by relativizing the output (amount of cargo delivered) of the sequence to the maximum possible output (cargo released from suspension 2 set as 100% efficiency) and considering the blank as background level:

$$Relativization\ (\%): \frac{Output\ signal\ (a.u.) - blank\ signal\ (a.u.)}{(100\%\ efficiency\ signal\ (a.u.) - blank\ signal\ (a.u.)} \ x\ 100$$

Based on these experiments, we calculated the efficiency of each connection process (Process efficiency) in the circular communication system (Figure 8B in main text) by applying the following set of equations:

*% Communication efficiency **1-2-3-1** = % Efficiency [**1-2** process] x % Efficiency [**2-3** process] x % Efficiency [**3-1** process] x 10^{-4}*

*% Communication efficiency **2-3-1** = % Efficiency [**2-3** process] x % Efficiency [**3-1** process] x 10^{-2}*

*% Communication efficiency **3-1** = % Efficiency [**3-1** process]*

In order to determinate the chemical information loss, we represented in Figure S15 the difference between the maximum ideal communication efficiency (100%) and the obtained efficiency value for each sequence [**1-2-3-1** (**S1**$_{\beta gal}$-**S2**$_{galox}$-**S3**$_{est}$-**S1**$_{\beta gal}$), **2-3-1** (**S2**$_{galox}$-**S3**$_{est}$-**S1**$_{\beta gal}$) and **3-1** (**S3**$_{est}$-**S1**$_{\beta gal}$)] at 24h (see Figure 8A in the manuscript).

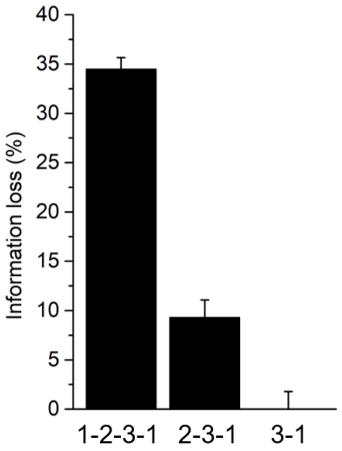

Figure S15. Representation of the chemical information loss in each sequence of the communication system after 24h. Error bars correspond to the s.d. from two independent experiments.

Boolean logic table

Table S4. Summary of the behaviour of the circular communication network in Boolean logic terms. The presence or absence of the input (lactose), encapsulated cargo or enzymes immobilized on the nanoparticles is represented by "1" (presence) and "0" (absence), respectively. The output signal is considered 0 when the normalized quantification of the $[Ru(bpy)_3]Cl_2$ fluorescence intensity is less than 30% of that found for the complete network.

Entry	(External trigger) Lactose	β-gal	Galox	(Cargo 2) Benzoate derivative	Esterase	(Cargo 3) TCEP	(Output) $[Ru(bpy)_3]Cl_2$ release
1	0	0	0	0	0	0	0
2	0	0	0	0	0	1	0
3	0	0	0	0	1	0	0
4	0	0	0	0	1	1	0
5	0	0	0	1	0	0	0
6	0	0	0	1	0	1	0
7	0	0	0	1	1	0	0
8	0	0	0	1	1	1	0
9	0	0	1	0	0	0	0
10	0	0	1	0	0	1	0
11	0	0	1	0	1	0	0
12	0	0	1	0	1	1	0
13	0	0	1	1	0	0	0

Entry	(External trigger) Lactose	β-gal	Galox	(Cargo 2) Benzoate derivative	Esterase	(Cargo 3) TCEP	(Output) $[Ru(bpy)_3]Cl_2$ release
14	0	0	1	1	0	1	0
15	0	0	1	1	1	0	0
16	0	0	1	1	1	1	0
17	0	1	0	0	0	0	0
18	0	1	0	0	0	1	0
19	0	1	0	0	1	0	0
20	0	1	0	0	1	1	0
21	0	1	0	1	0	0	0
22	0	1	0	1	0	1	0
23	0	1	0	1	1	0	0
24	0	1	0	1	1	1	0
25	0	1	1	0	0	0	0
26	0	1	1	0	0	1	0
27	0	1	1	0	1	0	0
28	0	1	1	0	1	1	0
29	0	1	1	1	0	0	0
30	0	1	1	1	0	1	0
31	0	1	1	1	1	0	0
32	0	1	1	1	1	1	0
33	1	0	0	0	0	0	0
34	1	0	0	0	0	1	0
35	1	0	0	0	1	0	0
36	1	0	0	0	1	1	0
37	1	0	0	1	0	0	0
38	1	0	0	1	0	1	0
39	1	0	0	1	1	0	0
40	1	0	0	1	1	1	0
41	1	0	1	0	0	0	0
42	1	0	1	0	0	1	0
43	1	0	1	0	1	0	0
44	1	0	1	0	1	1	0
45	1	0	1	1	0	0	0
46	1	0	1	1	0	1	0
47	1	0	1	1	1	0	0
48	1	0	1	1	1	1	0
49	1	1	0	0	0	0	0
50	1	1	0	0	0	1	0
51	1	1	0	0	1	0	0
52	1	1	0	0	1	1	0
53	1	1	0	1	0	0	0

Entry	(External trigger) Lactose	β-gal	Galox	(Cargo 2) Benzoate derivative	Esterase	(Cargo 3) TCEP	(Output) $[Ru(bpy)_3]Cl_2$ release
54	1	1	0	1	0	1	0
55	1	1	0	1	1	0	0
56	1	1	0	1	1	1	0
57	1	1	1	0	0	0	0
58	1	1	1	0	0	1	0
59	1	1	1	0	1	0	0
60	1	1	1	0	1	1	0
61	1	1	1	1	0	0	0
62	1	1	1	1	0	1	0
63	1	1	1	1	1	0	0
64	1	1	1	1	1	1	1

Table S5. Relative dye release when a component of the system is missing.

Missing element	Relative output (%)
-	100 ± 2.0
Lactose (External trigger)	19.6 ± 5.2
β-galactosidase	16.2 ± 3.1
Galactose oxidase	16.4 ± 3.0
Benzoate derivative (Cargo 2)	25.6 ± 12.0
Esterase	29.3 ± 1.0
TCEP (Cargo 3)	25.6 ± 7.2

Supplementary references

1. T. M. Godoy-Reyes, A. Llopis-Lorente, A. García-Fernández, P. Gaviña, A. M. Costero, R. Villalonga, F. Sancenón and R. Martínez-Máñez, *Org. Chem. Front.* **2019**, *6*, 1058.
2. J. A. Turkevich, P. C. Stevenson and J. Hillier, *Discuss. Faraday Soc.* **1951**, *11*, 55.
3. G. Frens, *Nat. Phys. Sci.* **1973**, *241*, 20.
4. R. Villalonga, P. Díez, A. Sánchez, E. Aznar, R. Martínez-Máñez and J. M. Pingarrón, *Chem. Eur. J.* **2013**, *19*, 7889.
5. K. L. Kelly, E. Coronado, L. L. Zhao and G. C. Schatz, *J. Phys. Chem. B* **2003**, *107*, 668.

Chapter 5. An Interactive Model of Communication between Abiotic Nanodevices and Microorganisms

An Interactive Model of Communication between Abiotic Nanodevices and Microorganisms

Beatriz de Luis,[a,b] Antoni Llopis-Lorente,[a,b] Paola Rincón,[a,b] José Gadea,[e] Félix Sancenón,[a,b] Elena Aznar,[a,b] Reynaldo Villalonga,[f] José Ramón Murguía,[a,b] and Ramón Martínez-Máñez*[a,b,c,d]

[a] Instituto Interuniversitario de Investigación de Reconocimiento Molecular y Desarrollo Tecnológico (IDM), Universitat Politècnica de València, Universitat de València, Camino de Vera s/n, 46022 Valencia, Spain. E-mail: rmaez@qim.upv.es

[b] CIBER de Bioingeniería, Biomateriales y Nanomedicina (CIBER-BBN), Spain.

[c] Unidad Mixta UPV-CIPF de Investigación en Mecanismos de Enfermedades y Nanomedicina, Universitat Politècnica de València, Centro de Investigación Príncipe Felipe, Valencia, Spain.

[d] Unidad Mixta de Investigación en Nanomedicina y Sensores, Universitat Politècnica de València, Instituto de Investigación Sanitaria La Fe, Valencia, Spain

[e] Instituto de Biología Molecular y Celular de Plantas (IBMCP), Universitat Politècnica de València, UPV-Consejo Superior de Investigaciones Científicas (CSIC), Valencia, Spain.

[f] Nanosensors & Nanomachines Group, Department of Analytical Chemistry, Faculty of Chemistry, Complutense University of Madrid, Madrid, Spain.

Published online: August 19, 2019

(Reprinted with permission from *Angew. Chem. Int. Ed.* **2019**, *58*, 14986.

5.1 Abstract

The construction of communication models at the micro-/nanoscale involving abiotic nanodevices and living organisms has the potential to open a wide range of applications in biomedical and communication technologies. However, this area remains almost unexplored. Herein, we report, as a proof of concept, a stimuli-responsive interactive paradigm of communication between yeasts (as a model microorganism) and enzyme-controlled Janus Au-mesoporous silica nanoparticles. In the presence of the stimulus, the information flows from the microorganism to the nanodevice, and then returns from the nanodevice to the microorganism as a feedback.

5.2 Introduction

The exchange of information by means of chemical messengers is the way of communication used by nature.[1,2] However, despite its potential to enable future technologies, the design of communication systems capable of transmitting information using chemical messengers between different micro/nanoscale entities is not an easy task and remains almost unexplored.[3] An appealing application in this field is to develop communication protocols of living cells with abiotic nanodevices.[4] Biological entities intrinsically react to their environment by means of molecular communication paths decoding the received stimuli and adapting to new conditions.[5] On the other hand, advances in nanoarchitectonics, materials science, and synthetic biology can provide the tools to design smart ensembles capable of translating a wide array of (bio)chemical stimuli into encoded messages for the next member of the information chain.[6] Recently, abiotic lipid vesicle-based protocells, microdroplets or fusion protein assemblies capable of

translating molecular information from the environment into a response from bacteria have been developed,[7] yet, similar systems using nanoparticles have not been reported.

In communication theory terms, communication is the process in which information is transmitted from one point to another.[8] In the linear model, the sender converts information into a code and this message is decoded by the receiver on another point. In the interactive model, a more sophisticated strategy, there is a feedback process (Scheme 1). First, a message is encoded by the sender and transmitted to the decoding receiver. Straightaway, the functions are reversed, and the receiver encodes and transmits a response to the original sender, which now acts as receiver. This two-way process facilitates building consortia between different populations to target a common goal.

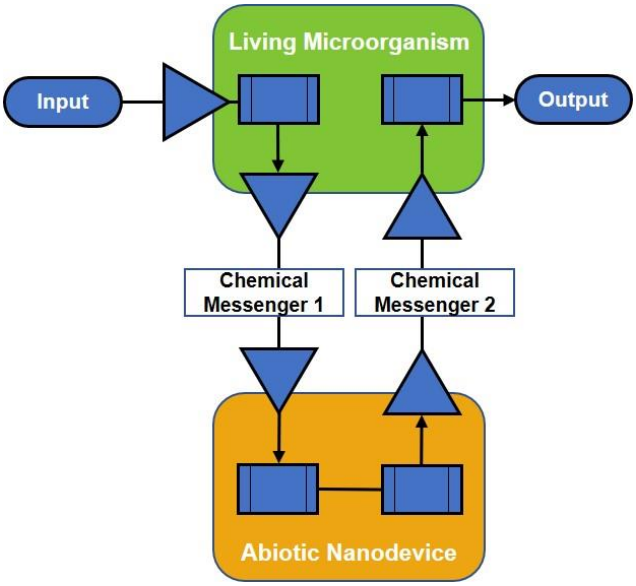

Scheme 1. The proposed interactive model of communication between living microorganisms and abiotic nanodevices represented as a flowchart as used in telecommunications.

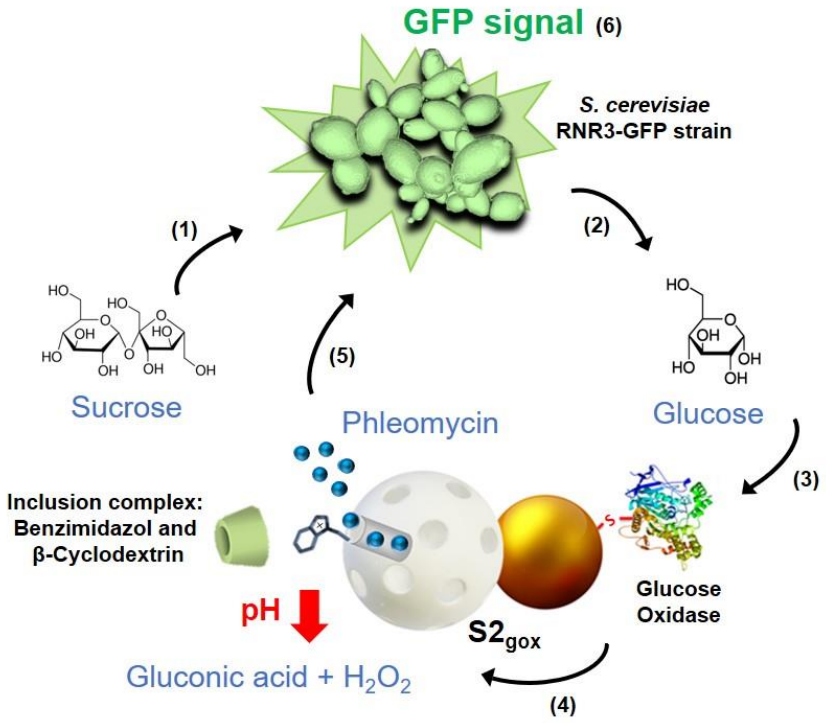

Scheme 2. Illustration of the sucrose-responsive interactive system of communication between GFP-expressing *S. cerevisiae* yeasts and Janus Au-mesoporous silica nanoparticles.

Herein, we present, to the best of our knowledge, the first interactive model of communication between living microorganisms (budding yeast *Saccharomyces cerevisiae*) and abiotic nanodevices (enzyme-controlled Janus Au-mesoporous silica nanoparticles), in which a molecular communication cascade is triggered in response to an environmental stimulus. The expression of green fluorescent protein (GFP) in the cytoplasm of *S. cerevisiae* cells[9] is produced as the output signal of the communication system. As illustrated in Scheme 2, this biunivocal communication (that is, two-way, one-to-one) starts with the input of sucrose (1), which is detected and transformed by yeasts into glucose and fructose (2). Glucose acts as chemical messenger that is then transmitted and sensed by glucose oxidase (GOx) on the abiotic nanodevice (3). Transformation of glucose to

gluconic acid induces the opening of the molecular gates on the mesoporous nanocarrier (4). Subsequently, phleomycin (a second chemical messenger) is released as a feedback message (5) to the microorganism that decodes the information and activates GFP transcription (6) producing a fluorescent signal.

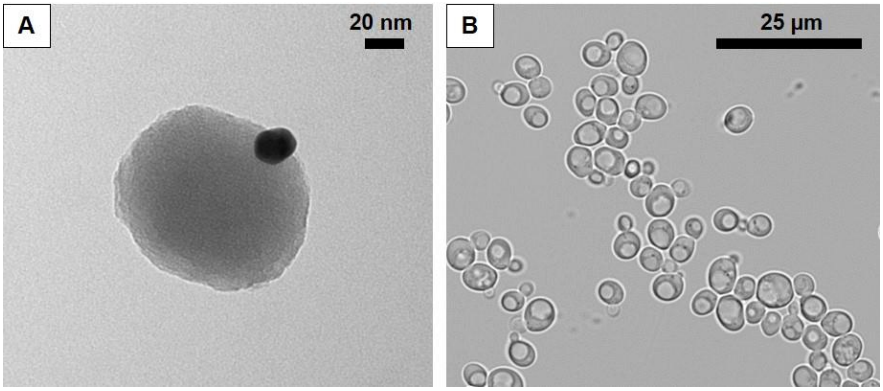

Figure 1. A) Transmission electron microscopy (TEM) image of a Janus Au-mesoporous nanoparticle. B) Transmitted light image of *S. cerevisiae* budding yeasts obtained by confocal microscopy.

We used budding yeast as a eukaryotic cell model of easy handling and manipulation.[10] Yeast cells avoid the internalization of nanoparticles unless permeability treatments such as electroporation, high temperature incubation, and presence of monovalent cations are applied.[11] This fact assures that the interaction process occurs by molecular communication through the medium and not as a result of nanoparticle internalization. The yeast strain used in our studies expresses GFP under the control of the RNR3 promoter. RNR3 gene transcription is induced upon exposure to DNA-damaging agents such as phleomycin.[12] As a nanodevice capable of producing a programmed response when a specific stimulus is present, we used a Janus Au-mesoporous silica architecture, the double-face nature of which allows designing systems with a double receiver-sender behaviour (Figure 1).[13] In particular, we used nanoparticles functionalized with GOx enzyme on the

gold face and a pH-responsive supramolecular nanovalve on the mesoporous face consisting of an inclusion complex between benzimidazole and β-cyclodextrin. Local gluconic acid produced by GOx in the presence of glucose causes the protonation of benzimidazole group ($pK_a = 5.55$)[14] and therefore the dethreading of the complex leading to the delivery of the entrapped cargo. Although biomimetic protocells have been previously used in communication processes, the use of mesoporous silica scaffolds offers additional appealing properties, such as high thermal and chemical stability, large loading capacity, versatility regarding the nature of cargos and a variety of molecular, and supramolecular gatekeepers which can be used for developing future communication systems.[15]

5.3 Results and discussion

In a first step, after nanoparticle preparation and characterization (see Supporting Information), we tested the ability of the nanodevice to recognize glucose and release the cargo with dye ($[Ru(bpy)_3]Cl_2$)-loaded nanoparticles (**S1$_{gox}$**). With this aim, we monitored cargo release from **S1$_{gox}$** in aqueous solution at pH 7.5 in absence and presence of glucose (1 mM). Delivery studies showed negligible cargo release in absence of glucose whereas the presence of the input led to opening of pores and a remarkable release of the dye (Figure S8). Moreover, we confirmed that no other monosaccharides and disaccharides induced cargo delivery from **S1$_{gox}$** (Figure S10).

Next, we evaluated the linear yeast-nanodevice communication pathway by combining yeast and **S1$_{gox}$** in water at pH 7.5, as an initial key step to build the interactive model of communication. Dye release was monitored by fluorescence spectroscopy in the absence and presence of the input (sucrose 2%). As shown in Figure 2, the results validate the establishment of a linear communication pathway

between the microorganism and the nanodevice in the presence of sucrose (blue curve, 74.8% release efficiency). In contrast, no dye release was triggered in the absence of sucrose (red curve) nor in the presence of sucrose and absence of yeast (black curve). This sucrose-recognition capability is ascribed to the abundance of invertase enzyme in the periplasmic space and cell walls of *S. cerevisiae*[16] (catalysing the hydrolysis of sucrose into fructose and glucose) and the subsequent connection with the glucose-responsive nanocarriers. Moreover, we also demonstrated that the $[Ru(bpy)_3]Cl_2$ released in these experiments did not induce significant toxicity in yeast cells (Figure S11).

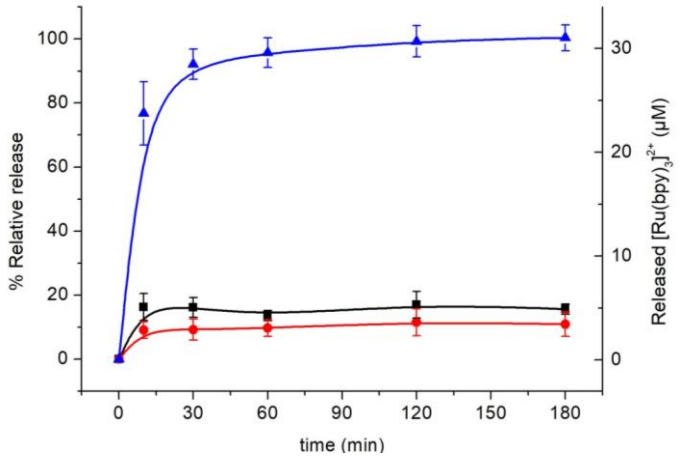

Figure 2. Kinetics of $[Ru(bpy)_3]Cl_2$ release from **S1$_{gox}$** in aqueous solution containing yeasts at pH 7.5 in the absence (red) and presence (blue) of sucrose (2%). A negative control (only sucrose and nanoparticles) was also tested (black). Error bars correspond to the s.d. from three independent experiments.

On a further step towards the construction of the interactive model of communication, we prepared nanoparticles loaded with the genotoxin phleomycin, which was expected to act as a feedback messenger to close the communication loop. Delivery kinetics (Figure S9) from the phleomycin-loaded nanodevice (**S2$_{gox}$**) were determined by measuring phleomycin absorbance at 300 nm in presence and

absence of glucose. After 3 h, the supernatants were added to fresh *S. cerevisiae* cultures (inoculated in yeast extract peptone dextrose (YPD) medium) and the mixtures were shaken at 28 °C for two hours. Then, the GFP signal expression was evaluated by confocal microscopy. Positive and negative control experiments were performed by adding or not free phleomycin to yeast cultures and incubating for two hours. A similar fluorescent response was obtained from yeast treated with free phleomycin and treated with phleomycin released from **S2$_{gox}$** in the presence of glucose (Figure S12). These results confirmed the potential of the nanodevice **S2$_{gox}$** to induce GFP expression in yeast upon glucose-induced delivery.

Encouraged by these findings, we addressed the complete interactive communication model in which the microorganism and the nanodevice **S2$_{gox}$** were expected to exchange chemical messengers through an aqueous medium. Yeast microorganisms were inoculated in fresh YPD and incubated until reaching mid-log exponential phase. Then, yeasts were washed three times and resuspended in YPD medium without glucose. For the final experiments, aqueous solutions at pH 7.5 containing the nanodevice **S2$_{gox}$** were mixed with yeast suspensions. Then, 1% sucrose (input) was added as the energy source necessary for gene expression in yeasts[17] and initiator of the communication network. Same experiments were performed with nanoparticles **S2** (lacking the GOx enzyme) as control. Confocal microscopy images showed that the communication system displayed a clear GFP-associated fluorescence when **S2$_{gox}$** was present (Figure 3a and Figure S13a), whereas the fluorescent signal was negligible when **S2** (lacking GOx) was used (Figure 3b and Figure S13b).

Quantification of the GFP-associated fluorescence intensity by analysis of confocal images revealed a marked 8-fold enhancement in cell emission for the complete yeast-**S2$_{gox}$** communication system (Figure 3c). As additional control experiments, we prepared nanodevice **S3$_{gox}$** (lacking the cargo) and nanodevice **S3**

(lacking both the cargo and GOx enzyme). No communication and therefore no GFP expression was observed when these nanoparticles were used (Figure S14). Altogether, confocal imaging experiments demonstrated that only in the presence of all components of the communication network, the GFP output signal was achieved. The behaviour of this interactive communication system between yeasts and nanoparticles can be summarized in a Boolean logic table (Table 1, see also Table S4), which corresponds to a 4-input 3-level AND logic gate (Scheme 3).

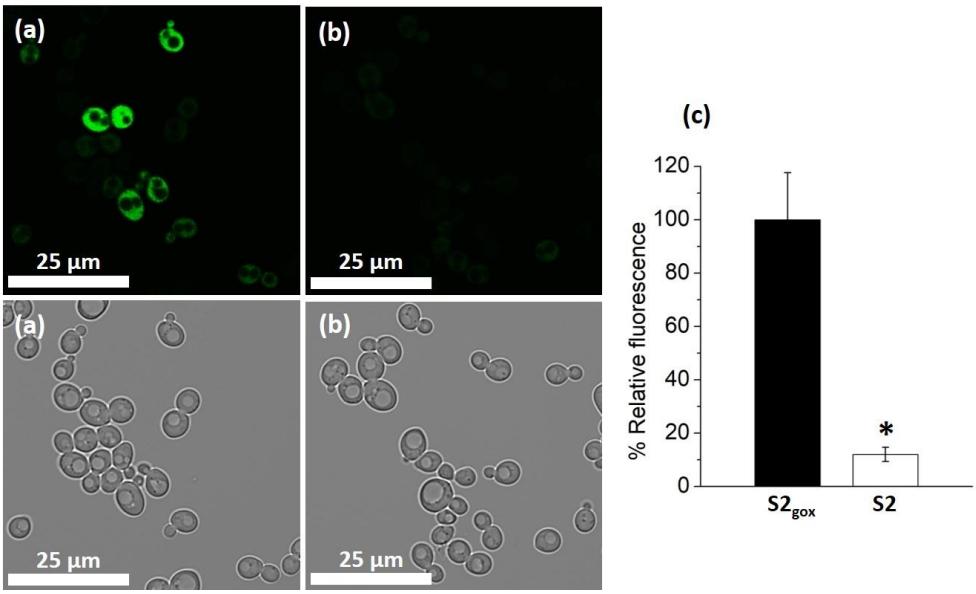

Figure 3. GFP signal induction in *S. cerevisiae* cells examined by confocal microscopy after 2 h for a) incubation with **S2$_{gox}$** and sucrose 1% and b) incubation with **S2** and sucrose 1%. Top, fluorescence images; bottom, transmission images. Additional images are provided in the Supporting Information (Figure S13). c) Normalized quantification of the GFP-associated fluorescence intensity for the two different treatments. Several fields of each condition in three independent experiments were analyzed obtaining similar results. Data represent the mean ± s.e.m. of three independent experiments (*$p < 0.01$).

Table 1. Summary of the behaviour of the communication system in Boolean logic notation. Presence of a component is represented as 1 and absence as 0. In the presence of the stimulus (1), the output signal (1) is only produced when all components are present. The output signal is considered 0 when the normalized quantification of the GFP-associated fluorescence intensity is less than 20% of that found for the complete systems, that is, Input 1, Yeast 1, Enzyme 1 and Cargo 1.

Input[a]	**Yeast**[b]	**Enzyme**[c]	**Cargo**[d]	**Output**[e]
0	1	1	1	0
1	0	1	1	0
1	1	0	1	0
1	1	1	0	0
0	0	1	1	0
0	1	0	1	0
0	1	1	0	0
1	0	0	1	0
1	0	1	0	0
1	1	0	0	0
1	0	0	0	0
0	1	0	0	0
0	0	1	0	0
0	0	0	1	0
0	0	0	0	0
1	1	1	1	1

[a] Sucrose 1 % [b] *S. cerevisiae* budding yeast [c] glucose oxidase in capped nanoparticles [d] phleomycin as cargo in capped nanoparticles [e] GFP fluorescent signal.

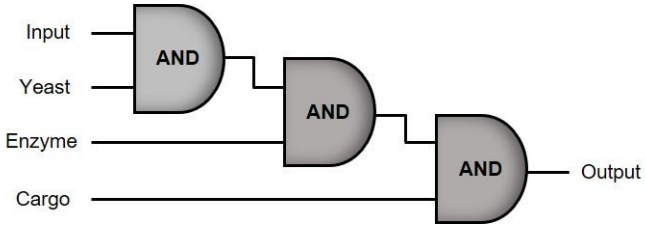

Scheme 3. 4-input 3-level AND logic gate corresponding to the logic Table 1 describing the behaviour of the communication system.

5.4 Conclusions

In conclusion, we have developed an interactive model of communication between abiotic nanodevices and living microorganisms. The information obtained by the sender (yeast cell) from the surroundings (sucrose as stimulus) is processed and transmitted to the receiver (nanoparticles), which in turn is capable of decoding the information and transmitting a response back to the original sender. This communication network employs enzymatic reactions and chemical messengers. In spite of being a proof of concept, these findings demonstrate how abiotic nanodevices and living microorganisms can be connected using molecular communication yielding systems with a collective behaviour. In addition, considering the large variety of molecules produced and secreted by living microorganisms, which can be processed by enzymatic receptors as well as the numerous different species potentially susceptible to be encapsulated in mesoporous silica nanoparticles, we believe that the proposed communication network represents a general versatile paradigm, which can inspire future research towards the development of novel technologies based on communication at the nanoscale. We also envision that the combination of different enzymes integrated on the same nanodevice could mimic the biological cascade necessary to synthesize *in situ* bioactive or functional molecules from precursors present in the environment, produced by organisms or released from the mesoporous support. Such *in situ*-produced bioactive or functional molecules could be implemented into the information network further increasing the scope of the proposed communication paradigm. Moreover, we also believe that the idea of tailoring synthetic nanodevices[18] and making them capable of communicating with cells can have impact in the design of new sensors, new strategies for diagnosis and personalized therapeutics.[19]

Acknowledgements. B. de L. is grateful to the Spanish Government for her FPU PhD fellowship. The authors wish to thank the Spanish Government (projects RTI2018-100910-B-C41 (MCUI/AEI/FEDER, UE) and CTQ2017-87954-P), the Generalitat Valenciana (project PROMETEO2018/024), the Comunidad de Madrid (Project IND2017/BMD-7642) and CIBER-BBN (NANOCOM project) for support.

5.5 References

1. a) B. Alberts, A. Johnson, J. Lewis, D. Morgan, M. Raff, K. Roberts, P. Walter in *Molecular Biology of the Cell*, 6th Ed., Garland Science, **2015**; b) C. M. Waters, B. L. Bassler, *Annu. Rev. Cell Dev. Biol.* **2005**, *21*, 319-346; c) J. Fleischer, J. Krieger. *Front. Cell Neurosci.* **2018**, *12*, 425; d) S. Nahavandi, S.-Y. Tang, S. Baratchi, R. Soffe, S. Nahavandi, K. Kalantar-zadeh, A. Mitchell, K. Khoshmanesh, *Small* **2014**, *10*, 4810-4826.
2. a) I. F. Akyildiz, F. Brunetti, C. Blánzquez, *Comp. Netw.* **2008**, *52*, 2260-2279; b) G. Li-Destri, L. Fichera, A. Zammataro, G. T. Sfrazzetto, N. Tuccitto, *Nanoscale* **2019**, 11, 14203-14209; c) N. Tuccitto, G. Li-Destri, G. M. L. Messina, G. Marletta, *Phys. Chem. Chem. Phys.* **2018**, *20*, 30312-30320.
3. A. Llopis-Lorente, P. Díez, A. Sánchez, M. D. Marcos, F. Sancenón, P. Martínez-Ruiz, R. Villalonga, R. Martínez-Máñez, *Nano Today* **2018**, *18*, 8-11.
4. a) J. L. Marzo, J. M. Jornet, M. Pierobon, *Curr. Drug Targets* **2019**, *20*, 800-807; b) E. J. Kwon, J. H. Lo, S. N. Bhatia, *PNAS* **2015**, *112*, 14460-14466; c) Y. Benenson, *Nat. Rev. Genet.* **2012**, *13*, 455-468.
5. a) D. Barcena Menendez, V. R. Senthivel, M. Isalan, *Curr. Opin. Biotechnol.* **2015**, *31*, 101-107; b) D. Malak, O. B. Akan, *Nano. Commun. Netw.* **2012**, 3, 19-35.
6. a) M. Komiyama, K. Yoshimoto, M. Sisido, K. Ariga, *Bull. Chem. Soc. Jpn*. **2017**, *90*, 967-1004; b) P. Stano, G. Rampioni, P. Carrara, L. Damiano, L. Leoni, P. L. Luisi *BioSystems* **2012**, *109*, 24-34; c) A. Llopis-Lorente, P. Díez, A. Sánchez, M. D. Marcos, F. Sancenón, P. Martínez-Ruiz, R. Villalonga, R. Martínez-Máñez, *Nat. Comm*. **2017**, *8*, 15511; d) C. Giménez, E. Climent, E. Aznar, R. Martínez-Máñez, F. Sancenón, M. D. Marcos, P. Amorós, K. Rurack, *Angew. Chem. Int. Ed.* **2014**, *53*, 12629-12633; e) R. Lentini, N. Y. Martín, S. S. Mansy, *Curr. Opin. Chem. Biol*. **2016**, *34*, 53-61; f) Y. Ding, L. E. Contreras-Llano, E. Morris, M. Mao, C. Tan, *ACS Appl. Mater. Interfaces* **2018**, *10*, 30137-30146; g) K. Ariga, X. Jia, J. Song, C.-T. Hsieh, S.-h. Hsu, *ChemNanoMat*. **2019**, *5*, 692-702.
7. a) R. Lentini, S. Perez Santero, F. Chizzolini, D. Cecchi, J. Fontana, M. Marchioretto, C. Del Bianco, J. L. Terrell, A. C. Spencer, L. Martini, M. Forlin, M. Assfalg, M. Dalla Serra, W. E. Bentley, S. S. Mansy, *Nat. Comm*. **2014**, *5*, 4012; b) R. Lentini, N. Y. Martín, M. Forlin, L. Belmonte, J. Fontana, M. Cornella, L. Martini, S. Tamburini, W. E. Bentley, O. Jousson, S. S. Mansy, *ACS Cent. Sci.* **2017**, *3*, 117-123; c) G. Rampioni, F. D'Angelo, M. Messina, A. Zennaro, Y. Kuruma, D. Tofani, L. Leoni, P. Stano, *Chem. Comm.* **2018**, *54*, 2090-2093; d) M. Schwarz-Schilling, L. Aufinger, A. Mückl, F. C. Simmel, *Integr. Biol.* **2016**, *8*, 564-570; e) R. Fernandes, V. Roy, H.-C. Wu, W. E. Bentley, *Nat. Nanotechnol.* **2010**, *5*, 213-217; f) A. Gupta, J. L. Terrell, R. Fernandes, M. B. Dowling, G. F. Payne, S. R. Raghavan, W. E. Bentley, *Biotechnol Bioeng*. **2012**, *110*, 552-562.

8. J. S. Chitode in *Communication Theory*, Technical Publications, Pune, **2010**.
9. W.-K. Huh, J. V. Falvo, L. C. Gerke, A. S. Carroll, R. W. Howson, J. S. Weissman, E. K. O'Shea, *Nature* **2003**, *425*, 686-691.
10. S. M. Burgess, T. Powers, J. C. Mell, *eLS* **2017**, DOI: 10.1002/9780470015902.a0000821.pub2.
11. a) N. Mas, I. Galiana, S. Hurtado, L. Mondragón, A. Bernardos, F. Sancenón, M. D. Marcos, P. Amorós, N. Abril-Utrillas, R. Martínez-Máñez, J. R. Murguía, *Int. J. Nanomed*. **2014**, *9*, 2597-2606; b) A. Agostini, L. Mondragón, A. Bernardos, R. Martínez-Máñez, M. D. Marcos, F. Sancenón, J. Soto, A. Costero, C. Manguan-García, R. Perona, M. Moreno-Torres, R. Aparicio-Sanchis, J. R. Murguía*, Angew. Chem. Int. Ed.* **2012**, *51*, 10556-10560.
12. Y. Endo-Ichikawa, H. Kohno, R. Tokunagat, S. Taketani, *Biochem. Pharmacol.* **1995**, *50*, 10, 1695-1699.
13. R. Villalonga, P. Díez, A. Sánchez, E. Aznar, R. Martínez-Máñez, J. M. Pingarrón, *Chem. Eur. J.* **2013**, *19*, 7889-7894.
14. G. Jerez, G. Kaufman, M. Prystai, S. Schenkeveld, K. K. Donkor, *J. Sep. Sci.* **2009**, *32*, 1087-1095.
15. a) E. Aznar, M. Oroval, L. Pascual, J. R. Murguía, R. Martínez-Máñez, F. Sancenón, *Chem. Rev.* **2016**, *116*, 561-718.
16. P. M. Gomes Barbosa, T. Pereira de Morais, C. A. de Andrade Silva, Fl R. da Silva Santos, N. F. Lisbo Garcia, G. G. Fonseca, R. S. Ribeiro Leite, M. F. da Paz, *Prep. Biochem. Biotechnol.* **2018**, *48*, 506-513.
17. M. P. Ashe, S. K. De Long, A. B. Sachs, *Mol. Biol. Cell* **2000**, *11*, 833-848.
18. a) K. Ariga, D. T. Leong, T. Mori, *Adv. Funct. Mater.* **2018**, *28*, 1702905; b) K. AC. Xu, S. Hu, X. Chen, *Mater. Today* **2016**, *19*, 516-532.
19. a) S. Hauert, S. N. Bhatia, *Trends Biotechnol*. **2014**, *32*, 448-455; b) I. F. Akyildiz, M. Pierobon, S. Balasubramaniam, *Proc. IEEE* **2019**, *107*, 858-865; c) S. G. Hays, W. G Patrick, M. Ziesack, N. Oxman, P. A. Silver, *Curr. Opin. Biotechnol*. **2015**, *36*, 40-49; d) F. Peng, Y. Tu, D. A. Wilson, *Chem. Soc. Rev.* **2017**, *46*, 5289-5310; e) E. Morris, M. Chavez and C. Tan, *Curr. Opin. Biotechnol.* **2016**, *39*, 97-104; f) F. Peng, Y. Tu, J. C. M. van Hest, D. A. Wilson, *Angew. Chem.* **2015**, *127*, 11828-11831.

5.6 Supporting Information

Chemicals

Tetraethyl orthosilicate (TEOS), *n*-cetyltrimethylammonium bromide (CTABr), sodium hydroxide (NaOH), gold(III) chloride trihydrate ($HAuCl_4 \cdot 3H_2O$), sodium citrate tribasic dihydrate, (3-mercaptopropyl) trimethoxysilane, paraffin wax, tris(2,2'-bipyridyl)dichlororuthenium(II) hexahydrate $[Ru(bpy)_3]Cl_2 \cdot 6H_2O$, phleomycin from *Streptomyces verticillus*, 3-mercaptopropionic acid, (3-iodopropyl) trimethoxysilane, benzimidazole, triethylamine, β-cyclodextrin, glucose oxidase from *Aspergillus niger*, *N*-(3-dimethylaminopropyl)-*N*'-ethylcarbodiimide hydrochloride (EDC), *N*-hydroxysuccinimide (NHS), D-(+)-glucose, D-(+)-saccharose, D-(+)-galactose, D-(−)-fructose, D-(+)-lactose monohydrate, 2,2'-azino-bis(3-ethylbenzothiazoline-6-sulfonic acid) diammonium salt (ABTS) and peroxidase from horseradish (HRP) were purchased from Sigma-Aldrich. Sodium sulfate anhydrous, sodium dihydrogen phosphate monohydrate, disodium hydrogen phosphate heptahydrate, ethanol, chloroform, toluene and acetonitrile were provided by Scharlau. Bacteriological peptone and yeast extract were purchased from Conda Lab. Agar was purchased from Sigma-Aldrich.

Yeast strain and culture conditions

RNR3-GFP *Saccharomyces cerevisiae* yeast strain used in this study was purchased from Life Technologies. It was obtained by tagging RNR3 (systematic name YIL066C) open reading frame (ORF) through oligonucleotide-directed homologous recombination.[1] The genotype of the parent haploid of the *S. cerevisiae* yeast strain used (ATCC 201388) is: MATα his3Δ1 leu2Δ0 met15Δ0 ura3Δ0. Standard methods for yeast culture and manipulation were used.

General methods

Powder X-ray diffraction (PXRD), transmission electron microscopy (TEM), N_2 adsorption-desorption isotherms, UV-visible and fluorescence spectrophotometry, dynamic light scattering (DLS) and elemental analysis techniques were employed for materials characterization. PXRD measurements were performed on a Seifert 3000TT diffractometer using CuKα radiation at low angles ($1.3 < 2\theta < 8.3$, with steps of 0.04 degrees and 3 seconds for step) and high angles ($35 < 2\theta < 80$ with steps of 0.04 degrees and 1 second for step). TEM images were acquired using a JEOL TEM-1010 Electron microscope working at 100 kV. Additionally, TEM coupled with energy dispersive X-ray spectroscopy (TEM-EDX) was used for element mapping using a JEOL TEM-2100F microscope. DLS studies were performed using a ZetaSizer Nano ZS (Malvern). N_2 adsorption-desorption isotherms were recorded on a Micromeritics TriStar II Plus automated analyzer. Samples were previously degassed at 90 °C in vacuum overnight and measurements were performed at 77 °K. UV-visible spectra were recorded with a JASCO V-650 Spectrophotometer. Fluorescence measurements were carried out in a JASCO FP-8500 Spectrophotometer. Elemental analysis was performed using a LECO CHNS-932 Elemental Analyzer. Confocal microscopy imaging was performed employing a Leica TCS SPE (Leica Microsystems Heidelberg GmbH) inverted laser scanning confocal microscope using oil objective HC PL APO 40x.

Synthesis of mesoporous silica nanoparticles (MSNPs)

1.00 g (2.74 mmol) of *n*-cetyltrimethylammonium bromide (CTABr) was dissolved in 480 mL of deionized water. Then, the pH was basified by adding 3.5 mL of a 2 $mol \cdot L^{-1}$ NaOH solution and the temperature was increased to 80 °C. Next, tetraethyl orthosilicate (TEOS) (5 mL, 22.4 mmol) was added dropwise into the solution. Magnetic stirring was kept for 2 hours to give a white suspension. Finally,

the solid was isolated by centrifugation, washed several times with water until neutral pH and dried at 70 °C overnight (as-synthesized **MSNPs**). To obtain the final mesoporous nanoparticles MCM-41 type (**MSNPs**), the as-synthesized solid was calcined at 550 °C in an oxidant atmosphere for 5 hours in order to remove the surfactant.

Synthesis of gold nanoparticles

Gold nanoparticles were synthesized following the Turkevich-Frens method.[2] 100 mL of a 0.3 mM $HAuCl_4 \cdot 3H_2O$ solution were brought to 135 °C under stirring and refluxing. Then, 1.5 mL of a 1 % sodium citrate solution was added to yield gold nanoparticles of *ca.* 20 nm. The initially pale-yellow colour turned to purple-black and finally red wine in 10 minutes. After this, the colloidal suspension was cooled to room temperature under stirring. This protocol was repeated 4 times until obtaining 400 mL of the colloidal gold nanoparticles suspension.

Synthesis of Janus Au-MS nanoparticles (S0)

180 mg of mesoporous silica nanoparticles MCM-41 type (**MSNPs**) were dispersed in 9 mL of an aqueous solution (6.7 % ethanol) followed by addition of *n*-cetyltrimethylammonium bromide (CTABr, 1 μM). The mixture was heated at 75 °C, and then 1 g of paraffin wax was added. Once the paraffin was melted, the mixture was vigorously stirred for 15 minutes using a homogenizer (Ultra-Turrax T-8, IKA). Then, the mixture was further stirred for 1 hour at 75 °C using a magnetic stirrer. The resulting Pickering emulsion was then cooled to room temperature, diluted with 10 mL of methanol and reacted with 200 μL of (3-mercaptopropyl) trimethoxysilane for 3 hours. The solid was collected by centrifugation and washed with methanol. For gold attachment, the partially mercapto-functionalized nanoparticles were dispersed in 68 mL of methanol and added over the 400 mL of

the colloidal gold nanoparticles suspension previously synthesized. The mixture was stirred overnight at room temperature. Then, the solid was isolated by filtration and exhaustively washed with chloroform and hexane. The solid was dried and ground. This process finally yielded the Janus Au-MS nanoparticles (**S0**).

Synthesis of S1

For the preparation of **S1**, 60 mg of **S0** were suspended in a concentrated solution of $[Ru(bpy)_3]Cl_2 \cdot 6H_2O$ (25 mg) in anhydrous acetonitrile (4 mL), and stirred overnight in order to achieve the loading of the pores. Then, the suspension was treated with 60 µL of (3-iodopropyl) trimethoxysilane for 5.5 hours. The solid was isolated by centrifugation, washed with acetonitrile and dried at 70 °C overnight. To functionalize the surface with benzimidazole moieties, 0.25 g of benzimidazole and 990 µL of triethylamine were mixed with 20 mL of toluene and heated for 20 min at 80 °C in order to prepare a saturated solution of benzimidazole. 10 mL of this suspension were added over 60 mg of the previously prepared nanoparticles. The mixture was stirred at 80 °C for three days. Afterward, the benzimidazole-functionalized solid was isolated by centrifugation and washed with toluene. To protect the gold face, 60 mg of the resulting solid was suspended in 5 mL of acetonitrile and reacted with 50 µL of 3-mercaptopropionic acid for 1 hour. This solid (**S0-benz**) was centrifuged, washed with toluene and with water and let to dry at 70 °C overnight. Next, the solid was suspended with 20 mg of β-cyclodextrin in 12.5 mL of 50 mM sodium phosphate buffer at pH 7.5 and stirred overnight. Finally, the suspension was centrifuged, washed thoroughly with 50 mM phosphate buffer at pH 7.5 and dried under vacuum. This process finally yielded the final solid **S1**.

Synthesis of $S1_{gox}$

8 mg of **S1** were suspended in 2 mL of 50 mM sodium phosphate buffer at pH 7.5. Then, 2 mg of *N*-(3-dimethylaminopropyl)-*N'*-ethylcarbodiimide hydrochloride (EDC), 2 mg of *N*-hydroxysuccinimide (NHS) and 1 mg of the enzyme glucose oxidase were added and the suspension was stirred overnight at 10 °C. The solid was isolated by centrifugation and washed several times with cold 50 mM sodium phosphate buffer (pH 7.5). The resulting $\mathbf{S1_{gox}}$ was kept wet in refrigerator until use.

Synthesis of S2

Solid **S2** was prepared following the same procedure described for **S1** but the loading process was carried out after the benzimidazole and 3-mercaptopropionic functionalization. 10 mg of the benzimidazole-functionalized solid was then suspended in 1 mL of a concentrated solution in ultrapure H_2O of the antibiotic phleomycin (10 mg, 6.5 mM) and stirred overnight at 10 °C. The solid was isolated by centrifugation and washed with cold ultrapure H_2O. The β-cyclodextrin capping was conducted following the same procedure described for **S1.** This process finally yielded the final solid **S2**, which was kept in refrigerator until use.

Synthesis of $S2_{gox}$

Solid $\mathbf{S2_{gox}}$ was prepared from **S2** following the same procedure described for $\mathbf{S1_{gox}}$. The resulting $\mathbf{S2_{gox}}$ was kept wet in refrigerator until use.

Synthesis of S3

Solid **S3** was prepared following the same procedure described for **S1** but the mesoporous container was not loaded.

Synthesis of $S3_{gox}$

Solid $\mathbf{S3_{gox}}$ was prepared from solid **S3** following the same procedure described for $\mathbf{S1_{gox}}$. The resulting $\mathbf{S3_{gox}}$ was kept wet in refrigerator until use.

Materials Characterization

Solids were characterized by standard techniques.

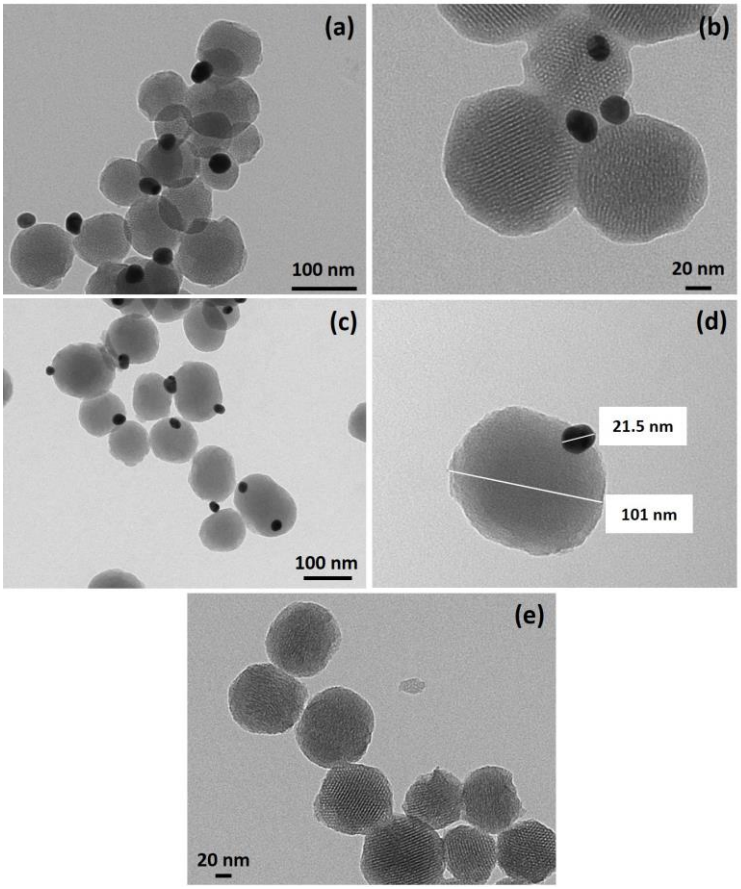

Figure S1. TEM images of the Janus Au-MS nanoparticles **S0** (a-d) and the **calcined MSNPs** (e).

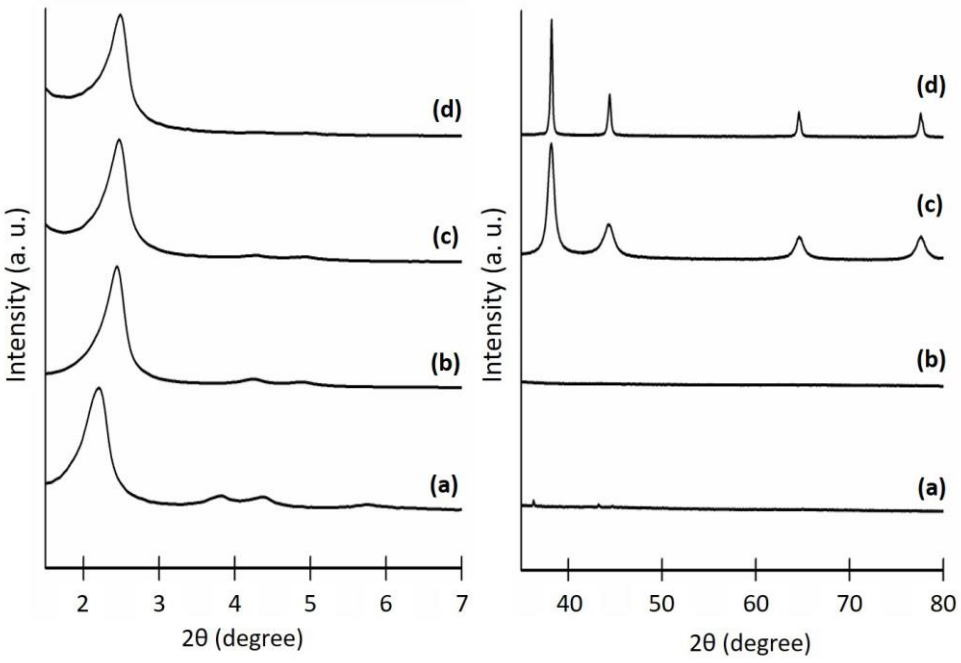

Figure S2. Powder X-ray diffraction patterns of the solids (a) **as-made MSNPs**, (b) **calcined MSNPs**, (c) Janus Au-MS nanoparticles **S0** and (d) solid **S1** at low (left) and high (right) angles.

Figure S2 shows powder X-ray diffraction patterns at low ($1.5 < 2\theta < 7$) and at high angles ($35 < 2\theta < 80$). At low angles, the **as-made MSNPs** (mesoporous silica nanoparticles) shows characteristic low-angle reflections. For the **calcined MSNPs**, we observed a slight displacement of the peaks related to the condensation of silanol groups during the calcination process. The low-angle typical peaks are preserved in the Janus Au-MS nanoparticles **S0** (c). The presence of the (100) peak in the PXRD patterns in the solid **S1** (d) indicated that the different chemical modifications, functionalization and cargo loading had not damaged the mesoporous structure. Moreover, the high-angle diffraction pattern of the Janus colloids **S0** and **S1** showed the cubic gold characteristic (111), (200), (220) and (331) diffraction peaks, confirming the presence of gold nanocrystals and the Janus Au-MS architecture.[3] Powder X-ray diffraction pattern of $\mathbf{S1_{gox}}$ was not obtained due to

the low quantity collected in the synthesis but the enzyme immobilization procedure is not expected to affect the mesoporous structure. Similar results in terms of characterization were obtained for solids **S2**, **S2$_{gox}$**, **S3** and **S3$_{gox}$** (data not shown).

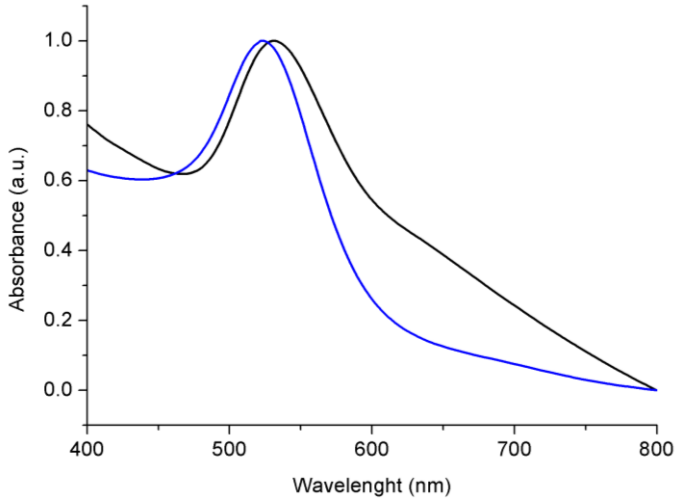

Figure S3. Normalized UV-Visible spectra of the gold nanoparticles (blue) and Janus Au-MS nanoparticles **S0** (black).

UV/vis measurements in aqueous solution were performed on the as-synthesized gold nanoparticles and on Janus Au-MS nanoparticles **S0** (by suspending 1 mg of solid in 1 mL of distilled water). The starting gold colloid shows a single absorption band at 522 nm, characteristic of the surface plasmon resonance of spherically shaped nanospheres with a diameter of *ca.* 20 nm (Figure S3). In the **S0** spectrum, there is a redshift of the absorbance maximum (533 nm) and a broadening of the band. These two facts are ascribed to the increase in the refractive index around the gold nanospheres due to the MS attachment and to light refraction produced by silica.[4]

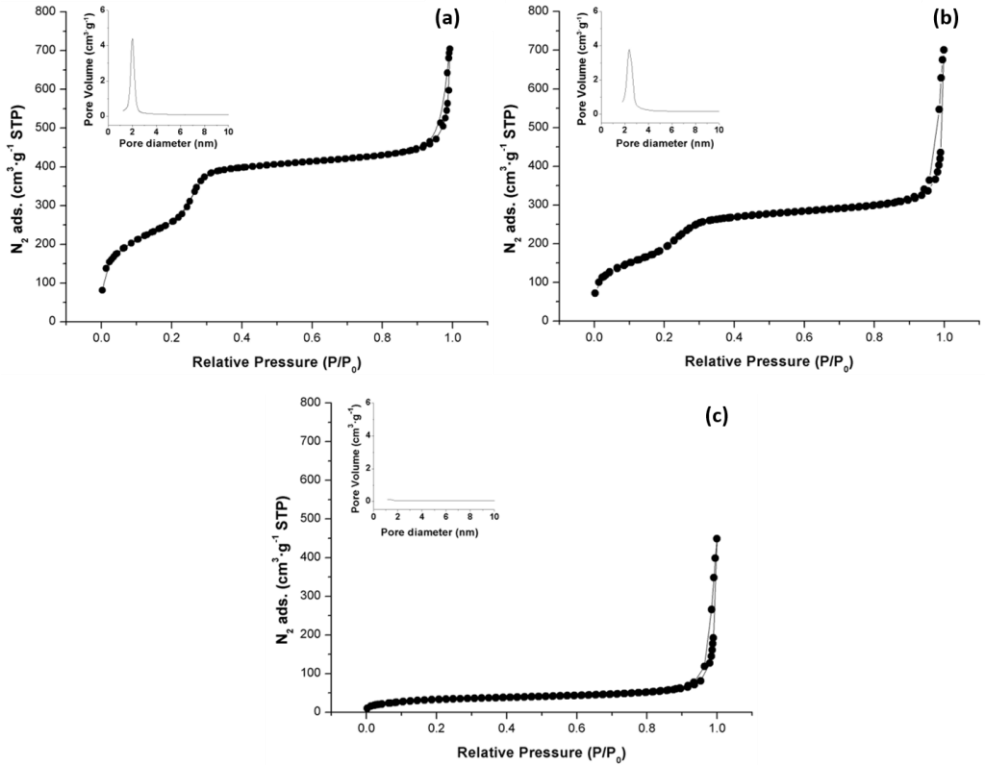

Figure S4. The N_2 adsorption-desorption isotherms for (a) the **calcined MSNPs**, (b) Janus Au-MS nanoparticles **S0** and (c) the loaded solid **S1**.

The N_2 adsorption-desorption isotherms (Figure S4) of the **calcined MSNPs** and Janus Au-MS nanoparticles **S0** show an adsorption step at intermediate P/P_0 value 0.3, which is characteristic for mesoporous solids with empty pores. This step is related to the nitrogen condensation inside the mesopores by capillarity. The absence of a hysteresis loop in this interval and the narrow BJH pore distribution suggest the existence of uniform cylindrical mesopores. Application of the BET model results in a value for the total specific surface of 950 $m^2 \cdot g^{-1}$ for **calcined MSNPs** and 693 $m^2 \cdot g^{-1}$ for Janus Au-MS nanoparticles **S0** as a consequence of the attachment of non-porous gold nanoparticles. Total specific surface area for **S1** significantly decreased to 124 $m^2 \cdot g^{-1}$ due to the cargo loading inside the mesopores.

In order to calculate pore size and total pore volume, BJH model was applied for $P/P_0 < 0.6$ (associated to adsorption inside the pores). N_2 adsorption-desorption isotherm for the functionalized and loaded solid **S1** shows a significant decrease in N_2 volume adsorbed and are flat when compared (at the same scale) to those from **MSNPs** and **S0**. This indicates that there is a significant pore blocking accordingly the loading and capping processes. BET specific values, pore volumes and pore sizes calculated from N_2 adsorption-desorption isotherms for **MSNPs**, Janus Au-MS nanoparticles **S0** and solid **S1** are listed in Table S1.

Table S1. BET specific surface values, pore volumes and pore sizes calculated from N_2 adsorption-desorption isotherms for selected materials.

Solid	S_{BET} [$m^2 \cdot g^{-1}$]	Pore Volume [$cm^3 \cdot g^{-1}$]	Pore size [nm]
Calcined MSNPs	950 ± 4	0.73	2.41
S0	693 ± 10	0.51	2.44
S1	124 ± 2	0.06	-

The hydrodynamic size and zeta potential of different solids were measured by dynamic light scattering (DLS) studies (Table S2, Figure S5). For carrying out the experiments, the corresponding materials were suspended in distilled water at pH 7 at a concentration of 0.01 $mg \cdot mL^{-1}$.

Table S2. Zeta potential (mV) and hydrodynamic size (nm) data.

Solid	Zeta Potential (mV)	Hydrodynamic Size (nm)
Calcined MSNPs	-31.5	114
S0	-30.4	127
S0-benz	-13.0	132
S1	-29.8	148
$S1_{gox}$	-34.9	156

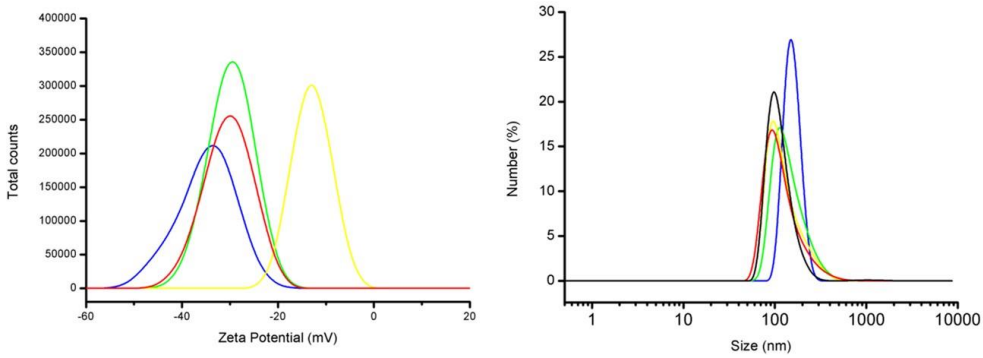

Figure S5. Zeta potential (left, mV) and hydrodynamic size (right, nm) graphic representations of **MSNPs** (black), Janus Au-MS nanoparticles **S0** (red), benzimidazole functionalized solid **S0-benz** (yellow), **S1** solid (green) and **$S1_{gox}$** (blue).

From elemental analysis data (Table S3), composition of solids was calculated. Considering the data obtained from the analysis of the unloaded and uncapped solid **S0-benz**, the amount of molecular gate $(CH_2)_3$-benzimidazole was determined as 23.3 mg·g^{-1}. The amount of $[Ru(bpy)_3]Cl_2$ loaded and β-CD content in **S1** was estimated to be 57.2 mg·g^{-1} and 11.9 mg·g^{-1}, respectively.

Table S3. Elemental analysis data.

Solid	% C	% H	% N
S0-benz	2.54	1.96	0.41
S1	5.50	1.61	1.16

The content of phleomycin encapsulated in **S2** and **S2$_{gox}$** was estimated by measuring the absorbance of the phleomycin in solution (λ_{abs} = 300 nm) before and after the capping process as well as all the washing steps until yielding the final solid. The calibration curve indicates an amount of 110.5 mg of phleomycin per g of **S2** and 72.1 mg per g of **S2$_{gox}$**.

The immobilization of the enzyme was confirmed by running an enzyme activity assay. The method we used in order to test glucose oxidase activity is based on the oxidation of glucose by glucose oxidase which gives gluconic acid and hydrogen peroxide. Then, hydrogen peroxide reacts with ABTS (2,2'-azino-bis(3-ethylbenzothiazoline-6-sulfonic acid) diammonium salt) in the presence of peroxidase (HRP) to form a blue-green product ($ABTS^{\cdot+}$) that can be followed UV-visible spectrophotometry (λ_{abs} = 418 nm).

Reactions for assaying glucose oxidase activity:

$$D\text{-}glucose + O_2 + H_2O \xrightarrow{\text{Glucose oxidase}} D\text{-}gluconic\ acid + H_2O_2$$

$$H_2O_2 + ABTS \xrightarrow{\text{HRP}} ABTS^{\cdot+} + H_2O$$

In a typical experiment, 250 µL of 1 M of glucose (180 mg·mL^{-1}), 250 µL of ABTS solution (1 mg·mL^{-1}) and 50 µL of HRP solution (2 mg·mL^{-1}) were placed in a quartz cuvette. All solutions have been prepared in 100 mM sodium phosphate buffer at pH 7.5. Then, 10 µL of either buffer (for blank), commercial enzyme solution in buffer (0.01 mg·mL^{-1}) or **S1$_{gox}$** suspension (5 mg·mL^{-1}) were added. The mixture was shaken and absorbance at 418 nm was monitored as a function of time.

Whereas no change was observed in the absence of nanoparticles or commercial enzyme, a strong blue-green colour appeared in the presence of those. The increase in absorbance ($ABTS^{\cdot+}$ formation) as a function of time in the presence of **S1$_{gox}$** and the commercial enzyme solution is depicted in Figure S6.

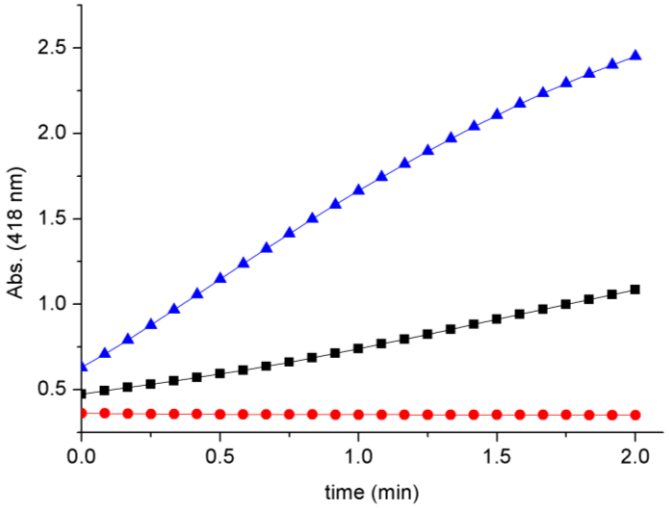

Figure S6. Absorbance at 418 nm ($ABTS^{\cdot+}$ formation) due to glucose oxidase activity on nanoparticles **S1$_{gox}$** (black), commercial enzyme solution (blue) and blank (red).

Enzyme activity on the nanoparticles was calculated by applying:

$$\frac{Enzyme\ Units}{g} = \frac{(\Delta - \Delta_{blank}) \cdot V_T \cdot F_D}{\varepsilon_{ABTS} \cdot l \cdot V_S \cdot C_S}$$

Where, Δ is the slope of the graph (min^{-1}), Δ_{blank} is the slope of the graph for the blank (min^{-1}), V_T is the total volume in the cuvette, F_D is the dilution factor, ε_{ABTS} is the molar extinction of ABTS at 418 nm (36,000 $M^{-1} \cdot cm^{-1}$), l is the optical path in the cuvette (1 cm), V_S is the volume of the sample added (mL), C_S is the concentration of sample added (g/mL).

The activity of glucose oxidase on **S1$_{gox}$** was determined to be 0.48 U per mg of solid whereas the activity of commercial glucose oxidase was determined to be 145.55 U per mg of commercial enzyme. From this data, the corresponding

amount of glucose oxidase on **S1$_{gox}$** was estimated to be 3.32 mg of enzyme per g of solid.

TEM-EDX mapping of the gold side of the nanodevice **S1$_{gox}$** shows that this area is rich in sulfur atoms indicating the preferential localization of the enzyme in the gold face. The presence of nitrogen atoms in the whole scaffold is attributed to the immobilized enzyme (gold face) as well as the benzimidazole moiety of the molecular gate (mesoporous silica face) (see Figure S7).

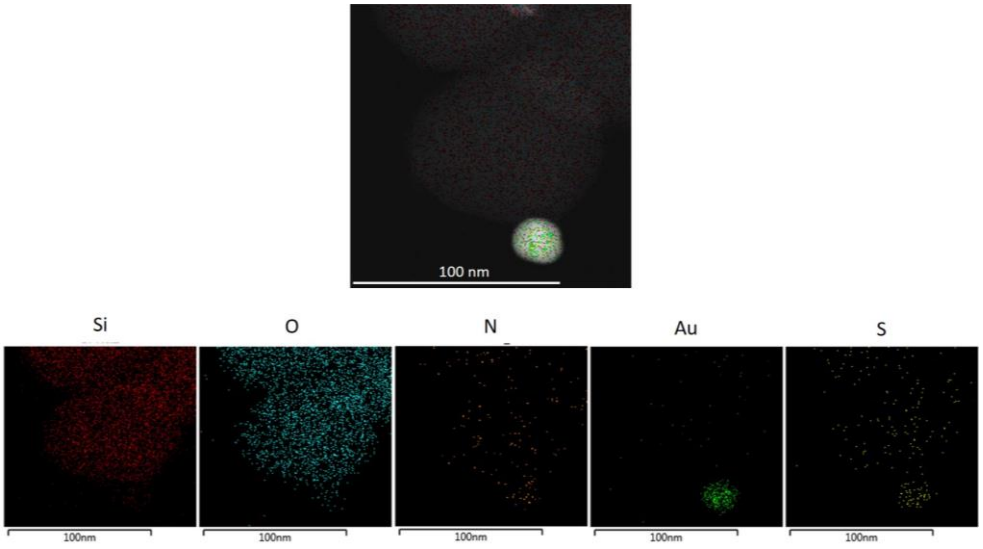

Figure S7. TEM-EDX element mapping of the gold region in the nanodevice **S1$_{gox}$**. Top: mapped area with layered atom composition. Bottom: mapping of different atoms.

Nanodevice sensing-actuating behaviour

Delivery studies

For release experiments of **S1$_{gox}$**, the corresponding refrigerated solution of nanoparticles was washed with an aqueous solution (pH 7.5, 20 mM Na_2SO_4), divided into two fractions and brought to a final concentration of 1 mg·mL^{-1}. Both fractions were incubated for 1 hour. Then, inputs (sulphate for blank and glucose

for sample) were added (time = 0 minutes) and samples were shaken over time. Aliquots were taken at scheduled times, centrifuged (2 minutes, 12000 rpm) to remove the nanoparticles and the absorbance of the solution at 595 nm measured ($[Ru(bpy)_3]Cl_2$ λ_{exc} = 453 nm, λ_{em} = 595 nm).

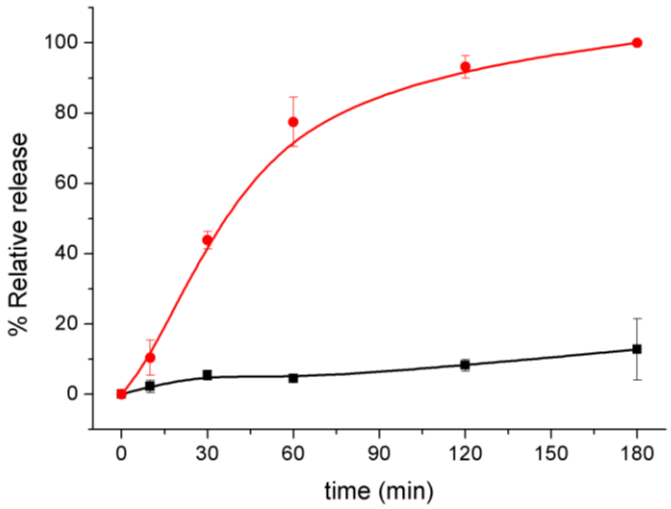

Figure S8. Normalized cargo release from **S1$_{gox}$** in the absence of input (black curve) and in the presence of glucose (red curve). Substrate added at 1 mM final concentration. Error bars correspond to the s.d. from three independent experiments.

For release experiments from **S2$_{gox}$,** the corresponding refrigerated solution of nanoparticles was washed with ultrapure water (pH 7.5), divided into two fractions and brought to a final concentration of 2.5 mg·mL^{-1}. Both fractions were incubated for 1 hour. Then, inputs (ultrapure water for blank and glucose for sample) were added (time = 0 minutes) and samples were shaken over time. Aliquots were taken at scheduled times, centrifuged to remove the nanoparticles (2 minutes, 12000 rpm) and the absorbance at 300 nm of the solution measured (phleomycin λ_{abs} = 300 nm).

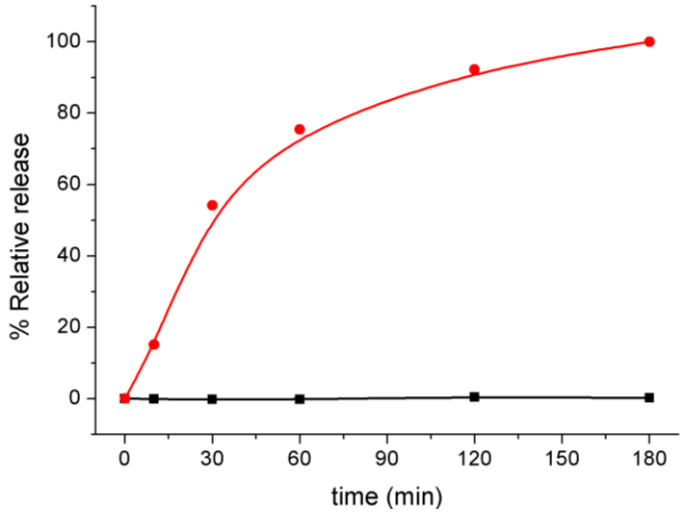

Figure S9. Normalized cargo release from **S2$_{gox}$** in the absence of input (black curve) and in the presence of glucose (red curve). Substrate added at 1 % final concentration (55.5 mM).

Selectivity in cargo delivery experiments

A refrigerated solution of **S1$_{gox}$** nanoparticles was washed with an aqueous solution (pH 7.5, 20 mM Na_2SO_4), divided into six fractions and brought to a final concentration of 1 mg·mL^{-1}. All fractions were incubated for 1 hour. Then, inputs (monosaccharides and disaccharides) were added (time = 0 minutes) and samples were shaken over time. Aliquots were taken after 3 hours, centrifuged to remove the nanoparticles (2 minutes, 12000 rpm) and the absorbance of the solution at 595 nm measured ($[Ru(bpy)_3]Cl_2$ λ_{exc} = 453 nm, λ_{em} = 595 nm).

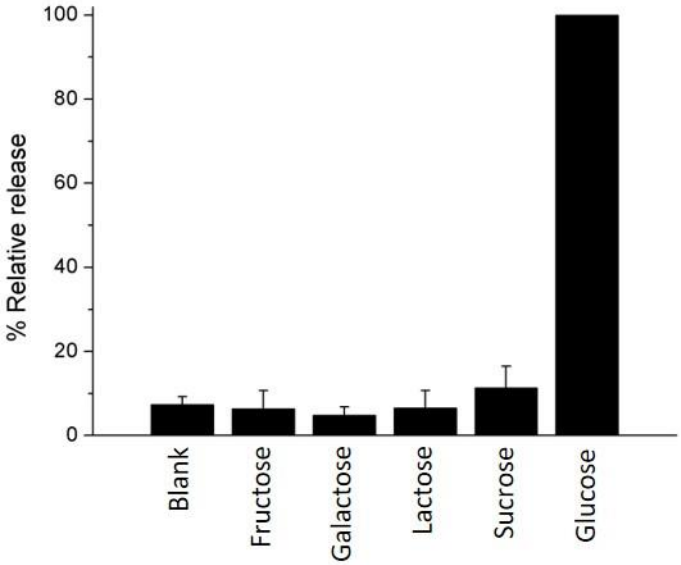

Figure S10. Normalized cargo release from **S1$_{gox}$** in the presence of different monosaccharides and disaccharides at 1 mM final concentration. Error bars correspond to the s.d. from three independent experiments.

Experiments with *S. cerevisiae*

Delivery studies in yeast-S1$_{gox}$ mixtures

A refrigerated solution of **S1$_{gox}$** was washed with ultrapure water (pH 7.5), divided into different fractions and brought to a final concentration of 1 mg·mL^{-1}. Parallelly, a refrigerated saturated culture (10^8 cells/mL) of *Saccharomyces cerevisiae* budding yeasts RNR3-GFP were washed with ultrapure water (pH 7.5) and concentrated to $1.5 \cdot 10^8$ cells/mL in each of the corresponding fractions. All fractions were incubated for 1 hour and then, inputs (ultrapure water for blank and sucrose at 2% of final concentration, 58.4 mM, for sample) were added (time = 0 minutes). Samples were shaken at 28 °C and aliquots were taken at scheduled times, centrifuged (2 minutes, 6000 rpm) the absorbance of the solution at 595 nm measured ($[Ru(bpy)_3]Cl_2$ λ_{exc} = 453 nm, λ_{em} = 595 nm).

Cell viability assays ([Ru(bpy)$_3$]Cl$_2$)

After incubation for 3 hours with different concentrations of [Ru(bpy)$_3$]Cl$_2$ in continuous shaking at 28 °C, yeast samples were diluted and approximately 300 cells were seeded in each YPD agar plate. After incubation for 48 h at 28 °C, colony formation was quantified (viable colony formation units normalized by untreated yeasts [Ru(bpy)$_3$]Cl$_2$ 0 µM).

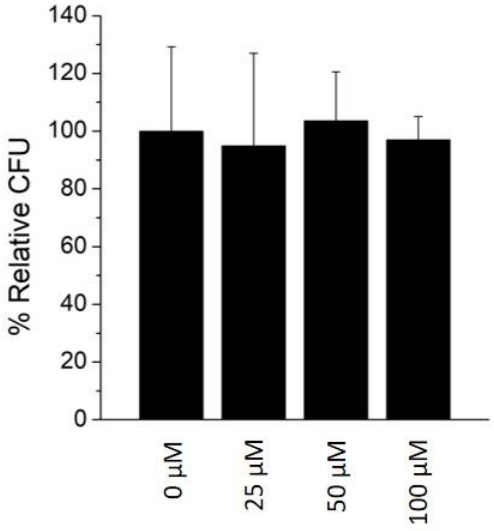

Figure S11. Cell viability assays of *S. cerevisiae* based on CFU counting. Samples were incubated with different concentrations of [Ru(bpy)$_3$]Cl$_2$ in presence of sucrose 2 %. Error bars correspond to the s.d. from two independent experiments.

Confocal fluorescence microscopy studies

S. cerevisiae RNR3-GFP were inoculated into fresh YPD (yeast extract peptone dextrose) and cultured for 4 hours at 28 °C in continuous shaking until reaching the log phase with an optical density (600 nm) of approximately 0.5.

- ***Studies of GFP-expression***

Aliquots of 2 mL of the freshly inoculated yeast suspension were centrifuged and concentrated to 150 µL. Then 50 µL of the supernatant of the release experiments of $\mathbf{S2_{gox}}$ in presence and absence of 1 % of glucose were added. Positive and negative controls were also carried out by adding or not free phleomycin (1.3 µM, 2 $\mu g \cdot mL^{-1}$). Samples were incubated in continuous shaking for two hours at 28 °C. Finally, the samples were centrifuged (2 minutes, 6000 rpm), washed two times with ultrapure water (pH 7.5) and the pellet was resuspended in 35 µL of ultrapure water.

Intracellular overexpression of green fluorescent protein (GFP) in yeasts was monitored by confocal microscopy (see Figure S12). In particular, the images were acquired employing a Leica TCS SPE inverted laser scanning confocal microscope using oil objective HC PL APO 40x with an excitation wavelength of 488 nm. Two-dimensional pseudo-colour images (255 colour levels) were gathered with a size of 1024x1024 pixels and Airy 1 pinhole diameter. Several fields of each condition in three independent experiments were performed obtaining similar results. Quantification of the fluorescence intensity was determined using ImageJ software.

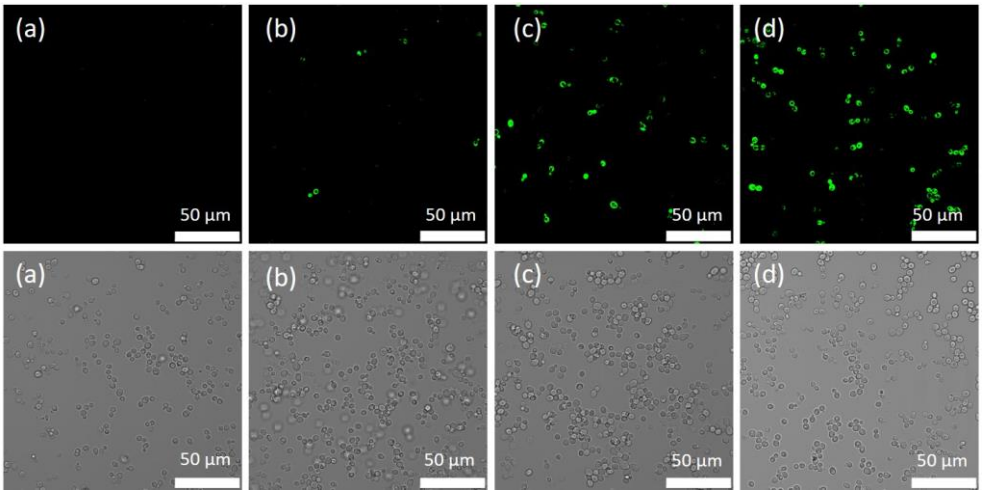

Figure S12. GFP signal induction in *Saccharomyces cerevisiae* cells examined by confocal microscopy after 2 hours for (a) negative control experiment (no phleomycin), (b) incubation with the supernatant from **S2$_{gox}$** suspensions, (c) incubation with the supernatant from **S2$_{gox}$**- glucose mixtures and (d) incubation with free phleomycin (1.3 µM (2 µg·mL^{-1}), positive control experiment). Above: fluorescence images, below: transmission images.

- ***Interactive communication experiments***

2 aliquots of 2 mL of the freshly inoculated yeast suspension were washed three times with YPD without glucose and resuspended in YPD without glucose medium at a pH of 7.5 until reaching 10 % of the total volume of the experiment. Parallelly, the refrigerated solutions of nanoparticles **S2** and **S2$_{gox}$** were washed three times with ultrapure water (pH 7.5), divided into the two fractions where yeasts have been already added and brought to a final concentration of 10 µg·mL^{-1}. Then, inputs at 1 % of final concentration (sucrose, 29.2 mM) were added and samples were incubated in continuous shaking for two hours at 28 °C. Finally, samples were centrifuged (2 minutes, 6000 rpm), washed two times with ultrapure water (pH 7.5) and the pellet was resuspended in 35 µL of ultrapure water.

Intracellular overexpression of green fluorescent protein (GFP) was measured and quantified as previously described (see Figure S13).

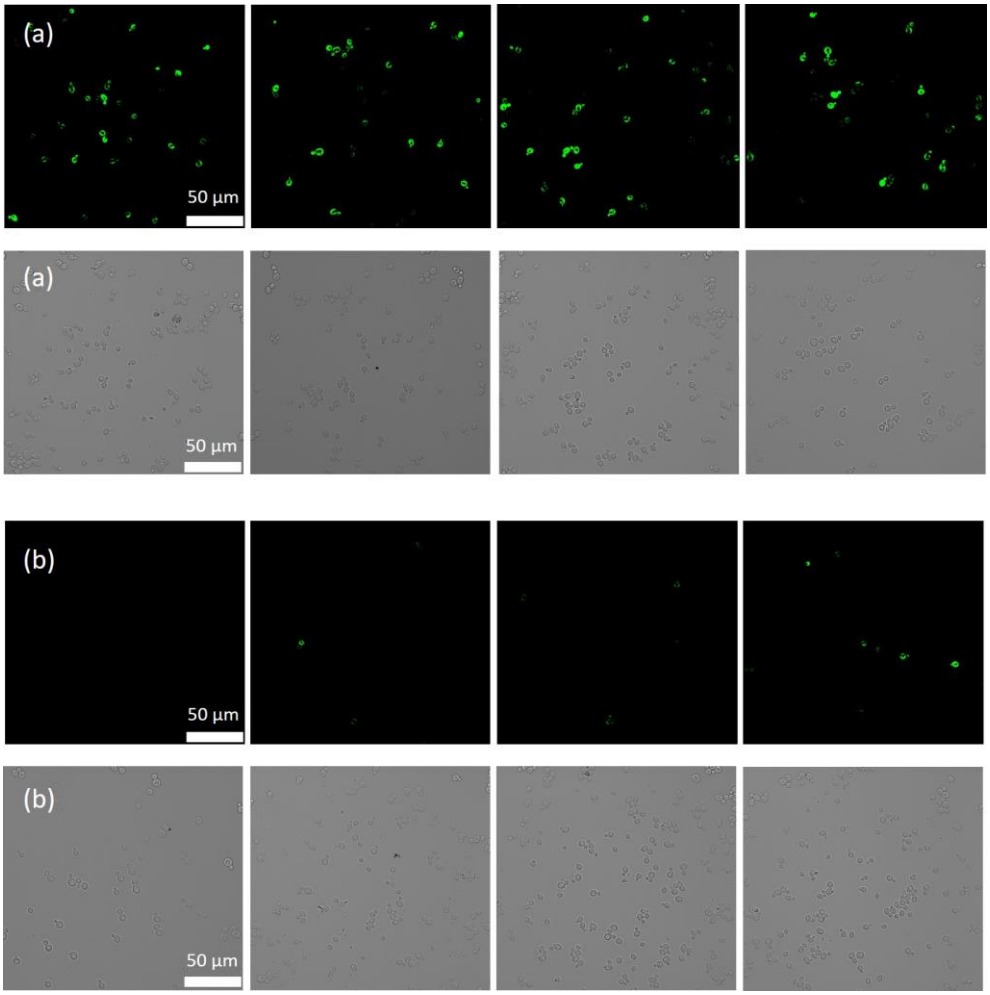

Figure S13. Confocal microscopy images of GFP signal induction in *Saccharomyces cerevisiae* cells after 2 hours for (a) incubation with **S2**$_{gox}$ and sucrose 1 % and (b) incubation with **S2** and sucrose 1 %. Above: fluorescence images, below: transmission images.

- ***Unloaded nanodevices studies***

The same procedure followed in the *Interactive communication experiments* was carried out but with unloaded solids **S3** and **S3$_{gox}$** (see Figure S14).

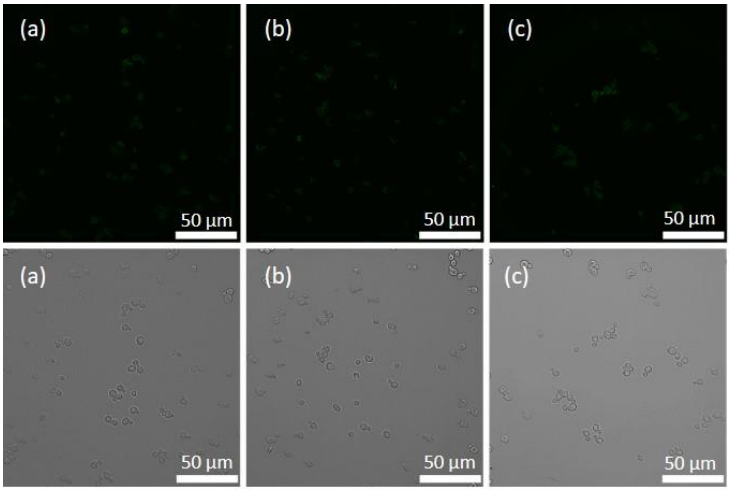

Figure S14. GFP signal induction in *S. cerevisiae* cells examined by confocal microscopy after 2 hours for (a) incubation without nanoparticles and with sucrose 1 % (b) incubation with **S3** and sucrose 1 % and (c) incubation with **S3$_{gox}$** and sucrose 1 %. Above: fluorescence images, below: transmission images.

Table S4. Summary of the confocal fluorescence microscopy studies of the yeast-nanoparticle communication system under different experimental conditions.

Input[a]	**Yeast**[b]	**Enzyme**[c]	**Cargo**[d]	**Output**[e]
+	+	–	–	–
+	+	+	–	–
+	+	–	+	–
+	+	+	+	+

[a] Sucrose 1 % [b] *S. cerevisiae* budding yeast [c] glucose oxidase in capped nanoparticles [d] phleomycin as cargo in capped nanoparticles [e] GFP fluorescent signal.

Cell viability assays (S3, $S3_{gox}$, S2 and $S2_{gox}$)

After incubation for 2 hours with the corresponding nanoparticles (**S3**, **$S3_{gox}$**, **S2** or **$S2_{gox}$**) in continuous shaking at 28 °C, yeast samples were centrifuged (2 minutes, 6000 rpm) and washed two times with ultrapure water (pH 7.5). Different dilutions were prepared and approximately 300 cells were seeded in each YPD agar plate. After incubation for 48 h at 28 °C, colony formation was quantified (viable colony formation units normalized by untreated yeasts NPs (-)).

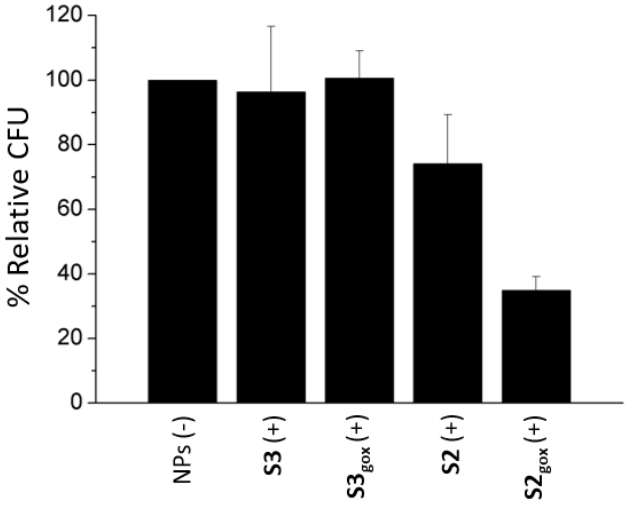

Figure S15. Cell viability assays of *S. cerevisiae* based on CFU counting. Samples were incubated without nanoparticles (negative control) or with different solids (**S3**, **$S3_{gox}$**, **S2** and **$S2_{gox}$**) at a concentration of 10 μg·mL^{-1} in presence of sucrose 1 %. Error bars correspond to the s.d. from three independent experiments.

Supplementary references

1. W-K. Huh, J.V. Falvo, L. C. Gerke, A. S. Carroll, R. W. Howson, J-S. Weissman and E. K. O'Shea, *Nature* **2003**, *425*, 686.
2. a) J. A. Turkevich, P. C. Stevenson and J. Hillier, *Discuss. Faraday Soc.* **1951**, *11*, 55; b) G. Frens, *Nat. Phys. Sci.* **1973***, 241,* 20*.*
3. A. Sánchez, P. Díez, P. Martínez-Ruíz, R. Villalonga and J. M. Pingarrón, *Electrochem. Commun.* **2013**, *30*, 51.
4. K. L. Kelly, E. Coronado, L. L. Zhao and G. C. Schatz, *J. Phys. Chem. B* **2003**, *107*, 66

Chapter 6. Nano-Programmed Cross-Kingdom Cell Communication

Nano-Programmed Cross-Kingdom Cell Communication

Beatriz de Luis,[a,b] Antoni Llopis-Lorente,[a,b] Javier Martínez-Latorre,[a,b] Félix Sancenón,[a,b] Carmelo López,[e] José Ramón Murguía,[a,b] and Ramón Martínez-Máñez[*a,b,c,d]

[a] Instituto Interuniversitario de Investigación de Reconocimiento Molecular y Desarrollo Tecnológico (IDM), Universitat Politècnica de València, Universitat de València, Camino de Vera s/n, 46022 Valencia, Spain. E-mail: rmaez@qim.upv.es

[b] CIBER de Bioingeniería, Biomateriales y Nanomedicina (CIBER-BBN), Spain.

[c] Unidad Mixta UPV-CIPF de Investigación en Mecanismos de Enfermedades y Nanomedicina, Universitat Politècnica de València, Centro de Investigación Príncipe Felipe, Valencia, Spain.

[d] Unidad Mixta de Investigación en Nanomedicina y Sensores, Universitat Politècnica de València, Instituto de Investigación Sanitaria La Fe, Valencia, Spain

[e] Instituto Universitario de Conservación y Mejora de la Agrodiversidad Valenciana, Universitat Politècnica de València (COMAV-UPV), Valencia, Spain.

Submitted

6.1 Abstract

The engineering of chemical communication at the micro/nanoscale is a key emergent topic in micro/nanotechnology, synthetic biology and related areas. However, the field is still in its infancy – previous advances, although scarce, have mainly focused on communication between abiotic micro/nanosystems or between microvesicles and living cells. Here, we have implemented a nano-programmed cross-kingdom communication involving two different cell types as well as tailor-made nanodevices acting as "nanotranslators". Information flows from the sender cells (bacteria) to the nanodevice and from the nanodevice to receiver cells (yeasts) in a hierarchical way, allowing communication between two microorganisms that otherwise would not interact.

6.2 Introduction

Living systems react to molecular signals in their environment via evolved biochemical sensory pathways that determine their adaptability, functioning and survival.[1] Moreover, chemical communication routes allow sharing information between peers and the orchestration of collective behaviours.[2] For instance, bacteria communicate via quorum sensing – i.e., individuals release signaling molecules (the so-called autoinducers or quorum molecules) and upon reaching a threshold cell-autoinducer concentration, collective functions (e.g., biofilm formation, virulence, genetic regulation) are activated.[3] Within a kingdom, organisms use similar pathways to communicate with a member of the same species (i.e., pheromones in the animal kingdom, quorum molecules in the bacteria kingdom, mating factors in fungi, etc.). In contrast, organisms of different kingdom do not usually communicate – communication is restricted unless a particular cross-

kingdom communication pathway has emerged providing a certain advantage during species evolution.[4]

The design of chemical communication networks at the micro/nanoscale is an emergent interdisciplinary topic with potential applications in diverse areas such as sensing, biomedicine, biotechnology and information and communication technologies.[5] In this scenario, despite advances in micro/nanotechnology and synthetic biology,[6] most of the micro/nanoparticles reported so far have been studied as single units, whereas the engineering of abiotic micro/nanosystems able to communicate is underexplored and represents a paradigm shift. In communication theory terms, communication involves the transmission of information from a sender to a receiver – i.e., the sender channels a message through a suitable medium to be decoded by the receiver.[5a] Communication is considered effective if it exerts the desired action on the receiver. This sender-receiver communication between two entities has served as the basis for developing communication systems at the micro/nanoscale. The few studies in this direction can be divided in two main categories: (i) communication between abiotic systems and (ii) communication between living and abiotic systems. Several strategies have been reported to communicate micro/nanoparticles, such as the utility of DNA-strand displacement reactions,[7] enzymatic cascades[8] and stimuli-responsive delivery systems.[9] Efforts to communicate abiotic with living systems have mainly relied on the incorporation of transcription-translation extracts in microscale compartments (i.e. lipid microvesicles) able to translate molecular information from the environment and/or encapsulated components into a suitable messenger to induce a response in cells.[10] Despite these reported examples, the demonstration of more complex pathways is a requirement to spur advances in the area with the future aim to integrate collectives of nano/microparticles and living systems with advanced functions.

In this context, we present as a proof-of-concept, to the best of our knowledge, the first realization of a programmed cross-kingdom communication involving two species of living cells enabled by tailor-made nanoparticles. The engineered scheme comprises, in the first place, communication from the first type of cells to the nanoparticles in response to an external stimulus. Subsequently, the nanoparticles decode the received chemical message and emit a new message detected by the second type of cells which trigger a second response. The overall network can be described as living-to-abiotic-to-living cascade-like communication in which an abiotic nanodevice acts as "nanotranslator" allowing communication between two cells from different kingdoms that otherwise would not interact. In particular, we employed *Escherichia coli* (prokaryotic cells, bacteria kingdom) and *Saccharomyces cerevisiae* (eukaryotic cells, fungi kingdom) as model microorganisms. The "nanotranslator" consists of mesoporous silica nanoparticles loaded with a molecular messenger (phleomycin) and capped with a glucose oxidase (GOx)-based responsive gatekeeper. As illustrated in Scheme 1C, communication is triggered in the presence of lactose (input) which is sensed and hydrolyzed by *E. coli* cells (β-galactosidase-expressing) into glucose and galactose. Glucose (first chemical messenger) is then detected by glucose oxidase (GOx) on the abiotic nanodevice, inducing the uncapping of the pH-sensitive gatekeeper and resulting in the release of phleomycin (second chemical messenger). Finally, in response to phleomycin, *S. cerevisiae* yeast cells activate a genetic cascade that leads to green fluorescent protein (GFP)[11] expression and the subsequent production of a fluorescence signal as the output of the communication network.

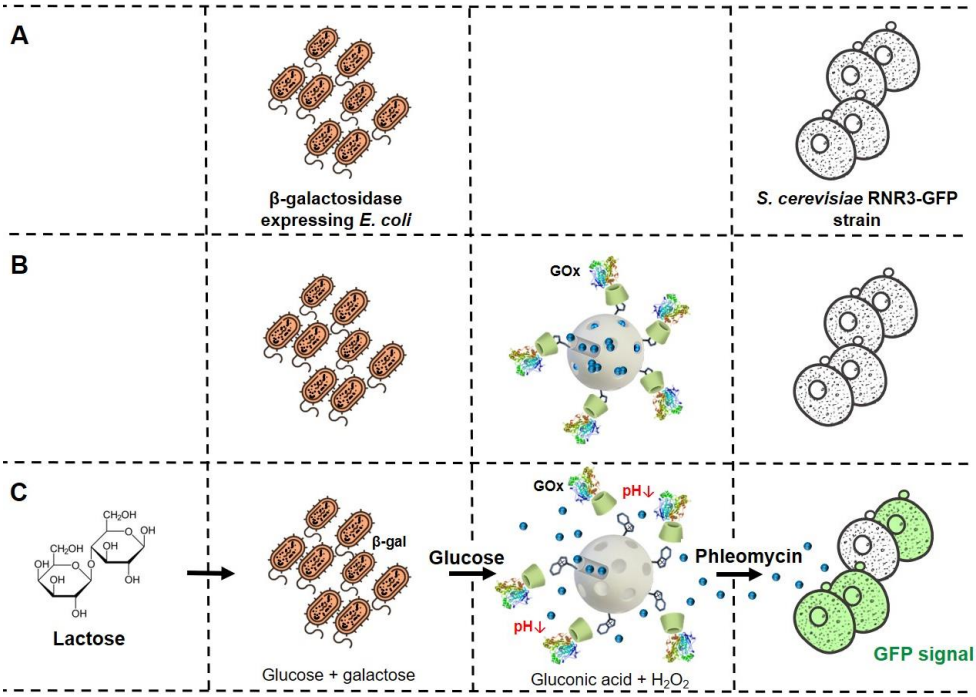

Scheme 1. Representation of the reported nano-programmed chemical communication paradigm between cells from different kingdoms. (A) *E. coli* (β-galactosidase-expressing) bacterium cells do not communicate with *S. cerevisiae* yeast cells under normal conditions. (B) Tailor-made mesoporous nanoparticles (loaded with phleomycin and capped with a GOx-based responsive gatekeeper) are added to enable communication. (C) Communication steps: bacterium cells convert lactose into glucose and galatose; glucose (first chemical messenger) is detected by the nanodevice inducing delivery of the entrapped phleomycin (second chemical messenger); finally, the receiver yeast cells sense phleomycin and respond by activating expression of GFP.

Interaction between species in our proposed system is carried out through an aqueous medium by means of chemical communication channels as both microorganisms have cell walls composed of proteins, lipids and polysaccharides that avoid the internalization of nanoparticles unless specific permeability treatments are applied.[12] The engineered bacterium used in our studies (*E. coli* DH5α) carries a plasmid (pTZ57R) encoding lacZ (β-galactosidase production) and ampicillin resistance. The budding yeast strain employed expresses GFP upon exposure to DNA-damaging agents since its transcription is controlled by the RNR3

promoter.[13] Accordingly, GFP fluorescence signal is triggered in presence of a genotoxin such as phleomycin. The “nanotranslator” is based on mesoporous silica nanoparticles due to the advantageous properties they present such as their chemical stability, large loading capacity and the great variety of cargoes which may be entrapped in their pores. Moreover, their surface can be decorated with a wide range of targeting groups, gatekeepers and enzymes showing a stimuli-responsive nature with tailor-made properties for versatile integration in communication scenarios.[14] In particular, our nanocarrier is based on mesoporous silica nanoparticles functionalized with benzimidazole (Bz) units on the external surface and capped by the formation of an inclusion complex with glucose oxidase-modified β-cyclodextrin (GOx-CD). This pH-sensitive supramolecular gatekeeper disassembles when glucose is present in the surroundings as the enzyme units produce gluconic acid inducing a local drop of pH and causing the protonation of benzimidazole moieties (pKa = 5.55)[15] – the disruption of the benzimidazole:β-cyclodextrin complex leads to the uncapping of the pores and the delivery of the entrapped cargo.

6.3 Results and discussion

To start with, we synthesized and characterized the sensing-actuating nanoparticles (see Supporting Information for details). We first prepared GOx-functionalized nanoparticles loaded with a fluorescent dye ($[Ru(bpy)_3]Cl_2$) as model cargo. The resulting nanoparticles had a spherical shape, a size of around 100 nm and a pore network as observed by transmission electron microscopy (Figure 1 and S1). In addition, powder X-ray diffraction, N_2 adsorption-desorption isotherms, dynamic light scattering, elemental analysis, enzymatic assays and TEM-EDX were used to complete their characterization (Figure S2 to S6). Then, we tested the ability

of the nanodevice to autonomously deliver the entrapped cargo upon exposure to glucose. To do so, we brought dye-loaded GOx-capped nanoparticles (**$NP_{GOx\text{-}Dye}$**) in aqueous solution (1 mg·mL^{-1}) at pH 7.5 and monitored cargo delivery in the presence and absence of glucose by measuring the fluorescent signal of the released dye. A clear release was observed in the presence of glucose due to the opening of the GOx-CD-Bz gatekeeper; whereas in contrast, cargo delivery was insignificant in the absence of glucose (Figure S7). Moreover, the specificity of the nanodevice was verified by confirming that cargo delivery was not observed in the presence of other saccharides, such as fructose, galactose, lactose and sucrose (Figure S9). After confirming the programmed sensing-actuating behaviour, we prepared similar nanoparticles loaded with phleomycin (**$NP_{GOx\text{-}Phl}$**) that would have a receiver-sender role and enable the full communication shown in Scheme 1. We also confirmed that **$NP_{GOx\text{-}Phl}$** was able to retain phleomycin and deliver it on-command in the presence of glucose (Figure S8).

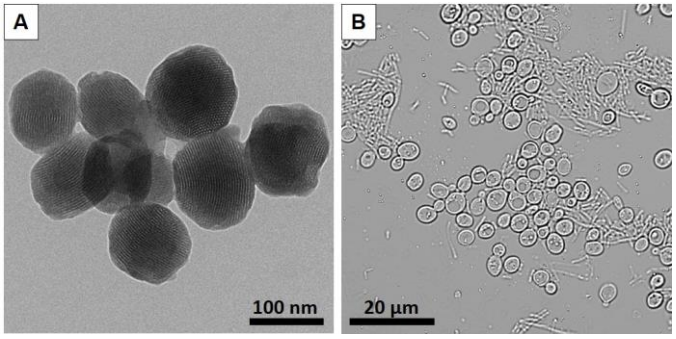

Figure 1. Images of the nanoparticles and microorganisms employed to construct the communication system. (A) Transmission electron microscopy (TEM) image of cargo-loaded GOx-functionalized gated mesoporous silica nanoparticles. (B) Bright field microscopy image of a co-culture of *Escherichia coli* bacterium cells (tubular morphology), and *Saccharomyces cerevisiae* yeast cells (nearly-spherical morphology).

As a next step and envisaging the final designed communication system (Scheme 1C), we then checked the response of the selected microorganisms to

their corresponding stimulus. First, for assessing the ability of engineered *E. coli* cells to process lactose, β-galactosidase expression was confirmed by qualitative and quantitative enzyme activity assays by means of X-Gal staining and *o*-nitrophenyl-β-D-galactopyranoside hydrolysis in aqueous medium (determined β-galactosidase activity = 8.0 $mU \cdot mL^{-1}$, culture OD = 0.5; see SI, page 265). Moreover, to test the response of yeast cells to phleomycin (chemical message), positive and negative control experiments were carried out by adding or not free phleomycin to yeast culture (at mid log exponential growth phase), that was further incubated for 3 hours in the presence of *E. coli*. When co-incubated (Figure 1B) and upon visualization by bright field microscopy (Figure 1B), *S. cerevisiae* yeast cells could be distinguished by their near-spherical shape with a size of around 5 µm, whereas *E. coli* bacterium cells exhibited their characteristic tubular morphology of around 0.5 µm of diameter and 5-10 µm in length. Experiments in the presence of phleomycin (as depicted in Figure S12) indeed revealed GFP expression in *S. cerevisiae* yeast cells when co-incubated with bacteria for three hours, in fructose-supplemented medium[16] (as carbon source).

Next, we set out to validate the first linear communication pathway of the network, i.e. communication between bacteria (acting as sender) and the nanodevice $\mathbf{NP_{GOx\text{-}Dye}}$ (acting as receiver). With this aim, we conducted a series of delivery studies in which *E. coli* bacterium cells ($4 \cdot 10^9$ $cells \cdot mL^{-1}$) and $\mathbf{NP_{GOx\text{-}Dye}}$ (1 $mg \cdot mL^{-1}$) were combined in aqueous solution (pH 7.5) in the absence or presence of lactose (2 %, as trigger of the communication). As additional control, dye release from $\mathbf{NP_{GOx\text{-}Dye}}$ in the absence of bacteria and the presence of lactose was also monitored. As plotted in Figure 2, a steady increase in cargo delivery ($[Ru(bpy)_3]Cl_2$) was observed in the complete combination (lactose+bacteria+nanodevice), whereas no substantial dye release was observed neither in the absence of lactose (bacteria+nanoparticle, red curve) nor in the presence of lactose and absence of

bacteria (lactose+nanoparticle, black curve). Altogether, this corroborates the establishment of a linear communication model: bacteria are able to hydrolyse lactose (input) and catalyse the formation of glucose, which is sensed by the GOx-capped nanodevice with the subsequent cargo delivery. In the absence of bacteria, the nanodevice is insensitive to lactose as this disaccharide is not recognized by the GOx enzyme.

Table 1. Summary of linear bacteria-**NP$_{GOx-Dye}$** communication experiments.

Condition	Input*	Bacteria*	Nanodevice*	Response*
a	+	+	+	+
b	-	+	+	–
c	+	–	+	–

* Presence or absence of input (lactose), bacteria and nanodevice is represented by + and –, respectively, whereas response refers to significant (+) or negligible (% < 20%) (-) cargo delivery.

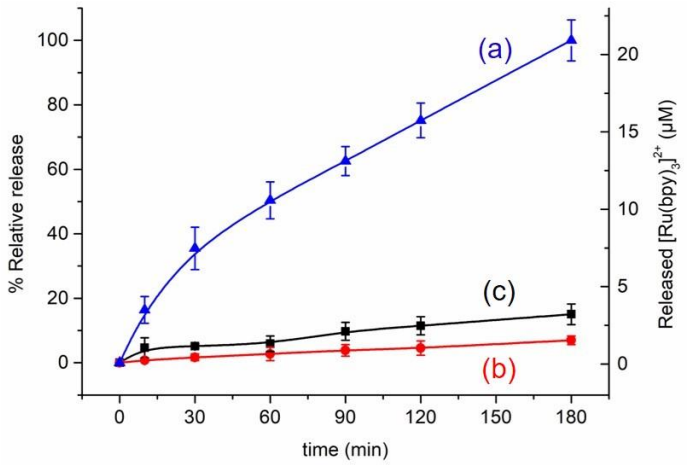

Figure 2. Validation of lactose-responsive linear communication pathway between *E. coli* cells (acting as sender) and the dye-loaded nanodevice **NP$_{GOx-Dye}$** (acting as receiver). Kinetics of cargo release ($[Ru(bpy)_3]Cl_2$) in aqueous solution at pH 7.5 containing **NP$_{GOx-Dye}$** and bacteria in the absence (b, red curve) and presence (a, blue curve) of lactose (2 %). As additional control, release from **NP$_{GOx-Dye}$** in the presence of lactose and absence of bacteria was also monitored (c, black curve). Error bars correspond to the s.d. from three independent experiments.

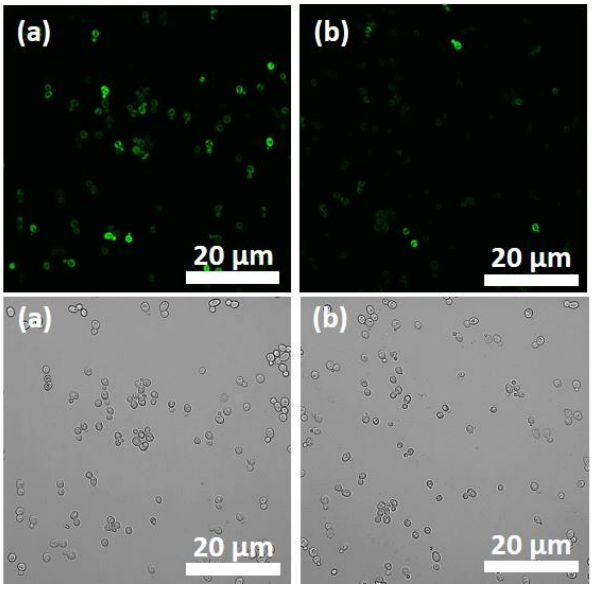

Figure 3. Validation of the glucose-responsive linear communication pathway between the phleomycin-loaded GOx-capped nanodevice **$NP_{GOx\text{-}Phl}$** (acting as sender) and *S. cerevisiae* yeast cells (acting as receiver). Monitorization of GFP fluorescence in *S. cerevisiae* yeast cells upon incubation with glucose (2 %) and (a) phleomycin-loaded GOx-capped nanodevice (**$NP_{GOx\text{-}Phl}$**) or (b) control nanoparticle **NP_{Phl}** (lacking the GOx enzyme). Top: fluorescence images, and bottom: bright field images. Samples were incubated for 3 hours.

In our subsequent set of experiments, we tested the second linear communication pathway, i.e. information transmission from the nanodevice to yeast cells. To do so, yeast cells ($1.5 \cdot 10^8$ cells·mL^{-1}) were incubated with phleomycin-loaded GOx-capped nanoparticles (**$NP_{GOx\text{-}Phl}$**) in aqueous medium at pH 7.5 containing glucose (2 %). As control, we additionally prepared phleomycin-loaded nanoparticles lacking the GOx enzyme, yet capped with β-cyclodextrin (**NP_{Phl}**), and incubated them with yeast cells under the same conditions. After three hours of incubation, induction of GFP expression was assessed by confocal fluorescence microscopy. As shown in Figure 3, the micrographs revealed a clearly higher fluorescent signal when yeast cells were incubated with **$NP_{GOx\text{-}Phl}$** (a), as compared to non-functional **NP_{Phl}** (b, lacking the enzyme). This confirms the ability

of **$NP_{GOx\text{-}Phl}$** to recognize glucose in the medium and deliver the phleomycin cargo (messenger) that triggers GFP expression in yeast cells. In nanoparticles lacking the GOx enzyme, the communication is disrupted.

After validating both linear communication pathways separately, we then constructed the complete nano-programmed cross-kingdom cell communication system. As depicted in Scheme 1, this involves a concatenated flow of information from the bacterium cells to the "nanotranslator" and subsequently to the yeast cells. To set up these experiments, yeast and bacteria were inoculated individually in fresh YPD medium and incubated until reaching mid-log exponential phase. Then, both microorganisms were brought together in YPD medium (glucose-free, supplemented with fructose) and mixed with an aqueous solution at pH 7.5 of **$NP_{GOx\text{-}Phl}$** (50 $\mu g \cdot mL^{-1}$). Then, 2 % of lactose (input of the communication) was added. As control, parallel experiments were carried out with nanoparticles **NP_{Phl}** (phleomycin-loaded β-cyclodextrin-capped nanoparticles lacking the GOx enzyme). Confocal fluorescence microscope images (Figure 4 and Figure S13) showed GFP-associated fluorescence when the "nanotranslator" **$NP_{GOx\text{-}Phl}$** was present, whereas the fluorescent signal was negligible when the incomplete nanoparticles **NP_{Phl}** were employed. Quantification of GFP-associated fluorescence intensity from three independent experiments (Figure 4e) revealed more than a 4-fold emission increase in the presence of **$NP_{GOx\text{-}Phl}$**, as compared to the control (i.e. **NP_{Phl}**). As additional control experiments to rule out any potential side interaction, we also prepared unloaded GOx-functionalized nanoparticles (**NP_{GOx}**), and unloaded nanoparticles also lacking GOx (**$NP_{Control}$**). As expected, no induction of GFP expression was observed in confocal fluorescence microscopy studies in the same conditions when using **NP_{GOx}** or **$NP_{Control}$**, indicating that there is not chemical information flow when the nanoparticles did not contain cargo or/and enzyme. These experiments demonstrate the hierarchical cross-kingdom communication of

bacterium cells with yeasts through the use of an abiotic "nanotranslator" involving the directional exchange of two chemical messengers (glucose and phleomycin). The behaviour of this communication network can be expressed in a Boolean logic table of 5 elements (i.e., the triggering input (lactose), the first microorganism (bacteria), the GOx enzyme on the nanodevice, the phleomycin cargo, and the receiver microorganism (yeast)). Among 32 possible entries (Table S4), only the complete system bacteria-**NP$_{GOx\text{-}Phl}$**-yeasts leads to effective cross-kingdom communication.

Table 2. Summary of different experimental conditions in communication studies involving bacteria-nanodevice-yeasts populations. Corresponding with a-d micrographs and quantification in Figure 4.

Cond.	Bacteria*	Enzyme*	Cargo*	NP*	Yeasts*	Output*
a	+	-	+	+	+	-
b	+	+	+	+	+	+
c	+	+	-	+	+	-
d	+	-	-	+	+	-
e	+	-	-	-	+	-

*Presence or absence of a component is represented by + and – respectively, whereas output refers to significant (+) or negligible (% < 25%) (-) GFP signal in receiver yeast cells.

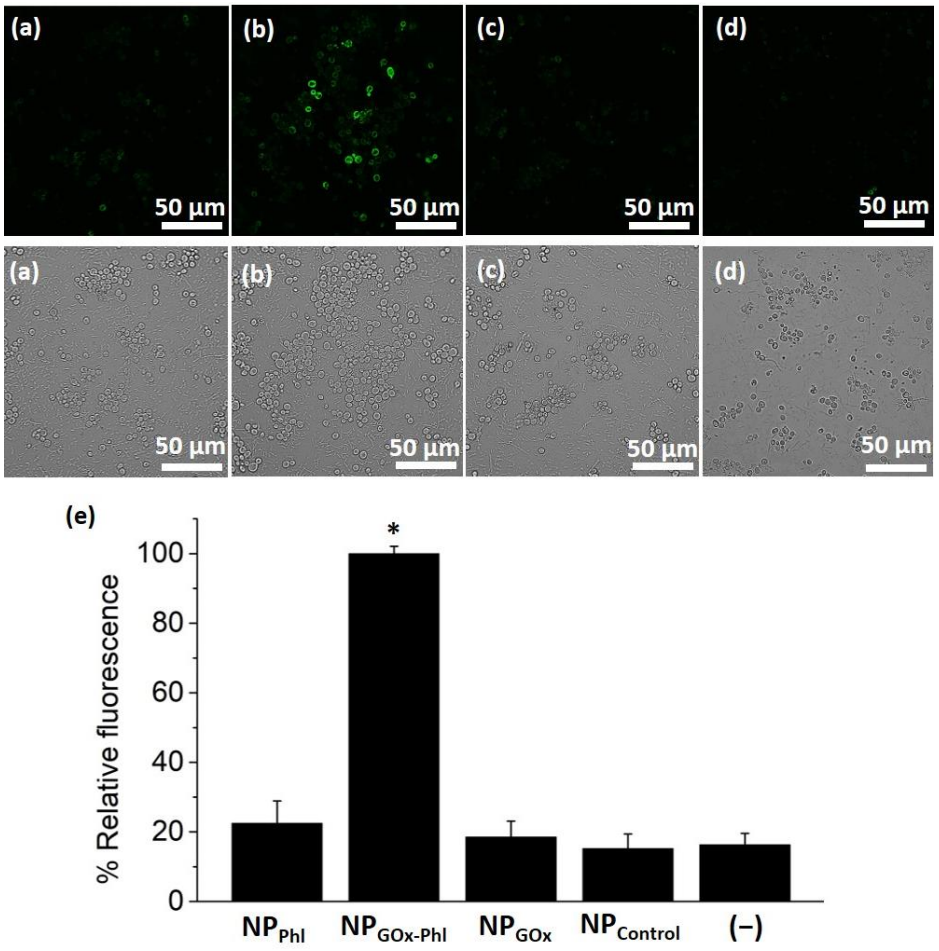

Figure 4. Validation of the nano-programmed cross-kingdom cell communication in mixtures of *E. coli* bacterium cells, nanoparticles and *S. cerevisiae* yeast cells. Evaluation of fluorescent signal from GFP expression in *S. cerevisiae* yeast cells upon incubation with *E. coli* bacterium cells, and nanoparticles, under different conditions (summarized in Table 2): (a) with phleomycin-loaded enzyme-lacking nanoparticles (**NP$_{Phl}$**), (b) with phleomycin-loaded GOx-functionalized "nanotranslator" (**NP$_{GOx-Phl}$**), (c) with unloaded GOx-functionalized nanoparticles (**NP$_{GOx}$**), and (d) with unloaded nanoparticles also lacking the GOx enzyme (**NP$_{Control}$**). Top: fluorescence images, and bottom: bright field images. Samples were incubated for 3 hours in medium containing 2 % lactose (input of the communication). Additional images are provided in the Supporting Information (Figure S13 and Figure S14). (e) Normalized quantification of the GFP-associated fluorescence intensity for the different experimental conditions. (-) represents control in the absence of nanoparticles (conditions in Table 2). Several fields of view of each condition were analyzed obtaining similar results. Data represent the mean ± s.e.m. of three independent experiments (*$p < 0.001$).

6.4 Conclusions

In summary, we report herein for the first time the nano-programming of a cross-kingdom cell communication, which involves two different cells and tailor-made nanoparticles acting as “nanotranslators”. In our proof-of-concept system, molecular information from the environment (lactose) is processed by β-galactosidase-expressing *E. coli* bacteria and transformed into a chemical signal (glucose). Glucose is detected by the nanoparticles – subsequently, the nanoparticles translate the chemical message “glucose” to the chemical messenger “phleomycin” which is understandable for the receiver microorganism (*S. cerevisiae*). In response to phleomycin, *S. cerevisiae* yeast cells activate a genetic cascade that leads to green fluorescent protein expression as the output of the communication. The whole network can be described as two hierarchically concatenated linear communication pathways – i.e. bacteria-nanodevice and nanodevice-yeast – which are independently validated. Cross-kingdom communication is demonstrated herein with functional nanoparticles that exhibited a double receiver-sender role, while communication is disrupted when the nanoparticles are incomplete.

With the development of “nanotranslators” that enable cross-kingdom communication a wide range of applications can be envisioned. For instance, we might communicate messages that instruct cells to halt physiological processes or initiate protective behaviours; designing particles that can enable plants and fungi talk to each other could help us to develop new ways to protect plants; while repurposing the finely honed language that some pathogens or cancer cells use to turn off the immune system may be a way to design new treatments for difficult-to-treat diseases. Ultimately, we envision that the cross-kingdom cell communication enabled by nanoparticles will provide new therapeutic and

diagnostic methods, biotechnological tools, ways to tune cellular behaviour and contribute to further increase our understanding of biological processes.

Acknowledgements. B. de Luis is grateful to the Spanish Government for her FPU PhD fellowship. The authors wish to thank the Spanish Government (projects RTI2018-100910-B-C41 and RTI2018-101599-B-C22 (MCUI/FEDER, EU)) and the Generalitat Valenciana (project PROMETEO 2018/024) for support.

6.5 References

1. a) N. Amy Yewdall, A. F. Mason, J. C. M. Van Hest, *Interface Focus* **2018**, *8*, 20180023; b) F. Marks, U. Klingmüller, K. Müller-Decker in *Cellular Signal Processing*, Garland Science, Boca Raton (USA), **2017**; c) Y. Tu, W. J. Rappel, *Annu. Rev. Condens. Matter Phys.* **2018**, *9*, 183-205.
2. a) M. E. Taga, B. L. Bassler, *Proc. Natl. Acad. Sci. U. S. A.* **2003**, *100*, 14549-14554; b) E. Ben-Jacob, I. Cohen, H. Levine, *Adv. Phys.* **2000**, *49*, 395-554; c) X. Zhao, X. Liu, X. Xu, Y. V. Fu, *Sci. Bull.* **2017**, *62*, 516-524.
3. C. M. Waters, B. L. Bassler, *Annu. Rev. Cell Dev. Biol.* **2005**, *21*, 319-346.
4. a) P. Williams, *Microbiology* **2007**, *153*, 3923-3938; b) D. F. Jarosz, J. C. S. Brown, G. A. Walker, M. S. Datta, W. L. Ung, A. K. Lancaster, A. Rotem, A. Chang, G. A. Newby, D. A. Weitz, L. F. Bisson, S. Lindquist, *Cell* **2014**, *158*, 1083-1093; c) V. Sperandio, A. G. Torres, B. Jarvis, J. P. Nataro, J. B. Kaper, *Proc. Natl. Acad. Sci. U. S. A.* **2003**, *100*, 8951-8956.
5. a) I. F. Akyildiz, F. Brunetti, C. Blázquez, *Comput. Networks* **2008**, *52*, 2260-2279; b) L. Wang, S. Song, J. Hest, L. K. E. A. Abdelmohsen, X. Huang, S. Sánchez, *Small* **2020**, *16*, 1907680.
6. a) K. Ariga, D. T. Leong, T. Mori, *Adv. Funct. Mater.* **2018**, *28*, 1702905. b) X. Zhang, L. Chen, K. H. Lim, S. Gonuguntla, K. W. Lim, D. Pranantyo, W. P. Yong, W. J. T. Yam, Z. Low, W. J. Teo, H. P. Nien, Q. W. Loh, S. Soh, *Adv. Mater.* **2019**, *31*, 1-48; c) B. C. Buddingh', J. C. M. Van Hest, *Acc. Chem. Res.* **2017**, *50*, 769-777.
7. a) A. Joesaar, S. Yang, B. Bögels, A. van der Linden, P. Pieters, B. V. V. S. P. Kumar, N. Dalchau, A. Phillips, S. Mann, T. F. A. de Greef, *Nat. Nanotechnol.* **2019**, *14*, 369-378; b) S. Yang, P. A. Pieters, A. Joesaar, B. W. A. Bögels, R. Brouwers, I. Myrgorodska, S. Mann, T. F. A. De Greef, *ACS Nano* **2020**, *14*, 15992-16002; c) P. Q. Ma, Q. Huang, H. D. Li, B. C. Yin, B. C. Ye, *J. Am. Chem. Soc.* **2020**, *142*, 3851-3861; d) E. Magdalena Estirado, A. F. Mason, M. Á. Alemán García, J. C. M. Van Hest, L. Brunsveld, *J. Am. Chem. Soc.* **2020**, *142*, 9106-9111.
8. a) B. C. Buddingh', J. Elzinga, J. C. M. van Hest, *Nat. Commun.* **2020**, *11*, 1652; b) T. Y. D. Tang, D. Cecchi, G. Fracasso, D. Accardi, A. Coutable-Pennarun, S. S. Mansy, A. W. Perriman, J. L. R. Anderson, S. Mann, *ACS Synth. Biol.* **2018**, *7*, 339-346; c) S. Sun, M. Li, F. Dong, S. Wang, L. Tian, S. Mann, *Small* **2016**, *12*, 1920-1927; d) Y. Qiao, M. Li, D. Qiu, S. Mann, *Angew. Chem. Int. Ed.* **2019**, *58*, 17758-17763.

9. a) C. Giménez, E. Climent, E. Aznar, R. Martánez-Máñez, F. Sancenón, M. D. Marcos, P. Amorós, K. Rurack, *Angew. Chem. Int. Ed.* **2014**, *53*, 12629-12633; b) A. Llopis-Lorente, P. Díez, A. Sánchez, M. D. Marcos, F. Sancenón, P. Martínez-Ruiz, R. Villalonga, R. Martínez-Máñez, *Nat. Commun.* **2017**, *8*, 15511; c) B. de Luis, A. Llopis-Lorente, P. Rincón, J. Gadea, F. Sancenón, E. Aznar, R. Villalonga, J. R. Murguía, R. Martínez-Máñez, *Angew. Chem. Int. Ed.* **2019**, *58*, 14986-14990; d) B. de Luis, Á. Morellá-Aucejo, A. Llopis-Lorente, T. M. Godoy-Reyes, R. Villalonga, E. Aznar, F. Sancenón, R. Martínez-Máñez, *Chem. Sci.* **2021**, *12*, 1551-1559.
10. a) R. Lentini, S. P. Santero, F. Chizzolini, D. Cecchi, J. Fontana, M. Marchioretto, C. Del Bianco, J. L. Terrell, A. C. Spencer, L. Martini, M. Forlin, M. Assfalg, M. D. Serra, W. E. Bentley, S. S. Mansy, *Nat. Commun.* **2014**, *5*, 4012; b) G. Rampioni, F. D'Angelo, L. Leoni, P. Stano, *Front. Bioeng. Biotechnol.* **2019**, *7*, 1; c) L. Aufinger, F. C. Simmel, *Chem. - A Eur. J.* **2019**, *25*, 12659-12670; d) R. Lentini, N. Y. Martín, M. Forlin, L. Belmonte, J. Fontana, M. Cornella, L. Martini, S. Tamburini, W. E. Bentley, O. Jousson, S. S. Mansy, *ACS Cent. Sci.* **2017**, *3*, 117-123; e) D. Toparlak, J. Zasso, S. Bridi, M. D. Serra, P. MacChi, L. Conti, M. L. Baudet, S. S. Mansy, *Sci. Adv.* **2020**, *6*, 4920-4938; f) X. Wang, L. Tian, Y. Ren, Z. Zhao, H. Du, Z. Zhang, B. W. Drinkwater, S. Mann, X. Han, *Small* **2020**, *16*, 1906394.
11. W. K. Huh, J. V. Falvo, L. C. Gerke, A. S. Carroll, R. W. Howson, J. S. Weissman, E. K. O'Shea, *Nature* **2003**, *425*, 686-691.
12. a) A. Agostini, L. Mondragõn, A. Bernardos, R. Martínez-Máñez, M. Dolores Marcos, F. Sancenõn, J. Soto, A. Costero, C. Manguan-García, R. Perona, M. Moreno-Torres, R. Aparicio-Sanchis, J. R. Murguía, *Angew. Chem. Int. Ed.* **2012**, *51*, 10556-10560; b) N. Mas, I. Galiana, S. Hurtado, L. Mondragón, A. Bernardos, F. Sancenón, M. D. Marcos, P. Amorós, N. Abril-Utrillas, R. Martínez-Máñez, J. R. Murguía, *Int. J. Nanomedicine* **2014**, *9*, 2597-2606.
13. Y. Endo-Ichikawa, H. Kohno, R. Tokunaga, S. Taketani, *Biochem. Pharmacol.* **1995**, *50*, 1695-1699.
14. E. Aznar, M. Oroval, L. Pascual, J. R. Murguía, R. Martínez-Máñez, F. Sancenón, *Chem. Rev.* **2016**, *116*, 561-718.
15. G. Jerez, G. Kaufman, M. Prystai, S. Schenkeveld, K. K. Donkor, *J. Sep. Sci.* **2009**, *32*, 1087-1095.
16. M. P. Ashe, S. K. De Long, A. B. Sachs, *Mol. Biol. Cell* **2000**, *11*, 833-848.

6.6 Supporting Information

Chemicals

Tetraethyl orthosilicate (TEOS), *n*-cetyltrimethylammonium bromide (CTABr), sodium hydroxide (NaOH), tris(2,2′-bipyridyl)dichlororuthenium(II) hexahydrate $[Ru(bpy)_3]Cl_2 \cdot 6H_2O$, phleomycin from *Streptomyces verticillus*, (3-iodopropyl)trimethoxysilane, benzimidazole, triethylamine, β-cyclodextrin, glucose oxidase from *Aspergillus niger*, D-(+)-glucose, D-(+)-saccharose, D-(+)-galactose, D-(−)-fructose, D-(+)-lactose monohydrate, 2,2′-azino-bis(3-ethylbenzothiazoline-6-sulfonic acid) diammonium salt (ABTS), peroxidase from horseradish (HRP), ampicillin sodium salt, *o*-nitrophenyl-β-D-galactopyranoside and 5-bromo-4-chloro-3-indolyl-β-D-galactopyranoside were purchased from Sigma-Aldrich. Sodium sulfate anhydrous, sodium dihydrogen phosphate monohydrate, disodium hydrogen phosphate heptahydrate, toluene and acetonitrile were provided by Scharlau. Bacteriological peptone, yeast extract, and Luria-Bertani broth were purchased from Conda Lab. Agar was purchased from Sigma-Aldrich.

Microorganisms strains and culture conditions

β-galactosidase-expressing *Escherichia coli* bacteria used in this study were obtained by transforming *E. coli* DH5α with pTZ57R plasmid which encodes for lacZ gene (β-galactosidase production) and ampicillin resistance using standard protocols.[1] Standard methods for bacteria culture and manipulation were used.

RNR3-GFP *Saccharomyces cerevisiae* yeast strain used in this study was purchased from Life Technologies. It was obtained by tagging RNR3 (systematic name YIL066C) open reading frame (ORF) through oligonucleotide-directed homologous recombination.[2] The genotype of the parent haploid of the *S.*

cerevisiae yeast strain used (ATCC 201388) is: MATα his3Δ1 leu2Δ0 met15Δ0 ura3Δ0. Standard methods for yeast culture and manipulation were used.

General methods

Powder X-ray diffraction (PXRD), transmission electron microscopy (TEM), N_2 adsorption-desorption isotherms, UV-visible and fluorescence spectrophotometry, dynamic light scattering (DLS) and elemental analysis techniques were employed for materials characterization. PXRD measurements were performed on a Seifert 3000TT diffractometer using CuKα radiation at low angles ($1.3 < 2\theta < 8.3$, with steps of 0.04 degrees and 3 seconds for step). TEM images were acquired using a JEOL TEM-1010 Electron microscope working at 100 kV. Additionally, TEM coupled with energy dispersive X-ray spectroscopy (TEM-EDX) was used for element mapping using a JEOL TEM-2100F microscope. DLS studies were performed using a ZetaSizer Nano ZS (Malvern). N_2 adsorption-desorption isotherms were recorded on a Micromeritics TriStar II Plus automated analyser. Samples were previously degassed at 90 °C in vacuum overnight and measurements were performed at 77 K. UV-visible spectra were recorded with a JASCO V-650 Spectrophotometer. Fluorescence measurements were carried out in a JASCO FP-8500 Spectrophotometer. Elemental analysis was performed using a LECO CHNS-932 Elemental Analyser. Confocal microscopy imaging was performed employing a Leica TCS SPE (Leica Microsystems Heidelberg GmbH) inverted laser scanning confocal microscope using a HC PL APO 40x oil objective.

Synthesis of mesoporous silica nanoparticles (MSNPs)

1.00 g (2.74 mmol) of *n*-cetyltrimethylammonium bromide (CTABr) was dissolved in 480 mL of deionized water. Then, the pH was basified by adding 3.5 mL of a 2 $mol \cdot L^{-1}$ NaOH solution and the temperature was increased to 80 °C. Next,

tetraethyl orthosilicate (TEOS) (5 mL, 22.4 mmol) was added dropwise into the solution. Magnetic stirring was kept for 2 hours to give a white suspension. Finally, the solid was isolated by centrifugation, washed several times with water until neutral pH and dried at 70 °C overnight (as-synthesized MSNPs). To obtain the final mesoporous nanoparticles MCM-41 type (**MSNPs**), the as-synthesized solid was calcined at 550 °C in an oxidant atmosphere for 5 hours in order to remove the surfactant.

Synthesis of $NP_{GOx\text{-}Dye}$

60 mg of **MSNPs** were suspended in anhydrous acetonitrile (4 mL) and reacted with 60 µL of (3-iodopropyl)trimethoxysilane for 5.5 h. The solid was isolated by centrifugation, washed with acetonitrile and dried at 70 °C overnight. To functionalize the surface with benzimidazole moieties, 0.25 g of benzimidazole and 990 µL of triethylamine were mixed with 20 mL of toluene and heated for 20 min at 80 °C to prepare a saturated solution of benzimidazole. 10 mL of this suspension were added over 60 mg of the previously prepared nanoparticles. The mixture was stirred at 80 °C for three days. Afterward, the benzimidazole-functionalized solid was isolated by centrifugation and washed with toluene and dried at 70 °C overnight yielding **S0** (benzimidazole-functionalized MSNPs). Next, the loading process was carried out by suspending the solid **S0** (25 mg) in 2 mL of a concentrated solution of $[Ru(bpy)_3]Cl_2 \cdot 6H_2O$ in anhydrous acetonitrile (2 $mg \cdot mL^{-1}$), and stirred overnight in order to achieve the loading of the pores. Finally, the solid was centrifuged, washed thoroughly with acetonitrile and dried under vacuum. Then, the loaded support (5 mg) was suspended in 2 mL of 50 mM phosphate buffer at pH 7.5 and capped by the addition of 2.5 mg of lyophilized β-cyclodextrin-modified glucose oxidase derivative (GOx-β-CD, synthesized as previously reported)[3] and stirred overnight at 10 °C. Finally, the solid was centrifuged, washed

thoroughly with 50 mM phosphate buffer at pH 7.5 and dried under vacuum. This process yielded nanodevice **$NP_{GOx\text{-}Dye}$**, which was kept wet in refrigerator until use.

Synthesis of NP_{Dye}

Nanoparticles **NP_{Dye}** were prepared from **S0** following the same procedure described for **$NP_{GOx\text{-}Dye}$** but the capping step was carried out with 2.5 mg of commercial β-cyclodextrin in 2 mL of 50 mM phosphate buffer at pH 7.5. The resulting material **$NP_{GOx\text{-}Dye}$** was kept wet in refrigerator until use.

Synthesis of $NP_{GOx\text{-}Phl}$

Nanodevice **$NP_{GOx\text{-}Phl}$** was prepared following the same procedure described for **$NP_{GOx\text{-}Dye}$** but the cargo loading process was carried out with phleomycin. To do so, 5 mg of **S0** were suspended in 1 mL of a concentrated solution in ultrapure H_2O of the antibiotic phleomycin (10 mg, 6.5 mM) and stirred overnight at 10 °C. The solid was isolated by centrifugation and washed with cold ultrapure H_2O. The GOx-β-CD capping was conducted following the same procedure described for **$NP_{GOx\text{-}Dye}$.** This process finally yielded **$NP_{GOx\text{-}Phl}$**, which was kept wet in refrigerator until use.

Synthesis of NP_{Phl}

Nanomaterial **NP_{Phl}** was prepared from **S0** following the same procedure described for **$NP_{GOx\text{-}Phl}$** but the capping step was carried out with 2.5 mg of commercial β-cyclodextrin in 2 mL of 50 mM phosphate buffer at pH 7.5. The resulting nanomaterial **NP_{Phl}** was kept wet in refrigerator until use.

Synthesis of NP_{GOx}

Nanomaterial **NP_{GOx}** was prepared following the same procedure described for **$NP_{GOx\text{-}Phl}$** but the mesoporous container was not loaded. The resulting **NP_{GOx}** was kept wet in refrigerator until use.

Synthesis of $NP_{Control}$

Nanomaterial **$NP_{Control}$** was prepared following the same procedure described for **NP_{Dye}** but the mesoporous container was not loaded. The resulting **NP_{Dye}** was kept wet in refrigerator until use.

Materials Characterization

Nanomaterials were characterized by standard techniques.

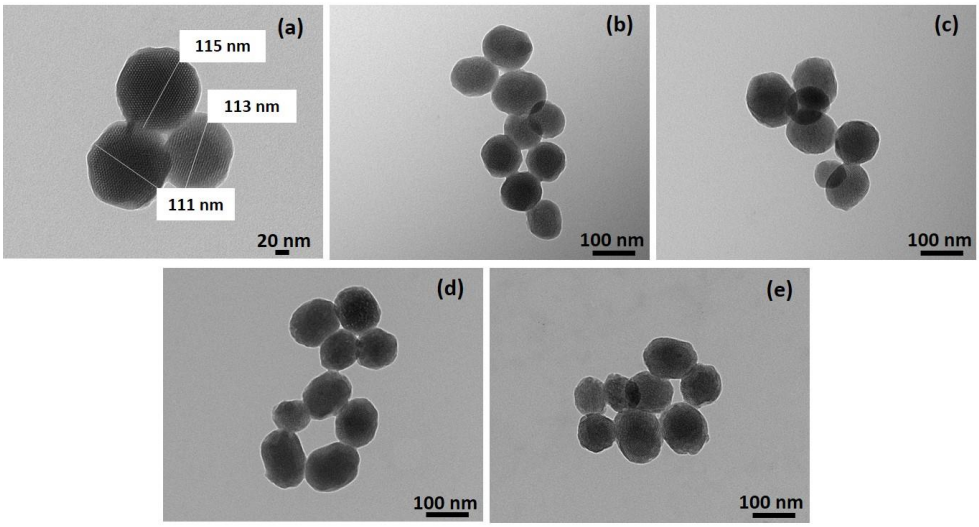

Figure S1. TEM images of the calcined mesoporous silica nanoparticles (**MSNPs**) (a-c) and the final nanodevice **$NP_{GOx\text{-}Dye}$** (d-e).

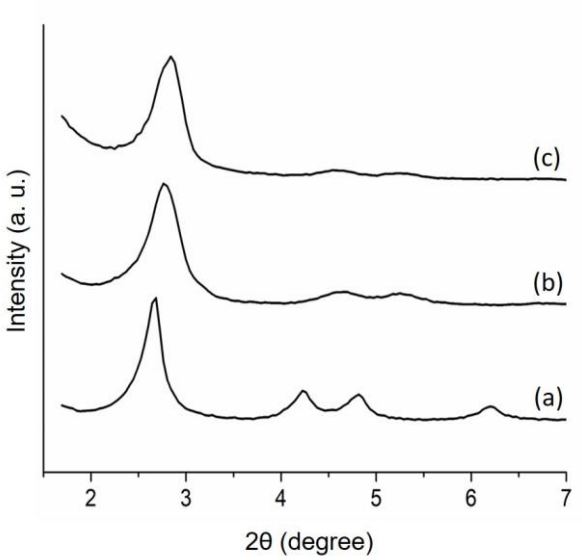

Figure S2. Powder X-ray diffraction patterns of the nanomaterials (a) **as-made MSNPs**, (b) **calcined MSNPs** and (c) benzimidazole-functionalized nanoparticles (**S0**).

Figure S2 shows powder X-ray diffraction patterns at low angles ($1.5 < 2\theta < 7$). The **as-made MSNPs** (mesoporous silica nanoparticles, a) exhibit characteristic low-angle reflections peaks of MCM-41 type mesoporous scaffolds. For the **calcined MSNPs** (b), we observed a slight displacement of the peaks related to the condensation of silanol groups during the calcination process. These low-angle typical peaks are preserved in the benzimidazole-functionalized nanoparticles (**S0**, c). The presence of the (100) peak in the PXRD patterns in the nanomaterial **S0** indicated that the functionalization had not damaged the mesoporous structure. Powder X-ray diffraction pattern of $\mathbf{NP_{GOx\text{-}Dye}}$, $\mathbf{NP_{GOx\text{-}Phl}}$, $\mathbf{NP_{Phl}}$, $\mathbf{NP_{GOx}}$ and $\mathbf{NP_{Control}}$ were not obtained due to the low quantity collected in the synthesis but neither the enzyme immobilization procedure nor the cargo loading step were expected to affect the mesoporous structure as they were performed under mild conditions.

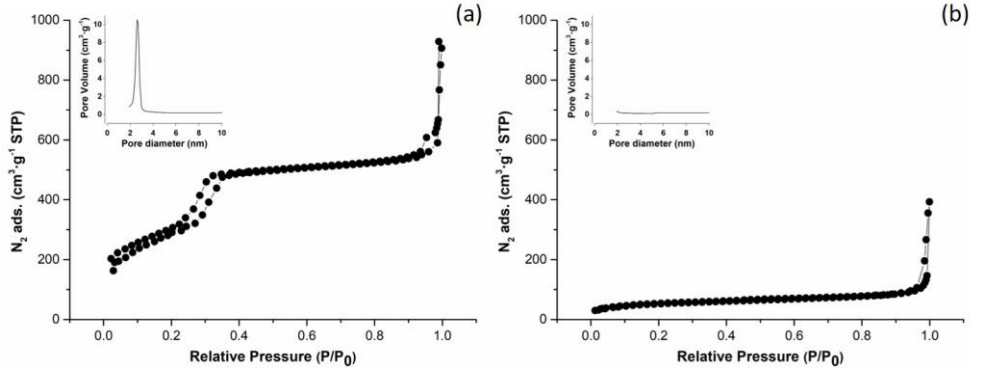

Figure S3. The N_2 adsorption-desorption isotherms for (a) the **calcined MSNPs** and the benzimidazole-functionalized nanomaterial (**S0**) loaded with $[Ru(bpy)_3]Cl_2$.

The N_2 adsorption-desorption isotherm of the **calcined MSNPs** shows an adsorption step at intermediate P/P_0 value 0.3, which is characteristic for mesoporous solids with empty pores. This step is related to the nitrogen condensation inside the mesopores by capillarity. The absence of a hysteresis loop in this interval and the narrow BJH pore distribution suggest the existence of uniform cylindrical mesopores. Application of the BET model results in a value for the total specific surface of 1084 $m^2 \cdot g^{-1}$ for **calcined MSNPs**. Total specific surface area for the benzimidazole-functionalized MSNPs (nanomaterial **S0**) loaded with $[Ru(bpy)_3]Cl_2$ significantly decreased to 191 $m^2 \cdot g^{-1}$ due to the cargo loading inside the mesopores. In order to calculate pore size and total pore volume, BJH model was applied for $P/P_0 < 0.6$ (associated to adsorption inside the pores). N_2 adsorption-desorption isotherm for the functionalized and loaded nanomaterial **S0** shows a significant decrease in N_2 volume adsorbed and is flat when compared (at the same scale) to that from **MSNPs**. This indicates that there is a significant pore blocking accordingly the loading and capping processes. BET specific values, pore volumes and pore sizes calculated from N_2 adsorption-desorption isotherms for both solids are listed in Table S1.

Table S1. BET specific surface values, pore volumes and pore sizes calculated from N_2 adsorption-desorption isotherms for selected nanomaterials.

Solid	S_{BET} [$m^2 \cdot g^{-1}$]	Pore Volume [$cm^3 \cdot g^{-1}$]	Pore size [nm]
Calcined MSNPs	1084 ± 1	0.88	2.53
Loaded S0	191 ± 3	0.09	-

The hydrodynamic size and zeta potential of different nanoparticles were measured by dynamic light scattering (DLS) studies (Table S2, Figure S4). For carrying out the experiments, the corresponding materials were suspended in distilled water at pH 7 at a concentration of 0.01 $mg \cdot mL^{-1}$.

Table S2. Zeta potential (mV) and hydrodynamic size (nm) data.

Nanomaterial	Zeta Potential (mV)	Hydrodynamic Size (nm)
Calcined MSNPs	-32.5	112
S0	-29.8	130
NP_{Dye}	-27.9	158
$NP_{GOx\text{-}Dye}$	-38.8	284

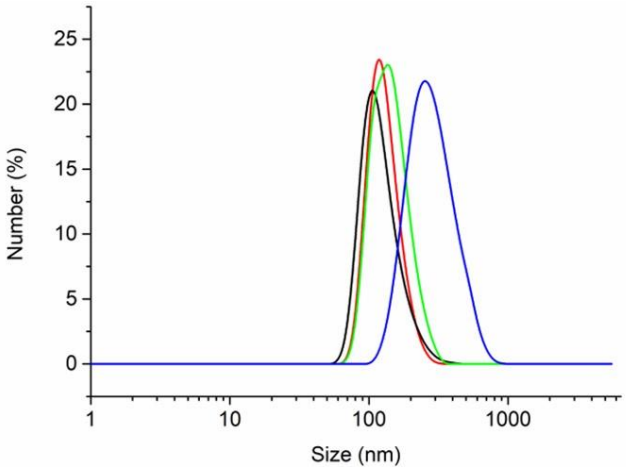

Figure S4. Hydrodynamic size (nm) graphic representation of **calcined MSNPs** (black), benzimidazole-functionalized MSNPs (nanomaterial **S0**, red), β-CD-capped and dye-loaded nanoparticles (**NP_{Dye}**, green) and dye-loaded GOx-β-CD-capped nanodevice **$NP_{GOx\text{-}Dye}$** (blue).

From elemental analysis data (Table S3), composition of the nanomaterial was estimated. Considering the data obtained from the analysis of the unloaded and uncapped nanoparticles (**S0**, benzimidazole-functionalized MSNPs), the amount of molecular gate $(CH_2)_3$-benzimidazole was determined as 29.0 $mg \cdot g^{-1}$.

Table S3. Elemental analysis data.

Nanomaterial	% C	% H	% N
S0	4.40	1.34	0.51

The content of phleomycin encapsulated in **$NP_{GOx\text{-}Phl}$** and **NP_{Phl}** was estimated by measuring the absorbance of the phleomycin in solution (λ_{abs} = 300 nm) before and after the capping process as well as all the washing steps until yielding the final nanoparticles. The calibration curve indicated an amount of 231.4 mg of phleomycin per g of **$NP_{GOx\text{-}Phl}$** and 268.1 mg per g of **NP_{Phl}**. The amount of

$[Ru(bpy)_3]Cl_2$ loaded in $\mathbf{NP_{GOx\text{-}Dye}}$ was estimated to be 39.8 $mg \cdot g^{-1}$ also by calibration. To infer so, the mesoporous scaffold was hydrolysed by incubating the nanoparticles with NaOH 20% at 40 °C for 1 hour and then the supernatant absorbance was measured.

The immobilization of the enzyme was confirmed by running an enzyme activity assay. The method we used in order to test glucose oxidase activity is based on the oxidation of glucose by glucose oxidase which gives gluconic acid and hydrogen peroxide. Then, hydrogen peroxide reacts with ABTS (2,2'-azino-bis(3-ethylbenzothiazoline-6-sulfonic acid) diammonium salt) in the presence of peroxidase (HRP) to form a blue-green product ($ABTS^{+\cdot}$) that can be followed UV-visible spectrophotometry (λ_{abs} = 418 nm).

Reactions for assaying glucose oxidase activity:

$$D\text{-}glucose + O_2 + H_2O \xrightarrow{\text{Glucose oxidase}} D\text{-}gluconic\ acid + H_2O_2$$

$$H_2O_2 + ABTS \xrightarrow{\text{HRP}} ABTS^{\cdot+} + H_2O$$

In a typical experiment, 250 µL of 1 M of glucose (180 $mg \cdot mL^{-1}$), 250 µL of ABTS solution (1 $mg \cdot mL^{-1}$) and 50 µL of HRP solution (2 $mg \cdot mL^{-1}$) were placed in a quartz cuvette. All solutions were prepared in 100 mM sodium phosphate buffer at pH 7.5. Then, 10 µL of either buffer (for blank), commercial enzyme solution in buffer (0.01 $mg \cdot mL^{-1}$) or $\mathbf{NP_{GOx\text{-}Dye}}$ (capped with GOx-β-CD and loaded with $[Ru(bpy)_3]Cl_2$), $\mathbf{NP_{GOx\text{-}Phl}}$ (capped with GOx-β-CD and loaded with phleomycin) or $\mathbf{NP_{Phl}}$ (capped with β-CD and loaded with phleomycin) suspension (5 $mg \cdot mL^{-1}$) were added. The mixture was shaken and absorbance at 418 nm was monitored as a function of time. Whereas no change was observed in the absence of nanoparticles or commercial enzyme (blank), a strong blue-green colour appeared in the presence of those. The increase in absorbance ($ABTS^{+\cdot}$ formation) as a function of

time in the presence of **NP$_{GOx-Dye}$**, **NP$_{GOx-Phl}$** or **NP$_{Phl}$** and the commercial enzyme solution is depicted in Figure S5.

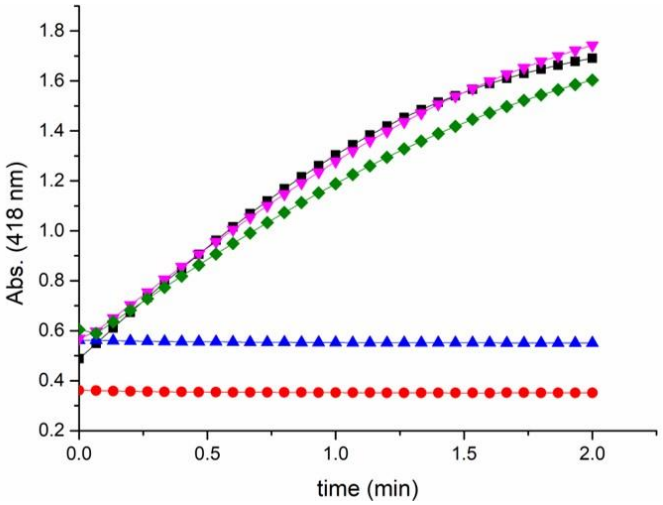

Figure S5. Absorbance at 418 nm ($ABTS^{+\cdot}$ formation) due to glucose oxidase activity on **NP$_{GOx-Dye}$** (pink), **NP$_{GOx-Phl}$** (green), **NP$_{Phl}$** (blue), commercial enzyme solution (black) and blank (red).

Glucose oxidase activity on the nanoparticles was calculated by applying the following formula:

$$\frac{Enzyme\ Units}{g} = \frac{(\Delta - \Delta_{blank}) \cdot V_T \cdot F_D}{\varepsilon_{ABTS} \cdot l \cdot V_S \cdot C_S}$$

Where, Δ is the slope of the graph (min^{-1}), Δ_{blank} is the slope of the graph for the blank (min^{-1}), V_T is the total volume in the cuvette, F_D is the dilution factor, ε_{ABTS} is the molar extinction of ABTS at 418 nm (36000 $M^{-1} \cdot cm^{-1}$), L is the optical path in the cuvette (1 cm), V_S is the volume of the sample added (mL) and C_S is the concentration of sample added ($g \cdot mL^{-1}$).

The activity of glucose oxidase on **NP$_{GOx\text{-}Dye}$** and **NP$_{GOx\text{-}Phl}$** was determined to be 1.90 U and 1.67 U per mg of solid, respectively, whereas the activity of commercial glucose oxidase was determined to be 125.06 U per mg of commercial enzyme. From this data, the corresponding amount of glucose oxidase on **NP$_{GOx\text{-}Dye}$** and **NP$_{GOx\text{-}Phl}$** was estimated to be 15.16 and 13.34 mg of enzyme per g of solid, respectively.

TEM-EDX mapping of nanodevice **NP$_{GOx\text{-}Dye}$** shows the presence of nitrogen atoms in the whole scaffold. This is attributed to the immobilized enzyme (glucose oxidase) as well as the benzimidazole moiety of the molecular gate (see Figure S6).

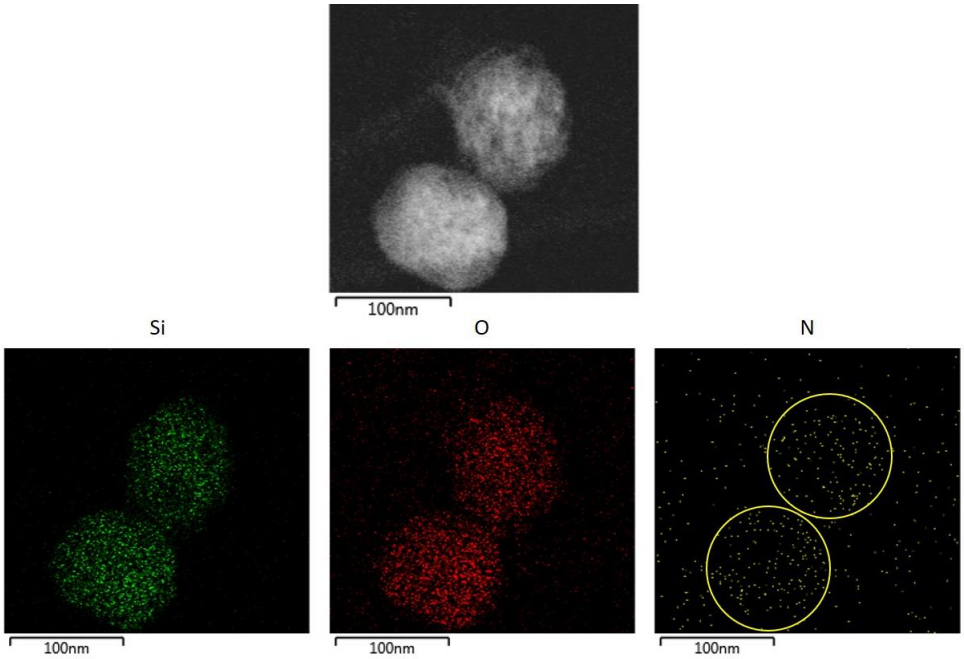

Figure S6. TEM-EDX element mapping of nanodevice **NP$_{GOx\text{-}Dye}$**.

Nanodevice sensing-actuating behaviour

Responsive delivery studies

For studying the glucose-responsive release behaviour of **$NP_{GOx\text{-}Dye}$**, the corresponding refrigerated solution of nanoparticles was washed with an aqueous solution (pH 7.5, 20 mM Na_2SO_4), divided into two fractions and brought to a final concentration of 1 mg·mL^{-1}. Both fractions were incubated for 1 hour. Then, either an aqueous aliquot (for blank) or glucose (1 mM, as input) were added (time = 0 minutes) and samples were shaken over time. Aliquots were taken at scheduled times, centrifuged (2 minutes, 12000 rpm) to remove the nanoparticles and the fluorescence of the solution at 595 nm was measured (λ_{exc} = 453 nm) to determine the relative cargo release.

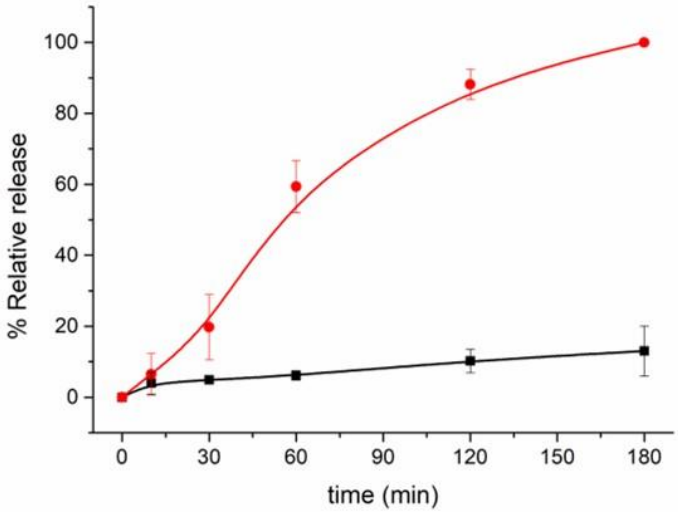

Figure S7. Relative cargo release from **$NP_{GOx\text{-}Dye}$** in the absence of input (black curve) and in the presence of glucose (red curve). Substrate added at 1 mM final concentration. Error bars correspond to the s.d. from three independent experiments.

For release experiments with **$NP_{GOx\text{-}Phl}$**, the corresponding refrigerated solution of nanoparticles was washed with ultrapure water (pH 7.5), divided into two fractions and brought to a final concentration of 2.5 mg·mL^{-1}. Both fractions

were incubated for 1 hour. Then, either ultrapure water (for blank) or glucose (as input) were added (time = 0 minutes) and samples were shaken over time. Aliquots were taken at scheduled times, centrifuged to remove the nanoparticles (2 minutes, 12000 rpm) and the absorbance at 300 nm of the solution measured (phleomycin λ_{abs} = 300 nm).

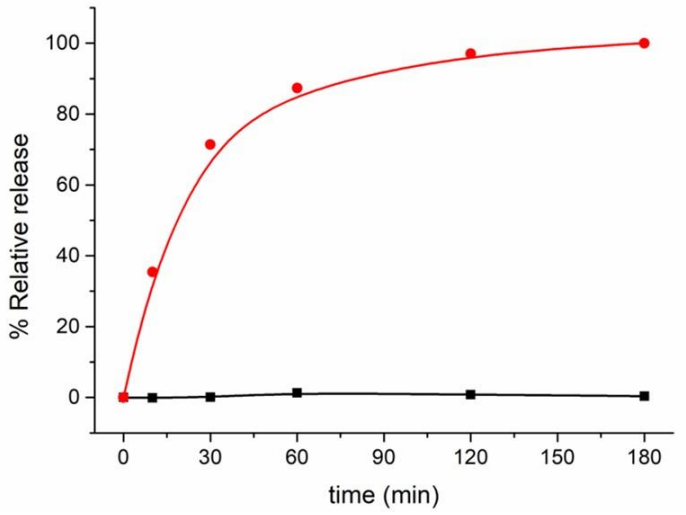

Figure S8. Relative cargo release from **$NP_{GOx\text{-}Phl}$** in the absence of input (black curve) and in the presence of glucose (red curve). Substrate added at 1 % final concentration (55.5 mM).

Selectivity in cargo delivery

A refrigerated solution of **$NP_{GOx\text{-}Dye}$** was washed with an aqueous solution (pH 7.5, 20 mM Na_2SO_4), divided into six fractions and brought to a final concentration of 1 mg·mL^{-1}. All fractions were incubated for 1 hour. Then, different monosaccharides (fructose, galactose, glucose) and disaccharides (lactose, sucrose) were added (time = 0 minutes) and samples were shaken over time. Aliquots were taken after 3 hours, centrifuged to remove the nanoparticles (2 minutes, 12000 rpm) and the fluorescence of the solution at 595 nm measured (λ_{exc} = 453 nm) to

determine the relative cargo release. A selective response to glucose was observed.

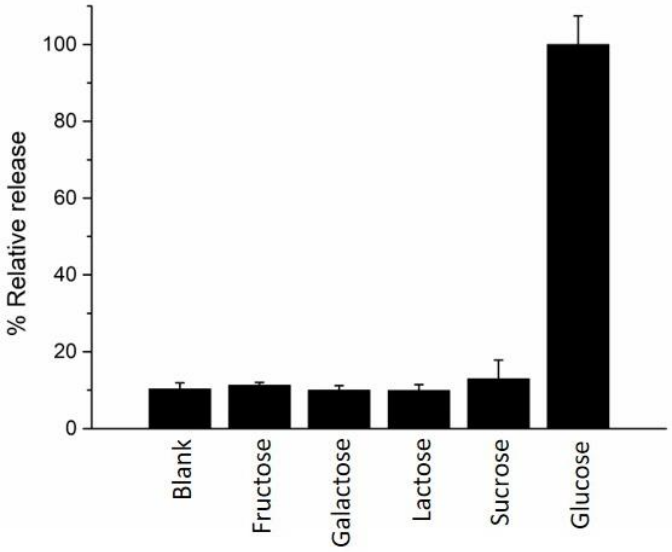

Figure S9. Relative cargo release from **$NP_{GOx\text{-}Dye}$** in the presence of different monosaccharides and disaccharides at 1 mM concentration. Error bars correspond to the s.d. from three independent experiments.

Cellular experiments

Bacterial β-*galactosidase activity assay*

The β-galactosidase activity of the engineered *E. coli* cells was confirmed by running a specific enzyme activity assay. The method employed is based on the hydrolysis of *o*-nitrophenyl-β-D-galactopyranoside by β-galactosidase which produces a yellow product (*o*-nitrophenol) that can be followed UV-visible spectrophotometry (λ_{abs} = 420 nm).

Reaction for assaying β-galactosidase activity:

$$o\text{–}nitrophenyl\text{–}\beta\text{–}D\text{–}galactopyranoside \xrightarrow{\text{β-Galactosidase}} o\text{–}nitrophenol + \beta\text{–}D\text{–}galactose$$

To run the assay, mid-exponential *E. coli* transformed with pTZ57R plasmid were grown in LBA (Luria-Bertani medium containing 50 $\mu g \cdot mL^{-1}$ of ampicillin) shaking at 37 °C until reaching an optical density of 0.5 at 600 nm.

600 µL of *o*-nitrophenyl-β-D-galactopyranoside solution (1.1 $mg \cdot mL^{-1}$) in ultrapure water at pH 7.5 were placed in a quartz cuvette. Then, 400 µL of either water (for blank) or bacterial culture (previously washed two times with ultrapure water) were added. The mixture was shaken and absorbance at 420 nm was monitored as a function of time. Whereas no change was observed in the absence of bacteria (blank), a yellow colour appeared in the presence of those. The increase in absorbance (*o*-nitrophenol formation) as a function of time in the presence of β-galactosidase-expressing *E. coli* is depicted in Figure S10.

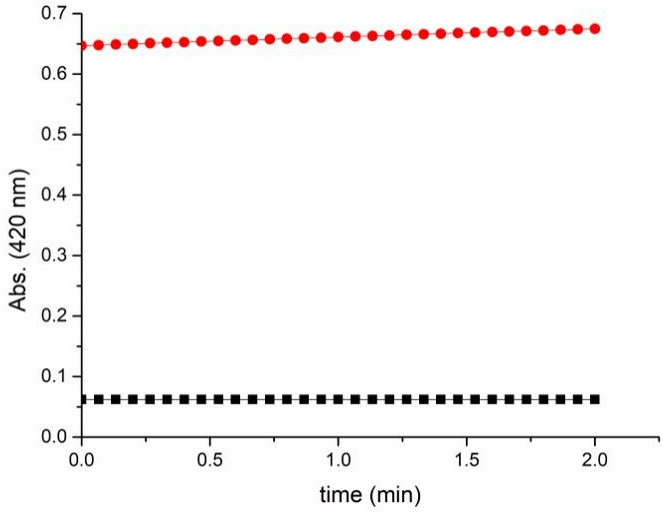

Figure S10. Absorbance at 420 nm (*o*-nitrophenol formation) due to β-galactosidase activity on *E. coli* cells (red) and blank (black).

Bacterial β-galactosidase activity was calculated by applying the previously explained formula (page 260) considering that the molar extinction of *o*-

nitrophenol ($\mathcal{E}_{ONP}$) is 4500 $M^{-1}\cdot cm^{-1}$ at 420 nm. The activity of β-galactosidase was determined to be 0.0077 U per mL of bacterial culture.

In addition, β-galactosidase activity was also confirmed by X-Gal staining. To so do, 40 µl of 5-bromo-4-chloro-3-indolyl-β-D-galactopyranoside (X-Gal, 20 $mg\cdot ml^{-1}$) in dimethylformamide was spread on LBA agar plates and let to dry. In parallel, *E. coli* cells were grown in LBA medium to an optical density of 0.5 at 600 nm, spread on the previously prepared X-Gal LBA agar plates and incubated at 37 °C for 30 hours.

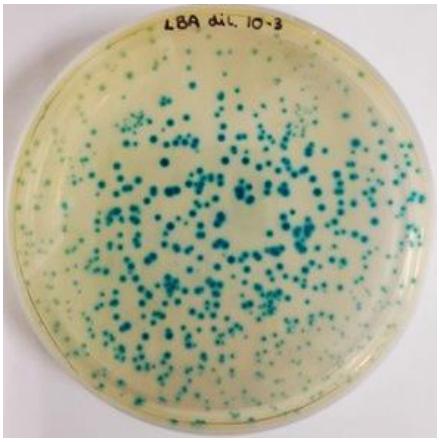

Figure S11. Observation of blue *E. coli* colonies after X-gal staining. The insoluble blue product formed after the dimerization of the hydrolysis products of bromo-4-chloro-3-indolyl-β-D-galactopyranoside (5-bromo-4-chloro-3-hydroxy-1H-indole) confirmed β-galactosidase activity in *E. coli.*

Studies of GFP-expression in yeasts-bacteria co-cultures

Intracellular overexpression of green fluorescent protein (GFP) in yeasts was monitored by confocal fluorescence microscopy. In particular, the images were acquired employing a Leica TCS SPE inverted laser scanning confocal microscope using a HC PL APO 40x oil objective with an excitation wavelength of 488 nm. Two-dimensional pseudo-colour images (255 colour levels) were gathered with a size of 1024x1024 pixels and Airy 1 pinhole diameter.

Experiments with free phleomycin (positive and negative GFP controls)

S. cerevisiae budding yeasts RNR3-GFP were inoculated into fresh YPD (yeast extract peptone dextrose) medium and cultured for 3.5 hours at 28 °C. β-galactosidase-expressing *E. coli* bacteria were inoculated into fresh LBA (Luria-Bertani medium containing 50 $\mu g \cdot mL^{-1}$ of ampicillin) and incubated for 2.5 hours at 37 °C. Both were shaken until reaching the log phase with an optical density (600 nm) of approximately 0.5, respectively.

For yeast control experiment, an aliquot of the freshly inoculated yeast suspension was washed three times with glucose-free YPD and resuspended in diluted glucose-free YPD (10 %, pH 7.5). For yeast-bacterium co-culture control experiments, aliquots of 2 mL of the freshly inoculated yeast suspension and aliquots of 2 mL of the freshly inoculated bacteria suspension were mixed, concentrated, washed three times with glucose-free YPD and resuspended in diluted YPD (10 %, pH 7.5). Medium dilution was done with ultrapure water (pH 7.5) and lactose (2 %) was also added. In total, four different conditions were studied: (a) yeast culture, (b) yeast-bacterium co-culture, (c) yeast-bacterium co-culture in the presence of phleomycin (2.6 μM, 4 $\mu g \cdot mL^{-1}$), and (d) yeast-bacterium co-culture in the presence of phleomycin (2.6 μM, 4 $\mu g \cdot mL^{-1}$) supplemented with fructose (1 %). Samples were incubated in continuous shaking for 3 hours at 28 °C. Finally, the samples were centrifuged (5 minutes, 6000 rpm), washed two times with ultrapure water (pH 7.5) and the pellet was resuspended in 40 μL of ultrapure water. Then, fluorescent GFP-associated signal was evaluated by confocal fluorescence microscopy (Figure S12). The registered fluorescent signals revealed the need for supplementing the aqueous media with an extra carbon source (fructose) to trigger effective GFP expression in yeasts (as they do not process lactose and glucose production by bacteria is relatively slow). As reported, transcription-translation processes require sufficient energy supply for activation.

As expected, a clear increase in GFP-associated yeast fluorescence was observed upon the addition of phleomycin to yeast-bacterium co-culture in fructose-supplemented medium (Figure 12-d).

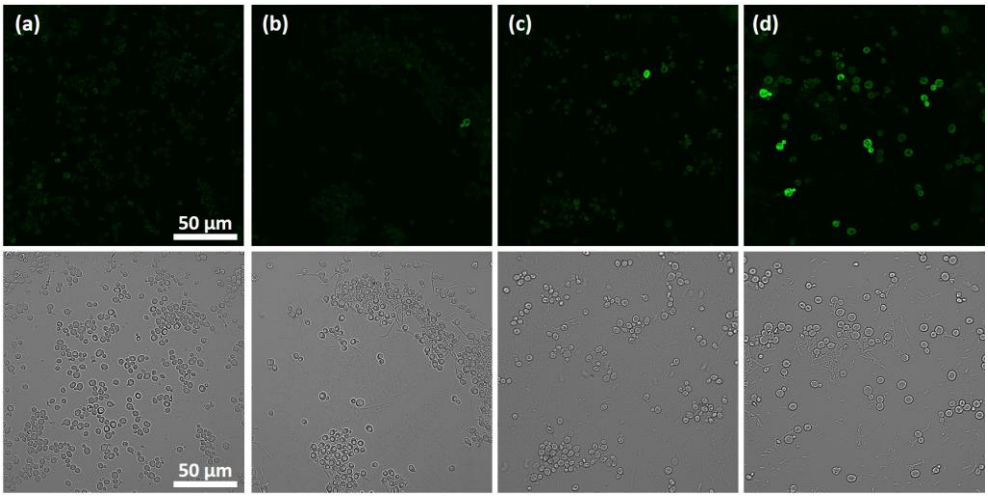

Figure S12. Evaluation of GFP signal induction in *S. cerevisiae* cells examined by confocal fluorescence microscopy after 3 hours in aqueous medium (glucose-free 10 % YPD with 2% lactose) under different conditions. (a) Yeast culture (negative control experiment). (b) Yeast-bacterium co-culture (negative control experiment). (c) Yeast-bacterium co-culture in the presence of phleomycin (2.6 µM). (d) Yeast-bacterium co-culture in the presence of phleomycin (2.6 µM) supplemented with fructose (1 %). Top: fluorescence images, bottom: bright field images.

Validation of lactose-responsive linear communication pathway between E. coli cells and $NP_{GOx\text{-}Dye}$

A refrigerated solution of **$NP_{GOx\text{-}Dye}$** was washed with ultrapure water (pH 7.5), divided into different fractions and brought to a final concentration of 1 $mg \cdot mL^{-1}$. In parallel, 2 mL of a mid-exponential β-galactosidase-expressing *E. coli* culture (optical density 0.5 at 600 nm) grown in LBA at 37 °C were washed with ultrapure water (pH 7.5) and concentrated to $4 \cdot 10^9$ $cells \cdot mL^{-1}$ in each of the corresponding fractions. **$NP_{GOx\text{-}Dye}$** and bacteria fractions were combined and incubated for 1 hour and then, either ultrapure water (for blank) and or lactose (2

%, as input) were added (time = 0 minutes). In parallel, release from **$NP_{GOx\text{-}Dye}$** in the presence of lactose and absence of bacteria was also monitored. Samples were shaken at 28 °C and aliquots were taken at scheduled times, centrifuged (5 minutes, 6000 rpm) and then the fluorescence of the solution at 595 nm was measured (λ_{exc} = 453 nm) to determine the relative cargo release. The obtained kinetics profile is plotted in Figure 2 of the main text.

Validation of the glucose-responsive linear communication pathway between the $NP_{GOx\text{-}Phl}$ and S. cerevisiae yeast cells

The refrigerated solutions of **$NP_{GOx\text{-}Phl}$** and **NP_{Phl}** were washed with ultrapure water (pH 7.5), divided into two fractions and brought to a final concentration of 10 $\mu g \cdot mL^{-1}$. In parallel, 2 mL of a mid-exponential RNR-GFP *S. cerevisiae* culture (optical density 0.5 at 600 nm) grown in YPD at 28 °C were washed with ultrapure water (pH 7.5), concentrated to $1.5 \cdot 10^8$ cells$\cdot mL^{-1}$ and added to **$NP_{GOx\text{-}Phl}$** and **NP_{Phl}** suspensions. Then, 2 % glucose was added to the mixtures and shaken at 28 °C for 3 hours. Finally, samples were centrifuged (5 minutes, 6000 rpm), washed two times with ultrapure water (pH 7.5) and the pellets were resuspended in 35 µL of ultrapure water. Finally, fluorescent GFP-associated signal was evaluated by confocal fluorescence microscopy (Figure 3, main text).

Validation of the nano-programmed cross-kingdom cell communication

S. cerevisiae budding yeasts RNR3-GFP were inoculated into fresh YPD (yeast extract peptone dextrose) and cultured for 3.5 hours at 28 °C. β-galactosidase-expressing *E. coli* bacteria were inoculated into fresh LBA and incubated for 2.5 hours at 37 °C. Both were kept in continuous shaking until reaching the log phase with an optical density (600 nm) of approximately 0.5, respectively.

Aliquots of 2 mL of the freshly inoculated yeast suspension and aliquots of 2 mL of the freshly inoculated bacteria suspension were mixed, concentrated, washed three times with glucose-free YPD and resuspended in glucose-free YPD at pH 7.5. In parallel, the refrigerated solutions of nanoparticles $\mathbf{NP_{GOx\text{-}Phl}}$ and $\mathbf{NP_{Phl}}$ were washed three times with ultrapure water (pH 7.5), divided into the two fractions where yeasts and bacteria have been already added and brought to a final concentration of 50 $\mu g \cdot mL^{-1}$. Media were supplemented with 1 % of fructose (final concentration). Then, an input of lactose (2 % final concentration, 55.5 mM) was added to each of the samples followed by incubation under continuous shaking for 3 hours at 28 °C. Finally, samples were centrifuged (5 minutes, 6000 rpm), washed two times with ultrapure water (pH 7.5) and the pellet was resuspended in 40 µL of ultrapure water. Intracellular overexpression of green fluorescent protein (GFP) was measured and quantified. Several fields of view for each condition in three independent experiments were registered obtaining similar results. Quantification of the fluorescence intensity was determined using ImageJ software.

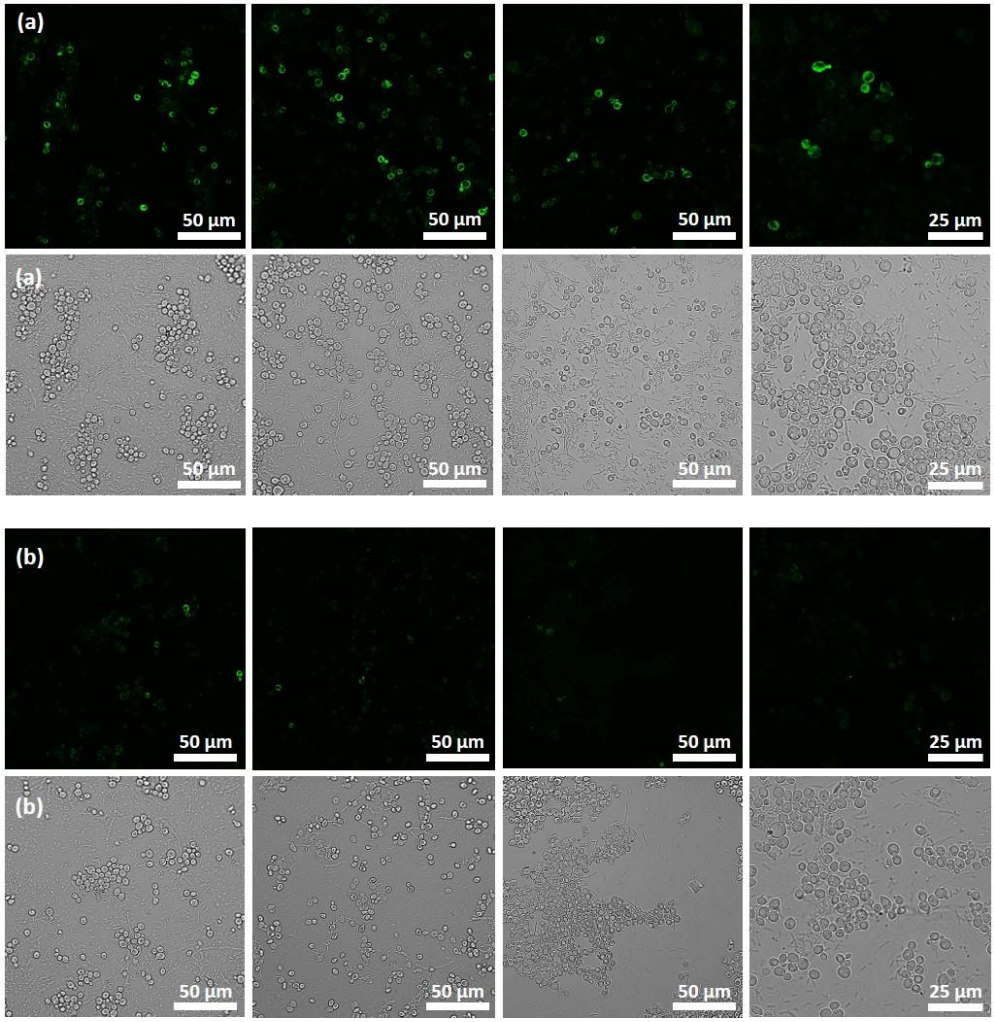

Figure S13. Validation of the nano-programmed cross-kingdom cell communication in mixtures of *E. coli* bacterium cells, nanoparticles and *S. cerevisae* cells. Representative confocal microscopy images of GFP signal induction in *S. cerevisiae* cells in bacteria-yeasts co-cultures after 3 hours for different conditions. *S. cerevisiae* yeast cells were incubated with (a) *E. coli* bacterium cells and phleomycin-loaded GOx-capped nanotranslator (**$NP_{GOx\text{-}Phl}$**); and (b) *E. coli* bacterium cells and control nanoparticles (**NP_{Phl}**, lacking GOx enzyme). Top: fluorescence images, and bottom: bright field images. Samples were incubated for 3 hours in medium containing 2 % lactose (input of the communication).

Additional control experiments with incomplete nanoparticles

The same procedure followed as described in the previous sections was carried out but using non-loaded GOx-functionalized nanoparticles (**NP_{Gox}**), and non-loaded GOx-lacking nanoparticles (**$NP_{Control}$**).

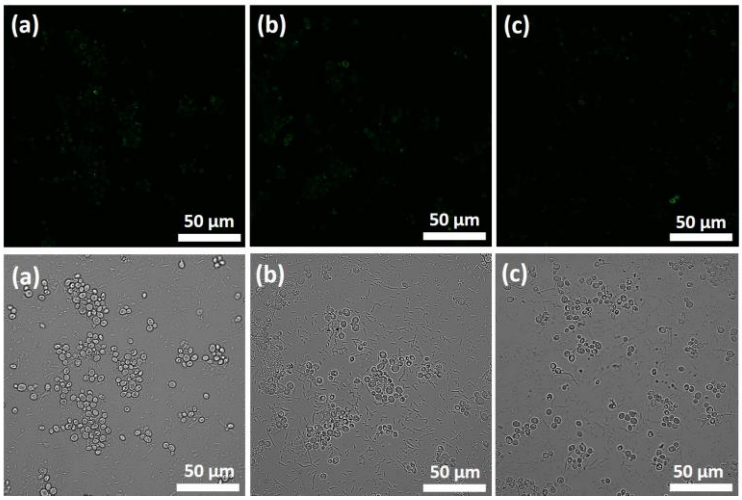

Figure S14. Additional control experiments. Representative confocal microscopy images of *S. cerevisiae* cells in bacteria-yeasts co-cultures after 3 hours for (a) incubation without nanoparticles, (b) incubation with unloaded GOx-functionalized nanoparticles (**NP_{Gox}**), and (c) incubation with unloaded GOx-lacking nanoparticles (**$NP_{Control}$**). Lactose 2 % was added in each mixture. Top: fluorescence images, and bottom: bright field images.

Table S4. Summary of the behaviour of the communication system in Boolean logic terms. Presence of a component is represented as 1 and absence as 0. In the presence of the input (1, lactose), the output signal (1) is only produced when all components are present. The output signal is considered 0 when the normalized quantification of the GFP-associated fluorescence intensity is less than 25 % of that found for the complete systems, that is, Input 1, Bacteria 1, Enzyme 1, Cargo 1 and Yeasts 1.

Entry	Input	Bacteria	Enzyme	Cargo	Yeasts	Output
1	0	0	0	0	0	0
2	0	0	0	0	1	0
3	0	0	0	1	0	0
4	0	0	0	1	1	0
5	0	0	1	0	0	0
6	0	0	1	0	1	0

Entry	Input	Bacteria	Enzyme	Cargo	Yeasts	Output
7	0	0	1	1	0	0
8	0	0	1	1	1	0
9	0	1	0	0	0	0
10	0	1	0	0	1	0
11	0	1	0	1	0	0
12	0	1	0	1	1	0
13	0	1	1	0	0	0
14	0	1	1	0	1	0
15	0	1	1	1	0	0
16	0	1	1	1	1	0
17	1	0	0	0	0	0
18	1	0	0	0	1	0
19	1	0	0	1	0	0
20	1	0	0	1	1	0
21	1	0	1	0	0	0
22	1	0	1	0	1	0
23	1	0	1	1	0	0
24	1	0	1	1	1	0
25	1	1	0	0	0	0
26	1	1	0	0	1	0
27	1	1	0	1	0	0
28	1	1	0	1	1	0
29	1	1	1	0	0	0
30	1	1	1	0	1	0
31	1	1	1	1	0	0
32	1	1	1	1	1	0
26	1	1	0	0	1	0
27	1	1	0	1	0	0
28	1	1	0	1	1	0
29	1	1	1	0	0	0
30	1	1	1	0	1	0
31	1	1	1	1	0	0
32	1	1	1	1	1	1

Supplementary references

1. J. Sambrook, E. R. Fritsch and T. Maniatis in *Molecular Cloning: A Laboratory Manual*, 2nd ed., Cold Spring Harbor Laboratory Press, NY, USA, **1989**.
2. W-K. Huh, J.V. Falvo, L. C. Gerke, A. S. Carroll, R. W. Howson, J-S. Weissman and E. K. O'Shea, *Nature* **2003**, *425*, 686-691.
3. a) E. Aznar, R. Villalonga, C. Giménez, F. Sancenón, M. D. Marcos, R. Martínez-Máñez, P. Díez, J. M. Pingarrón and P. Amorós, *Chem. Commun.* **2013**, *49*, 6391-6393; b) M. Holzinger, L. Bouffier, R. Villalonga and S. Cosnier, *Biosens. Bioelectron.* **2009**, *24*, 1128-1134; c) K. Hamasaki, H. Ikeda, A. Nakamura, A. Ueno, F. Toda, I. Suzuki and T. Osa, *J. Am. Chem. Soc.* **1993**, *115*, 5035-5040.

Chapter 7. Conclusions and Perspectives

The development of mesoporous materials equipped with molecular gates as stimuli-responsive delivery systems is an exciting area in nanotechnology which has been widely exploited in nanomedicine and sensing applications in the last decade. However, more advanced functionalities cannot be achieved by simple devices but by designing programmed communities acting coordinately. In this context, this PhD Thesis has explored the construction of stimuli-responsive nanodevices based on mesoporous silica nanoparticles with implemented communication capabilities and the evaluation and optimization of such communicative performance in different scenarios.

The first chapter of this PhD Thesis has been dedicated to introducing concepts related to nanotechnology, mesoporous silica materials, stimuli-responsive gated materials, Janus particles, biocomputing and chemical communication as well as recent developments in such fields.

In the second chapter, the objectives developed in the following experimental chapters have been stated.

The third chapter reported a biocomputing delivery system based on Janus gold-mesoporous silica nanoparticles capable of chemically communicating with the environment and processing the information mimicking a 1-to-2 demultiplexer Boolean logic function which results in a programmed cargo release even in cellular media. The design is based on the incorporation of two enzymes as chemical information-processing counterparts which transform a certain combination of stimuli in the solution into “chemical messengers” that uncap the pores triggering payload release. The work desmonstrate the use of enzyme-functionalized hybrid mesoporous nanodevices as a valuable and versatile strategy to tailor different biocomputing elements that may be implemented in individual nanoparticles acting according to environmental information. We envisage the interconnection of these nanodevices by means of chemical communication, creating complex networks that operate as advanced electronic circuitries performing sophisticated logic tasks. In the field of drug delivery, this strategy may open unexploited prospects in smart therapies and personalized treatments.

In the fourth chapter, it is presented a circular model of communication within a network of three different enzyme-functionalized Janus nanoparticles via a hierarchically programmed exchange of chemical messages. The system is based on the double receiver-sender behaviour of enzyme-functionalized hybrid mesoporous nanodevices, which sense and transform inputs delivering their entrapped cargo which acts as input of the subsequent nanodevice. Although the presented design is a proof of concept which leads to a dye release as final output, it illustrates the potential of using abiotic nanodevices to design multistep signaling pathways. It also demonstrates how artificial nanodevices can be connected by means of molecular communication, yielding systems that show a collective

synergic behaviour. We believe that the idea of developing multicomponent nanoscale cooperative communities capable of communicating may open new directions in the near future in areas such as biomedicine and information and communication technologies.

In the fifth chapter, an interactive chemical communication system between enzyme-functionalized Janus nanoparticles and a living organism (engineered GFP-expressing *Saccharomyces cerevisiae* budding yeast) has been developed. GFP expression in yeasts occurs after biunivocal communication in which the sender (yeast) detects an input, sends a chemical message to the receiver (abiotic nanodevice), and the receiver decodes and processes the information channeling a message back to the original sender. These findings demonstrate how our abiotic nanodevices can be connected to living microorganisms by means of molecular communication leading to systems with a cooperative behaviour.

In the sixth chapter, it is presented a linear communication system between two different microorganisms (engineered β-galactosidase-expressing *Escherichia coli* bacteria and engineered GFP-expressing *Saccharomyces cerevisiae* budding yeasts) mediated by an enzyme-functionalized capped mesoporous nanodevice which acts as a chemical translator. Both microorganisms are cocultivated with no interaction between them. Upon exposure to an input, the nanotranslator is able to translate bacterial messages into a chemical language which is understood by yeasts triggering GFP expression. We believe this strategy of connecting cells lays the foundations of advanced functions previously unaddressed in sensing and biomedicine.

A general conclusion that can be extracted from this PhD Thesis is that enzyme-functionalized hybrid mesoporous nanodevices display communication capabilities which can be exploited in different scenarios. Enzymes provide gated hybrid nanodevices with processing tools to read (bio)chemical information from

the environment and transform them into chemical species that trigger cargo delivery only in the presence of certain specific stimuli. Considering the large variety of molecules which can be processed by enzymatic receptors, the wide range of developed stimuli-responsive gatekeepers as well as the numerous different species potentially susceptible to be encapsulated in mesoporous silica nanoparticles, almost limitless combinations may be envisaged to establish communication pathways between entities that otherwise could not naturally interact. We envision this could allow the development of swarms of nanodevices able to interact with their neighbours and local environment leading to advanced systems with new cooperative functionalities.

In summary, we have presented in this PhD Thesis the design, preparation, and evaluation of enzyme-functionalized hybrid mesoporous nanodevices with communicative capabilities exhibiting different behaviours: environment-nanodevice communication, nanodevice-nanodevice communication and nanodevice-microorganism communication involving linear, interactive and circular communicative models within networks of up to three members. It is our hope that the results presented in this PhD Thesis will inspire the development of new advanced strategies with smart materials in different areas such as nanomedicine, sensing and communication technologies.

Gracias al Ministerio de Educación, Cultura y Deporte por el contrato concedido para realizar esta tesis doctoral.